PEKING UNIVERSITY
UNIVERSITÉ LIBRE DE BRUXELLES

DOCTORAL THESIS

Measurement of the differential cross section of Z boson production in association with jets at the LHC

Author:
Qun WANG

Supervisor:
Prof. Yong BAN (PKU)
Prof. Laurent FAVART (ULB)

June 2018

PEKING UNIVERSITY
UNIVERSITÉ LIBRE DE BRUXELLES

Abstract

Doctor in Science

Measurement of the differential cross section of Z boson production in association with jets at the LHC

by Qun WANG

This thesis presents the measurement of the differential cross section of Z boson production in association with jets (Z+jets) in proton-proton collision at the center-of-mass energy of 13 TeV. The data has been recorded with the CMS detector at the LHC during the year 2015, corresponding to an integrated luminosity of 2.19 fb^{-1}. A study of the CMS muon High Level Trigger (HLT) with the data collected in 2016 is also presented.

The goal of analysis is to perform a first measurement at 13 TeV of the cross sections of Z+jets as a function of the jet multiplicity, its dependence on the transverse momentum of the Z boson, the jet kinematic variables (transverse momentum and rapidity), the scalar sum of the jet momenta, and the balance in the transverse momentum between the reconstructed jet recoil and the Z boson. The results are obtained by correcting the detector effects, and are unfolded to particle level. The measurement are compared to four predictions using different approximations: at the leading-order (LO), next-to-leading-order (NLO) and next-to-next-to-leading order (NNLO) accuracy. The first two calculations used MADGRAPH5_AMC@NLO interfaced with PYTHIA8 for the parton showering and hadronisation, one of which includes matrix elements (MEs) at LO, another includes one-loop corrections (NLO). The third is a fixed-order calculation with NNLO accuracy for Z+1 jet using the N-jettiness subtraction scheme (N_{jetti}). The fourth uses the GENEVA program with an NNLO calculation combined with higher-order resummation.

A series of studies on the HLT double muon trigger are also included. Since 2015 the LHC reached higher luminosity, more events are produced inside the CMS detector per second, which resulted in more challenges for the trigger system. The work presented includes the monitoring, validation and the calibration of the muon trigger paths since 2016.

Key words: physics, CMS, standard model, Quantum Chromodynamics, cross section, Z boson, jets, MADGRAPH5_AMC@NLO, GENEVA, high level trigger.

Acknowledgements

As a joint PhD, I have received supports from both Peking University and Université Libre de Bruxelles. The research projects in this thesis were funded by China Scholarship Council.

First of all, I would like to thank my promotors Prof. Yong Ban and Prof. Laurent Favart for supervising with their guidance, support and advices during the PhD period. I started to join the high energy physics in 2013 with supervision of Prof. Ban. He taught me the general workflow of particle reconstruction, he gave lectures on high energy physics experiment, and he gave me lots of suggestions and supports on research. Prof. Ban also encouraged me to apply the joint PhD program with Université Libre de Bruxelles, which revealed a new start in my life. Laurent welcomed me in Brussels the first I arrived. Laurent is so nice to introduce me to the whole laboratory, gave me private lectures on QCD theory, supported me to attend a few summer schools and conferences. He is very patient when we discuss questions, and correct my expression of physics in English. Thanks to my two kind supervisors, I improved my understanding of physics and ability to perform physics analysis.

I would like to thank the members of my jury, Prof. Yajun Mao, Prof. Pascal Vanlaer, Dr. Hannes Jung, Prof. Yanwen Liu and Dr. Anastasia Grebenyuk to go through the entire manuscript and provide both conceptual and textual comments, this truly improved the quality of my manuscript. I would like to express gratitude to Prof. Qiang Li, who guided my first research in CMS experiments. Thanks to him, my first work went smooth and I learned a lot from that experience. I am grateful to Philippe, Anastasia, Hugues and Feng to help me with data analysis work and I enjoy the time working with them. I would like to thank the members of my community Barbara Clerbaux and Gilles De Lentdecker to follow my status in the study. I am also thankful to my colleagues David, Reza, Cécile, Yifan, Zixuan, Wenxing, Amandeep, Diego, Yannick, and many other nice colleague in IIHE. Thanks for making my life in Belgium more colorful. I would like to thank my colleagues and friends in China also, they are Zijun, Zhaoru, Daneng, Fengyun, Yahui… It is my honor to know all of you and I appreciate all the nice memories we have created.

In the end, I would like to thank my family for their understandings, supports and trust. I am also thankful to my future family-in-law for their sweet care and understanding. I also want to thank my love Patrick Connor for being there with me. I am very lucky to have all you in my life.

Contents

List of Figures

List of Tables

Chapter 1

Introduction

The standard model (SM) of particle physics describes the elementary particles and the interactions between them: the strong, the weak and the electromagnetic interactions. A number of experimental results from the high energy experiments, such as the Tevatron at Fermilab between 1983 and 2011, the Large Electron-Positron Collider (LEP) at CERN between 1989 and 2000, the Hardon-Electron Ring Accelerator (HERA) at DESY between 1992 and 2007, the Large Hadron Collider (LHC) at CERN from 2010, show good agreement between the measurement and theoretical predictions estimated by SM at different energy scales. One very important discovery in particle physics recently is the Higgs boson, the cornerstone and the last missing piece of the SM, which has been found by CMS and ATLAS experiments at the LHC in 2012. The Higgs boson is the scalar gauge boson causing the electroweak symmetry breaking and explains how the particles could obtain a mass without violating the gauge invariance of the theory.

LHC, as the current most powerful particle accelerator, provides a chance to explore the particle physics at TeV energy scale. Since 2015, the proton-proton (p-p) collisions have been taking place in the LHC at a center-of-mass energy $\sqrt{s} = 13$ TeV, which is the highest energy ever reached in laboratory. After the discovery of the Higgs, the properties of the Higgs, more precise measurements of SM physics at high energy and searches for new particle physics beyond SM still need to be done.

Due to the high energy at the LHC, a huge majority of the events taking place will contain jets (groups of hadrons) and the multiplicity of jets is higher than ever observed before. The study of the jet production is therefore crucial both for the understanding of the production mechanism itself and for the estimation of their production in association with particles like the Higgs boson, the top quark or in search for new physics.

The research to be presented in this thesis is the differential cross section measurement of Z boson production in association with jets from the p-p collisions at the center-of-mass energy of 13 TeV [1]. The measurements of this process provide stringest tests on the perturbative quantum chromodynamics (pQCD), and is crucial for understanding and modeling of QCD interactions. This process is also a dominant background for a number of SM processes such as Higgs productions and $t\bar{t}$ production, as well as in some searches for physics beyond the SM. With the data taken during 2015, precise measurements of the differential cross section of Z + jets could be achieved. These studies of this process help us significantly to exploit the potential of the LHC experiments.

Comparison of the measurements with predictions motivates Monte Carlo (MC) generator development and improves our understanding of the prediction uncertainties.

I made significant contributions to the presented data analysis. I was in charge of the measurement of Z+jets in the di-muon channel. My contributions that covered the complete analysis including the di-electron channel, were studies the dominant background $t\bar{t}$ with novel methods; Implemented new variables of the p_T balance (Jets-Z balance, JZB; p_T balance) in DY measurement, and performed all the related cross check; Studied the effects from QCD background, checked pileup stability, unfolded the measurement to the particle level, computed the uncertainties from various sources and extracted the differential cross sections.

The physics analysis presented in the thesis is similar in many aspects to the Z+jets cross section obtained at 8 TeV and detailed in the PAS SMP-13-007 [2]. More identical details are illustrated in this reference and the internal notes AN-13-049 [3]. The Z+jets cross section measurement with data collected in 2016 is on-going. Besides the variables we measured with data collected in 2015, some more interesting variables and more phase space will be covered.

Another work mentioned in this thesis is the validation and the calibration of CMS muon trigger since 2016. The general trigger system is introduced, and the methods to monitor and measure the trigger efficiency are also explained. At the end, the trigger scale factors have been computed, which is an important correction factor needed in the Z+jets measurements to compensate the difference between the data events detected in the CMS detector and the MC simulation.

This thesis includes six chapters: the theory elements related to the SM; the general introduction of the experimental setup, CMS; the events reconstructions; the physics analysis mentioned above; the conclusion and the validation and calibration of the muon trigger paths in appendix.

Chapter 2

Theory Elements

“What is matter made of?” That is the question bothered human since thousands years ago. Ancient Chinese philosopher believed that the matter is made of five elements: wood, fire, earth, metal and water. Since 17H century, it was found that everything consists of atoms, with a scale of 10^{-10} m. In 1897, J.J. Thomson’s discovery of the electron revealed the opening of the elementary particle physics. In 1909, Rutherfold’s famous scattering experiment showed the nucleus, with the size of 10^{-14} m, is at the center of the atom. With the discoveries of the proton, neutron, photon, muon, neutrino, quarks and gluons, the particle physics is more and more accomplished. Thanks to those great scientists, we know the atom is made of electrons orbiting around a nucleus, which is composed of protons and neutrons consisting of quarks. These elementary particles and the interactions between them are described by a comprehensive theory called Standard Model (SM) [4, 5, 6, 7].

In this chapter, a brief introduction to the Standard Model of particle physics will be provided. In particular, it gives an overview of the fundamental particles, the relationship between them and their interactions.

2.1 Standard Model

The Standard Model of particle physics provides the best description of the elementary particles and their interactions at the most fundamental level. All the interactions can be described by four forces: the strong force, the weak force, the electromagnetic force and the gravitational force. The gravitational force, which can be neglected at elementary level if the energy is lower than the Planck scale (1.22×10^{19} GeV), is not included in the SM.

According to the SM, the elementary particles are classified as fermions and bosons depending on whether they have integer or half integer spin, as illustrated in figure 2.1. The fermions, constituting the matter, include six types of quarks and leptons with spin $\frac{1}{2}$. Quarks and leptons are grouped in three different generations, and each generation is a heavier copy of the first one. Except ν, all particles form 2^{nd} and 3^{rd} generations are unstable. All the quarks and leptons have associated antiparticles with the same mass but opposite charges and parities.

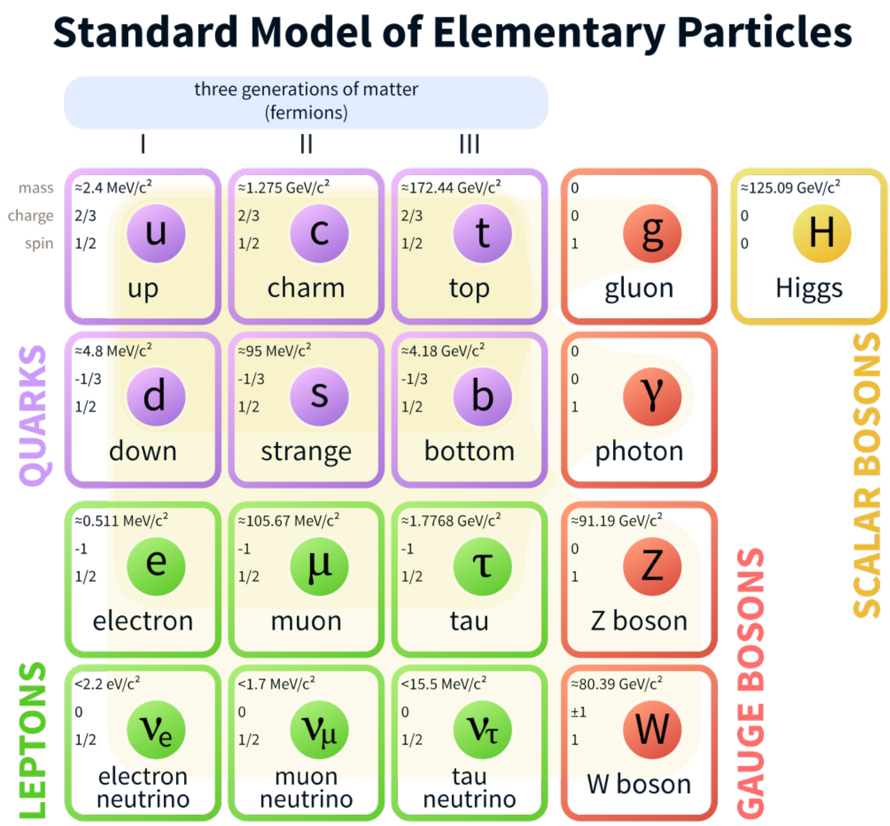

FIGURE 2.1: Overview of the elementary particles of the SM.

Quarks include the up (u), down (d) quark in the first generation; charm (c), strange (s) quark in the second generation; top (t) and bottom (b) quark in the third generation, and each quark carries the colour charge such that they can interact through the strong force, and are strongly bounded to other quarks to form hadrons. The u, c and t quarks have $\frac{2}{3}$ electric charge, while the d, s and b quarks have $-\frac{1}{3}$ charge. Besides the electric charge, quarks also carry the weak isospin. Hence they can also interact through the electromagnetic and weak force. No isolated free quarks have been observed. The bound states of three quarks form $baryons$, such as the proton or the neutron, and the combinations of a quark and an anti-quark yield a $meson$, for example the pion or the kaon. Mesons and baryons are referred to as hadrons, which are subjected to the strong interactions.

Leptons include electron e, electron neutrino v_e, muon μ, muon neutrino v_μ, tau τ, tau neutrino v_τ. The three neutrinos do not carry electromagnetic charge, so they only interact through the weak interactions, making them very difficult to be observed. The other leptons, e μ and τ carrying electric charge -1, can interact both electromagnetically and via the weak interaction.

Bosons, with an integer spin, include the mediators of the forces in the SM and the scalar boson, the Higgs. The mediators of the strong interaction are eight gluons (g), while the $W^\pm$ and Z bosons mediate the weak force, and the photon (γ) for the electromagnetic force. No mediator for the gravitational force has been discovered so far. The four type of forces and some of their characteristics are detailed in the table 2.1

TABLE 2.1: Illustrations of the four type of force, their mediators, range and relative strength

Interaction	mediators	Range	Relative strength
Strong	8 gluons	10^{-15}	1
Weak	$W^+,\ W^-,\ Z$	10^{-18}	10^{-14}
Electromagnetic	photon	∞	10^{-3}
Gravitational	graviton?	∞	10^{-43}

Finally, the scalar boson, the Higgs, is the quantum manifestation of the Higgs field, leading the $W^{\pm}$ and Z boson and the fermions obtaining their masses. The Higgs boson is a boson with no spin, electric charge nor colour charge, and has been discovered in 2012.

2.2 The Equations Governing the Interactions

The SM is a quantum field theory that groups the electroweak theory (EWK) together with the quantum chromodynamics (QCD), which includes the electromagnetic, weak and strong interactions. The SM is a gauge theory based on the $SU(3)_C \times SU(2)_L \times U(1)_Y$ symmetry group. The first term $SU(3)_C$ corresponds to the group of strong interactions with colour transformations between gluons and quarks. The second and third terms $SU(2)_L \times U(1)_Y$ form the group symmetry of the electromagnetic and weak interactions, where L refers to the left chiral nature of the $SU(2)$ coupling, and Y to the corresponding $U(1)$ symmetry acting on the weak hypercharge.

The fundamental objects and their associated quantum fields are listed:

- Fermi fields: ψ
- Electroweak boson fields: W^1, W^2, W^3, B
- Gluon fields: G_a
- Higgs fields: φ

Three gauge fields W^1, W^2, W^3 are associated to the $SU(2)_L$ with three generators that can be expressed as half of the Pauli matrices:

$$\begin{aligned} T_1 &= \frac{1}{2}\sigma_1 = \frac{1}{2}\begin{pmatrix} 0 & 1 \\ 1 & 0 \end{pmatrix} \\ T_2 &= \frac{1}{2}\sigma_2 = \frac{1}{2}\begin{pmatrix} 0 & -i \\ i & 0 \end{pmatrix} \\ T_3 &= \frac{1}{2}\sigma_3 = \frac{1}{2}\begin{pmatrix} 1 & 0 \\ 0 & -1 \end{pmatrix} \end{aligned} \tag{2.1}$$

The generators T^a satisfy the Lie algebra:

$$[T^a, T^b] = i\epsilon^{abc}T_c\ , \quad \epsilon^{123} = 1 \tag{2.2}$$

where ϵ^{abc} is an fully anti-symmetric tensor.

Given all the field of the SM the corresponding Lagrangian can be written down with satisfying causality, gauge invariance and Lorentz invariance. The Lagrangian is theoretically possible to describe all the interactions in the SM.

2.2.1 The Electroweak Interaction

The electroweak interaction is the unified description of two fundamental interactions: the electromagnetic and weak interactions. This unification is accomplished under an $SU(2)_L \times U(1)_Y$ gauge group. There are three massless gauge boson states with different weak isospin from $SU(2)_L$ (W^1, W^2, W^3), and one single massless gauge boson state with weak hypercharge from $U(1)_Y$. The weak hypercharge Y carried by the matter fields is related to the electric charge Q and the weak isotopic charge T^3 with:

$$Y = Q - T^3. \tag{2.3}$$

The Lagrangian for a massless free fermion field ψ belonging to a $SU(2)_L \times U(1)_Y$ representation can be written as:

$$\mathcal{L} = i\bar{\psi}\gamma^\mu \partial_\mu \psi \tag{2.4}$$

This expression 2.4 is not invariant under a $SU(2)_L \times U(1)_Y$ transformation. The ψ is transformed as:

$$\psi \to \psi' = exp(i\tfrac{1}{2}g_W T^k \Lambda^k(x))exp(i\tfrac{1}{2}g'_W Y\alpha(x))\psi, \tag{2.5}$$

where g_W represents the $SU(2)_L$ gauge coupling and g'_W is the $U(1)_Y$ gauge coupling. The matrices T^k form a representation of the $SU(2)_L$ weak isospin algebra and Y is a scalar forming a representation of the $U(1)_Y$ algebra. The first term represents an $SU(2)_L$ local rotation around the axis $\Lambda^k(x)$ in the space of the weak isospin, and the second term represents a local phase shift $\alpha(x)$ in the space of weak hypercharge.

To make the Lagrangian gauge invariant, a covariant equivalent D_μ is introduced to replace the partial derivatives ∂_μ:

$$(D_\mu)_{ij} = \delta_{ij}\partial_\mu + ig_W(T^k W^k_\mu)_{ij} + ig'_W Y\delta_{ij}B_\mu, \tag{2.6}$$

Moreover, this also introduces interaction between the gauge files and the fermionic fields as indicated by the presence of terms involving both the gauge and the fermionic fields.

Finally the Lagrangian of the electroweak interaction is gauge invariant and is written as:

$$\mathcal{L}_{\text{EW}} = i\bar{\psi}\gamma^\mu D_\mu\psi - \tfrac{1}{4}W^{\mu\nu}_a W^a_{\mu\nu} - \tfrac{1}{4}B^{\mu\nu}B_{\mu\nu} \tag{2.7}$$

for $a = 1, 2, 3$. The $W^a_{\mu\nu}$ and $B_{\mu\nu}$ in the Lagrangian stands for the field strength tensor of the $SU(2)_L$ gauge field W_a and $U(1)_Y$ gauge field B, respectively. They are given by:

$$\begin{aligned} W^a_{\mu\nu} &= \partial_\mu W^a_\nu - \partial_\nu W^a_\mu - g_W \epsilon^{abc} W^b_\mu W^c_\nu, \\ B_{\mu\nu} &= \partial_\mu B_\nu - \partial_\nu B_\mu. \end{aligned} \tag{2.8}$$

The third term in the definition of $W^a_{\mu\nu}$ indicates the self-interaction of the W^a bosons and is a direct consequence of the non-Abelian nature of $SU(2)$.

Applying the spontaneous symmetry breaking from $SU(2)_L \times U(1)_Y$ to $U(1)_{em}$ of the Brout-Englert-Higgs mechanism, the $W^\pm$, Z^0 bosons and the photon are produced. Here, $U(1)_{em}$ and $U(1)_Y$ are different copies of $U(1)$. The spontaneous symmetry breaking makes the W^3 and B bosons coalesce into two bosons: the Z^0 boson and the photon (γ),

$$\begin{pmatrix} \gamma \\ Z^0 \end{pmatrix} = \begin{pmatrix} \cos\theta_W & \sin\theta_W \\ -\sin\theta_W & \cos\theta_W \end{pmatrix} \begin{pmatrix} B \\ W^3 \end{pmatrix} \tag{2.9}$$

where θ_W is the weak mixing angle. This introduces a mismatch between the mass of the Z^0 and the mass of the $W^\pm$ particles, denoted as M_Z and M_W, respectively:

$$M_Z = \frac{M_W}{\cos\theta_W}. \tag{2.10}$$

While the W^1 and W^2 bosons is given by:

$$W^\pm = \frac{1}{\sqrt{2}}(W^1 \mp iW^2). \tag{2.11}$$

2.2.2 The Quantum Chromodynamics

QCD is a quantum field theory, non-abelian relying on the gauge symmetry group $SU(3)$ to describe the strong interactions between quarks and gluons. Superficially QCD appears like a stronger version of the QED with one extra charge of colour, and with eight gluons replacing the single photon. There are three type of colour charge: red, blue and green. A quark carries any single colour, while an antiquark carries anticolour, while eight types of gluons, as the mediator of the strong interaction, carry a combination of the colours and anticolours. The eight gluons can be written: $r\bar{g}$, $g\bar{r}$, $r\bar{b}$, $b\bar{r}$, $g\bar{b}$, $b\bar{g}$, $\frac{1}{2}(r\bar{r} - g\bar{g})$ and $\frac{1}{\sqrt{6}}(r\bar{r} + g\bar{g} - 2b\bar{b})$.

However, no free quarks have been detect, which would be observed with fractionally charged particles. Non-observation of free quarks is explained by the hypothesis of $colour\ confinement$, implying that quarks are always observed to be confined to bound colourless states. $Color\ confinement$ is one of the two main properties of QCD, and the other properties is $asymptotic\ freedom$: the quarks can be treated as quasi-free particles rather than being strongly bound within the proton at high energy scale, which scale range is accessible in high-energy collider experiments, such as the LHC.

The gauge invariant QCD Lagrangian can be written as:

$$\mathcal{L}_{\rm QCD} = \bar{\psi}_i \left(i(\gamma^\mu D_\mu)_{ij} - m\,\delta_{ij}\right)\psi_j - \frac{1}{4}G^a_{\mu\nu}G^{\mu\nu}_a \tag{2.12}$$

where ψ_i is the quark field in the fundamental representation of the $SU(3)$ gauge group. D_μ is the gauge covariant derivative, given in 2.16; the γ^μ are Dirac matrices; the variable m corresponds to the quark mass; the $G^a_{\mu\nu}$ represents the gauge invariant gluon field strength tensor, with the index a running over the eight colour degrees of freedom of the gauge group. The $G^a_{\mu\nu}$ is derived from the gluon field $\mathcal{A}_\mu$, as given by:

$$G^a_{\mu\nu} = \partial_\mu \mathcal{A}^a_\nu - \partial_\nu \mathcal{A}^a_\mu - g_s f^{abc}\mathcal{A}^b_\mu \mathcal{A}^c_\nu \tag{2.13}$$

where g_s is the $SU(3)$ gauge coupling strength, and f^{abc} are the structure constants of $SU(3)$. Given QCD is a non-Abelian gauge theory, the last term in 2.13 gives rise to gluon self-interactions. The transformations of quark field are given by:

$$\psi \to \psi' = exp(i\tfrac{1}{2}g_s T^a \mathcal{A}^a)\psi, \tag{2.14}$$

where the matrices T^a form the representation of the $SU(3)$ colour algebra. The matrices T^a are related to the Gell-Mann matrices λ^a [1] by:

$$T^a = \tfrac{1}{2}\lambda^a. \tag{2.15}$$

The covariant derivatives D_μ are provided by:

$$(D_\mu)_{ij} = \partial_\mu \delta_{ij} + i g_s (T^a \mathcal{A}^a_\mu)_{ij} \tag{2.16}$$

where the indices i and j run over the triplet representation of the colour group. The last item of the Lagrangian represents the gluon field dynamics.

2.2.3 The Running of Coupling Constants

The coupling constants, the strength of the different interactions, are found not to be constant, which makes the fundamental interactions more complex. Especially for

[1] The Gell-Mann matrices λ^a:

$$\lambda^1 = \begin{pmatrix} 0 & 1 & 0 \\ 1 & 0 & 0 \\ 0 & 0 & 0 \end{pmatrix}, \quad \lambda^2 = \begin{pmatrix} 0 & -i & 0 \\ i & 0 & 0 \\ 0 & 0 & 0 \end{pmatrix}, \quad \lambda^3 = \begin{pmatrix} 1 & 0 & 0 \\ 0 & -1 & 0 \\ 0 & 0 & 0 \end{pmatrix},$$

$$\lambda^4 = \begin{pmatrix} 0 & 0 & 1 \\ 0 & 0 & 0 \\ 1 & 0 & 0 \end{pmatrix}, \quad \lambda^5 = \begin{pmatrix} 0 & 0 & -i \\ 0 & 0 & 0 \\ i & 0 & 0 \end{pmatrix}, \quad \lambda^6 = \begin{pmatrix} 0 & 0 & 0 \\ 0 & 0 & 1 \\ 0 & 1 & 0 \end{pmatrix},$$

$$\lambda^7 = \begin{pmatrix} 0 & 0 & 0 \\ 0 & 0 & -i \\ 0 & i & 0 \end{pmatrix}, \quad \lambda^8 = \frac{1}{\sqrt{3}}\begin{pmatrix} 1 & 0 & 0 \\ 0 & 1 & 0 \\ 0 & 0 & -2 \end{pmatrix}$$

QCD, it is tightly related to confinement, which is the fact that quarks and gluons are not observed freely.

The strength of the interaction between a photon and an electron is determined by the coupling at the QED vertex. According to QED theory, there are always spontaneous electric pair creation and annihilation taking place in the vacuum, called quantum fluctuation. An electron will induce such pairs forming electric dipoles surrounding itself, those dipoles will align in a specific direction due to the electric field of the electron forming a shielding cloud. This effect is called vacuum polarization. Far away from the electron, we observe some effective coupling, the effective coupling constant of electromagnetic interaction:

$$\alpha_{em} = \frac{e^2}{4\pi} \approx 1/137 \tag{2.17}$$

If getting closer and closer to the electron through the shielding cloud, one shows more sensitive to the bare electron charge, and the corresponding effective coupling constant becomes larger and larger.

As for QCD, a non-Abelian gauge theory to describe the strong interaction, there are not only pairs of quark and antiquark creation and annihilation resulting in colour dipoles, but also loops of gluons in the neighbourhood of a quark. During the vacuum polarization, the former screens the colour field, while the latter reinforces the colour field. Therefore, the effective strong coupling constant depends on the number of quark flavors and colours. In fact, the gluon loop effect dominates and the effective coupling constant is found to increase with the distance: large distance resulting in strong coupling leads to the confinement of the quarks inside hadrons; the quarks appear to be more free while they interact at a large energy scale Q. The strong coupling constant is found to be close to unity with the energy scale around 200 MeV, defined as Λ_{QCD}. If energy scale of an observer is far above the value of Λ_{QCD} (Q $\gg \Lambda_{QCD}$), the strong interaction can be computed using a perturbative approach. Otherwise, the non-perturbative effects dominate. When the reaction energy is very high, the quarks and gluons are seen as free particles, known as the asymptotic freedom.

In general, the running of the coupling constant α can be obtained formally by the renormalization group equation (RGE):

$$Q^2 \frac{\partial \alpha}{\partial Q^2} = \beta(\alpha) \tag{2.18}$$

The β function encodes the energy scale dependence of the coupling constant α. The one-, two- and three-loop β-function in QCD was calculated already in papers [8, 9, 10], respectively. In QED, the first non-vanishing term is found to be:

$$\beta_{QED}(\alpha_{em}) = \frac{1}{3\pi}\alpha_{em}^2 + \dots \tag{2.19}$$

which is positive. The α_{em} increases with the energy scale, and the first-order dependence of the coupling constant can be written as:

$$\alpha_{em}(Q^2) = \frac{\alpha_{em}(\mu_R^2)}{1 - \frac{\alpha_{em}(\mu_R^2)}{3\pi} log \frac{Q^2}{\mu_R^2}} \tag{2.20}$$

where the μ_R^2 stands for an arbitrary energy scale chosen for QED renormalization. This formula describes the coupling constant evolution between the renomarlisation scale μ_R and the physical scale Q.

When it comes to QCD, the β function is expanded in powers of α_s in a perturbative way. In the case of two loops:

$$\beta_{QCD}(\alpha_s) = Q^2 \frac{\partial \alpha_s}{\partial Q^2} = -\sum_{i=0}^{\infty} \beta_i \alpha_s^{i+2} = -b\alpha_s^2(1 + b'\alpha_s + O(\alpha_s)), \tag{2.21}$$

where

$$b = \frac{11C_F - 2n_f}{12\pi}, b' = \frac{51C_F - 19n_f}{2\pi(11C_F - 2n_f)} \tag{2.22}$$

here $C_F = (n_c^2 - 1)/2n_c$, n_c is the number of colour. The n_f is the number of active quark flavours. The strong coupling constant $\alpha_s(Q^2)$ is found to decrease when increase the energy scale Q^2 shown. Considering the first non-vanishing term, this leads to:

$$\alpha_s(Q^2) = \frac{\alpha_s(\mu_R^2)}{1 + \frac{11C_F - 2n_f}{12\pi}\alpha_s(\mu_R^2) log \frac{Q^2}{\mu_R^2}} \tag{2.23}$$

The dependence of Strong coupling constant on the energy scale is shown in figure 2.2.

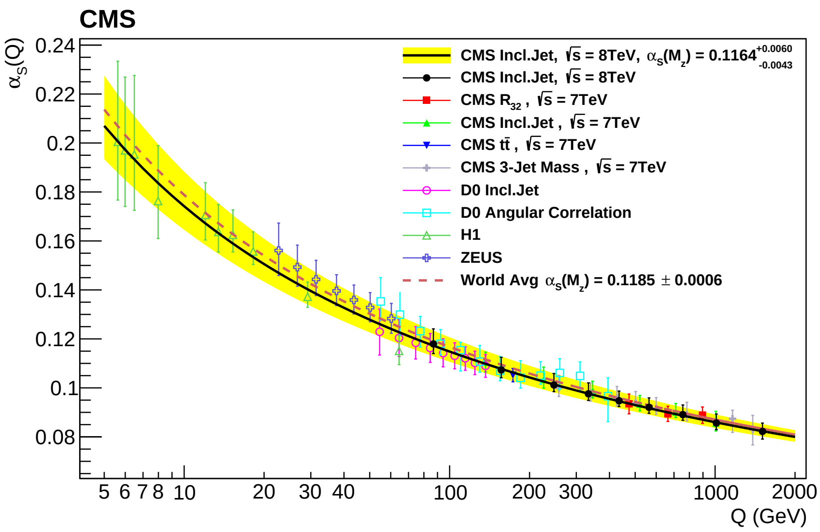

FIGURE 2.2: The strong coupling $\alpha_s(Q)$ (solid line) and its total uncertainty (band) as determined in [11] using a 2-loop solution to RGE as a function of the energy scale Q.

2.3 Z + Jets in Proton-Proton Collision

In the thesis, the production of Z boson in association with jets at CMS is presented, which is dominated by the Drell-Yan process. The Drell Yan process occurs at high energy in hadron-hadron scattering, first suggested by Sidney Drell and Tung-Mow Yan in 1970 [12]. It takes place when a quark from one hadron and an antiquark from another hadron annihilate, creating a virtual photon or a Z boson which decays into a charged lepton-antilepton pair. As mentioned in section 2.2.2, quarks and gluons are confined in hadrons, in high energy collisions, short time interactions ($t \sim 1/Q$) can be seen as taking place on quasi-free partons (quarks or gluons), called asymptotic freedom In these conditions, one may apply the factorization property. According to factorization, the hadron cross section expression can be separated into the hadron intrinsic structure and the partonic cross section. The hadronic structure, mainly in the non-perturbative regime, is described in terms of Parton Distribution Functions (PDFs), while the partonic cross section can be computed using a perturbative approach of the electroweak and strong interactions. Even though the property of factorization and the universality of PDFs is observed experimentally, it is not always proven and only assumed to be true. However, in the case of the DY process, a theoretical proof of factorization has been established [13].

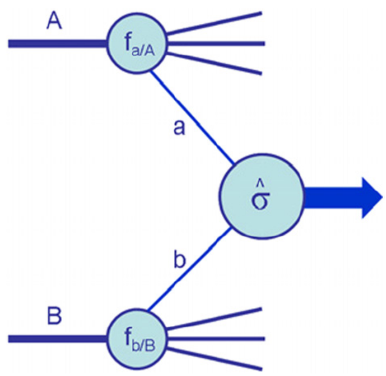

FIGURE 2.3: The interaction between two hadrons according to QCD factorization theorem.

The hadronic cross section of the DY process $\sigma_{AB\to l^+l^-+X}$, illustrated in figure 2.3, where A and B are hadrons and X some hadronic activity due to the proton break-ups, with the PDF $f_{q/A}(x)$ and the corresponding partonic cross sections with at lowest-order $\hat{\sigma}_{q\bar{q}\to l^+l^-}$, can be written as:

$$\sigma_{AB\to l^+l^-+X} = \sum_q \int dx_1 dx_2 f_{q/A}(x_1,\mu_F^2) f_{\bar{q}/B}(x_2,\mu_F^2) \times \hat{\sigma}_{q\bar{q}\to l^+l^-}(\alpha_s(\mu_R^2), Q^2/\mu_R^2, \mu_F^2) + (q \leftrightarrow \bar{q}) \tag{2.24}$$

where μ_R^2 is the renormalization scale, and μ_F^2 is the factorization scale. Due to the asymptotic freedom, the partonic cross sections can be computed with a perturbative approach, and the factor $\hat{\sigma}$ can be expanded in powers of the strong coupling constant α_s:

$$\hat{\sigma}_{q\bar{q}\to l^+l^-} = [\hat{\sigma}_0 + \alpha_s(\mu_R^2)\hat{\sigma}_1 + \ldots]_{q\bar{q}\to l^+l^-} \tag{2.25}$$

The μ_F^2 and μ_R^2 dependencies are in principle vanishing after the summation over all the orders. However, it is not feasible to compute an infinite number of terms. Which means that a choice made for μ_F^2 and μ_R^2 will lead to specific cross section predictions. In the case of the DY production, the typical choice of the factors is $\mu_F^2 = \mu_R^2 = M_Z^2$, and the uncertainties are obtained by scale variations in the range $M_Z/2 \leq \mu \leq 2M_Z$ [14, 15].

To describe the DY process, the annihilation of a quark-antiquark pair into a virtual photon or a Z boson subsequently into an oppositely charged lepton pair is considered. The partonic cross section of DY process can be computed based on the matrix element of the Feynman diagram at leading order or higher order in α_s, as illustrated in figure 2.4. The total cross section at leading order, separated into the γ^* (σ_{γ^*}), Z production (σ_Z) and the interference between them ($\sigma_{\text{interference}}$), is found to be:

$$\begin{aligned}\sigma_0(q\bar{q} \to l^+l^-) &= \sigma_{\gamma^*} + \sigma_{\text{interference}} + \sigma_Z \\ &= \frac{4\pi\alpha^2}{3\hat{s}n_c}[Q_q^2Q_l^2 + 2Q_qQ_lV_lV_q\chi_1(\hat{s}) + (A_l^2 + V_l^2)(A_q^2 + V_q^2)\chi_2(\hat{s})]\end{aligned} \tag{2.26}$$

where

$$\chi_1 = \frac{1}{\sin^2 2\theta_W}\frac{\hat{s}(\hat{s} - M_Z^2)}{(\hat{s} - M_Z^2)^2 + M_Z^2\Gamma_Z^2}, \chi_2 = \frac{1}{\sin^4 2\theta_W}\frac{\hat{s}^2}{(\hat{s} - M_Z^2)^2 + M_Z^2\Gamma_Z^2}. \tag{2.27}$$

The $\hat{s} = x_1x_2s$ represent the center-of-mass energy of the two interacting partons coming from the AB center-of-mass energy s. The n_c is the number of colours, Q_q and Q_l are the electric charges of quark and lepton, while $V = T^3 - 2Q\sin^2\theta_W, A = T^3$and Γ_Z is the total decay width of the Z boson.

The Feynman diagram at LO for DY does not contain any QCD vertex interaction, as shown in 2.4. When considering matrix elements at next-to-leading order (NLO), three types more of Feynman diagram need to be included: the quark (or antiquark) radiate a gluon, condition of gluons in the initial state and gluon loop corrections. For higher order cases like next-to-next-to-leading order (NNLO), gluon-gluon interactions can occur to produce a Z boson with two partons. With higher order term calculations, a more precise estimation of the cross section can be obtained. A K-factor, the ratio of cross section at LO+NLO to LO predictions, has been computed and reached values up to 130% affecting both the normalisation and the shape of the distributions as shown in figure 2.5. The cross section at NNLO prediction has been computed and compared also, with no significantly changing on the shape compared to NLO [14, 15].

2.3.1 Parton Distribution Functions

Parton Distribution Functions (PDFs) [16] involved in the QCD factorization formula have to be extracted for the parton from measurements at some energy scale Q_0^2 and then evolved using pQCD evolution equations to another energy scale Q^2. The knowledge of the PDF are mainly extracted from deep inelastic scattering (DIS) measurements at the lepton-hadron collider HERA [17, 18] and from fixed target scattering experiments. Hadron colliders, such as LHC, can also provide some constraints by

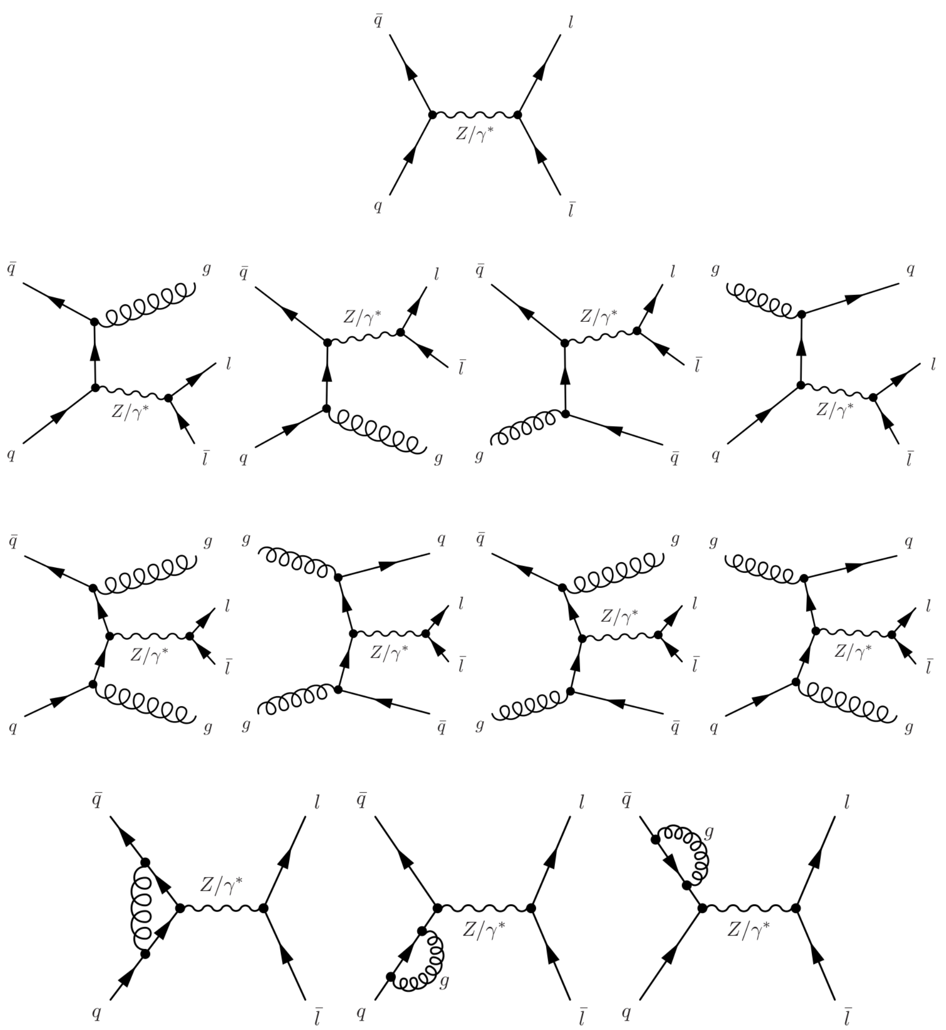

FIGURE 2.4: Feynman diagrams for the Drell-Yan process at different orders. The top diagram is the leading order matrix element of Drell-Yan process without strong coupling that has no parton production in the final state. The second row of the diagrams shows the next-to-leading order of Drell-Yan process resulting in one parton produced in the final state. The third row represents the third order of Drell-Yan process leading to two partons in the final state.The last row provides the next-to-leading order of Drell-Yan process with virtual gluon loops in the initial state that will interfere with first order leading to α_s corrections.

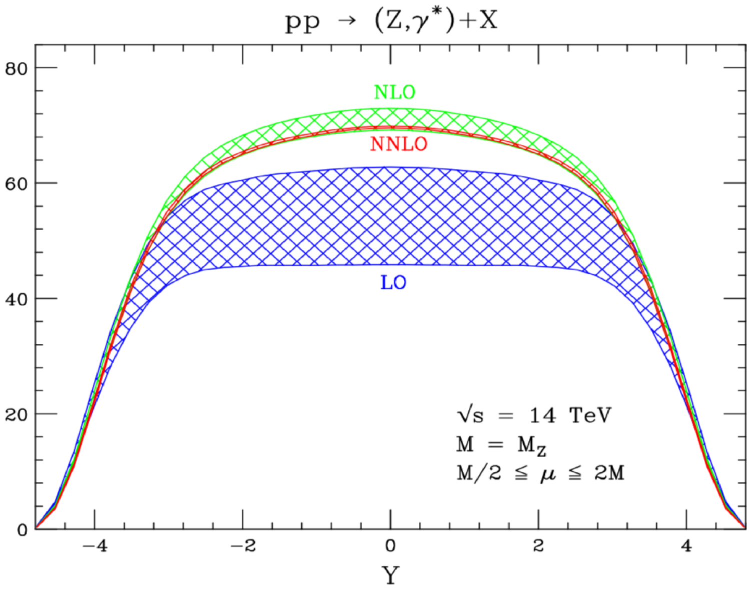

FIGURE 2.5: Theory predictions at LO, NLO and NNLO of the rapidity distributions for Z boson produced in p-p collision at center-of-mass energy of 14 TeV. The bands indicate the factorization and renormalization scale uncertainties, obtained by scale variations in the range $M_Z/2 \leq \mu \leq 2M_Z$

studying e.g. the DY process [19]. The main characteristic of the PDF is that they depend on the hard scale at which the hadron is probed. At large Q^2, the detailed structure of the hadron is seen as resulting of many gluons and quarks carrying small momentum fraction of the hadron. While, a low Q^2 leads to a coarse resolution inside the hadron and results in a fewer visible partons with larger longitudinal momentum fractions.

Given the PDFs at some Q_0^2, they can be evolved to another scale Q^2 using the Dokshitzer-Gribov-Lipatov-Altarelli-Parisi (DGLAP) [20, 21, 22, 23] equations:

$$Q^2\frac{\partial}{\partial Q^2}\begin{pmatrix} q_i(x,Q^2) \\ g(x,Q^2)\end{pmatrix} = \frac{\alpha_s(Q^2)}{2\pi}\sum_{q_j,\bar{q}_j}\int_x^1 \frac{d\xi}{\xi}\times\begin{pmatrix} P_{q_iq_j}(\frac{x}{\xi},\alpha_s(Q^2)) & P_{q_ig}(\frac{x}{\xi},\alpha_s(Q^2)) \\ P_{gq_j}(\frac{x}{\xi},\alpha_s(Q^2)) & P_{gg}(\frac{x}{\xi},\alpha_s(Q^2))\end{pmatrix}\begin{pmatrix} q_j(\xi,Q^2) \\ g(\xi,Q^2)\end{pmatrix} \tag{2.28}$$

where the $q_i(x,Q^2)$ and $g(x,Q^2)$ stand for the PDF corresponding to the quark (or anti-quark) with flavor i and to the gluon, respectively. The functions $P_{ab}(\frac{x}{\xi},\alpha_s(Q^2))$ are the splitting functions and have a perturbative expansion in terms of the running constant α_s:

$$P_{ab}(\frac{x}{\xi},\alpha_s(Q^2)) = P^0_{ab}(\frac{x}{\xi}) + \frac{\alpha_s}{2\pi}P^1_{ab}(\frac{x}{\xi}) + \dots \tag{2.29}$$

The leading order splitting functions $P^0_{ab}(\frac{x}{\xi})$ can be interpreted as the probabilities of getting a type a parton from a parton b, carrying a fraction $\frac{x}{\xi}$ of the momentum and a transverse momentum squared much less than Q^2. Figure 2.6 illustrates NNPDF2.3 PDFs at Q^2=2 GeV^2 and Q^2=100 GeV^2. The gluon, up quark and down quark distribution are included. These plots are produced by TMDploter [24, 25].

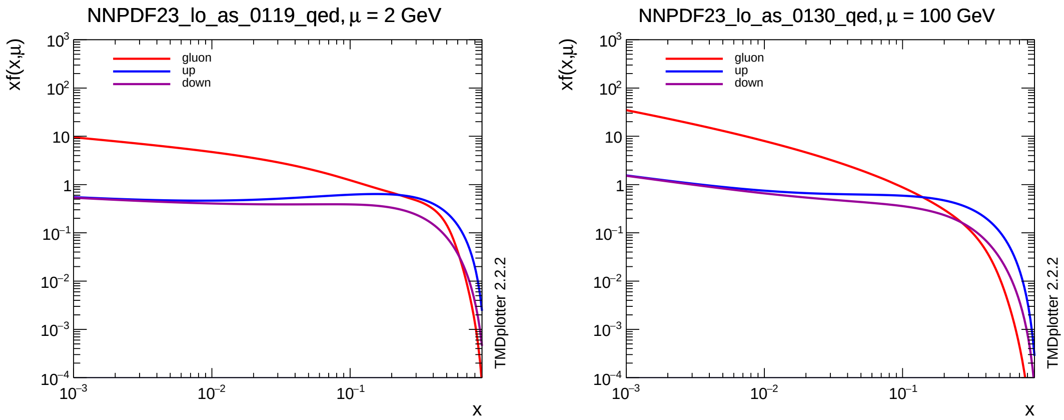

FIGURE 2.6: PDF of the proton for the gluon, up quark and down quark, at a scale of Q^2=2 GeV^2 (left) and Q^2=100 GeV^2 (right) with NNPDF [26] parameterisation v2.3 LO with α_s=0.130.

2.4 Monte Carlo Simulation

In principle, using phenomenological models for the non-perturbative part, and calculating the harder process in pQCD, one can obtain a prediction for a particular hard process studied at the LHC. However, all these calculations are still extremely complex. The structure of the event recorded at the LHC is also complicated. To obtain analytic and numeric computations, Monte Carlo (MC) [27, 28] programs are developed to simulate realistic events and the detector response. There are many different MC generators to simulate high energy processes and allow the comparison of the theoretical calculations with measurements. Figure 2.7 illustrates a general picture of an event during single proton-proton collision. The procedures of event generation for Drell-Yan process in p-p collision by MC generator are listed as:

- the fully differential cross section for the process is calculated under consideration for the interaction of two incident partons extracted from the colliding hadrons.
- The hadronic differential cross sections is calculated from the partonic cross sections convoluted with appropriate PDF (as explained in equation 2.24).
- The actual particles involved in the process are generated in some phase space the cross section computed in the previous step.
- Modeling of initial state radiation (ISR).
- Similar radiations take place for the final state particles, final state radiation (FSR).
- Eventual short-life particles (e.g. Z boson) are decayed producing additional final state particles.
- Simulate the multiple parton interactions (MPI), due to the additional parton-parton interactions happening in parallel with the hard interaction.

- Remnant of the colliding hadrons needs to be taken into account for a correct balance in momentum and charge
- simulate the hadronization for all the partons produced in the final state;
- As final step, long-life particle decay, such as τ leptons or B-hadrons, while those reaching the detector are left intact.

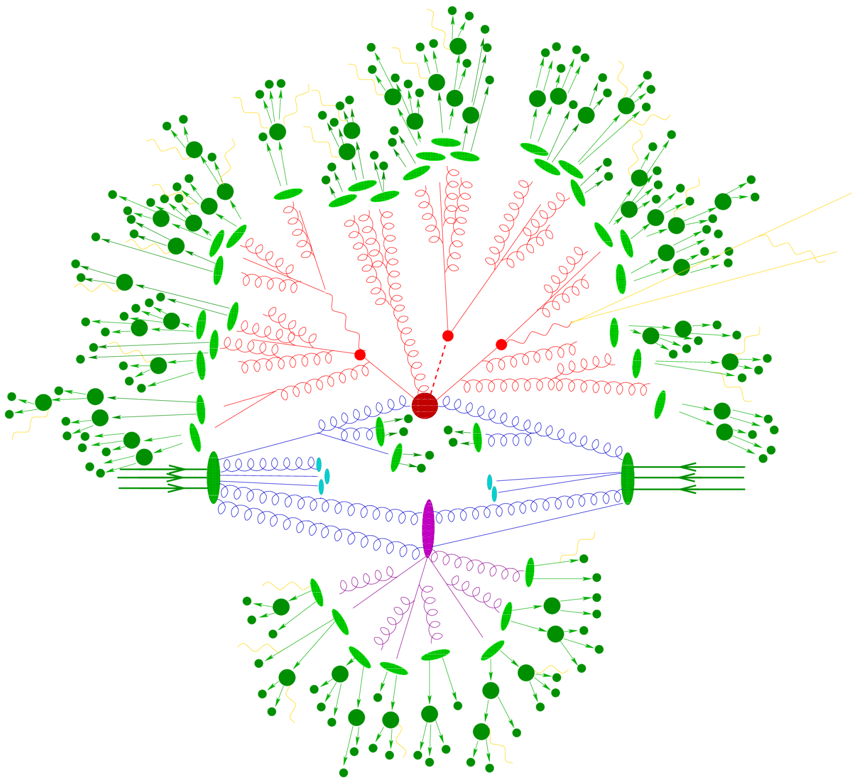

FIGURE 2.7: Sketch of a hadron-hadron collision as simulated by a Monte-Carlo event generator. The red blob in the center represents the hard collision. The purple blob indicates a secondary hard scattering event. Parton-to-hadron transitions are represented by light green blobs, dark green blobs indicate hadron decays, while yellow lines signal soft photon radiation [29].

There are MC generators with different configurations. In the present analysis, simulations of MADGRAPH5_AMC [30] generator and GENEVA [31, 32] both interfaced to PYTHIA8 [33] are used for the theoretical predictions. Hence, a simple introduction of MADGRAPH5_AMC, PYTHIA8 and GENEVA will be described.

2.4.1 MADGRAPH5_AMC@NLO

The MADGRAPH5_AMC@NLO program is a fully automated MC tool, merging all the features of MADGRAPH5 [34] and of AMC@NLO [35] in a unique framework. It can be interfaced with a second MC program, such as PYTHIA, to implement parton shower and hadronization effects. MADGRAPH5_AMC@NLO contains all ingredients that are necessary to perform an NLO, possibly plus parton shower, computation. It has modules responsible for one-loop matrix elements computation for arbitrary processes, and also keeps a choice of possible calculations at LO level. Therefore, a few possibilities of computations are included, and listed explicitly in an order of increasing complexity:

- fLO: a tree- and parton-level computation, at leading order. No shower is involved, and observables are reconstructed by means of the very particles that appear in the matrix elements.
- fNLO: the same as fLO, except for the perturbative accuracy at NLO. The computation will involve both tree-level and one-loop matrix elements.
- LO+PS: uses the matrix elements of an fLO computation, and matches them to parton showers.
- NLO+PS: same as LO+PS, except for the fact that the underlying computation is an NLO rather than an LO one. The matching of the NLO matrix elements with parton showers is done according to the MC@NLO formalism.
- MLM-merged: combines several LO+PS samples, which differ by final-state multiplicities (at the matrix-element level). Two different approaches, called k_T-jet and shower-k_T schemes, may be employed.
- FxFx-merged: combines several NLO+PS samples, which differ by final-state multiplicities.

Having all of these different simulation possibilities embedded in MADGRAPH5_-AMC@NLO, a process-independent framework, allows one to investigate multiple scenarios while being guaranteed of consistency. In the present analysis, two different predictions of MADGRAPH5_AMC@NLO have been used: MADGRAPH5_AMC@NLO including matrix elements (ME) computed at LO for up to 4 partons, interfaced with PYTHIA8 using k_T-MLM scheme; MADGRAPH5_AMC@NLO with ME at NLO for up to 2 partons, interfaced with PYTHIA8 using FxFx merging scheme. The comparison between the two predictions helps to study the impact of perturbative corrections at the LO or NLO.

The central idea of MADGRAPH5_AMC@NLO is that: regardless of theory under consideration and of the perturbative order, the structure of a cross section is essentially independent of the process and it can be written in a code once and for all. Conversely, matrix elements are obviously theory- and process-dependent, but it can be computed starting from a very limited number of formal instructions. One method, constructing the model given a Lagrangian by deriving its Feynman rules, is used for MADGRAPH5_AMC@NLO to assemble the matrix elements. At the LO, it is fully automated in FEYNFULES [36, 37, 38]. NLO cross sections face some extra difficulties, because Feynman rules are not sufficient for a complete calculation: one needs at least UV counterterms, possibly plus other rules necessary to carry out the reduction of one-loop amplitudes. To solve this issue, MADGRAPH5_AMC@NLO has been implemented with special configurations, FKS (Frixione, Kunszt, and Signer) subtraction [39, 40, 41]. Hence, the generated events by MADGRAPH5_AMC@NLO at NLO contain events within the infrared safe region, and the counterevents corresponding to soft and collinear singularities.

2.4.2 PYTHIA

The PYTHIA [42, 43, 33] program is a standard tool for the generation of high-energy collisions, comprising a coherent set of physics models for the evolution from a few-body hard process to a complex multihadronic final state. It contains a library of hard processes and models for initial state radiation (ISR) and final state radiation (FSR), multiple parton interactions (MPI), beam remnants, string fragmentation and particle decays. It could be interfaced with PDF libraries.

PYTHIA8 can generate hard processes at LO focusing on 2→1 and 2→2 processes with some 2→3 processes available, matched with a DGLAP evolution at an approximate Next-to-Leading-Log level (NLL) for the simulation of the PS. Due to lack of loop corrections, there are infrared divergences happening in the low transverse momentum (p_{T}) regions of the emitted partons. In order to take into account the significant multiple gluon emissions, PS needs to be implemented on top of the lower order matrix elements to compensate missing the gluon emission effects. The idea is to implement the parton evolution through computing the splitting functions of partons with varied virtuality scales. The evolution starts from the scale associated to the parton subject to parton shower down to the lower values until reaching a designed threshold.

In the case of FSR, the evolution forwards in physical time, with a single mother parton replaced by two daughter partons at each branching, yielding the momentum conservation principle. The virtuality energy scale decreases through sequential gluons radiations or quark-antiquark pair production, resulting in softer and softer radiations in the cascade. While, ISR is implemented through backwards in physical time: the parton evolution begins from the hard interaction to the radiation position happening far before it. As a consequence, the emitted gluons becomes harder and harder when approaching to the hard scattering center. When the virtuality energy scale is close to Λ_{QCD}, the outcoming partons from parton shower start to be bounded to form particles, called hadronization. Hadronization is based solely on the Lund string fragmentation framework [44]. The model postulates that partons within 1 fm are connected by gluon strings, with energies proportional to their lengths. When the length between two partons gets larger, the energy of their string is high enough to create a new pair of partons, bounded with one of original partons to form a new string system. These strings keep breaking up until the created quarks in the ends can form on-mass-shell hadrons, which remain stable or decay to more stable particles. This phenomenological depiction is modeled according to observed hadronic spectroscopy and lattice QCD studies.

2.4.3 GENEVA

The GENEVA [31, 32] Monte Carlo produces Drell-Yan events by combining the fully-differential NNLO matrix elements with higher-order gluon resummation in the 0-jettiness [2] resolution variable, τ, also known as beam thrust and defined in [45]. The

[2] N jettiness (τ_N) is a global event shape, which is defined for events with N signal jets. N jettiness yields a factorization formula with inclusive jet and beam functions

0-jettiness resummation is carried out to the τ dependent next-to-next-to-leading logarithmic (NNLL'$_\tau$) approximation, which consistently incorporates all singular virtual and real NNLO corrections. The resulting parton-level events by GENEVA are further combined with parton showering and hadronization provided by PYTHIA8. It thus provides a natural perturbative connection between the NNLO calculation and the parton shower regime, including a systematic assessment of perturbative uncertainties.

As mentioned, GENEVA combines several different ways to obtain theoretical predictions for collider processes: fixed-order (FO) perturbative theory, resummed perturbative theory and predictions using parton shower algorithms. FO predictions are necessary for a precise description of hard emissions, that neither resummation nor parton shower could describe correctly. For observables sensitive to many soft and collinear emissions generating large logarithms, FO predictions are not suitable, while resummation and parton showers are necessary and appropriate. Resummed perturbative theory allows to carry out the resummation beyond the LL or even strongly-ordered limit and is therefore more accurate than parton shower. The resummation is obtained by resumming the logarithmic terms in τ/Q, where Q is the scale, to all order in the strong coupling constant, α_s.

The basis of the GENEVA MC framework is the formulation of the perturbative inputs in terms of "MC cross section", which are well defined partonic jet cross sections according to which the events are distributed, and which can be systematically computed to the desired perturbative in FO and resummed perturbative theory [32, 46, 47]. The MC cross sections are defined in terms of an N-jet resolution variable τ_N and formally include the contributions of an arbitrary number of unresolved emissions below a resolution cutoff $\tau_N < \tau_N^{cut}$. In the present case, we require events with 0, 1 and 2 partons, which are distributed according to

$$\begin{aligned} \Phi_0 \; events : \frac{d\sigma_0^{MC}}{d\Phi_0}(\tau_0^{cut}), \\ \Phi_1 \; events : \frac{d\sigma_1^{MC}}{d\Phi_1}(\tau_0 > \tau_0^{cut}; \tau_1), \\ \Phi_2 \; events : \frac{d\sigma_{\geq 2}^{MC}}{d\Phi_2}(\tau_0 > \tau_0^{cut}; \tau_1 > \tau_1^{cut}). \end{aligned} \tag{2.30}$$

where Φ_N represents the N-parton final state phase space. The exclusive 0-jet MC cross section is defined by $\tau_0 < \tau_0^{cut}$, the exclusive 1-jet MC cross section by $\tau_0 > \tau_0^{cut}$ and $\tau_1 < \tau_1^{cut}$, and the inclusive 2-jet MC cross section by $\tau_0 > \tau_0^{cut}$ and $\tau_1 > \tau_1^{cut}$. In this way all the partonic phase space is covered. Adding the 1-jet and 2-jet events, we can also defined the inclusive 1-jet MC cross section as

$$\frac{d\sigma_{\geq 1}^{MC}}{d\Phi_1}(\tau_0 > \tau_0^{cut}) = \frac{d\sigma_1^{MC}}{d\Phi_1}(\tau_0 > \tau_0^{cut}; \tau_1) + \int \frac{d\Phi_2}{d\Phi_1}\frac{d\sigma_{\geq 2}^{MC}}{d\Phi_2}(\tau_0 > \tau_0^{cut}; \tau_1 > \tau_1^{cut}) \tag{2.31}$$

which is defined by $\tau_0 > \tau_0^{cut}$ and does not depend anymore on τ_1^{cut}.

Using the events in Eq 2.30, the cross section for any observable X is given by:

$$\begin{aligned}\sigma(X) = &\int d\Phi_0 \frac{d\sigma_0^{MC}}{d\Phi_0}(\tau_0^{cut}) M_X(\Phi_0) \\ &+ \int d\Phi_1 \frac{d\sigma_1^{MC}}{d\Phi_1}(\tau_0 > \tau_0^{cut}; \tau_1) M_X(\Phi_1) \\ &+ \int d\Phi_2 \frac{d\sigma_{\geq 2}^{MC}}{d\Phi_2}(\tau_0 > \tau_0^{cut}; \tau_1 > \tau_1^{cut}) M_X(\Phi_2),\end{aligned} \tag{2.32}$$

where $M_X(\Phi_N)$ is the measurement function that computes the observable X for the N-parton final state Φ_N. This cross section is not identical to the exact fixed-order result, because for any unresolved emissions the observable is rather calculated on the projected phase space point than on the exact Φ_M. The difference vanishes in the limit $\tau_N^{cut} \to 0$.

The GENEVA, for the first time in a MC, combines higher order resummation at NNLL with NNLO ME calculation. For the GENEVA, parton showers and hadronization are provided by PYTHIA8 using same tune CUETP8M1 as for MG5_AMC.

Chapter 3

The Experimental Setup

This chapter is dedicated to the introduction on the experimental setup used in the presented particle physics analysis work. The first part provides a brief introduction on the Large Hadron Collider (LHC) [48]. The geometric structure and few crucial physics characteristics of LHC is included to provide a global picture of the collider. The second part presents the Compact Muon Solenoid (CMS) detector [49] which is used to detect and measure the particles produced in physics processes taking place in the hadron collider. The LHC and CMS provide us the possibility to study the particle physics at the TeV energy scale.

3.1 The Large Hadron Collider

3.1.1 Introduction

The Large Hadron Collider (LHC) is the most powerful particle accelerator in the world and it is located on the France-Swiss border, at CERN (European Organization for Nuclear Research). The LHC reuse the Large Electron-Positron Collider (LEP) [50] tunnel and its injection chain. It has a circumference of 27 km runs 100 meters underground, and has four main experiments, ALICE, ATLAS, CMS, LHCb, as shown in the figure 3.1.

The energy obtainable of a circular accelerator is limited by the radius of the machine and by the strength of the dipole magnetic field that keeps particles on their orbits. The size of tunnel, magnets, cavities and other essential elements of LHC represents the main constraints that determine the design energy of 7 teraelectronvolts (TeV) per proton, or 5.02 TeV per nuclear in heavy ion beams. The first research run of LHC (RunI) took place from 2010 till 2012 with an energy of 3.5 TeV per proton in the begining, and up to 4 TeV from 2012 on. After two years of shut down time for upgrade, LHC restarted in early 2015 for its second research run (RunII), with 6.5 TeV per beam, and will collect data until the end of 2018.

The prime motivation of LHC was to search for the Higgs boson, which could be used to elucidate the nature of electroweak symmetry breaking. The physics goals also include the precise measurements of Standard Model (SM) particle physics in the phase space regions never reached before, searches for beyond SM physics, searches

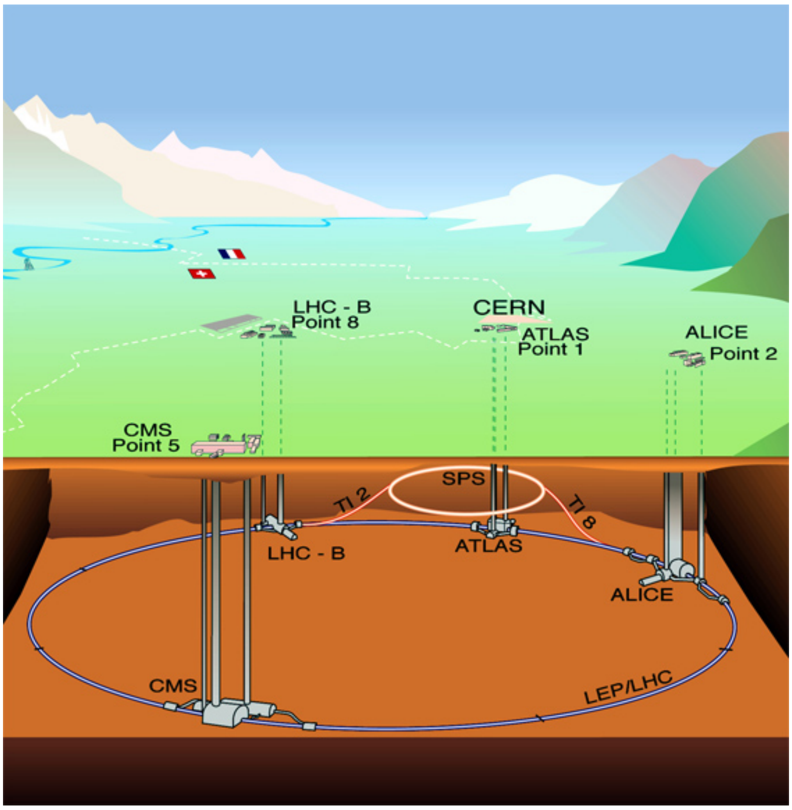

FIGURE 3.1: This figure shows the location of the LHC, the four main experiments (ALICE, ATLAS, CMS, LHCb), as well as the pre-accelerator of the injected proton bunches SPS.

for particles or phenomena responsible for dark matter. In addition to the studies of proton-proton collisions, the heavy ion collisions provide a chance to study quark-gluon plasma (QGP). Quark-gluon plasma is a phase of QCD that is believed to be a stage about 10^{-6} second after the universe born from the Big Bang. In 2012, CERN announced the discovery of the Higgs boson, which confirmed the existence of Brout-Englert-Higgs mechanism. Since, the properties of Higgs boson are being studied and measured in detail.

3.1.2 Proton injection and acceleration

Protons are produced in a duoplasmatron source that is obtained by injecting hydrogen gas. The duoplasmatron applies electrical field to break down the gas into its constituent protons and electrons. Protons are then sent to a radio frequency quadrupole (QRF) to speed up and focus. After that, protons are accelerated in Linear accelerator 2 (LINAC2) until they reach an energy of 50 MeV. Then, they are injected into Proton Synchrotron Booster (PSB) to reach an energy of 1.4 GeV. The beam bunches are then fed to the Proton Synchrotron (PS) bunches are split and accelerated up to 25 GeV. In the Super Proton Synchrotron (SPS), protons are accelerated to 450 GeV, and finally transferred to the LHC (both in a clockwise and an anticlockwise directions) where they are accelerated for about 20 minutes up to the final energy (3.5 TeV in 2011, 4 TeV in 2012, 6.5 TeV in 2015-17). The whole acceleration chain is illustrated in figure 3.2.

In the LHC, under norminal operating conditions, each proton beam contains 2808 bunches, with each bunch containing about 10^{11} protons.

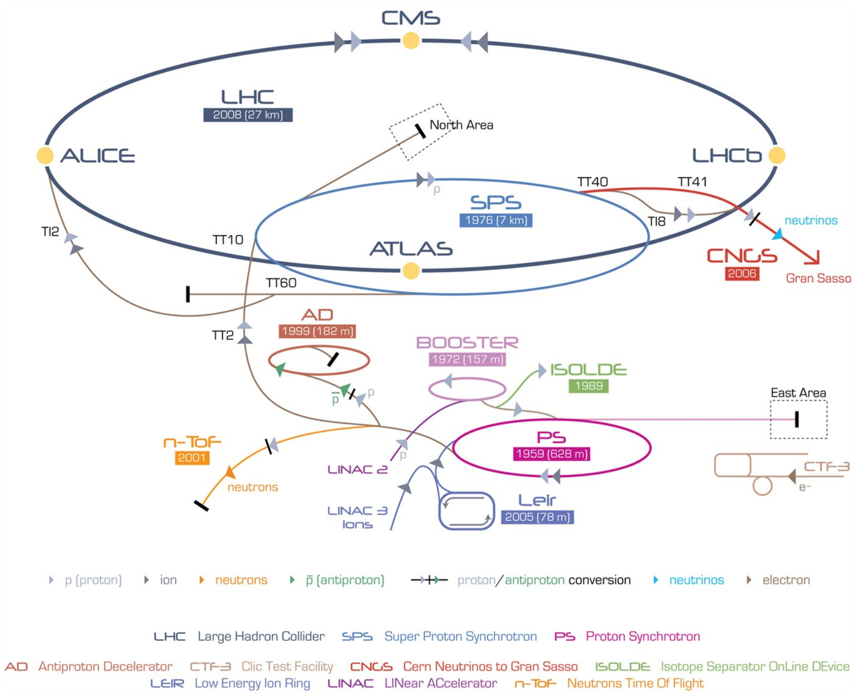

FIGURE 3.2: The CERN accelerator complex. Protons pass through the LINAC2, the PS booster, the PS, the SPS and finally the LHC

In the LHC, protons circulate in a vacuum tube and are manipulated using electromagnetic divices: 1232 dipole magnets keep protons in their circular orbits, 392 quadrupole magnets focus and defocus the beam, and accelerating cavities that accelerate protons and keep them at a constant energy by compensating for energy losses. In the LHC, the maximum energy that can be achieved is limited by the strength of the dipole field. The LHC dipoles use niobium-titanium (NbTi) cables, which become superconducting below a temperature of 10 K (LHC operates at 2 K). The dipole magnets are designed to provide 8.3 T over their length when a current of 11 850 A flows in the dipoles.

3.1.3 Luminosity

Luminosity (L) is one of the most important parameters of an accelerator. It qualifies the beam collision intensity and is proportional to the number of collisions that can be produced per cm^2 and per second. The number of events per second produced in the LHC collisions can be described with the luminosity and the total p-p cross section (σ)

$$N_{events} = L\sigma \tag{3.1}$$

The nominal design luminosity of the LHC is $10^{34} cm^{-2} s^{-1}$. There are two kinds of luminosities: instantaneous luminosity ($\mathcal{L}$) and integrated luminosity L_{int}. The instantaneous luminosity only depends on the beam parameters:

$$\mathcal{L} = \frac{N_b^2 n_b f_{rev} \gamma}{4\pi \epsilon_n \beta^*} F \tag{3.2}$$

where N_b is the number of protons in each bunch, n_b the number of colliding bunches per beam, f_{rev} the revolution frequency, γ the Lorentz boost factor, ϵ_n the normalized emittance, β^* the beta function at the collision point, and F the geometric luminosity reduction, a factor coming from the crossing angle of the two beams.

The integrated luminosity L_{int} is the integral of the instantaneous luminosity $\mathcal{L}$ over a given range of time:

$$L_{int} = \int_{t_0} \mathcal{L}(t) dt \tag{3.3}$$

3.2 The CMS Detector

3.2.1 Introduction

The Compact Muon Solenoid (CMS) detector is a multi-purpose apparatus, designed for precision measurements of SM physics, the search and the study of the recently discovered Higgs boson, and for searches for new particles, phenomena, and even extra dimensions in the Universe. In order to meet these physics goals, the CMS detector is required to have: good muon identification and momentum resolution over a wide range of momenta and angles, good dimuon mass resolution ($\approx$ 1% at 100 GeV); good charged-particle momentum resolution and reconstruction efficiency in the inner tracker; good electromagnetic energy resolution, good diphoton and dielectron mass resolution ($\approx$ 1% at 100 GeV), and efficient photon and lepton isolation at high luminosities; good missing-transverse-energy and dijet-mass resolution, requiring hadron calorimeters with a large hermetic geometric coverage and with fine lateral segmentation.

The overall layout of CMS is shown in figure 3.3. The CMS detector is 21 metres long, 15 m of diameter, 14,000 tonnes of weight. CMS is composed of different sub-detectors and one 4 T superconducting solenoid. The orgin of the right-handed coordinate system adopted by CMS is at the nominal collision point, while the *y*-axis points vertically upward, the *x*-axis points radially inward toward the center of the LHC. Therefore, the *z*-axis points along the beam in an anticlockwise direction.

From the inner to the outer, CMS detector is made up of the inner tracking system, the electromagnetic calorimeter (ECAL), the hadron calorimeter (HCAL), the superconducting magnet and the muon system. The details of the magnet and these various sub-detectors will be described in the next section.

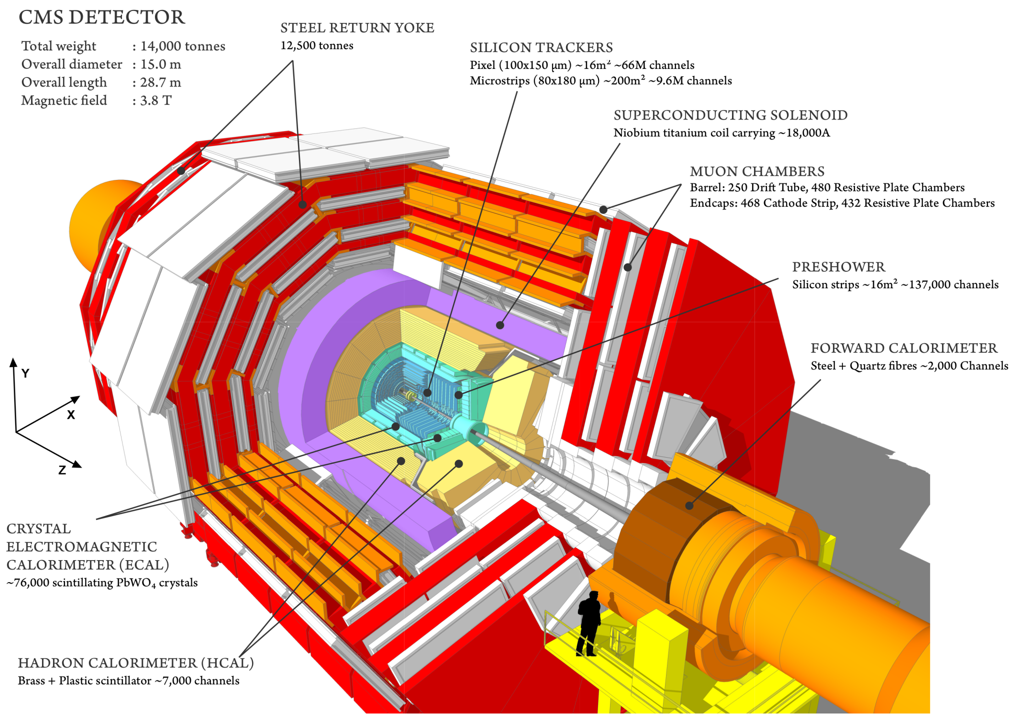

FIGURE 3.3: The CMS detector.

3.2.2 Superconducting Magnet

The superconducting solenoid magnet for CMS, with a diameter of 6 m and a length of 12.5 m, is the largest superconducting magnet ever built, and the CMS's heaviest component. It is made of 10,000-t iron yoke and 220-t cold mass [1] to generate a field of 4 Tesla. The cold mass is the 4-layer winding made from a stabilised reinforced niobium-titanium (NbTi) conductor. The 4 T magnet field, 100000 times stronger than the Earth's, is requested to bend the charged particles flying outwards from the collision point. The bending trajectories of particles serve two purposes:

- identify the charge of the particle: in an homogeneous magnet field, positively and negatively charged particles bend opposite directions
- measure the momentum (p_T) of the particle: high-momentum charged particles bend less compared with low-momentum ones in the same magnetic field according to $p_T = 0.3BR$ (B is the magnetic field intensity in Tesla and R the radius of curvature in m, p_T in GeV)

3.2.3 Inner Tracking System

Inner tracking system is designed to provide precise and efficient measurement of trajectories of charge particles from LHC beam collision, and precise reconstruction of primary and secondary vertices (from b and tau decay). The CMS tracker is composed of a pixel detector with three barrel layers located at mean radii of 4.4cm, 7.3cm and

[1]Cold mass is defined as the part of CMS solenoid operating at liquid helium temperature $-268.5°$C

10.2cm and a silicon strip tracker with 10 barrel layers outwards to a radius of 1.1m. The CMS tracker is completed with endcaps of two disks in the pixel detector and 3 plus 9 disks in the strip tracker to extend the tracker coverage up to $|\eta| < 2.4$. In total, the CMS tracker is composed of 1440 pixel and 15148 strip detector modules. A schematic cross-section through the CMS tracker is illustrated in figure 3.4.

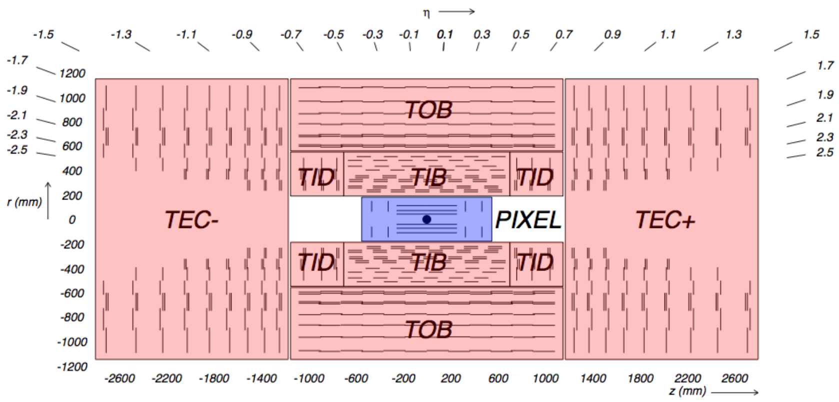

FIGURE 3.4: Schematic cross-section through the CMS tracker. The pixel detector is marked as blue and the silicon strip tracker is marked as red, while the black lines represent detector modules. The strip tracker is divided to TIB (Tracker Inner Barrel), TOB (Tracker Outer Barrel), TID (Tracker Inner Disks) and TEC (Tracker End Cap).

The strip tracker consists of single sided p-on-n type silicon micro-strip sensor, divided in sub-detectors: a TIB (Tracker Inner Barrel), a TOB (Tracker Outer Barrel), TEC (Tracker End Cap) and TID (Tracker Inner Disks). The TIB comprises 4 layers and covers up to $|z|$< 65 cm, using silicon sensors with thickness of 320 μm.The TOB is made of 6 layers with a half-length of $|z|$<110 cm, using thicker silicon sensors (500 μm) to maintain a good S/N (signal/noise) ratio. Each TEC is made of 9 disks extending into the region 120 cm < $|z|$ < 280 cm, while the TID comprises 3 small disks that fill the gap between TIB and the TEC. The thickness of the silicon sensors is 320 μm for the TID and 3 innermost ring of the TEC and 500 μm for the rest of the TEC.

The pixel system is the closest to the interaction region. The pixel detector is essential for the reconstruction of secondary vertices, and forming seed tracks for the outer track reconstruction and high level trigger (HLT). The sensors for the silicon pixel detector adopt the so called n-on-n concept. The pixels consist of high dose n-implants introduced into a high resistance n-substrate. It consists of three barrel layers (BPix) with two endcap disks (FPix), which give 3 tracking points over almost the full η-range. It contributes precise tracking points in $r-\phi$ and z in order to achieve the optimal vertex position resolution. In total, the impact parameter resolution achieved by the inner tracker is about 15 μm, and the resolution on the transverse momentum is about 2.0% for 100-GeV charged particles.

3.2.4 Electromagnetic Calorimeter

The Electromagnetic Calorimeter (ECAL) is designed to identify electrons and photons, and measure their energy with good resolution since most of the energies of electrons and photons is deposited within the ECAL. The ECAL is a hermetic homogeneous calorimeter made of 61,200 lead tungstate ($PbWO_4$) scintillating crystals mounted in the central barrel part, closed by 7324 crystals in each of the 2 endcaps , and one preshower detector in front of the endcap crystals. The crystals emit blue-green scintillation light with a broad maximum at 420-430 nm, detected by the photodetectors of silicon avalanche photodiodes (APDs) in the barrel and vacuum phototriodes (VPTs) in the endcaps.

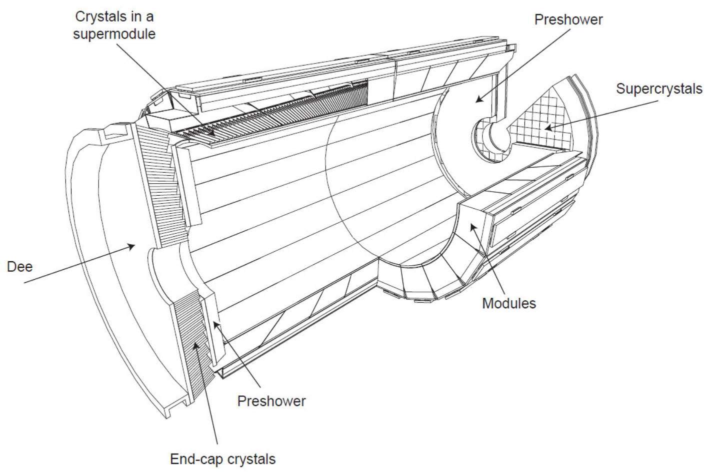

FIGURE 3.5: Geometric view of one quarter of the ECAL.

The ECAL is divided into three parts: one barrel, two endcaps and preshowers, as shown in the figure 3.5. The barrel part of the ECAL (EB) covers the pseudorapidity range $|\eta|$<1.479 with 61,200 $PbWO_4$ crystals. The barrel granularity is 360-fold in ϕ, and (2×85)-fold in η. The crystals have a trapered shape, slightly varying with position in η, mounted in a quasi-projective geometry to avoid cracks aligned with particle trajectories. The crystal cross-section corresponds to approimately 22 × 22 mm^2 at the front face , and 26 × 26 mm^2 at the rear face. The crystal length is 230 mm corresponding to 25.8 X_0. The barrel crystal volume is 8.14 m^3 and the weight is 67.4 t.

The endcaps of the ECAL (EE) cover the rapidity range 1.479 < $|\eta|$ < 3.0. The endcap consists of identically shaped crystals grouped in mechanical units of 5×5 crystals (supercrystals) consisting of a carbon-fibre alveola structure. Each endcap is divided into 2 $Dees$, and each Dee holds 3662 crystals. The crystals have a front face cross section of 28.62 ×28.62 mm^2, a rear face cross section of 30×30 mm^2 and a length of 220 mm (24.7 X_0). The endcaps crystal volume is 2.90 m^3 and its weight is 24.0 t.

The preshower detector cover the rapidity range 1.653 < $|\eta|$ < 2.6. It is designed to identify neutral pions in the endcaps, also identify electrons against minimum ionizing particles, and improves the position determination of electrons and photons with high granularity.

The performance of the ECAL was measured with a test beam. The energy resolution, measured by fitting a Gaussian function to the reconstructed energy distributions, has been parameterized as a function of energy:

$$(\frac{\sigma}{E})^2 = (\frac{S}{\sqrt{E}})^2 + (\frac{N}{E})^2 + C^2, \tag{3.4}$$

where S is the stochastic term, N the noise and C the constant term. The stochastic term has three contributions: event-to-event fluctuations in the lateral shower containment; photostatistics contributions; fluctuations in the energy deposited in the preshower absorber with respect to what is measured in the preshower silicon detector. While for noise term, it is electronics noise, digitization noise, and pileup noise. The energy resolution measured with electron beams having momenta between 20 and 250 GeV/c confirmed the expectations, and the coefficients are S = 0.028 $\sqrt{GeV}$, N = 0.12 GeV and C = 0.003 [51]. The energy resolution has also been measured for a series of 25 runs where the test beam was directed at locations uniformly covering a 3×3 array of crystals. In this case a resolution of 0.5% was measured for 120 GeV electrons.

3.2.5 Hadron Calorimeter

The Hadron Calorimeter (HCAL) is extremely important for the measurement of hadron jets and neutrinos or exotic particles resulting in apparent missing transverse (E_T^{miss}) energy. Therefore, the HCAL design maximizes material inside the magnet coil in terms of interaction lengths to absorb the hadronic shower totally, in order to minimize the non-Gaussian tails in the energy resolution and provide good containment and hermeticity for the E_T^{miss} measurement.

Figure 3.6 illustrates the longitudinal view of the HCAL. The HCAL contains four parts including the hadron barrel (HB), the endcap (HE), the outer (HO) and the forward (HF) calorimeters to cover the pseudorapidities up to 5.0. The hadron calorimeter barrel (HB) is radially restricted between the outer extent of the electromagnetic calorimeter (R = 1.77 m) and the inner extent of the magnet coil (R=2.95m). The HB is an assembly of two half barrels, each composed of 18 identical 20° wedges in ϕ paralleling to the beam axis, with 16 towers in η covering the pseudorapidity region $|\eta|$ <1.4. The wedges are composed of fourteen flat brass alloy absorber plates, amongst one innermost and two outermost absorber layers made of stainless steel for structural strength. Between the stainless steel and brass absorber plates, there are 17 active plastic scintillator tiles interspersed. The individual tiles of scintillator are machined to a size of $\Delta\eta \times \Delta\phi$ = 0.087× 0.087 and instrumented with a single wavelength shifting fiber (WLS) , and the total number is 2304.

The endcap hadron calorimeter (HE) covers the pseudorapidity region $1.3 < |\eta| < 3.0$, interlocked with the HB. The geometry of the HE is similar to that of the HB. The HE consists of 14 η towers with 5° segmentation. For the 5 outermost tower (at smaller η) the ϕ segmentation is 5°. For the 8 innermost towers the ϕ segmentation is 10° twice larger in order to accommodate the bending radius of the WLS fiber readout, whilst the η segmentation varies from 0.09 to 0.35 at the highest η.

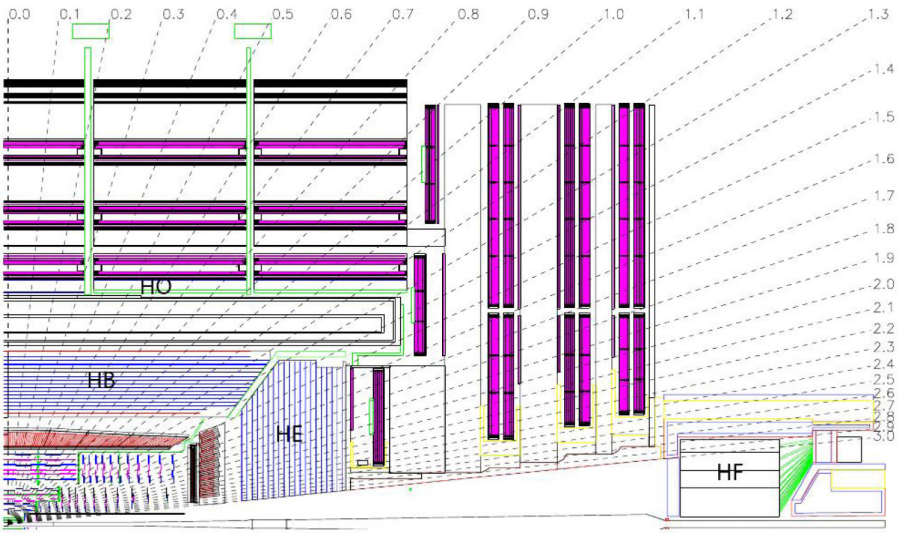

FIGURE 3.6: Longitudinal view of the CMS detector showing the location of the HCAL: the hadron barrel (HB), the endcap (HE), the outer (HO) and the forward (HF) calorimeters

The hadron outer (HO) detector is made of layers of scintillators with a thickness of 10 mm. It is placed outside the solenoid and covers the region $|\eta| < 1.26$. The HO is divided into 5 rings covering 2.54 m in z-axis. All the rings have one layer at a radial distance of 4097 mm, while the central ring has one more layer at a radial distance of 3850 mm. The HO samples the energy from penetrating hadron showers leaking through the rear of the calorimeters, serving as a "tail-catcher" after the solenoid. In return, the HO increases the effective thickness of the hadron calorimetry to over 10 interaction lengths, reducing the tails in the energy resolution function. It also improves the E_T^{miss} resolution.

The hadron forward (HF) calorimeters is composed of steel absorbers and embedded radiation hard quartz fibers, which provide a fast collection of Cherenkov light. The HF is located at 11.2 m from the interaction point, and the depth of the absorber is 1.65 m. Since the neutral component of the hadron shower is preferentially sampled, leading to narrower and shorter hadronic showers, the HF is preferably suited for the congested environment in the forward region. There are 13 towers in η, all with a size of $\Delta\eta \approx$0.175, except for the lowest-η tower with $\Delta\eta \approx$0.1 and the highest-η tower with $\Delta\eta \approx$0.3. The ϕ segmentation of all towers is $10°$, except for the highest-η one which has $\Delta\phi = 20°$. Overall, the HF consists of 900 towers.

The energy resolution of the hadron calorimeter was measured by the CMS Collaboration [52, 53] and can be parameterized as a function of energy with a stochastic term and a constant term:

$$\text{barrel, endcap:} \frac{\sigma}{E} = \frac{120\%}{\sqrt{E}} \oplus 9.5\% \tag{3.5}$$

$$\text{forward:} \frac{\sigma}{E} = \frac{280\%}{\sqrt{E}} \oplus 11\% \tag{3.6}$$

where E is given in GeV.

3.2.6 Muon Detector

The muon detector is one of the highlighted design of the CMS detector, with the purpose of identifying muons, measuring their momentum and contributing to the event triggering. The muon system consists of about 25,000 m^2 of detection planes. The muon chambers had to be inexpensive, reliable, and robust. Three types of gaseous detectors are used. In the barrel region, where the neutron induced background is small, the muon rate is low and the 4-T magnetic field is uniform and mostly contained in the steel yoke, the drift tube (DT) chambers are deployed. While in the endcap region, where the muon rate, the neutron induced background and the magnetic field is large and non-uniform, cathode strip chambers (CSC) are used. Moreover, resistive plate chambers (RPC) are used in both the barrel and the endcap regions. The overview of the muon system is shown in the figure 3.7

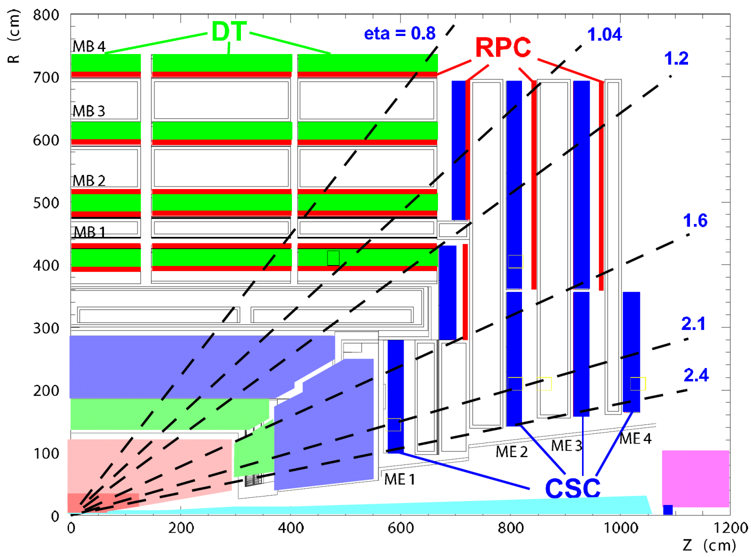

FIGURE 3.7: Longitudinal view of the muon system, including the RPC, CSC and DT.

The barrel drift tube (DT) chambers are divided into 4 stations interspersed among the layers of the return yoke, covering the pseudorapidity region $|\eta| < 1.2$. The first three stations contain four layers: three layers of 180 chambers to measure the muon coordinate in the $r-\phi$ bending plane, and one layer of 70 chambers to provide a measurement in the z direction. The fourth station doesn't contain the z-measuring direction. Each DT chamber has 1 or 2 RPCs coupled to it. The DT chamber in station 1 and 2 is sandwiched between two RPCs. In station 3 and 4, the DT chamber is comprised with one RPC. So a high-p_T muon crosses up to 6 RPCs and 4 DT chambers, producing up to 44 measured points in the DT system from which a muon-track candidate can be built.

The Muon Endcap (ME) system is made up of 468 cathode strip chambers (CSCs) in the 2 endcaps, covering the pseudorapidity region $0.9 < |\eta| < 2.4$. CSCs has four muon station (ME1, ME2, ME3, ME4), separated by the iron disks of the flux return yoke thick enough to isolate the electrons in the showers. Each CSC has trapezoidal shape and consists of 6 gas gaps, each gap having a plane of radial cathode strips and a plane of anode wires running perpendicularly to the strips. When a charged particle traversing a chamber results in the gas ionization and subsequent electron avalanche, that produces a charge on the anode wire and an image charge on a group of cathode strips. The signal on the wires is fast and is used in the Level-1 Trigger. But it leads to a coarser position resolution, which is compensated by precise position measurements made by determining the center-of-gravity of the charge distribution induced on the cathode strips.

These RPCs (covering the pseudorapidity $|\eta| < 2.1$) are operated in avalanche mode to ensure good operation at high rates (up to 10 kHz/cm^2), and have double gaps with a gas gap of 2 mm. RPC provide a fast response with good time resolution but with a coarser position resolution than the DTs or CSCs. Therefore, RPCs can identify unambiguously the correct bunch crossing. For the trigger, RPCs use the coincidences between stations to reduce background, to improve the time resolution, and to achieve a good p_T resolution.

3.2.7 Trigger System

In the LHC, the beam crossing interval is 25 ns, corresponding to a bunch crossing frequency of 40 MHz. At each crossing of the proton bunches, around 25 collisions took place during the 8 TeV pp collision run and 40 collisions for 13 TeV run. It is impossible to process and store all the events detected, a trigger system is then developed to select the most interesting events and reduce the rates. The rate reduction, by at least a factor of 10^6, is achieved by two steps: Level-1 (L1) Trigger and High-Level Trigger (HLT).The L1 Trigger uses coarsely segmented data from the calorimeters and the muon system, while holding the high-resolution data in pipelined memories in the front-end electronics. The L1 Trigger helps to reduce the rate from 40 MHz down to 100 kHz. While HLT is investigating deeper the L1 selected events in order to further reduce the rate to 100 kHz to be able to save the full granularity information of all the CMS subdetectors. The architecture of the trigger system is shown in figure 3.8.

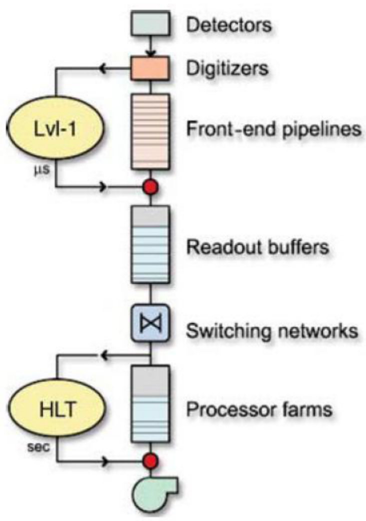

FIGURE 3.8: Architecture of the CMS Trigger System.

The L1 Trigger [54], shown in figure 3.9, consists of custom-designed, largely programmable electronics with a fixed time interval of 3.2 μs. The L1 Trigger hardware is implemented in Field Programmable Gate Array (FPGA) technology, while application specific integrated circuits (ASICs) and programmable memory lookup tables (LUT) are also widely used to fit the requirements of speed, density and radiation resistance. The L1 Trigger has local, regional and global components. The Local Triggers, also called Trigger Primitive Generators (TPG), are based on the energy deposits in calorimeter trigger towers and track segments or hit patterns in muon chambers, respectively. Regional Triggers combine their information and use pattern logic to determine ranked and sorted trigger objects such as energy or momentum and quality, based on detailed knowledge of detectors and trigger electronics and on the amount of information available. The Global Calorimeter and Global Muon Triggers determine the highest rank calorimeter and muon objects across the entire experiment and transfer to the Global Trigger, the top entity of the Level-1 hierarchy. The decision to reject an event or to accept it for the further evaluation by the HLT is determined by the Trigger Control System (TCS). The TCS in the Global Trigger checks if all parts of the CMS detector are in a position to accept a trigger by using feedback from the “Trigger Throttling System (TTS)”, verifies if some additional conditions are fulfilled and then sends out the L1A signal via the “Trigger, Timing and Control (TTC)” system. An important requirement for the Level-1 Trigger is that the decision must be sent out soon enough so that all the detector data are still available in the readout pipelines: the L1T latency is currently limited to about 4 μs or 160 clock cycles of the LHC’s 40 MHz clock. This imposes significant constraints on the L1T electronics.

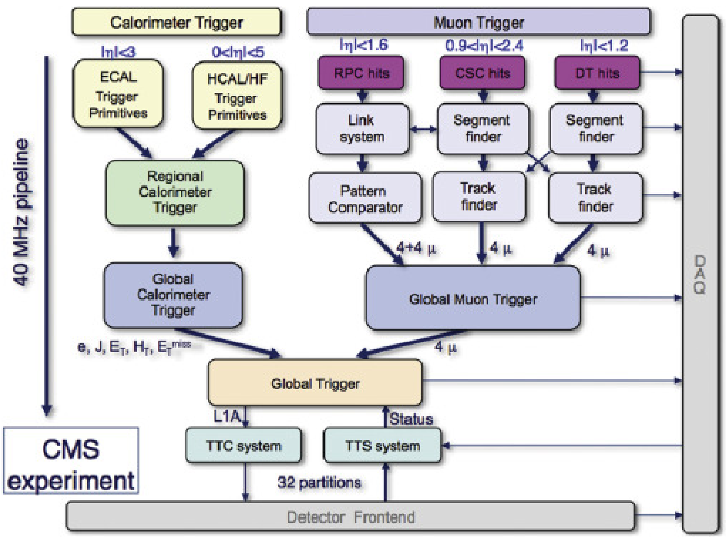

FIGURE 3.9: Architecture of Level-1 Trigger.

The HLT is a software system implemented in a filter farm of about one thousand commercial processors. The HLT has access to the complete read-out data and can therefore perform complex calculations similar to those made in the analysis off-line software if required for specially interesting events. After L1 Trigger, the data from the Front-end pipelines are transferred to readout buffers. After further signal processing of zero-suppression or data-compression, the data are placed in dual-port memories for access by the DAQ system. Each event, with a size of about 1.5 MB (pp interactions), is contained in several hundred front-end readout buffers. Through the “switching networks”, data from a given event are transferred to a processor. Each processor runs the same high-level trigger (HLT) software code to reduce the Level-1 output rate of 100 kHz to 100 Hz for mass storage.

Various strategies guide the development of the HLT code. Only those objects and regions of detector needed are reconstructed, other than all possible objects. Events are to be discarded as soon as possible. This leads to the idea of partial reconstruction and to the notion of many virtual trigger levels, calorimeter and muon information are used. The specific case of double muon HLT is discussed in details in Appendix A.

Chapter 4

Events Reconstruction

4.1 Track and Vertex Reconstruction [55]

The reconstruction of vertices and trajectories of charged particles is vital in the harsh environment of proton proton collisions at the LHC. The track and vertex reconstructions rely on silicon pixel and micro-strip tracker, embedded in a solenoid magnetic field of 4T. The high single point resolution from the tracker system translates into excellent momentum resolution and precise extrapolation of charged particle trajectories to the interaction region. In turn, the reconstruction of primary and secondary vertices, the identification of the decays of long-lived particles could be achieved.

The reconstruction of charged tracks is done in three stages. The first stage provides seeds for further reconstruction, based on pairs of hits which are selected to be compatible with the interaction region and a lower p_T limit, where multiple scattering is also taken into account. The second stage collects the full set of the hits for a charge particle track, with a first estimation of the track parameters calculated from the seed. It is based on a combinatorial Kalman filter [56] approach. A crucial component of the reconstruction is the fast and efficient selection of compatible sensors and hits which is facilitated by the hermeticity of the layers. The third stage consists of a least-squares fit in the form of a Kalman filter for the final estimation of the track parameters. The reconstruction is also fully efficient for muons in the acceptance. Due to the highly non-Gaussian energy loss distribution, electrons constitute a special challenge for track reconstruction, "Gaussian Sum Filter" (GSF) which will be introduced later.

The algorithm for vertex finding and fitting is also the Kalman filter. In the vertex fitting, the possible contamination of the associated tracks from other vertices needs to be considered. The use of robust fit procedures reduces the impact of such outliers on the estimated position. The standard version of a robust fitter is the "trimmed Kalman vertex fitter" (TKF): if the χ^2-probability of the least compatible track is < 5% the track is removed and the fit is re-iterated. An alternative is the "adaptive vertex fitter" (AVF): a weight is assigned to each track as a function of its χ^2-contribution. The weights are determined following an annealing procedure in order to avoid local minima. The AVF is less sensitive to high levels of contamination, but shows to yield a slightly better vertex position resolution and to be faster than the TKF.

Primary vertex candidates are obtained by clustering preselected tracks along the beam line, and the candidates are fitted, and filtered according to their compatibility with the beam line and their χ^2 and finally ranked by the sum of the p_T^2 of associated tracks. The efficiency for reconstruction and correctly tagging the primary vertex of the signal event depends on the number of charged tracks produced at the vertex. While, secondary vertices are reconstructed with the TKF. Secondary vertex candidates are validated using a selection on the distance to the primary vertex and an upper cut on the invariant mass.

4.2 Particle Flow

The Particle Flow (PF) [57] event reconstruction algorithm is well developed in the CMS experiment, and widely used by most of the analyses. The PF algorithm aims at reconstructing and identifying all the stable particles by combining all the informations of CMS sub-detetectors, under the form of charged-particle tracks, calorimeter clusters, and muon tracks. The particle flow event reconstruction improves the identification of electrons, muons, photons, charged hadrons and neutral hadrons, and help the reconstruction of jets and the missing transverse energy (MET).

Most stable particles produced in the proton-proton collisions have rather low p_T. For example, in a quark or gluon jet with total p_T of 500 GeV/c, the average p_T carried by the stable constituent particles is of the order of 10 GeV/c. For the jet with p_T below 100 GeV, the average p_T of the stable constituent particles reduce to a few GeV/c, which is typical of the decay chains of exotic particles. In order to disentangle the production of these exotic particles from the dominant standard model (SM) background processes, it is essential to accurately reconstruct and identify as many of the final stable particles as possible.

The working chain of particle flow must provide high efficiency and low fake rate. These constraints led to the development of advanced iterative tracking and calorimeter clustering algorithms. Moreover, a link algorithm is developed to connect the tracking and clustering elements. More details about iterative tracking, calorimeter clustering and link algorithm will be described in the following sections.

4.2.1 Iterative Tracking

The momentum of charged hadrons is measured by the tracker with a resolution vastly superior to that of the calorimeters for p_T up to several hundreds of GeV/c. Moreover, the tracker provides precise measurements of the charged-particle direction at the production vertex before important deviation by the magnetic field during the propagation to the calorimeters. Since around two third of the energy of a jet is carried by the charged particles, the tracker therefore stands for the cornerstone of the particle-flow event reconstruction.

The charged particles missed by the tracking algorithm could be detected by the calorimeters, with lower efficiency, largely degraded energy resolution and biassed direction. In order to avoid this situation, the tracking efficiency must be as close to 100% as possible. The tracking fake rate, on the contrary, must be kept small because the fake tracks would lead to large energy excesses.

An iterative-tracking strategy [58] was adopted to achieve both high efficiency and low fake rate. First, tracks are seeded and reconstructed with very tight criteria, leading to a moderate tracking efficiency, but a negligibly small fake rate. In the later steps, the procedure removes hits unambiguously assigned to the tracks found in the previous iteration, and loosen track seeding criteria. The softer seeding criteria increases the tracking efficiency, while the hit removal allows to keep low value of the fake rate. In the first three iterations, tracks originating from within a thin cylinder around the beam axis are found with an efficiency of 99.5% for isolated muons in the tracker acceptance, and larger than 90% for charged hadrons in jets. The fourth and fifth iterations have relaxed constraints on the vertex orign, which allows the reconstruction of secondary charged particles originating from photon conversions and nuclear interactions in the tracker material, and from the decay of long-lived particles, such as K_S^0's or Λ's.

4.2.2 Calorimeter Clustering

There are four purposes of a clustering algorithm in the calorimeters: detect and measure the energy and direction of stable neutral particles, such as photons and neutral hadrons; separate these neutral particles from the energy deposits from charged hadrons; reconstruct and identify electrons and all accompanying Bremsstrahlung photons; and help the energy measurement of charged hadrons in case the track parameters were not determined accurately, especially for low-quality or high-p_T tracks. A specific clustering algorithm has been developed with aim of a high detection efficiency for low-energy particles, and a separation of close energy deposit. The clustering is performed separately in each sub-detector: ECAL barrel, ECAL endcap, HCAL barrel, HCAL endcap, the first and second layers of preshower detector.

The clustering algorithm is made up of three steps. First is “cluster seeds”, identified as local calorimeter cell with maximum energy larger than a given energy. Second is “topological clusters”, which is grown from the seeds by aggregating with at least one side in common with a cell already in the cluster, and with an energy above a given threshold. These thresholds represent the deviations of the electronics noise in the ECAL (80 MeV in the barrel and 300 MeV in the end-caps) and in the HCAL (up to 800 MeV). In the last step, “particle-flow clusters” from those topological clusters are used as seeds. The energy of each cell of all particle-flow clusters are shared according to the cell-cluster distance, with an iterative determination of the cluster energies and positions.

4.2.3 Link Algorithm

When a particle passes through the CMS detector, several particle-flow elements could be activated, such as one charged particle track, several calorimeter clusters, or muon tracks. After the tracking and clustering elements are obtained by the previous two steps, a link algorithm is developed to connect these elements to reconstruct single particle and avoid any double counting from different detectors. The link algorithm is tentatively performed for each pair of elements in the event, and computes a distance between any two linked elements to quantify the quality of the link.

To link a charge-particle track and a calorimeter cluster, the track is first extrapolated from its last measured hit in the tracker to the ECAL or HCAL. The track is linked to any given cluster if the extrapolated position in the corresponding calormeter is within the cluster boundaries. In an attempt to take the gaps between calorimeter cells, cracks between calorimeter modules into consideration, the cluster is enlarged by up to the size of a cell in each direction. This also accounts for the uncertainty on the position of the shower maximum, and for the effect of multiple scattering for low-momentum charged particles.

In order to collect the energy of all Bremsstrahlung photons emitted by electrons, tangents to the tracks are extrapolated to the ECAL from the intersection points between the track and each of the tracker layers. A cluster would be linked to the track as a potential Bremsstrahlung photon if the extrapolated tangent position is within the cluster boundaries.

It is similar for the link between two calorimeter clusters, such as between an ECAL and a PS cluster, or between a HCAL and an ECAL cluster. They would be linked when the cluster position in the more granular calorimeter (PS or ECAL) is within the cluster envelope in the less granular calorimeter (ECAL or HCAL).

The last type of link is between a charge-particle track in the track and a muon track in the muon system. A global fit between two tracks returns an acceptable χ^2 [49]. When there are several global muons fit with one given muon track and several tracker tracks, only the global muon with the minimum value of χ^2 returns.

4.3 Muons

The muons [59] are one of the particles that can be precisely measured and well reconstructed in the CMS detector. The muons have 2.2 μs of lifetime, a mass of 105 MeV (200 times heavier than the electron), and have small energy loss when traversing matters. When the muons go through the CMS detectors, they leave tracks in the inner tracker and muon system.

There are two reconstruction approaches for the muons: Global Muon reconstruction (outside-in) and Tracker Muon reconstruction (inside-out). In the first case, for each standalone-muon track from muon detector, a matching tracker track is found by comparing parameters of two tracks. A global-muon track is fitted combining hits from the tracker track and standalone-muon track, using Kalman filter technique. At large transverse momenta, $p_{\mathrm{T}} \geq 200$ GeV$/c$, the global-muon fit can improve the momentum resolution compared to the tracker-only fit. In the second case, all tracker tracks with $p_{\mathrm{T}} > 0.5$ GeV$/c$ and with total momentum $p > 2.5$ GeV$/c$ are considered as possible muon candidates, and are extrapolated to the muon system taking into account the magnetic field, the average expected energy losses, and multiple coulomb scattering in the detector material. If at least one muon segment from muon detector matches the extrapolated track, the corresponding tracker track qualifies as a Tracker Muon. The extrapolated track and the segment are considered to be matched if the distance between them if the local x is less than 3 cm or if the value of the pull for local x is less than 4 cm, where the pull is defined as the difference between the position of the matched segment and the position of the extrapolated track, divided by their combined uncertainties.

Tracker Muon reconstruction is more efficient than the Global Muon reconstruction at low momenta, $p \leq$ 5GeV$/c$, because it requires only a single muon segment in the muon detector, whereas Global Muon reconstruction is designed to have high efficiency for muons penetrating through more than one muon station and typically requires segments in at least two muon stations.

Reconstructed muons are fed into the CMS particle flow (PF) algorithm. For Muons, the particle-flow approach applies particular selection criteria to the muon candidates reconstructed with the Global and Tracker Muon algorithms described above. The requirements are based on various quality parameters from the muon reconstruction, as well as use information from other subdetectors.

To distinguish between prompt muons and those from weak decays within jets, the isolation of a muon is evaluated relative to its p_{T} by summing up the energy in geometrical cones ($\Delta R = \sqrt{(\Delta\phi)^2 + (\Delta\eta)^2}$) surrounding the muon. One strategy sums reconstructed tracks (track based isolation), while another uses charged hadrons and neutral particles coming from PF (PF isolation). Tight and loose working points are defined to achieve efficiencies of 95% and 98%, respectively. They are tuned with simulated tight muons from Z$\rightarrow \mu\mu$ with p_{T} > 20 GeV. The values for the tight and loose working points for PF isolation within ΔR< 0.4 are 0.15 and 0.25 respectively for the data collected at Run II.

4.4 Electrons

The electrons [60] are reconstructed by associating a track reconstructed in the silicon detector with a cluster of energy in the ECAL. The electron properties are estimated by clustering the energy deposited in the ECAL, building the electron track, and associating two inputs. As the bremsstrahlung radiation severely affects the track propagation, a dedicated tuning of the trajectory building and a Gaussian Sum Filter track fit are used. In order to maximize the performace, a mixture of a stand-alone approach [61] and the complementary global "particle-flow" (PF) algorithm is also applied.

The electron energy usually spreads out over several crystals of the ECAL. This spread can be quite small when electrons lose little energy via bremsstrahlung before reaching ECAL. For an electron produced in CMS, the effect induced by radiation of photons can be large: 33% (86%) of electron energy is radiated before it reaches the ECAL where the intervening material is minimal $\eta \approx 0$ (maximal $|\eta| \approx$ 1.4). In order to measure the initial energy of the electron accurately, it is vital to collect the energy of the radiated photons which mainly spreads along the ϕ direction because of the bending of the electron trajectory in the magnetic field. Two clustering algorithms are used to measure the intial energy of the electrons. They are the "hybrid" algorithm in the barrel, and the "multi-5×5" in the endcap. The hybrid algorithm exploits the geometry of the ECAL barrel (EB) and properties of the shower shape, collecting the energy in a small window in η and an extended window in ϕ. It starts with a seed crystal, which contains most of the energy deposited in any considered region with a minimum energy of 1 GeV. Arrays of 5×1 crystals, with energies larger than 0.1 GeV, are added around the seed crystal and grouped into clusters. If the distinct cluster has a seed array with energy larger than 0.35 GeV, it will be added in the final global cluster collection, called the supercluster (SC). The multi-5×5 algorithm is used in the ECAL endcaps (EE), where crystals are not arranged in an $\eta \times \phi$ geometry. The starting points are the seed crystals with local maximal energy relative to their four direct neighbours, with energy larger than 0.18 GeV. Around these seeds and beginning with the largest E_T, the energy is collected in clusters of 5×5 crystals. If the energy of these clusters is larger than 1 GeV, within 0.07 in η and 0.3 rad in ϕ from each seed crystal, they are grouped into an SC. The energy-weighted positions of all clusters belonging to an SC are then extrapolated to the planes of the preshower, with the most energetic cluster as reference point. The preshower energies around the reference point are added to the SC energy.

The electron tracks are reconstructed with a dedicated tracking procedure to collect the hits efficiently, while preserving an optimal estimation of track parameters over the large range of energy fractions lost through bremsstrahlung. There are two steps in the electron track reconstruction: seeding and tracking. The seeding consists of finding and selecting the two or three first hits in the tracker from which the track can be initiated. It is of primary importance since its performace greatly affects the reconstruction efficiency. Two complementary algorithms, the ECAL-based seeding and the tracker-based seeding, are used and their combined results. The ECAL-based seeding starts from the SC energy and position, used to estimate the electron trajectory in the first layers of the trackers, and selects electron seeds from all the reconstructed seeds. The tracker-based seeding relies on tracks of charged particles, extrapolated towards the ECAL and matched to an SC. The tracker-based seeding is developed as part of the PF-reconstruction algorithm starting with the KF algorithm, which can reconstruct accurately the electron trajectory when bremsstrahlung is negligible. If the KF algorithm failed, indicating potential presence of significant bremsstrahlung, a dedicated Gaussian sum filter (GSF) [62] is used to fit the tracks. While the tracking consists of the track building and track fitting. The track building is initiated with the selected electron seeds, and based on the combinatorial KF method. The combinatorial KF method proceeds each electron seed iteratively from the track parameters provided in each layer, including one-by-one the information from each successive layer. The compatibility between the predicted and the found hits in each layer is chosen not to be too restritive, in order to follow the electron trajectory in case of bremsstrahlung and to maintain good efficiency. Once the hits are collected, a GSF fit is performed to estimate the track parameters.

The electron candidates are constructed from the association of a GSF track and a cluster in the ECAL. For ECAL-seeded electrons, this requires a geometrical matching between the GSF track and the SC within $\Delta\eta \times \Delta\phi$=0.02×0.15. For tracker-seeded electrons, a global identification variable is defined using an MVA technique that combines information on track observables, the electron PF cluster observables, and the association between the two. For electrons seeded through both approaches, a logical OR is applied on the two selections. The overall efficiency is ≈93% for electrons from Z decay, and the reconstruction efficiency measured in data is compatible to the simulatied one.

4.5 Z Bosons

The Z boson candidates are reconstructed from the oppositely charged lepton pair ($\mu^+\mu^-$ or e^+e^-) with two highest transverse momenta. The four-momentum vector of the Z boson are obtained from the sum of the two charged leptons' four-momentum:

$$p_Z = p_{l1} + p_{l2} \tag{4.1}$$

In order to reduce the background contamination, the Z boson candidate is required to have a reconstructed invariant mass between 71 and 111 GeV.

4.6 Jets

Jets are reconstructed using particle flow particles and the anti-k_T clustering algorithm [63], with a distance parameter of R = 0.4 for Run II (R = 0.5 for Run I). The anti-k_T algorithm starts with two definition of distances d_{ij} (between entities i and j) and d_{iB} (between entity i and the beam (B)):

$$d_{ij} = min(k_{ti}^{2p}, k_{tj}^{2p})\frac{\Delta_{ij}^2}{R^2}; \tag{4.2}$$

$$d_{iB} = k_{ti}^{2p} \tag{4.3}$$

where $\Delta_{ij}^2 = (y_i - y_j)^2 + (\phi_i - \phi_j)^2$ and k_{ti}, y_i and ϕ_i are respectively the transverse momentum, rapidity and azimuth of particle i, and R is the distance parameter. The clustering proceeds by identifying the smallest of the two type distances d_{ij} and d_{iB}. If it is d_{ij}, entities i and j will be recombined to one entity. If it is d_{iB}, entity i will be called as a jet, and removed from the list of entities. This procedure will continue until no entities are left.

The PF-jet performance greatly benefits from two effects [64]: Firstly, approximately 90% of the measured jet energy is reconstructed as the charged hadrons and photons, which are measured precisely by tracker and ECAL respectively. While only the remaining 10% are reconstructed as neutral hadrons, which are measured only with HCAL with a poorer resolution. Secondly, a dedicated calibration can be applied to reconstruct particles. As a consequence, a good jet response would be reached, and the jet energy resolution is also highly improved. Besides, the additional $p_{\mathrm{T,offset}}$ per jet due to pile-up (PU) particles need to be considered and subtracted. The average $p_{\mathrm{T,offset}}$ per primary vertex for 2015 data [65], which is similar to the Run I data, is illustrated in figure 4.1. In the central region, approximately 50% of $p_{\mathrm{T,offset}}$ is coming from charged

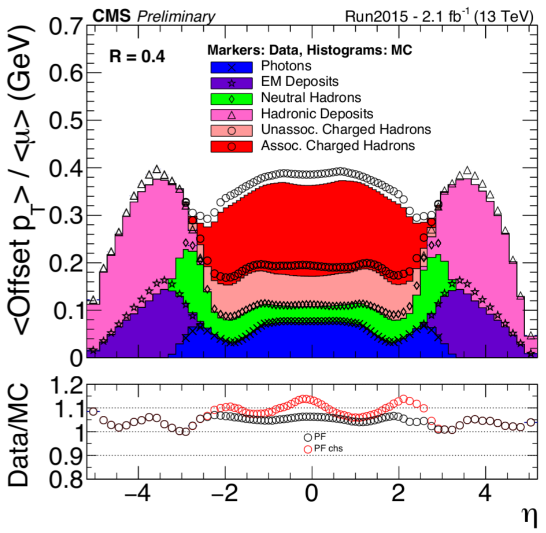

FIGURE 4.1: Average jet $p_{\mathrm{T,offset}}$ due to PU per primary vertex and PF-particle type vs η with 2015 data, unassoc. charged hadrons refer to charged PU. <μ> refers to the average pileup.

particles unambiguously associated to PU vertex. These particles can be subtracted from the event prior to the jet clustering to reduce the impact of PU. This Charged Hadron Subtraction (CHS), which is explained in the later section, is applied to correct the jet momentum reconstruction from PU.

The jet energy corrections (JEC) relate the energy of the reconstructed jets on average to the energy at particle level. The primary JEC factors are derived from simulated event relative to the generator jets, and only the remaining, small differences between the response in data and simulation are corrected for using data-driven methods. Since the latter corrections are derived as data-to-simulation ratios, potential biases of the methods cancel to first approximation. The first factor in the JEC subtracts the $p_{\mathrm{T,offset}}$ due to PU contributions. It is an average correction derived from the global per-event jet area and $p_{\mathrm{T,offset}}$ density ρ, which is described as a function of η and p_{T} from simulated events. The second, JEC factor corrects for the p_{T} and η dependence of the average jet response due to the calorimeter non-linearities and p_{T} thresholds, the different detector properties along η, and geometric effects. The jet energy scale (JES) is also validated in data, and small remaining differences to the simulation are converted into a residual correction factor. After application of the corrections, the JEC uncertainty at Run II is shown in figure 4.2. At low p_{T}, the uncertainties are dominated by the PU-correction uncertainty.

4.7 Pileup

Given the proton-proton collisions instantaneous luminosity at the LHC the data sample contains a significant number of additional interactions per bunch crossing, known as pileup (PU). The origin of pileup deposits are various, however most pileup jet are built from low p_{T} QCD jet production from collisions. To reconstruct the pileup in

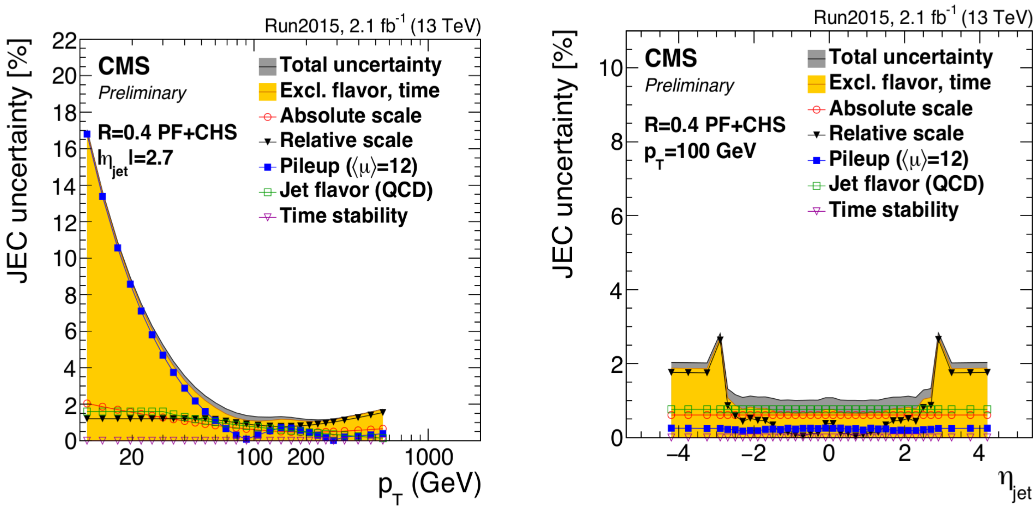

FIGURE 4.2: Relative JEC uncertainty and its dependences in p_T and η, $<\mu>$ refers to the average pileup

the events, a vertex reconstruction is performed on all charged tracks. The primary vertex reconstruction efficiency is 70% for a pileup vertex. In 2015 the average pileup multiplicity varied from around 20 at the beginning of the highest luminosity fills to below 10 in the tails of the fills with lower instantaneous luminosity, as illustrated in figure 4.3.

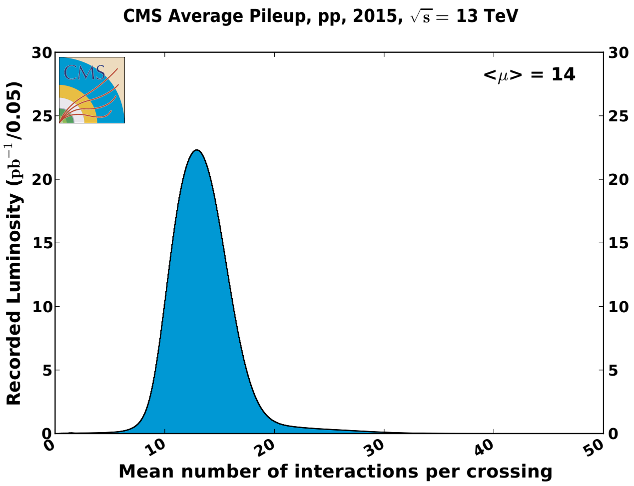

FIGURE 4.3: Average pileup in 2015

There are two types of pileup: out-of-time pileup and in-time pileup. The pileup comes from the additional inelastic proton-proton interactions within the same bunch crossing, known as in-time pileup. The additional contributions in the signal readout from the previous and next bunch crossings, known as out-of-time pileup. The influence of out-of time pileup on the events is much smaller than the ones from in-time pileup. To reduce the effect from in-time pileup, the Charged Hadron Subtraction (CHS), as mentioned in section 4.6, is implemented. The method is: the charged hadrons associated with vertices other than the primary interaction vertex, chosen to be the one with the highest sum p_T over its associated tracks, are removed from the list of PF candidates.

This procedure strongly reduces the dependence of the jet energy, improving the jet energy resolution at low p_T. The energy of PF+CHS jets is corrected to account for residual pileup and nonlinear calorimetric response, as a function of η and p_T.

In general, the Monte Carlo samples are generated with a PU scenario quite close to the data one. The simulated events are reweighted in order to better match the data PU distribution. In the analysis of 2015 data, MADGRAPH sample uses the pileup simulation with double Poisson distribution, which simulates better the data. The Poisson distribution could be used to describe the pileup with fixed luminosity. At the LHC, the luminosity varies in different period of the proton-proton collisions. So it is better to use double Poisson distribution to make sure that the low and high pileup would be better described. The number of reconstructed vertices is obtained using the minimum bias p-p cross-section of 69 mb. The distribution of the number of vertices after reweighting is illustrated in figure 4.4.

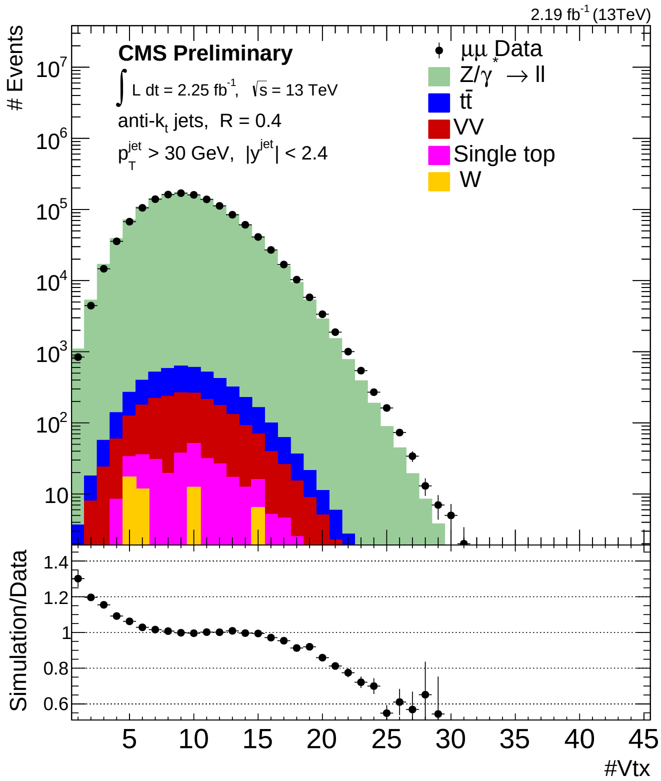

FIGURE 4.4: Distribution of the number of vertices in the data and in the MC after reweighting

Chapter 5

Z Boson production in Association With Jets

This chapter presents the measurement of the differential cross section of Z boson production in association with jets from proton-proton collisions at the center-of-mass energy of 13 TeV, where Z stands for a Z/γ^{*} around the Z boson mass within the [71, 111] GeV interval. The first data at this energy recorded by CMS detector in 2015 are used, corresponding to an integrated luminosity of 2.19 fb^{-1}. The cross section is presented as a function of jet multiplicity and jet kinematic, rapidity and transverse momentum of the individual jets. The transverse momentum balance between the Z boson and the jets are also studied. The measurements are compared with the predictions with multileg NLO predictions using the FxFx merging scheme, with multileg LO predictions using the MLM matching scheme, with Z+1 *jet* NNLO fixed order calculations and with GENEVA fully-differential NNLO calculation for Drell-Yan production combined with higher-order resummation in the 0-jettiness resolution variable.

5.1 Introduction

The process of Z boson in association with jets at LHC is central both for physics measurements and for the study of detector response. The decay of Z boson in charged leptons (two muons or two electrons) has a high reconstruction efficiency, and contaminated with marginal amounts of background, which offers an ideal condition for the study of hadronic jet production. The measurements of this process provide stringest tests on the perturbative quantum chromodynamics (pQCD), and is crucial for deep understanding and modeling of QCD interactions. The high center-of-mass energy at the CERN LHC allows the production of an electroweak boson along with a number of jets with large transverse momenta. A precise knowledge of the kinematic dependencies in processes with large jet multiplicity is essential to exploit the potential of the LHC experiments. Comparison of the measurements with predictions motivates additional Monte Carlo (MC) generator development and improves our understanding of the prediction uncertainties. Moreover, the production of Z+jets is also important background for a number of Standard Model (SM) processes, such as single top, $\mathrm{t\bar{t}}$ production, vector boson fusion, WW scattering, and Higgs boson production, as well as searches for physics beyond the SM. A precise understanding of Z+jets is therefore highly desirable for these searches and measurements. The present measurement of differential cross sections of Z+jets is performed for the first time at a center-of-mass of 13 TeV.

The cross section of this process has been measured at lower energies, by CDF and D0 collaborations with proton-antiproton ($p\bar{p}$) collision at a center-of-mass energy $\sqrt{s}$ = 1.96 GeV [66] by ATLAS and CMS collaborations from proton-proton (pp) collision at a center-of-mass energy $\sqrt{s}$ = 7 TeV [67, 68, 69] and by CMS at a center-of-mass energy $\sqrt{s}$ = 8 TeV [70].

5.1.1 Measured Observables

The differential cross sections are measured as a function of the following variables:

- Exclusive and inclusive jet multiplicities, N_{jets}
- Transverse momenta ($p_T(Z)$) of Z boson for $N_{jets} \geq 0, 1$
- Transverse momenta of the jet for $N_{jets} \geq 1, 2, 3$
- Rapidity y of the jet for $N_{jets} \geq 1, 2, 3$
- Scalar sum of the jets transverse momentum (H_T) for $N_{jets} \geq 1, 2, 3$
- p_T balance between the Z boson and the sum of the reconstructed jets for $N_{jets} \geq 1, 2, 3$:

$$p_T \text{ balance} = |\vec{p}_T(Z) + \sum_{\text{jets}} \vec{p}_T(j_i)| \tag{5.1}$$

- Jets-Z balance (JZB)

$$\text{JZB} = |\sum_{\text{jets}} \vec{p}_T(j_i)| - |\vec{p}_T(Z)| \tag{5.2}$$

The jet multiplicity is a variable, which give a general view about the agreement between measurement and different predictions. The comparisons can test different MC generators, and also estimate their reliability in different configuration as number of jets. In the analysis, the inclusive jet multiplicity refers to designate the events with at least N jets, and exclusive jet multiplicity refers to the events with exactly N jets.

The jet kinematic variables and H_T are measured for events with a minimum jet multiplicity of 1,2 and 3. The measured distributions of these variables make it possible to quantify the level of agreement between data and theory. It is extreme interesting regarding a particular matching scheme. For example, the transverse momentum of small-p_T jets with matrix elements (ME) calculation leads to divergences, where the merging of ME and parton shower (PS) occurs. It is extreme interesting regarding a particular matching scheme.

The balance between the Z boson and jet transverse momenta is also studied through the observables p_T balance and JZB , where the sums run over jets with p_T > 30 GeV and $|y|$ < 2.4. The hadronic activities not reconstructed in these jets will lead to an imbalance that translates into p_T^{balance} and JZB values different from zero. This includes hadronic activity in the forward region ($|y|$ > 2.4), which is the dominant contribution according to the simulation. Gluon radiation in the central region, not clustered in a jet ($p_T > 30$), will also contribute to the imbalance. The JZB variable has two signs of value: the value will be positive when the hadronic activity not included is in the direction of the Z boson, and the value will be negative while the hadronic activity not included is in the opposite direction of the Z boson. The JZB variable is also studied for the conditions of $p_T(Z)$ below and above 50 GeV. The (p_T^{balance}) observable is particularly relevant for the study of the core of the distribution where the hadronic activity that is unaccounted for leads to the peak of the distribution shift to larger values.

The Z boson transverse momentum, $p_T(Z)$, can be described through fixed-order calculations in pQCD, at small transverse momentum this requires resummation of multiple soft-gluon emissions to all order in perturbative theory [71, 72]. The variable of inclusive $p_T(Z)$ is very sensitive to the Z boson reconstruction. The measurement of the distribution of $p_T(Z)$ for events with at least one jet could help to understand the balance in the transverse momentum between the jets and the Z boson, and can be used for the comparison amongst theoretical predictions which deal with multiple soft-gluon emissions with different ways.

5.2 Data and Monte Carlo Samples

5.2.1 Data Samples

The data collected during the run D of year 2015 (25 ns minimum proton brunch spacing mode) is used for the analysis. The data containing Z→ $\mu^+\mu^-(ore^+e^-)$ events are listed in the table 5.1 and certified according to internal working group, corresponding to an integrated luminosity of 2.19 fb^{-1}. The analysis is based on miniAOD version 2 using CMSSW release CMSSW_7_6_X and the latest Jet Energy Corrections (JEC) [73, 74].

TABLE 5.1: Data sets and JSON file used in the analysis.

Name	#Events	$\mathcal{L}(pb^{-1})$
/DoubleMuon/Run2015D-16Dec2015-v1/MINIAOD	39445366	2250.29
/DoubleEG/Run2015D-16Dec2015-v2/MINIAOD	70832713	2250.91

5.2.2 Simulation Samples

The signal and background processes are predicted from Monte Carlo (MC) based simulations, while the response of the detector is simulated with GEANT4 [75]. The samples of signal and background used in the analysis can be found in the table 5.2. The simulation of signal (DYJetsToLL in the table 5.2) is generated with MADGRAPH5_-AMC@NLO (MG5_AMC) [30] using the FxFx merging scheme [76], and restricted to oppositely charged leptonic Z boson decay with an invariant mass above 50 GeV. The initial- and final- state parton shower and hadronization is performed with PYTHIA8 using the CUETP8M1 tune [77]. The matrix elements (ME) includes Z + 0,1,2 jets NLO computation, giving a LO accuracy for Z + 3 jets. In the matrix elements (ME) calculation, the NNPDF 3.0 NLO PDF [78] is used and the strong coupling constant $\alpha_s(m_Z)$ is set to 0.118 at the Z boson mass scale. The native cross section obtained from the generator is used.

The simulation samples of background used are $\mathrm{t\bar{t}}$ (TT), single top (ST), double vector boson and W+jets. The $\mathrm{t\bar{t}}$ and single top backgrounds are generated using POWHEG [79] interfaced with PYTHIA8. The total cross section of $\mathrm{t\bar{t}}$ production is normalized to the prediction with NNLO accuracy in QCD and NNLL for the soft gluon radiation resummation calculated with TOP++ 2.0 [80]. The double vector boson electroweak productions are generated with MG5_AMC (WZ), POWHEG (WW), both interfaced to PYTHIA8, and with PYTHIA8 alone (ZZ). The total cross section of WZ and ZZ diboson samples are normalised to the NLO prediction calculated with MFCM 6.6, whereas cross section of WW samples are normalised to NNLO prediction [81]. W+jets sample is generated by MG5_aMC with a NLO prediction, interfaced with PYTHIA8. The cross section of W+jets is normalised to native cross section. For all the samples, the strong coupling constant and PDF uncertainties are estimated using the LHC4PDF recommendations [82, 83] with CT10, NNPDF2.3 and MSTW2008 sets.

The signal process (Z → ll + jets) also contains the Z decay in $\tau^+\tau^-$, which is considered as a background subtracted during the unfolding procedure. The contribution of this background after the event selections is lower than 1%.

TABLE 5.2: Simulation samples used in the analysis. The number of generated events and corresponding cross sections are presented.

Name	# Events	σ (pb)
Signal		
DYJetsToLL_M-50_TuneCUETP8M1_13TeV-amcatnloFXFX-pythia8	28500769	6025.2
Background		
TT_TuneCUETP8M1_13TeV-powheg-pythia8	87995547	831.76
ST_tW_top_5f_inclusiveDecays_13TeV-powheg-pythia8_TuneCUETP8M1	1e+06	35.6
ST_tW_antitop_5f_inclusiveDecays_13TeV-powheg-pythia8_TuneCUETP8M1	749400	35.6
ST_s-channel_4f_leptonDecays_13TeV-amcatnlo-pythia8_TuneCUETP8M1	998400	10.32
ST_t-channel_5f_leptonDecays_13TeV-amcatnlo-pythia8_TuneCUETP8M1	2995200	216.99
WJetsToLNu_TuneCUETP8M1_13TeV-amcatnloFXFX-pythia8	24156124	60290
WWTo2L2Nu_13TeV-powheg	1979988	12.21
WZJets_TuneCUETP8M1_13TeV-amcatnloFXFX-pythia8	1937499	4.4
ZZ_TuneCUETP8M1_13TeV-pythia8	985600	15.4

5.3 Event Selection

The final state particles in Z+jets process are identified and reconstructed with the particle flow (PF) event algorithm, as mentioned in section 4.2, which combines all the informations of CMS sub-detectors to accurately reconstruct and identify as many of the final stable particles as possible. In the analysis, certain event selection cuts are applied to reduce the contaminations from background processes while maintaining sufficient amount of the signal events. In this section, the selections applied on the events are introduced: the trigger applied on charged isolated leptons, the kinematic selections on charged isolated leptons, the cuts on Z mass, and the selections on jets. Moreover, the efficiencies and the scale factors used to correct the small differences between the data and simulation are also included.

5.3.1 Trigger

The data samples used for this analysis were collected with unprescale double muon or double electron triggers depending on the channel. For the muon channel, the events passing one of the two following triggers are selected:

```
HLT_Mu17_TrkIsoVVL_Mu8_TrkIsoVVL_DZ
HLT_Mu17_TrkIsoVVL_TkMu8_TrkIsoVVL_DZ
```

while for electron channel, the corresponding unprescaled trigger is:

```
HLT_Ele17_Ele12_CaloIdL_TrackIdL_IsoVL_DZ
```

These triggers guarantee the selected events having two muons or two electrons candidates coming from the same primary vertex.

5.3.2 Charged Isolated Leptons

This analysis aims to study the production of Z boson in association with jets. The Z boson decays into two oppositely charged muons ($\mu^+\mu^-$) or electrons ($\mathrm{e}^+\mathrm{e}^-$). The selections on muons and electrons will be introduced as following.

The muon candidates are reconstructed with PF algorithm, requested to satisfy the $Tight\ identification$ criterion (table 5.3) recommended by the Muon POG [84]. To distinguish between reconstructed muons and those from weak decays within jets, a cut on the isolation of the muon is required:

$$I_{ISO}^{PF} = [\sum^{charged} p_\mathrm{T} + max(0, \sum^{neutral} p_\mathrm{T} + \sum^{EM} p_\mathrm{T} - 0.5 \sum^{PU} p_\mathrm{T})]/p_\mathrm{T}^{\mu} \leq 0.25, \tag{5.3}$$

where the sums run over the corresponding particles inside a cone of radius $\Delta R = \sqrt{(\Delta\phi)^2 + (\Delta\eta)^2} = 0.4$ around the muon candidate, for charged hadrons ($charged$), the neutral hadrons ($neutral$), photons (EM), charged particles from the pileup (PU). Since neutral pileup particles deposit on average half as much energy as charged pileup particles, the contamination in the isolation cone from neutral particles coming from pileup interactions is estimated as $0.5\sum^{PU} p_\mathrm{T}$, and it is subtracted in PFIsoCorr. While the 0.25 value corresponds to the standard $Loose\ isolation$ cut. Finally, the muons are required to have p_T > 20 GeV with $|\eta|$ < 2.4.

A comparison of data and simulation of the muon isolation variable I_{ISO}^{PF} is illustrated in figure 5.1. An good agreement between data and simulation for values below 0.25.

TABLE 5.3: List of cuts applied for the *Tight identification* of muons for Run-II

Variable	Cut
`isGlobalMuon()`	$= 1$
`isPFMuon()`	$= 1$
χ^2/`ndof of global muon track`	< 10
`number of muon-chamber hit`	> 0
`number of matched station`	> 1
`dxy`	< 0.2 cm
`dz`	< 0.5 cm
`number of pixel hits`	> 0
`number of tracker layers with hits`	> 5

When the value of I_{ISO}^{PF} is larger than 0.3, the disagreement is mainly due to the presence in the data of QCD background, which is not included in the simulated background list and negligible in the final selection.

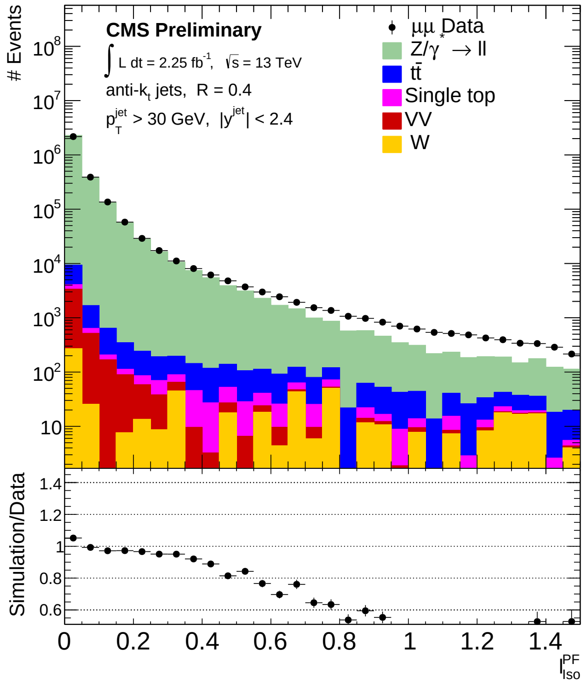

FIGURE 5.1: Data to simulation comparison of the muon isolation variable.

Similarly the electron candidates are selected from the particle flow electron collection. They are additionally requested to satisfy the *Medium identification* criterion as defined by the EGammma POG [85], details are given in table 5.4.

They are also required to be isolated with a PF isolation smaller than 15% of the electron p_{T}.

$$I_{ISO,\rho}^{PF} = [\sum^{charged} p_{\mathrm{T}} + max(0, \sum^{neutral} p_{\mathrm{T}} + \sum^{EM} p_{\mathrm{T}} - \rho EA)]/p_{\mathrm{T}}^{\mu} \leq 0.15 \quad (5.4)$$

TABLE 5.4: List of cuts applied for the Medium identification of electrons.

Variable	Barrel Cut	Endcap Cut
`dEtaIn`	< 0.0103	< 0.00733
`dPhiIn`	< 0.0336	< 0.114
`sigmaIEtaIEta`	< 0.010	< 0.02883
`H/E`	< 0.0876	< 0.0678
`|1/E-1/P|`	< 0.0174	< 0.0898
`d0vtx`	< 0.0118	< 0.0739 cm
`dzvtx`	< 0.373	< 0.602 cm
`vtxFit`	`true`	`true`
`mHits`	≤ 2	≤ 1

where the sums run over the corresponding particle inside a cone of radius $\Delta R \leq 0.3$. The term ρEA represents a correction for pileup effects, where ρ, the level of diffuse noise, corresponds to the amount of transverse momentum added to the event per unit area. Finally, we restrict the electron kinematic to $p_{\mathrm{T}} > 20$ GeV and $|\eta| \leq 1.442$ or $1.566 \leq |\eta| \leq 2.4$, where η refers to the supercluster η.

5.3.3 Z bosons

The Z boson candidates are reconstructed from the lepton pair ($\mu^+\mu^-$ or e^+e^-) with two highest transverse momenta. The four-momentum vector of the Z boson are obtained as the sum of the two charged lepton four-momentum:

$$p_Z = p_{l1} + p_{l2} \tag{5.5}$$

The lepton pair must be made of oppositely charges particles, with an invariant mass between 71 GeV and 111 GeV.

5.3.4 Jets

The PF jet candidates are clustered using the anti-k_{T} algorithm, with a distance parameter of R = 0.4. To keep all charged particles originating from the Z boson vertex and correct the jet momentum reconstruction from pileup effects, the Charged Hadron Subtraction (CHS) is applied.

The $Loose\ identification$ criterion provided by the JetMET POG is applied in order to avoid misidentification and to increase noise rejection. The list of cuts constitutes the $Loose\ identification$ criterion is given in the table 5.5. Besides, the jets are required a separation, $\Delta R = \sqrt{(\Delta\phi)^2 + (\Delta\eta)^2}$, between the reconstructed jets and the lepton candidates to be larger than 0.4.

To remove jets coming from the pileup, a cut on the Multi-Variate Analysis (MVA) variable, $puMVA > -0.2$ [86] is applied. The pileup contamination is also reduced by

TABLE 5.5: List of cuts applied for the PF jet loose ID criteria.

Jet Variables	Cut
`Charged Hadron Fraction`	> 0.0
`Charged Multiplicity`	> 0
`Charged EM Fraction`	< 0.99
`Neutral Hadron Fraction`	< 0.99
`Neutral EM Fraction`	< 0.99

the ch To ensure a good quality of tracking information, jets with $|y| \geq 2.4$ are removed from the collection. In the end, the jet collection is ordered by decreasing p_{T} value.

5.3.5 Efficiencies and scale factors

For each step of the lepton selection, i.e. trigger, lepton identification, and lepton isolation, there is a non-zero probability to miss a lepton, which would have been poorly reconstructed or ended up into some dead part of the detector. In order to correct such effects, the different type of efficiencies must be computed.

The efficiencies of the triggers used in the analysis are evaluated using so-called "reference trigger" method, which is introduced in details in chapter A. Once the trigger efficiencies of data and MC are obtained, scale factors are computed by taking the ratio of data over MC efficiency. The trigger scale factors of muon and electron channel as a function of $|\eta|$ of the two leptons are shown in the figure 5.2, 5.3.

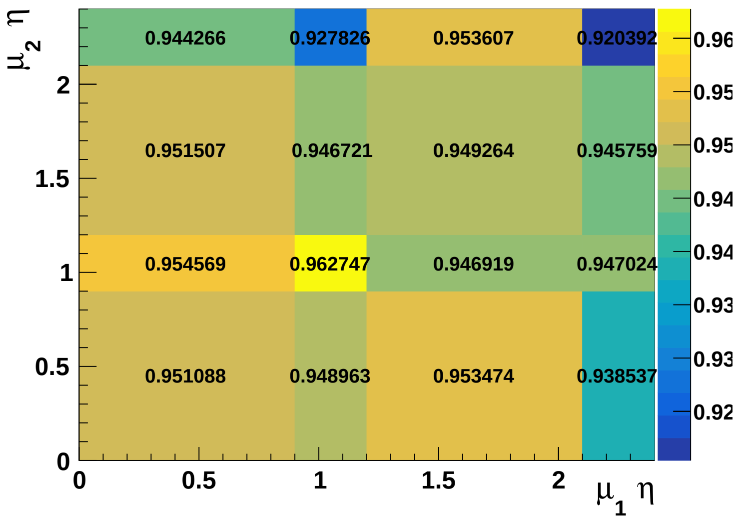

FIGURE 5.2: Double muon trigger scale factor as a function of two lepton pseudorapidities for the muon channel ($\mu\mu$).

However, we do not apply absolute efficiency correction at this level as it will be taken into consideration by the unfolding procedure, detailed in section 5.7.2. But we apply a scale factor to the MC yields to compensate the measured differences between

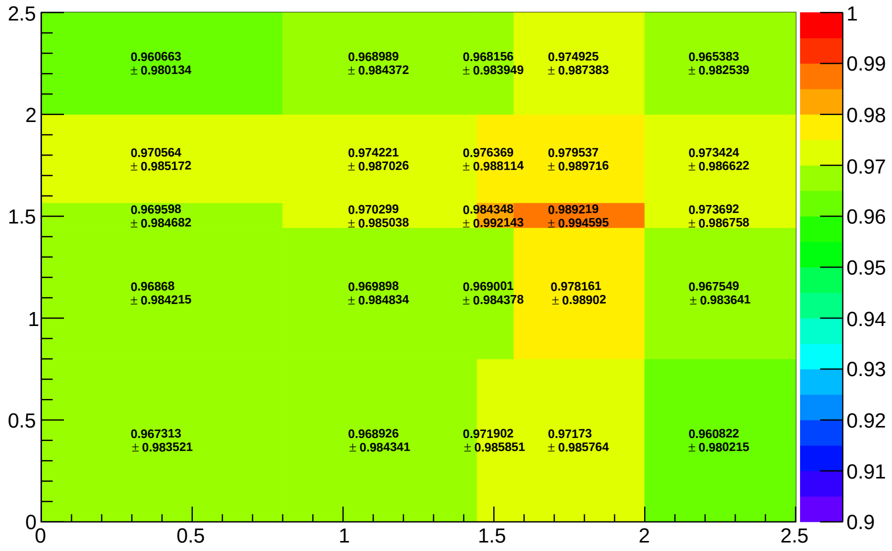

FIGURE 5.3: Double electron trigger scale factor as a function of two lepton pseudorapidities for the electron channel (ee).

data and MC efficiencies. For the trigger rescaling, the scale factor is applied on the leptons pair. When dealing with identification and isolation efficiencies, the scale factor is given as a function of p_{T} and $|\eta|$ of one lepton, and applied to each of the two leptons constituting the Z boson. The identification and isolation scale factors for the muon decay channel listed in table 5.6 and 5.7, while the ones for the electron decay channel are given in table 5.8. All the scale factors are the official numbers provided by the Muon and Egamma POGs, except the muon trigger scale factor that was estimated for this analysis. The muon trigger scale factor are provided as a function of the η of two muons. The muon η value has been divided into four region: the central (0.0<$|\eta|$ $\leq$0.9), the overlap (0.9<$|\eta|$ $\leq$1.2), the endcap (1.2<$|\eta|$ $\leq$2.1) and the forward region (2.1<$|\eta|$ <2.4)

TABLE 5.6: Muon Identification scale factors (Data/MC) for Tight ID.

GeV	$0 < \|\eta\| \leq 0.9$	$0.9 < \|\eta\| \leq 1.2$	$1.2 < \|\eta\| \leq 2.1$	$2.1 < \|\eta\| \leq 2.4$
$20 < p_{\mathrm{T}} \leq 25$	0.975 ± 0.003	0.978 ± 0.005	0.993 ± 0.002	0.978 ± 0.004
$25 < p_{\mathrm{T}} \leq 30$	0.983 ± 0.002	0.976 ± 0.003	0.990 ± 0.001	0.976 ± 0.003
$30 < p_{\mathrm{T}} \leq 40$	0.984 ± 0.001	0.980 ± 0.001	0.992 ± 0.001	0.978 ± 0.001
$40 < p_{\mathrm{T}} \leq 50$	0.987 ± 0.001	0.980 ± 0.001	0.991 ± 0.000	0.978 ± 0.001
$50 < p_{\mathrm{T}} \leq 60$	0.982 ± 0.001	0.977 ± 0.002	0.989 ± 0.001	0.973 ± 0.003
$60 < p_{\mathrm{T}} \leq 120$	0.986 ± 0.002	0.984 ± 0.004	0.991 ± 0.002	0.964 ± 0.008
$120 < p_{\mathrm{T}} \leq 300$	1.000 ± 0.000	1.000 ± 0.000	1.000 ± 0.000	1.000 ± 0.000

TABLE 5.7: Muon Isolation scale factors (Data/MC) for loose Iso.

	$0 < \|\eta\| \leq 0.9$	$0.9 < \|\eta\| \leq 1.2$	$1.2 < \|\eta\| \leq 2.1$	$2.1 < \|\eta\| \leq 2.4$
$20 < p_{\mathrm{T}} \leq 25$	1.004 ± 0.003	1.003 ± 0.004	1.000 ± 0.002	1.006 ± 0.003
$25 < p_{\mathrm{T}} \leq 30$	0.998 ± 0.001	1.000 ± 0.003	1.002 ± 0.001	0.999 ± 0.002
$30 < p_{\mathrm{T}} \leq 40$	1.001 ± 0.001	1.001 ± 0.001	1.002 ± 0.001	1.000 ± 0.001
$40 < p_{\mathrm{T}} \leq 50$	1.000 ± 0.000	0.999 ± 0.000	1.000 ± 0.003	1.000 ± 0.000
$50 < p_{\mathrm{T}} \leq 60$	1.000 ± 0.000	1.000 ± 0.001	1.000 ± 0.000	1.000 ± 0.001
$60 < p_{\mathrm{T}} \leq 120$	1.000 ± 0.000	1.000 ± 0.001	1.000 ± 0.001	1.001 ± 0.001
$120 < p_{\mathrm{T}} \leq 300$	1.000 ± 0.000	1.000 ± 0.000	1.000 ± 0.000	1.000 ± 0.000

TABLE 5.8: Electron Identification scale factors (Data/MC) for Medium ID and Isolation.

GeV	$0 < \|\eta\| \leq 0.8$	$0.8 < \|\eta\| \leq 1.442$	$1.566 < \|\eta\| \leq 2.0$	$2.0 < \|\eta\| \leq 2.5$
$10 < p_{\mathrm{T}} \leq 20$	1.007	1.090	0.984	1.036
$20 < p_{\mathrm{T}} \leq 30$	0.971	0.983	0.937	0.986
$30 < p_{\mathrm{T}} \leq 40$	0.985	0.987	0.975	0.963
$40 < p_{\mathrm{T}} \leq 50$	0.986	0.987	0.993	1.006
$50 < p_{\mathrm{T}} \leq 2000$	0.989	0.986	1.006	1.009

5.4 Pileup Reweighting and Stability Check

5.4.1 Pileup reweighting

The distribution of the number of pileup interactions (here estimated by the number of vertices) has been generated for the MC samples. The pileup distributions from the MC samples are very close to the one observed in data, but still need to be improved. Hence pileup reweighting is introduced to achieve it. Figure 5.4 shows the data to MC comparison for the number of reconstructed vertices obtained using a minimum bias p-p cross-section of 69 mb, as well as the effect of varying this cross-section by 5%.

The variable of the multivariate discriminator puMVA is used to reduce the contribution of jets coming from pileup. To justify this selection criteria and to illustrate the quality of the pileup treatment, the number of reconstructed jets per data event containing a reconstructed Z boson candidate as a function of number of vertices with various puMVA cuts (puMVA > -0.1, puMVA > -0.2, puMVA > -0.3) is shown in figure 5.5. The cut puMVA > -0.2 is applied on both data and MC. The three cuts show similar effects. So we choose the cut (puMVA > -0.2) which has been used in the previous analysis. A good description of data by the MC is also observed. The measured number of vertices distribution is well contained within the quoted systematics.

5.5 Backgrounds

The dominant background in the analysis is the production of $t\bar{t}$ pairs. Its contribution is estimated from sample of data dominated by the $t\bar{t}$ events and obtained by replacing

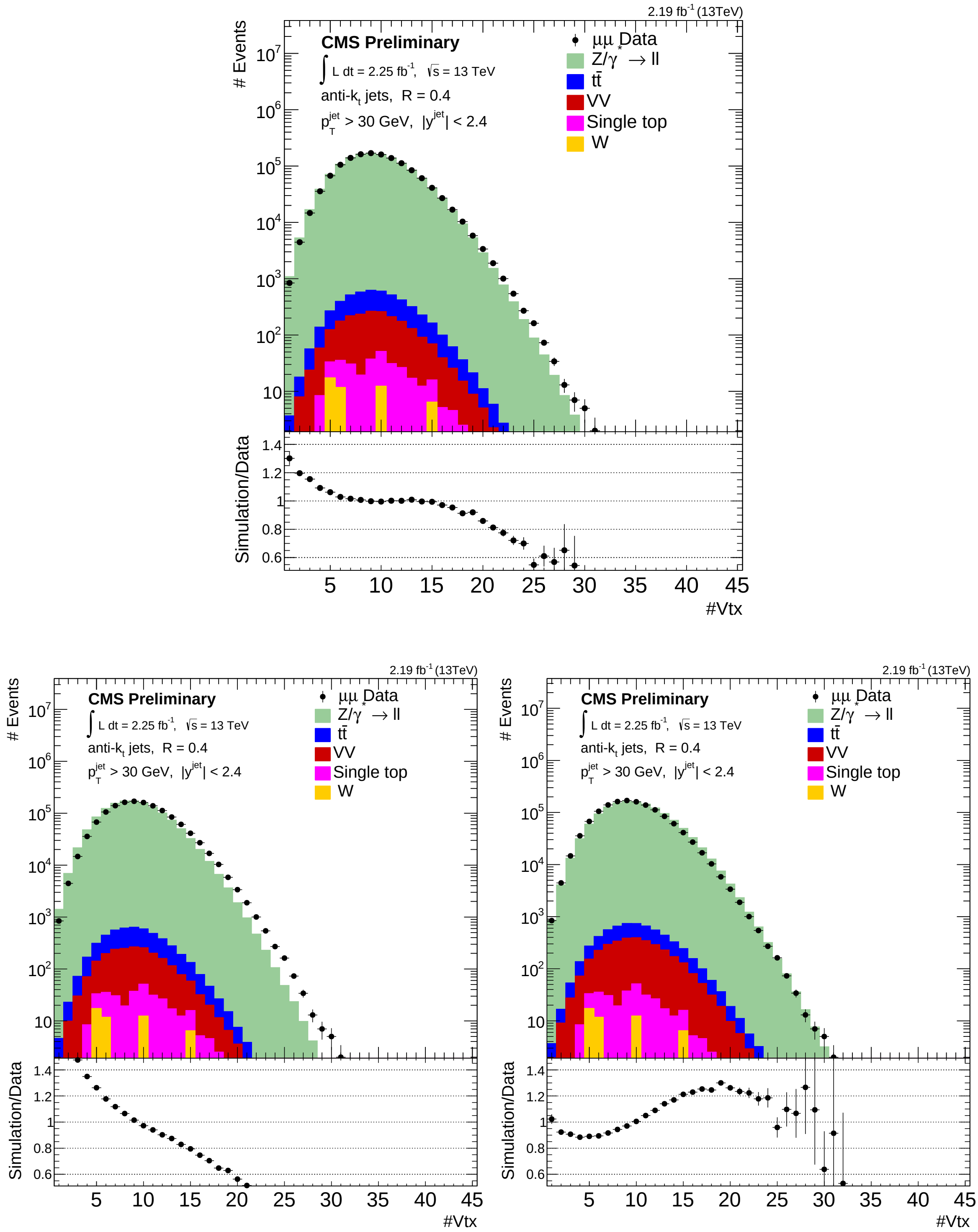

FIGURE 5.4: Data/MC comparison of the number of vertices using the minimum bias cross-section of 69 mb (top), 95% minimum bias cross-section (bottom left), 105% minimum bias cross-section (bottom right) for reweighting.

the $\mu\mu$ or $e\,e$ selection with $e\mu$ selection. The double muon (electron) trigger is replaced by single muon trigger HLT_IsoTkMu20. All the other criteria are the same.

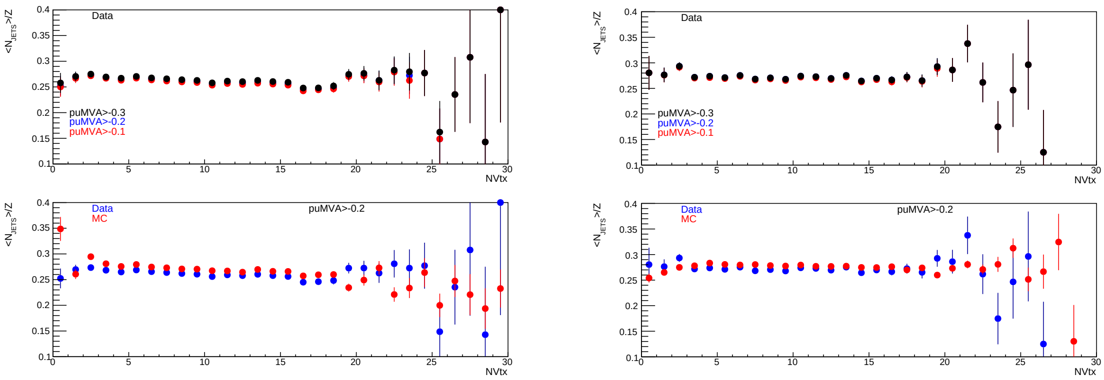

FIGURE 5.5: Validation of pileup jet rejection. The average number of jets per event containing a Z boson is shown as a function of the number of vertices for both muon (left) and electron (right) decay channel, with various puMVA thresholds (-0.1, -0.2, -0.3). Data/MC comparison with puMVA>-0.2 is shown in the bottom plots.

The data to MC comparison of all kinematic dependences of interest in the main analysis is shown in the figure 5.6 to 5.9.

There is not p_T or η dependence in the comparison of $e\mu$ channel, except the jet multiplicity, in particular for 4 jets and more. Hence, the $t\bar{t}$ MC simulation has been reweighted by the ratio of data over MC depending only on the exclusive jet multiplicity for one jet or more. No reweight is applied for the value of the exclusive jet multiplicity of zero, because the DY process is dominant and little statistics fluctuation from DY will cause a huge effect on the factor, which is obvious on the right figure in 5.6. The stastistical uncertainty on the factor is considered as one source of the systematic uncertainty in the analysis. The reweight factors applied to the $t\bar{t}$ MC sample are given in table 5.9.

The Z decay in $\tau^+\tau^-$ is considered as background and will be subtracted during the unfolding procedure, as described in section 5.7.2. The upper limit on QCD background has been estimated from data by selecting a same sign leptons sample. The comparison between the same sign and oppositely sign data is shown in figure 5.10. For both muon and electron channel, the contamination is below 2% for the multiplicity up to 3 jets. Since QCD background is negligible, it has not been included in the analysis.

The other background contributions are estimated from the MC event generators, which are normalised to their highest order calculated SM cross section, as describe in subsection 5.2.2. The yields of those estimated background are subtracted from data before unfolding. In general, the background contamination is below the percent level, but increases with the number of jets, reaching 15% for jet multiplicity for 4 and above due to the dominant background $t\bar{t}$ production, as shown in figures 5.11 and 5.12.

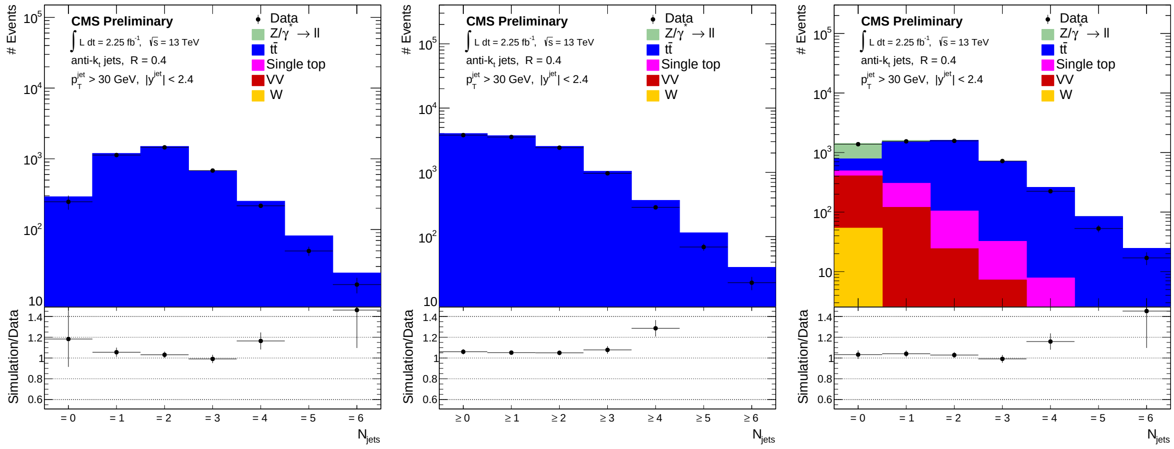

FIGURE 5.6: The subtracted data (data-X, X refers to simulations except $t\bar{t}$) and the $t\bar{t}$ simulation distributions of the exclusive (left) jet multiplicity and inclusive (middle) jet multiplicity, and the data and the simulations of the exclusive (right) jet multiplicity in the $e\mu$ channel. The error bars on the data points correspond to the statistical errors.

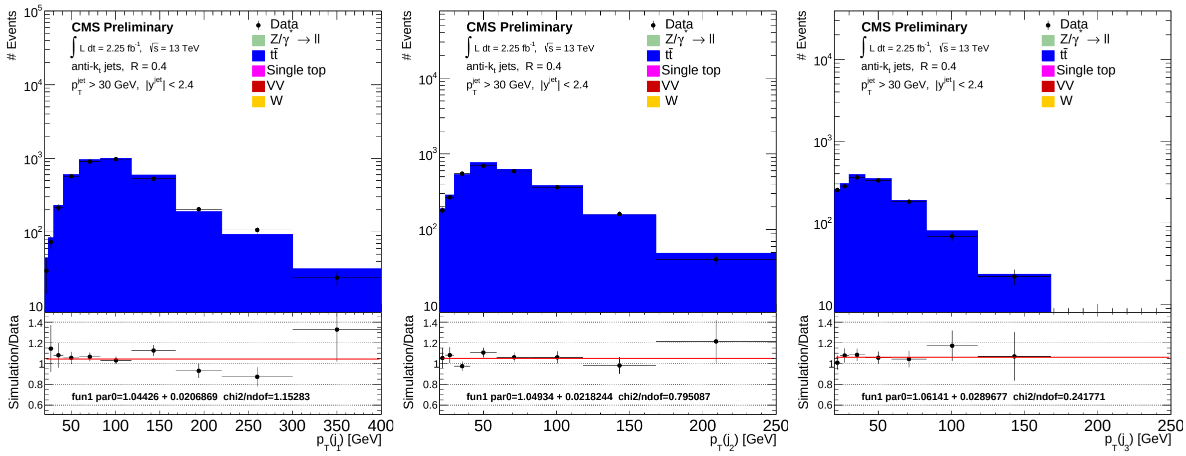

FIGURE 5.7: The subtracted data (data-X, X refers to simulations except $t\bar{t}$) and the $t\bar{t}$ simulation distributions of the transverse momenta of the three highest p_{T} jets in the $e\mu$ channel. The error bars on the data points correspond to the statistical errors.

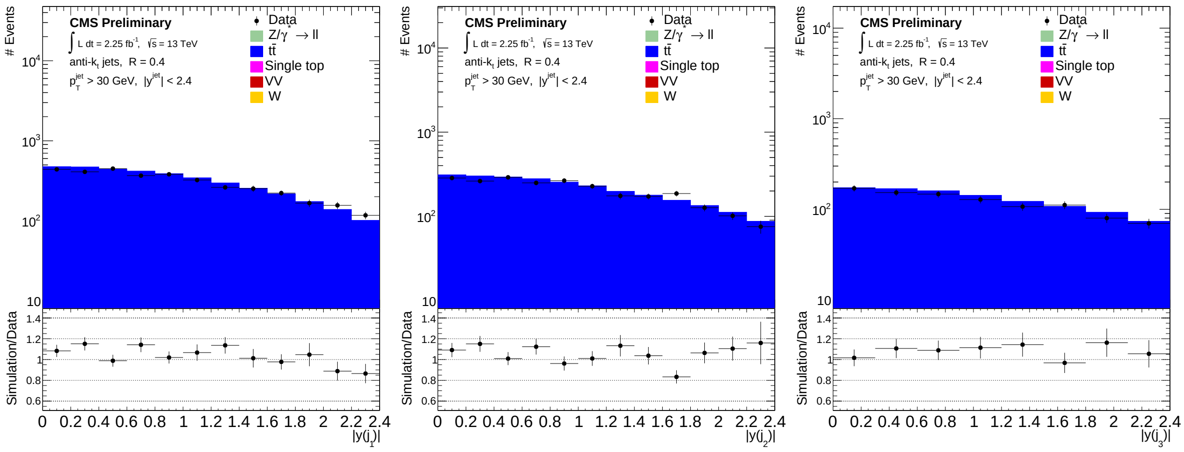

FIGURE 5.8: The subtracted data (data-X, X refers to simulations except $t\bar{t}$) and the $t\bar{t}$ simulation distributions of the rapidity of the three highest p_T jets in the $e\mu$ channel. The error bars on the data points correspond to the statistical errors.

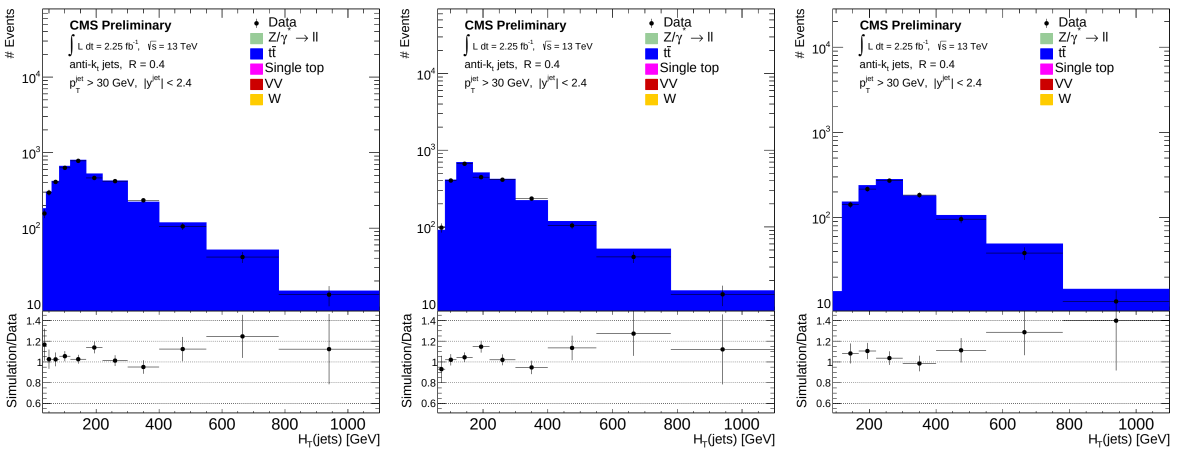

FIGURE 5.9: The subtracted data (data-X, X refers to simulations except $t\bar{t}$) and the $t\bar{t}$ simulation distributions of H_T of the jets for inclusive jet multiplicities of one, two and three in the $e\mu$ channel. The error bars on the data points correspond to the statistical errors.

TABLE 5.9: Scale factor (C) applied to the $t\bar{t}$ MC sample.

N_j	C	uncertainty
1	0.94	$\pm$ 0.04
2	0.97	$\pm$ 0.03
3	1.01	$\pm$ 0.04
4	0.86	$\pm$ 0.06
5	0.61	$\pm$ 0.09
6	0.68	$\pm$ 0.17
7	0.28	$\pm$ 0.19

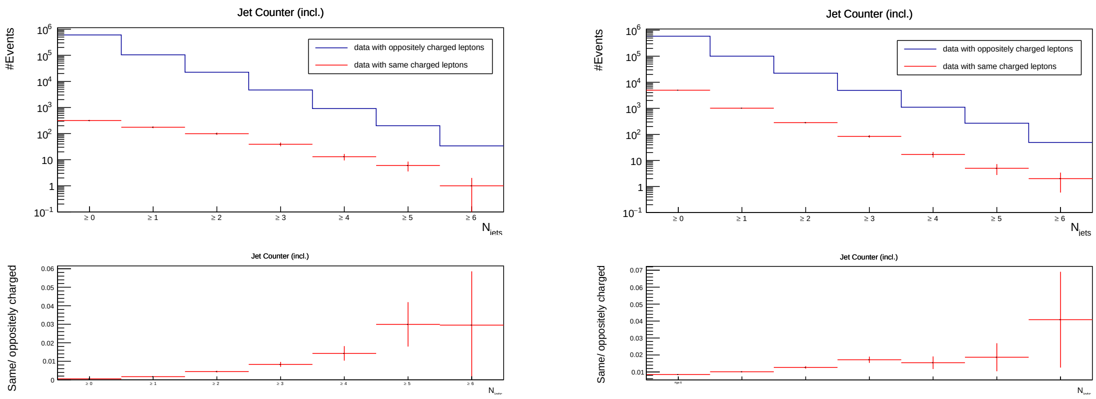

FIGURE 5.10: Comparison of same sign over oppositely sign leptons data as a function of inclusive jet multiplicity for the $\mu\mu$ sample (left) and for the ee sample (right).

5.6 Results at Detector Level

When the event selections, the pileup reweighting, scale factors of lepton and $t\bar{t}$ production have been applied, we get the distribution of observables as mentioned in section 5.1.1 at the detector level for both data and simulations. A good description of the data by the simulation in both decay channels is achieved and shown in this section. In each plot, a ratio of simulation over data is presented in the lower part, and the error bars on the data points only correspond to the statistical errors from both data and simulation.

Data to simulation comparisons of jet multiplicities are presented in figure 5.11 and 5.12 for inclusive multiplicity and exclusive multiplicity. A good agreement is found for jet multiplicities up to 3 jets MG5_AMC FxFx sample corresponding to 2 partons generated in the final state at NLO, and 3 partons at LO. Above a multiplicity of 4, the jets are simulated only by Parton Shower (PS) of PYTHIA8. These distributions illustrate well the low level of background contamination, below the percent level for the inclusive cross section, and increasing with the number of jets mainly due to the contribution from $t\bar{t}$ production, close to 10% for a jet multiplicity of 3 and above.

The leptons p_T, η, ϕ, $\Delta\phi$ and the separation between leptons ΔR distributions are shown in figures 5.13 and 5.14 for the muon channel. For practical reasons, Figs 5.13

and 5.14 do not correspond to the final version of the data analysis. Differences between the two version are very marginal except the integrated value of the lumonisity that has been reestimated from 2.22 to 2.19 fb^{-1} A good agreement between the data and MC is observed in the full phase space.

The distributions relative to the reconstructed Z boson candidate are shown in figures 5.15 and 5.16. A good description of the invariant mass, the rapidity and the transverse momentum ($p_T(Z)$) is observed. The Rochester corrections [1] have been applied to the $\mu\mu$ samples to compensate for misalignment of the tracker in CMS detector.

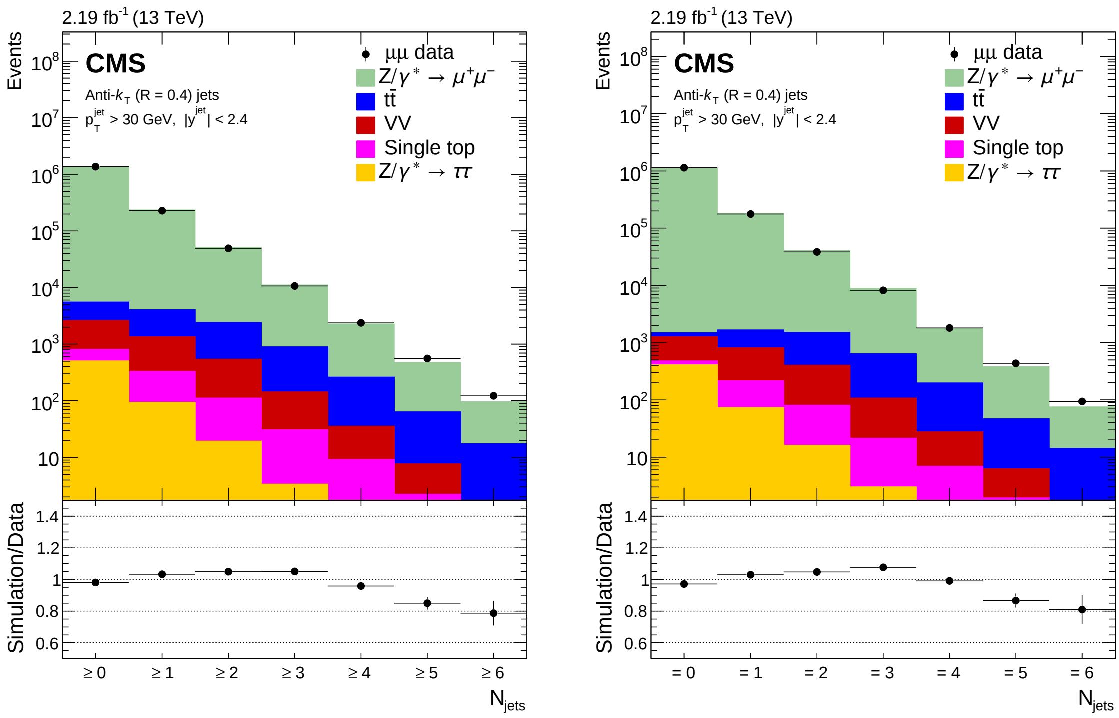

FIGURE 5.11: Data to simulation comparison of inclusive jet multiplicity (left) and exclusive jet multiplicity (right) obtained for the $\mu\mu$ sample.

As mentioned, the matrix elements of MG5_AMC FxFx sample include up to 2 partons NLO computation, and LO approximation for 3 partons. Good agreements have been observed for the inclusive multiplicity and exclusive multiplicity for up to 3 jets. Moreover, due to the limited statistics the variables related to jet are shown only up the third jet. The data to simulation comparison of the jet transverse momenta for the 3 first jets are presented in figure 5.17, separately. Figure 5.18 present the H_T distributions of the jets for inclusive jet multiplicities from 1 to 3. The rapidity distributions of the first three jets are shown in figure 5.19. All data distributions are well reproduced by the MC simulation. Unfolding and a complete study of the systematics is nevertheless needed before trying to conclude on a possible marginal disagreement.

One highlight of this analysis is the global transverse momentum balance, which has been studied by reconstructing two different variable p_T balance between the Z boson

[1] Rochester momentum correction [87], which is derived as a function of muon charge and angular observables, by means of Z boson peak which has been already well understood. Regarding this analysis, this effect has influenced the statistics by within 1%

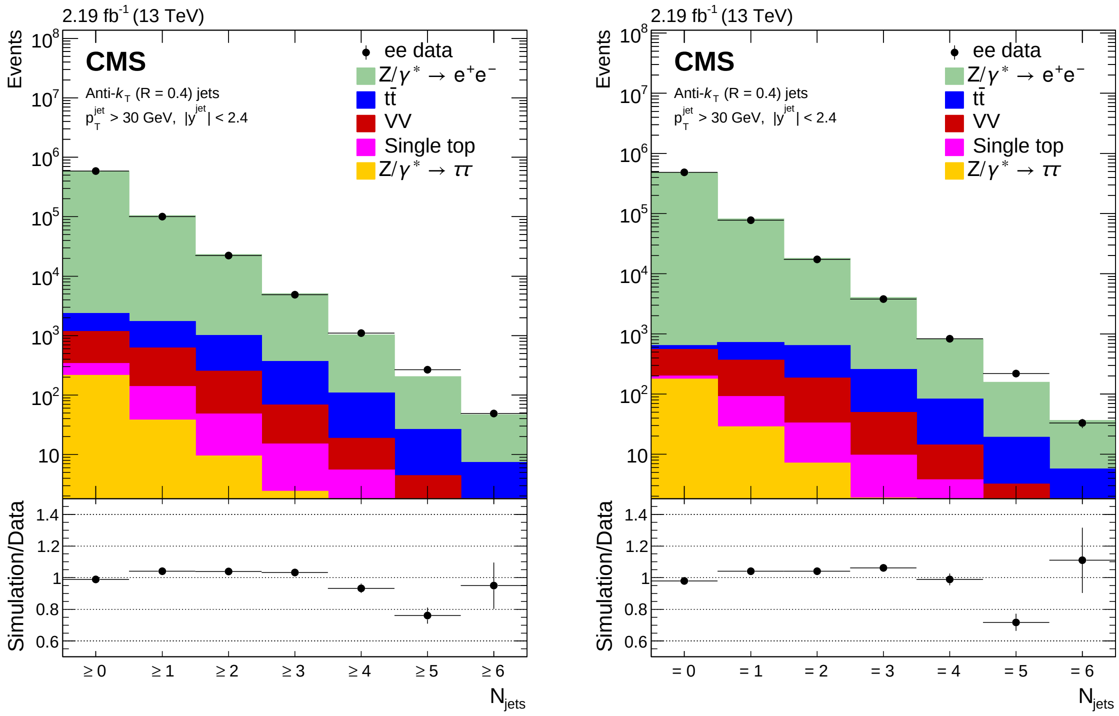

FIGURE 5.12: Data to simulation comparison of inclusive jet multiplicity (left) and exclusive jet multiplicity (right) obtained for the ee sample.

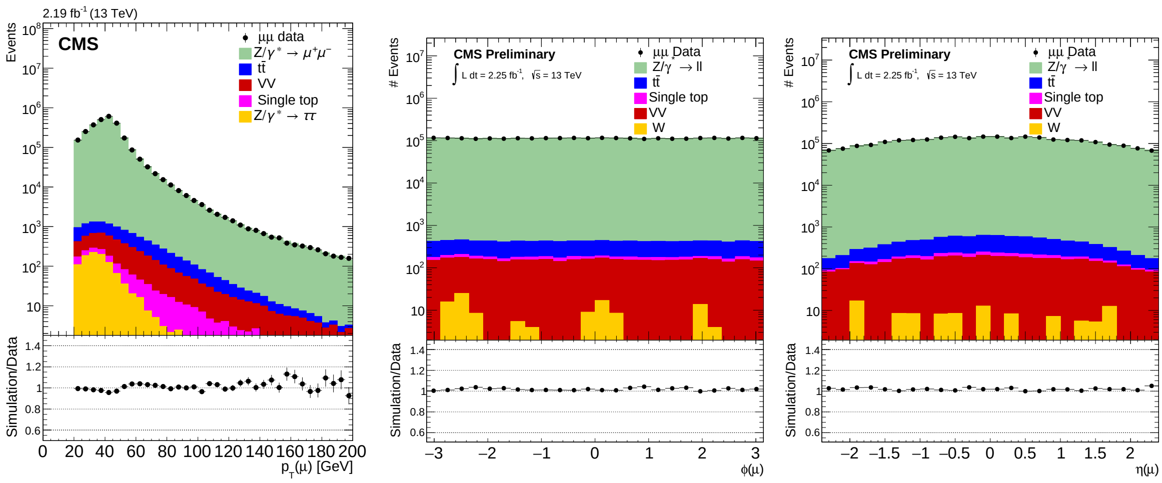

FIGURE 5.13: Data to simulation comparison of muon transverse momenta, $p_T(\mu)$, azimuthal angle, $\phi(\mu)$ and pseudo-rapidity, $\eta(\mu)$. Note that each event of the $\mu\mu$ sample has two entries in the histograms.

and the sum of the reconstructed jets ($p_T^{bal} = |\vec{p}_T(Z) + \sum_{\text{jets}} \vec{p}_T(j_i)|$), and using the Jet-Z Balance (JZB=$|\sum_{\text{jets}} \vec{p}_T(j_i)| - |\vec{p}_T(Z)|$). Though correlated, the p_T^{bal} allows us to focus on the peak of the distribution with a larger statistics, while the JZB keeps a sign information.

Figure 5.20 shows the p_T^{bal} distribution for inclusive one, two and three jet multiplicities. The $t\bar{t}$ background does not peak at the same place as the signal and has a broader

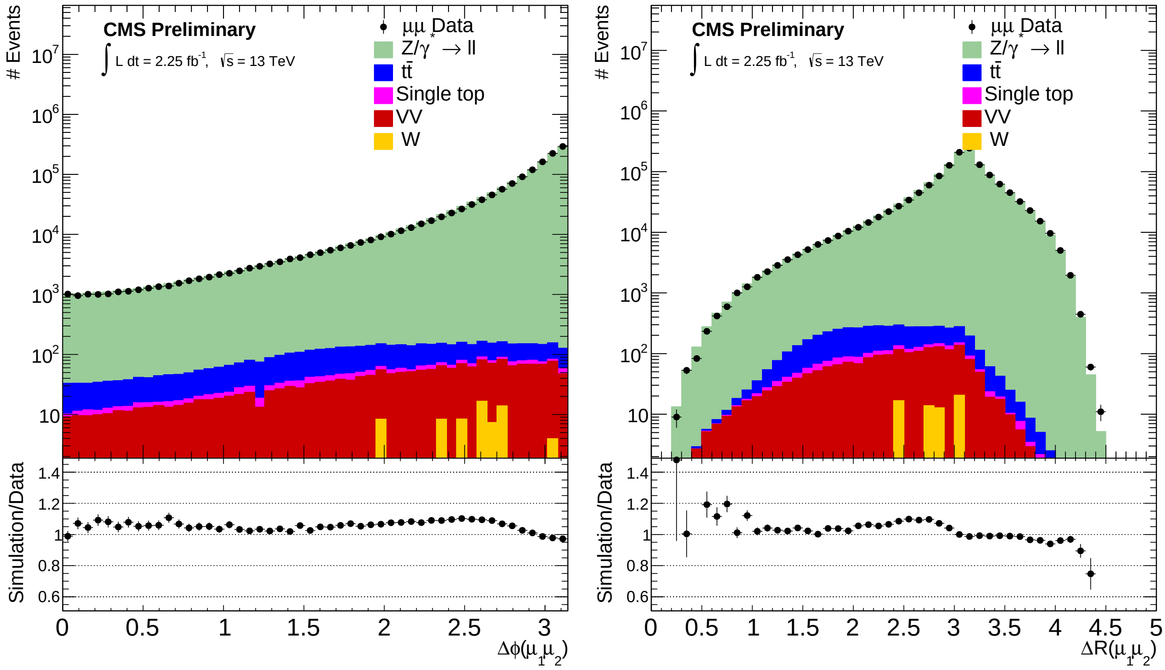

FIGURE 5.14: Data to simulation comparison of the two muon correlations in azimuthal angle, $\Delta\Phi(\mu_1\mu_2)$ and separation, $\Delta R(\mu_1\mu_2)$.

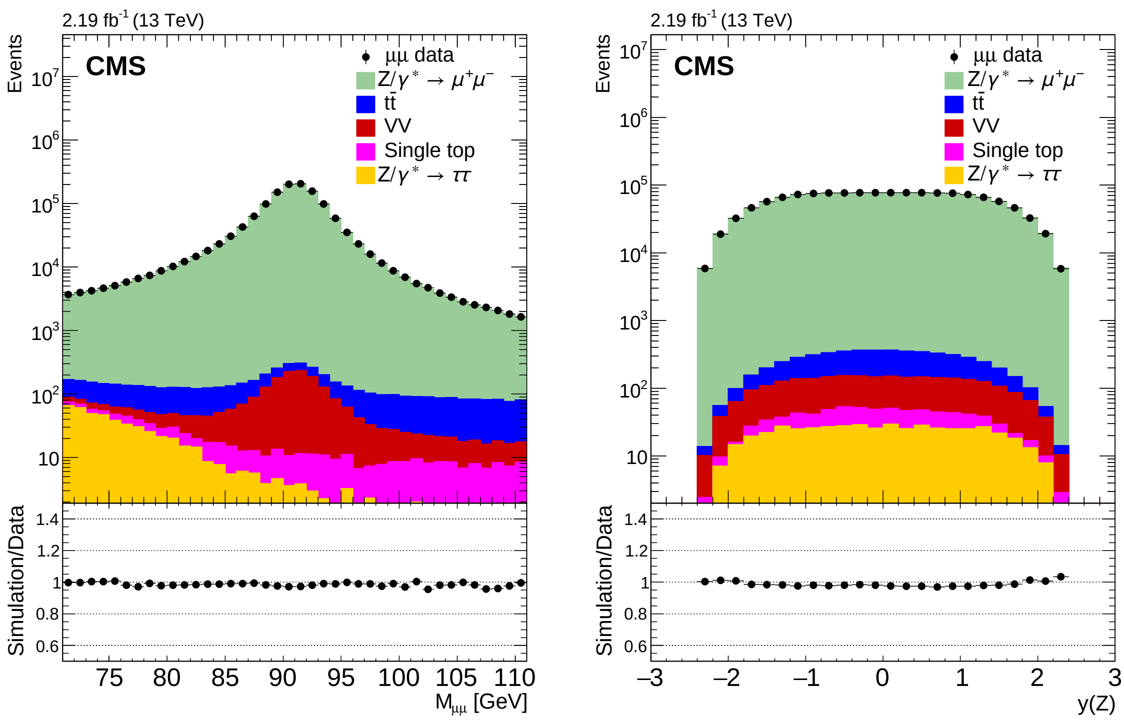

FIGURE 5.15: Data to simulation comparison of the Z candidate invariant mass and rapidity for the $\mu\mu$ sample.

spectrum, because the transverse momentum is carried away by neutrinos which enhances the imbalance on p_{T}^{bal} . Figure 5.21 presents the JZB distribution for the inclusive

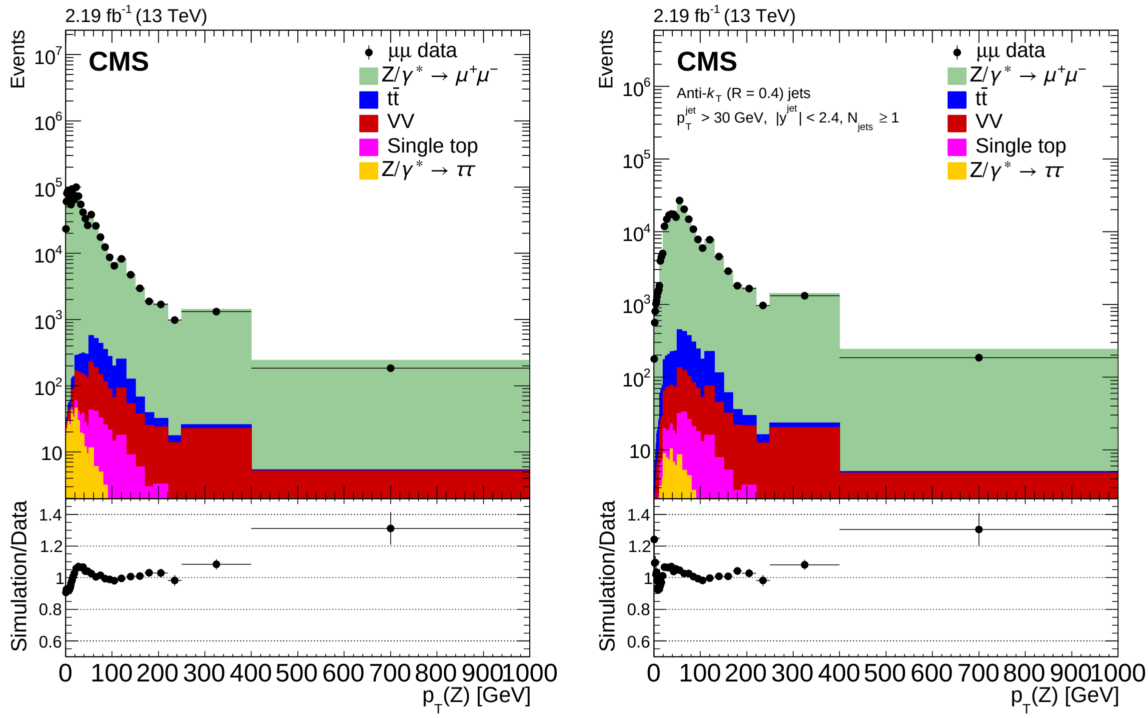

FIGURE 5.16: Data to simulation comparison of the Z candidate transverse momentum for the $\mu\mu$ sample for inclusively zero jet (left) and one jet (right).

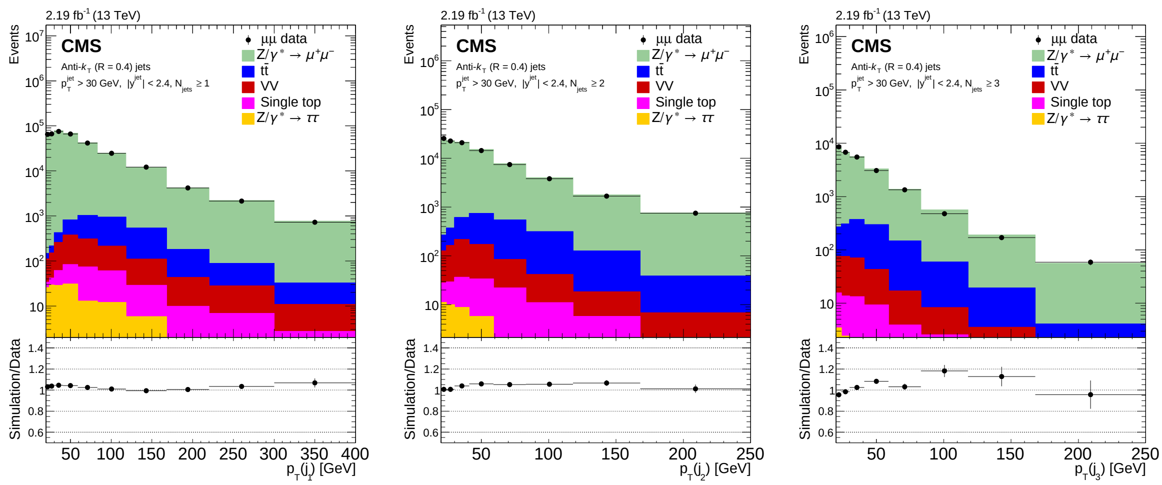

FIGURE 5.17: Data to simulation comparison of jet transverse momenta for the 3 first jets obtained for the $\mu\mu$ sample.

one jet in the full phase space, and for the condition of $p_T(Z)$ below and above 50 GeV. The JZB variable has two signs of value: the value will be positive when some hadronic activities are not included is in the direction of Z boson, and the value will be negative when the hadronic activity is not included in the opposite direction of Z boson. The $t\bar{t}$ background is asymmetric, making a larger contribution to the positive side of the distribution because the transverse energy is carried away by neutrinos from W

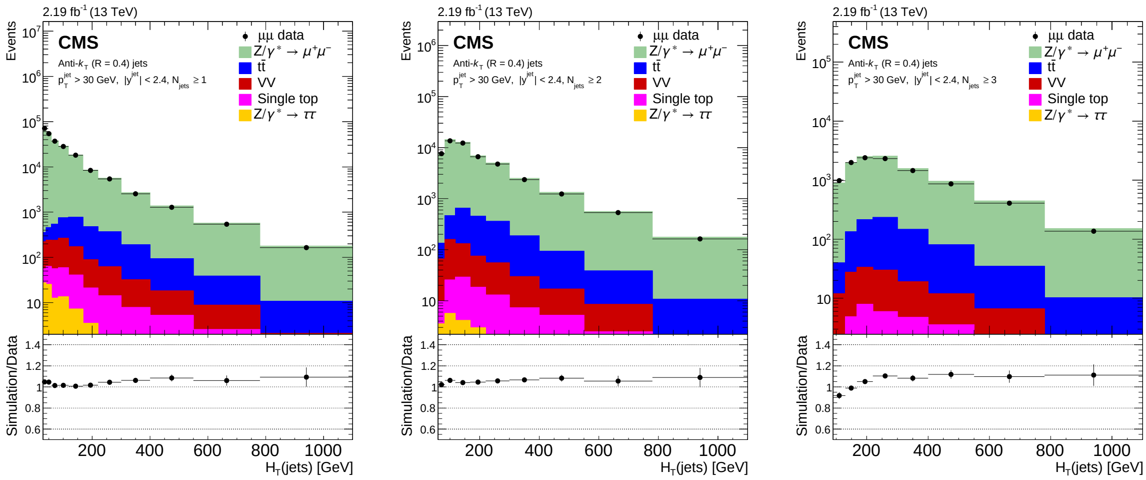

FIGURE 5.18: Data to simulation comparison of H_T of the jets for inclusive jet multiplicities of 1 (left), 2 (middle) and 3 (right) obtained for the $\mu\mu$ sample.

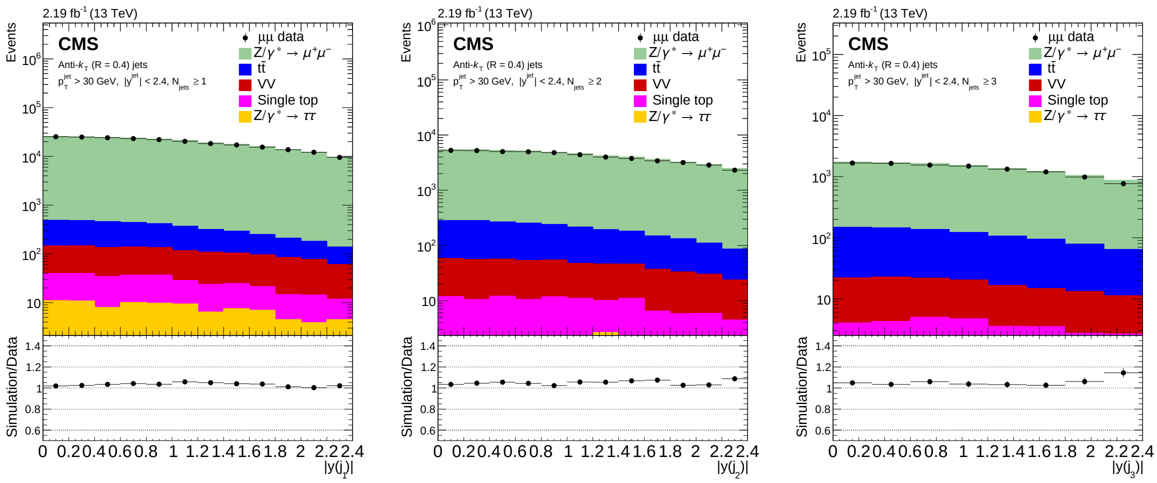

FIGURE 5.19: Data to simulation comparison of jet rapidity distributions for the 3 first jets obtained for the $\mu\mu$ sample.

decays leading to a reduction in the negative term of the JZB expression. Overall the agreement between data and simulation before background subtraction is good and differences are about 10%.

Equivalent analysis of electron decay channel has been performed by colleague of Z+jet group. Good agreement is found. To illustrate it in the Appendix B. The muon and the electron channel will be combined in the measurement.

5.7 Detector Effect Corrections

In any experiments, the distribution of the measured observables differ from the corresponding "true" physics quantities, due to the limited detector performances, or

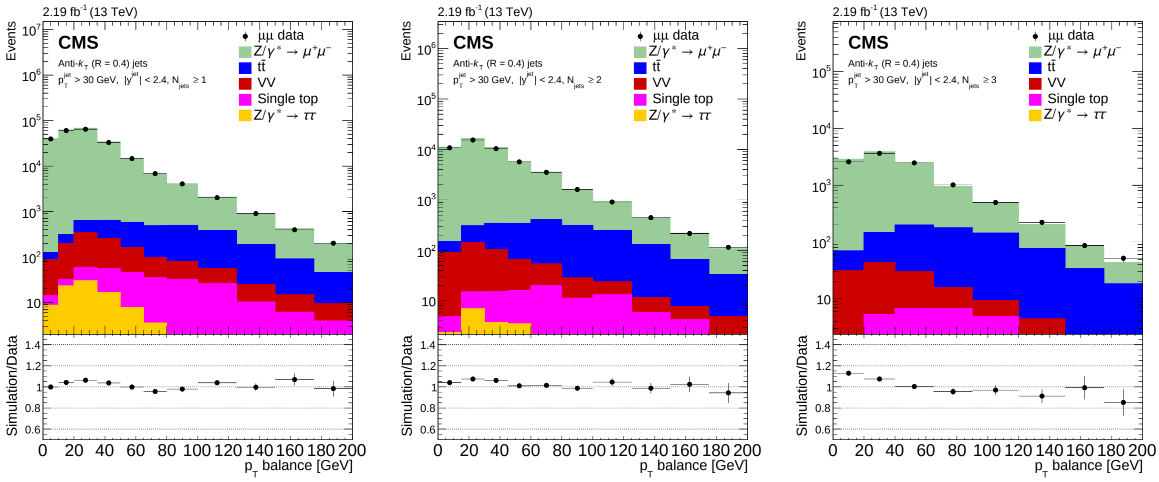

FIGURE 5.20: Distribution of events as a function of the transverse momentum balance between the Z boson and the sum of the jets for inclusively one jet (left) two jets (middle) and three jets (right) for the $\mu\mu$ sample.

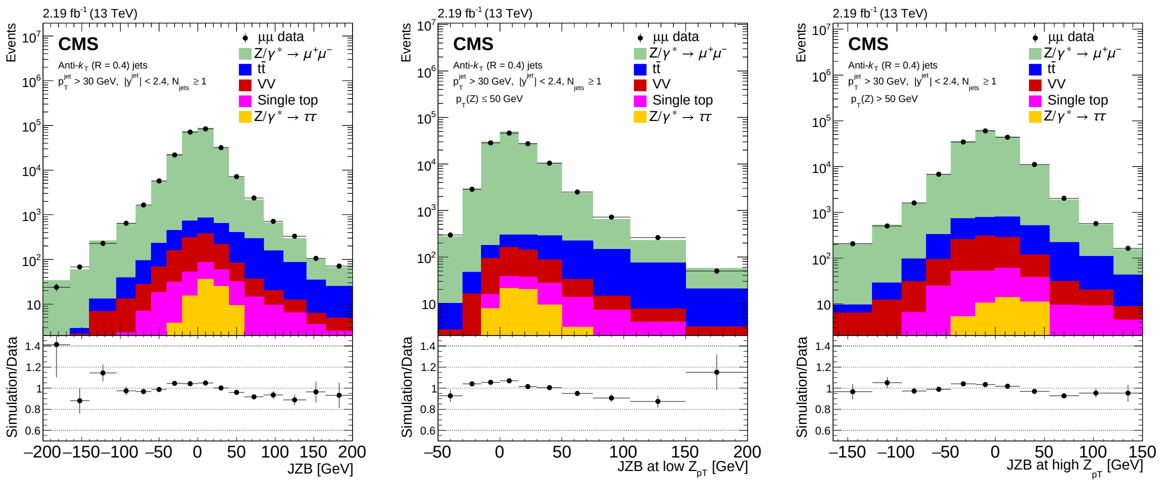

FIGURE 5.21: Distribution of events as a function of JZB variable (see text), for the full phase space (left) and limited to $p_{\mathrm{T}}(Z) < 50\mathrm{GeV}$ (middle) and $p_{\mathrm{T}}(Z) > 50\mathrm{GeV}$ (right) for the $\mu\mu$ sample.

physics effects such as QED and QCD radiative corrections. For instance, the observed jet transverse momentum p_{T}^{reco} could smear from the true transverse momentum p_{T}^{true} due to the finite detector efficiency. It is the same case for the other interesting measured observables, such as jet multiplicities, jet pseudorapidities, lepton transverse momentum and the transverse momentum balance between jets and Z boson.

The fiducial cross sections are obtained by subtracting the simulated backgrounds from the data distributions, correcting the background subtracted data distributions back to the particle level using a procedure named unfolding, which takes into account the detector effects such as detection efficiency and resolution. Due to the detector response and to suppress the background contaminations, the data measurement is obtained by applying some kinematic selection cuts. A proper phase space at generator level is also needed before starting the unfolding procedure.

5.7.1 Phase Space at Generator Level

The particle level values refer to the stable leptons from the decay of Z boson and to the jets built from the stable particles, including hadrons, leptons, and neutrinos, using the same algorithm as for the detector level jets. The momenta of all the photons whose ΔR distance to the leptons axis is smaller than 0.1 are added to the lepton momentum to account for the effects of QED final state radiation, and leptons are "dressed". The Z boson is reconstructed from the momenta of the two highest p_{T} muons (or electrons). The phase space for the cross section measurement is restricted to events with p_{T} > 20 GeV and $|\eta|$ <2.4 for leptons, and with a Z boson mass between 71 GeV and 111 GeV. Jets are required to have p_{T}>30 GeV, $|y|$ <2.4 and a spatial separation from the dressed lepton of ΔR>0.4. This defines the phase space of the following cross section measurements.

5.7.2 Unfolding Method

To extract the cross section and to correct for the detector effects an unfolding procedure is applied to distributions obtained after background subtraction. The unfolding procedure is MC dependent since one has to create a mapping between the true value (generated) of the observable and the reconstructed (measured) value distorted due to detector effects. This mapping is contained in the response matrix where each element (i, j) is related to the probability that the observable, generated in the i^{th} bin, would be measured in the j^{th} bin. It could happen that the observable in the i^{th} cannot match with that in any bin of reconstructed level, which is defined as missing events. On the contrary, the observable in the j^{th} of reconstructed level can not match with any bin of generated level, it is named as fake events. One can correct the observable distribution in data using the inverted response matrix, after the subtraction of fake events and before adding the missing events. This leads to the data distribution at particle level.

Since the response matrix needs to be inverted to use. Direct inversion of the matrix as well as procedure trying to overcome the instability related to the inversion of the response matrix, based on its Singular Value Decomposition (SVD) and described in [88], can be used via the RooUnfold framework. Another way is based on Bayes' theorem and described in [89], which does not require the inversion of the response matrix and thus avoids any trouble encountered with the matrix inversion. The main advantages of the unfolding using the iterative Bayesian method is:

- it is theoretically well grounded;
- it does not require matrix inversion;
- it can be applied to multidimensional problems;
- it can use cells of different sizes for the distribution of the true and the experimental values;

- it can take into account any kind of smearing and migration from the true values to the observed ones;
- it can be implemented in a short, simple and fast program, which deals directly with distributions and not with individual events.

In this analysis, the unfolding is performed using the iterative Bayesian method (D'Agostini iterative method) implemented in the RooUnfold toolkit. In this method, the best estimate of the true number of events $\hat{n}_i$ inside one particular bin i is:

$$\hat{n}_i = \frac{1}{\epsilon_i} \sum_{j=1}^{n_{bins}} n_j^{obs} P(i_{gen}|j_{reco}) \tag{5.6}$$

where $0 \leq \epsilon_i \equiv \sum_{j=1}^{n_{bins}} P(j_{reco}|i_{gen})$ gives the efficiency of observing an event generated in bin i; n_j^{obs} is the observed events in bin j; the matrix $P(i_{gen}|j_{reco})$ is the smearing matrix, describing the cell-to-cell migrations. The smearing matrix is defined as:

$$P(i_{gen}|j_{reco}) = \frac{P(j_{reco}|i_{gen})P_0(i_{gen})}{\sum_{k=1}^{n_{bins}} P(j_{reco}|i_{gen})P_0(k_{gen})} \tag{5.7}$$

in which $P_0(i_{gen})$ indicates the initial probability for the event to be generated in bin i, with $\sum_{k=1}^{n_{bins}} P_0(k_{gen})$=1. From the unfolded events we can estimate the true total number of events, the final probabilities of the event to be generated in bin i and the overall efficiency:

$$\begin{aligned} \hat{N}_{true} &= \sum_{i=1}^{n_{bins}} \hat{n}_i, \\ \hat{P}(i_{true}) &= \frac{\hat{n}_i}{\hat{N}_{true}}, \\ \hat{\epsilon} &= \frac{N_{obs}}{\hat{N}_{true}}. \end{aligned} \tag{5.8}$$

If the initial distribution $P_0(i_{gen})$ is not consistent with the data, it will not agree with the final distribution $\hat{P}(i_{true})$. The closer the initial distribution is to the true distribution, the better the agreement is. In order to achieve better agreements, the $P_0(i_{gen})$ of all the matrix is requested to be larger than 60%. Since the $\hat{P}(i_{true})$ obtained from the simulated data lies between $P_0(i_{gen})$ and the true one, it is better to proceed iteratively:

1. choose the initial distribution $P_0(i_{gen})$ from the best knowledge of the process under study.
2. calculated $\hat{N}_{true}$ and $\hat{P}(i_{true})$.
3. make a χ^2 comparison between $\hat{n}_i$ and $n_{0,i}$ (the initial expected number of events $n_{0,i} = P_0(i_{gen})N_{obs}$).
4. replace $P_0(i_{gen})$ by $\hat{P}(i_{true})$, and $n_{0,i}$ by $\hat{n}_i$, then start again. If after the second iteration the value of χ^2 is small enough, stop the iteration; otherwise go to step 2.

The D'Agostini iterative method converges towards the maximum likelihood solution, which is affected by large fluctuations. The amplitude of the fluctuations increases with the number of iterations. In the analysis the number of iterations is chosen to minimize artificial fluctuations. Random replicas of the unfolded histogram are generated, folded using the response matrix and unfolded back. The number of iterations chosen to maximize the compatibility of the resulting histograms with the original one used to generate the replicas. The compatibility is quantified using a χ^2 test, which is degraded when fluctuations are introduced. In addition, it is checked that by folding back the unfolded histogram using the response matrix we obtain an histogram compatible with the original histogram before the unfolding.

Figure 5.22 5.23 presents some examples of the response matrices used for the unfolding. They have been obtained with the signal simulation sample. Figure 5.22 is the response matrix for the variable of the jet exclusive multiplicity, illustrating that the percentage of reconstructed ($Reco$) events in bin i from the generator level (Gen) events in j, e.g. in row 3, the events with 2 jets at Gen level 75% are reconstructed with 2 jets, 19% with 1 jet, 4% with 3 jets, and 1% with no jet. When choosing the step of bins for the response matrix, one needs to be optimized considering statistics and resolution by checking the number of events per bin. It is important to avoid the large uncertainty from unfolding. In case of jet pseudo-rapidity distribution 5.24, the distribution being relatively flat and the resolution being small with respect to the bin size, the response matrices are almost completely diagonal and the present method is therefore equivalent to a bin-to-bin correction. Figure 5.25 5.26 5.27 presents the response metrix used for the variable jets H_T, p_{T} balance and JZB.

5.8 Uncertainties

The uncertainties in the analysis are of two types: statistical uncertainties and systematic uncertainties. The statistical uncertainties from measured spectra and response matrices are propagated to the final results by mean of the unfolding procedure which provides the covariance matrices with finite number of events. Systematic uncertainties originate from several sources, while the dominant ones come from jet energy scale (JES). Other important contributions are the background estimation, the jet energy resolution, the measured efficiency of trigger, lepton reconstruction, and the lepton identification. Finally, the pileup and luminosity uncertainties are also considered.

The contributions mentioned are listed in the table 5.12 for the case of the jet exclusive multiplicity for the combination of both muon and electron channel:

- Jet energy scale (JES)
  By rescaling the reconstructed jet p_{T} distribution up and down in data, one can compute the difference between each of them and the nominal spectrum as the uncertainty. The rescaling factors is assigned as $p_{\mathrm{T}}-$ and $\eta-$dependent numbers,and they vary from 1% up to 5% within the kinematic selection constraint [90, 91]. It typically amounts to 5% for a jet multiplicity of one and increases with the number of reconstructed jets.

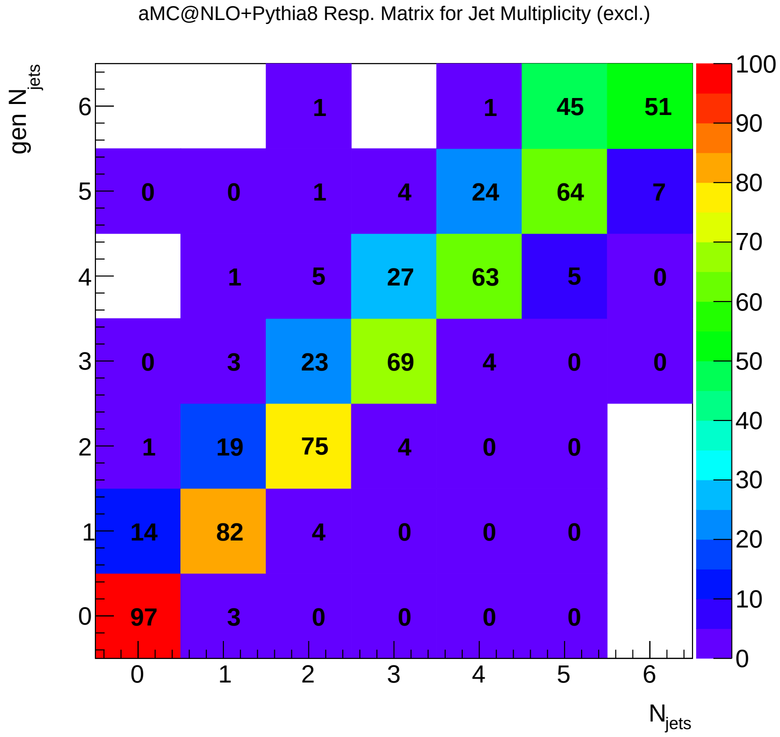

FIGURE 5.22: Response matrix used for the unfolding procedure for the variable of the jet exclusive multiplicity for the $\mu\mu$ channel. Numbers are expressed in percents.

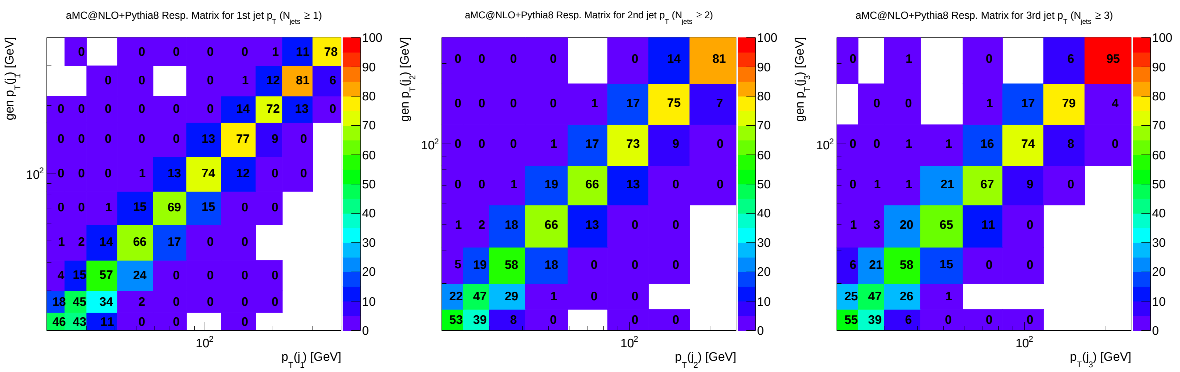

FIGURE 5.23: Response matrix used for the unfolding procedure for (left) first jet transverse momentum, (middle) second jet transverse momentum and (right)the third jet transverse momentum for $\mu\mu$ channel. Numbers are expressed in percents.

- Jet energy resolution (JER)
  The uncertainty in the jet resolution is responsible for the bin-to-bin migrations that is corrected by the unfolding. It is estimated and the resulting uncertainty is typically 1%.
- Efficiency Correction (Eff)
  The uncertainty from the measured efficiency (Eff) of trigger, lepton reconstruction, and lepton identification is set as global factor on reconstructed distribution

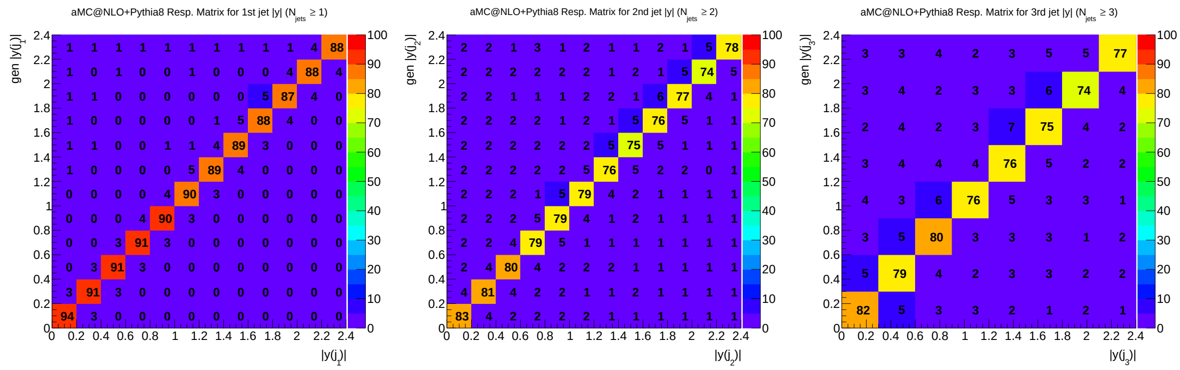

FIGURE 5.24: Response matrix used for the unfolding procedure for (left) the first jet rapidity, (middle) second jet rapidity and (right) third jet rapidity for $\mu\mu$ channel.

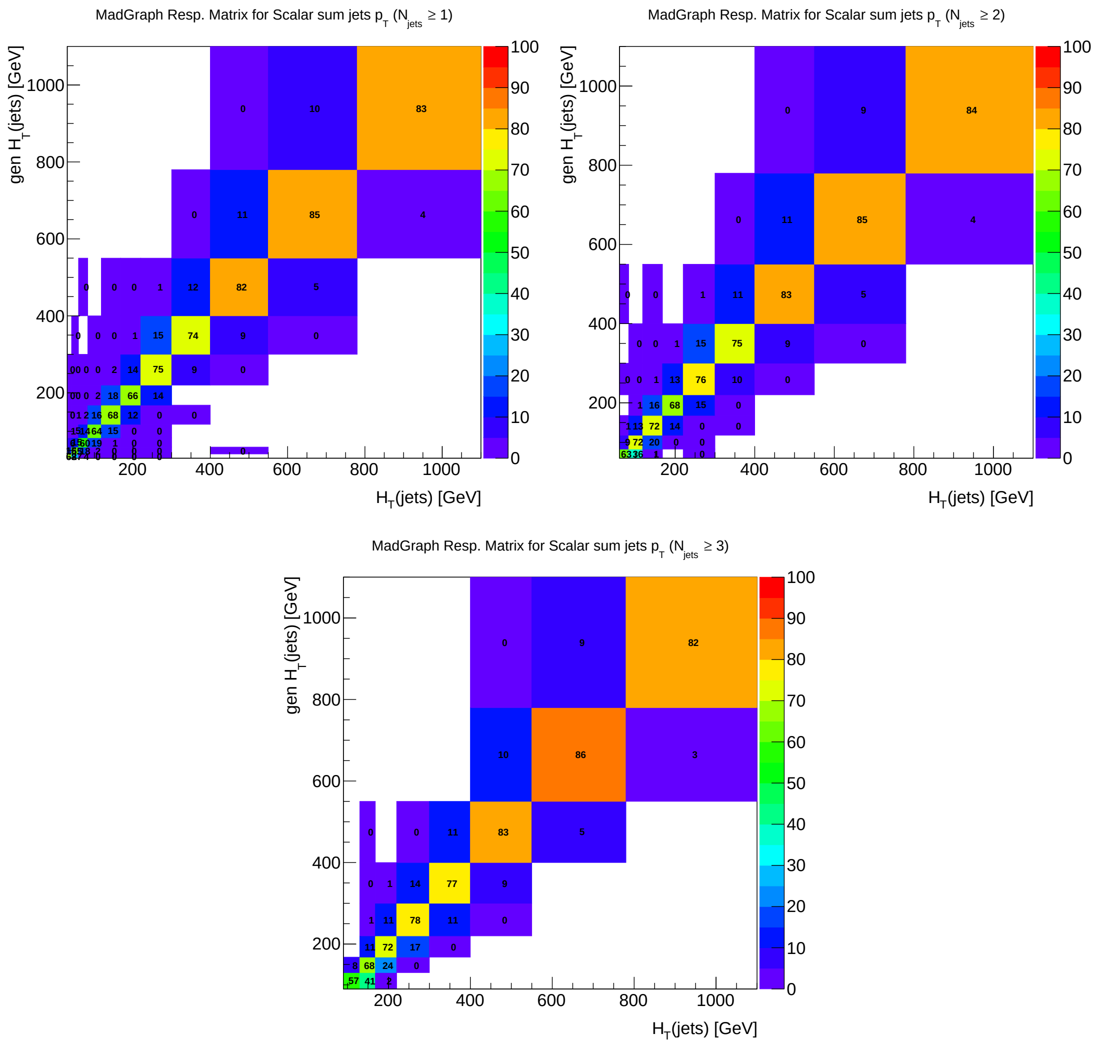

FIGURE 5.25: Response matrix used for the unfolding procedure for the jets H_T for inclusive jet multiplicities of 1 (left), 2 (middle) and 3 (right) in the $\mu\mu$ decay channel.

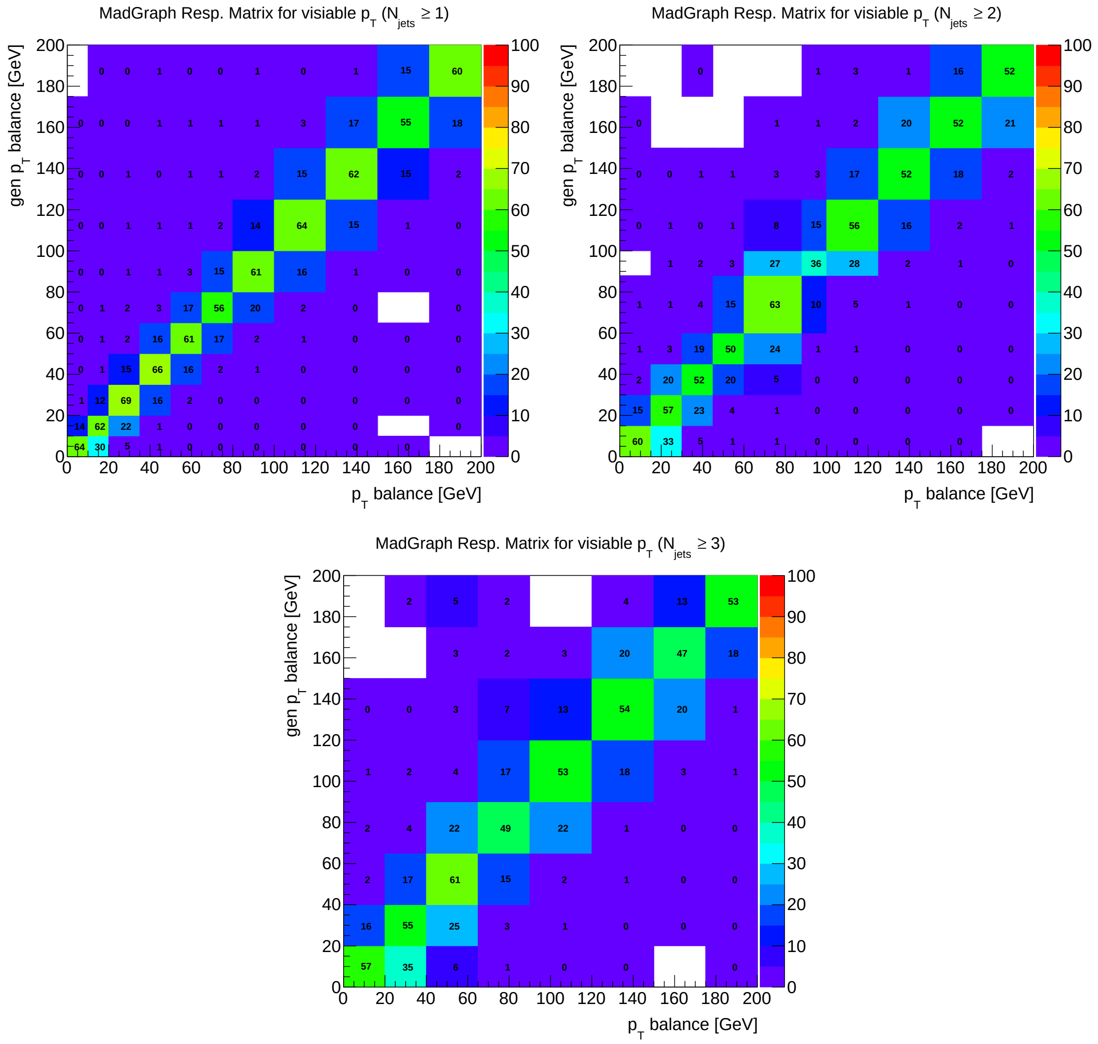

FIGURE 5.26: Response matrix used for the unfolding procedure for p_{T} balance for the jet multiplicity $N_{jets} \geq 1$ (left), $N_{jets} \geq 2$ (middle) and $N_{jets} \geq 3$ (right) for $\mu\mu$ channel.

in data for both channels. These uncertainties amount to a total uncertainty of 2% up to 4% for events with leptons of large transverse momenta.

- Luminosity (Lumi)
  The uncertainty in the measurement of the integrated luminosity is 2.3%.

- Background estimation (Bkg)
  The dominant background contributions comes from the reweighting procedure for the $t\bar{t}$ simulation. It is estimated to be less than 1% for jet multiplicity below 4.

- Lepton energy scale (LES) and resolution (LER)
  The method to estimate the LES is similar to JES uncertainty, we rescale the simulated signal distribution up and down. The uncertainty of LER is assessed by smearing the momenta of leptons in signal sample. The propagated uncertainties of LES and LER is quite small, 0.3% in every bin of the measured distribution.

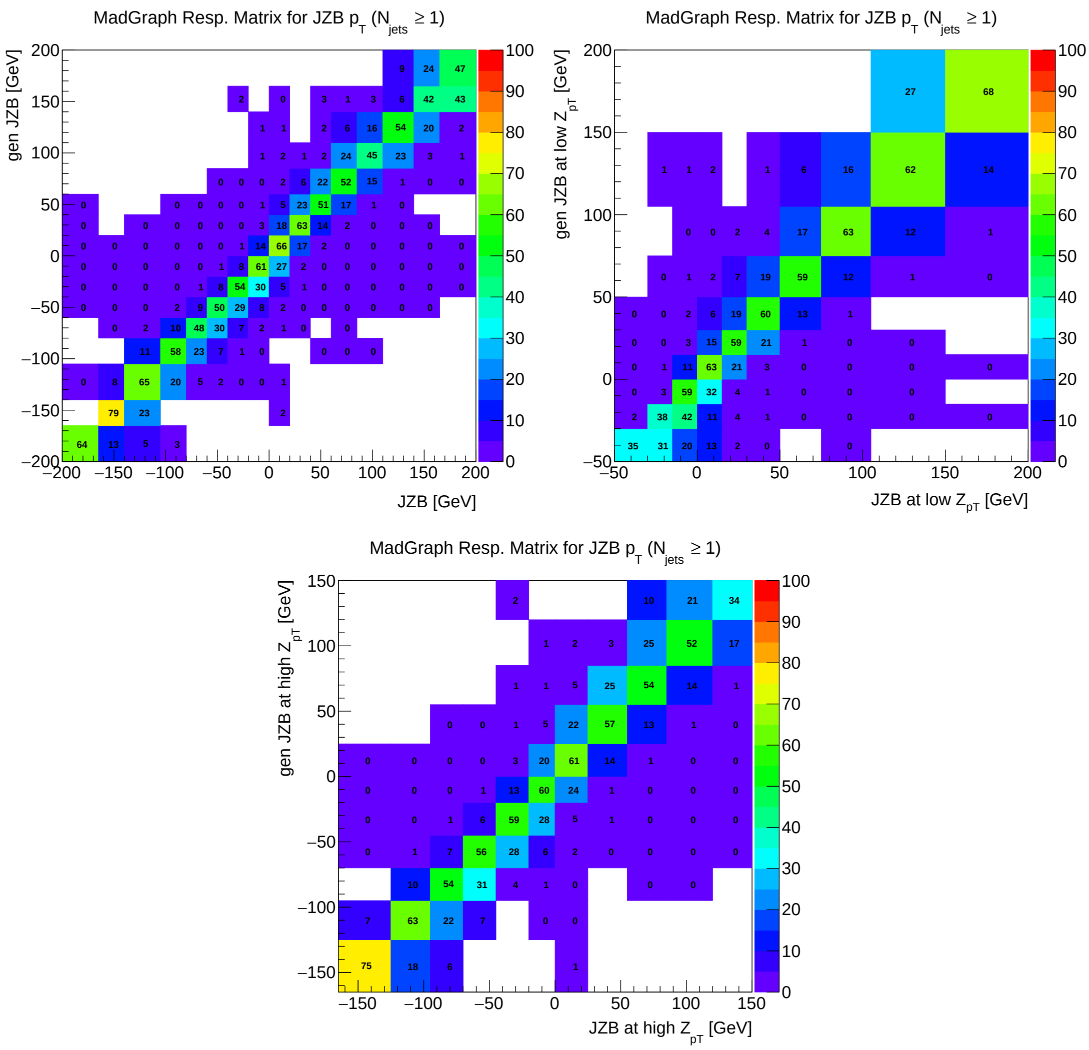

FIGURE 5.27: Response matrix used for the unfolding procedure for JZB variable (left), with extra cut p_T(Z)<50 GeV (middle) and p_T(Z)>50GeV (right) in the $\mu\mu$ decay channel.

- Pileup (PU)
  The pileup modelling uncertainty is estimated through varying the minimum bias cross section by $\pm 5\%$. The effect is within 1% except for the large jet multiplicity region.

- Unfolding (Unf)
  Due to the finite binning a different distribution will lead to a different response matrix. This uncertainty is estimated by weighting the simulation to agree with the data in each distribution and building a new response matrix. The weighting is done using a finer binning than for the measurement. The difference between the unfolded results obtained with the nominal MC and the reweighted one is taken as the systematic uncertainty, denoted $Unfmodel$. An additional uncertainty comes from the finite size of the simulation sample used to build the response matrix. This source of uncertainty is denoted $Unfstat$ in the table and is included in the systematic uncertainty of the measurement.

All these systematic uncertainties are added in quadrature assuming each uncertainty source is independent, yielding to the total systematic uncertainty.

5.9 Differential Cross Sections

In the analysis, we have checked the data/MC distribution comparisons at the detector level, estimated MC background, obtained the response matrices with DY+jets samples, estimated the computed the uncertainties. After having subtracted the background and unfolded data, the measured differential cross sections as functions of observables in both $\mu\mu$ and ee channels are obtained through dividing the number of events after unfolding by the integrated luminosity and the bin width for each bin.

5.9.1 Comparison of two channels

The measurements of the differential cross section in $\mu\mu$ and ee decay channels should be consistent. Before combining the two channels' results, the compatibility between the two channels should be checked. The differential cross section of two channel as functions of the exclusive jet multiplicities, the first leading jet transverse momenta, the first leading jet rapidity and the jet H_{T} for inclusive multiplicity of one are shown in figures 5.28 and 5.29

The differential cross sections as a function of the exclusive jet multiplicity of two channels are compatible except at the large jet multiplicity region, where we do not have enough statistics. Concerning the differential cross section as a function of the leading jet transverse momentum (p_{T}), the result is compatible in the low jet p_{T} value region (p_{T}<170 GeV). When taking into account the total systematic uncertainty, the difference in the high jet p_{T} region stands below two sigma. For the distributions of the first leading jet rapidity and scalar sum of jets p_{T} for $N_{jets} \geq 1$, no large discrepancy is found when considering the total systematic uncertainty.

5.9.2 Theoretical Predictions

The measured differential cross sections of both $\mu\mu$ and ee decay channels, together with full systematic and statistical uncertainties, are presented in this section. The measured differential cross sections are compared to four calculations: two multileg calculations, one fixed order calculation and one combination of the fully-differential NNLO calculation with the NNLL′ resummation, as following (also summary in table 5.10):

- MADGRAPH5_AMC@NLO version 2.2.2 (denoted MG5_AMC [30]) interfaced with PYTHIA8, includes matrix elements (MEs) computed at leading order (LO) for the five processes $pp \to Z + N\ partons, N = 0, 1...4$ and matched to the parton shower using the k_{T}-MLM [92, 93] scheme with the matching scale set at 19 GeV.

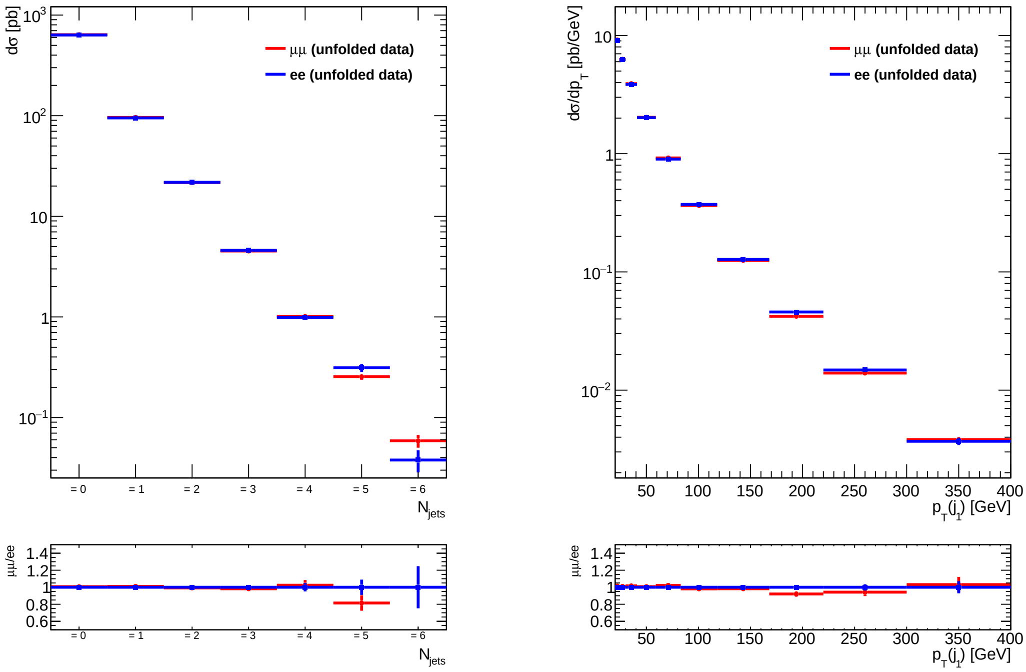

FIGURE 5.28: Comparison of measured cross sections between the $\mu\mu$ and the ee decay channels as a function of the exclusive jet multiplicity (left) and the first leading jet transverse momenta (right). The error bars only stand for the statistical uncertainties of unfolded data.

PYTHIA8 is used to include initial- and final-state parton showers and hadronisation. Its settings are defined by the CUETP8M1 tune, the NNPDF 2.3 LO parton distribution function (PDF) is used, and the strong coupling $\alpha_s(m_Z)$ is set to 0.130.

- MG5_AMC interfaced with PYTHIA8, with MEs computed at NLO for the three processes $pp \rightarrow Z + N\ partons, N = 0, 1, 2$ and merged with the parton shower using the FxFx scheme with the merging scale set at 30 GeV. The NNPDF 3.0 NLO PDF is used and $\alpha_s(m_Z)$ is set to 0.118. This calculation is also employed to derive nonperturbative corrections for the fixed-order prediction discussed in the following.
- GENEVA 1.0-RC2 MC program, where an NNLO calculation for Drell-Yan production is combined with higher-order resummation [31, 32]. Logarithms of the 0-jettiness resolution variable, τ, also known as beam thrust (defined in Ref. [94]), are resummed at NNLL including part of the next-to-NNLL (N^{3}LL) approximation. The accuracy refer to the τ dependence of the cross section, denoted NNLL$'_\tau$. The PDF set PDF4LHC15 NNLO [83] is used, and $\alpha_s(m_Z)$ is set to 0.118. The parton showering and hadronisation is provided by PYTHIA8 using the same tune for MG5_AMC.
- NNLO calculation for Z + 1jet using the N-jettiness subtraction scheme for the real emissions [95, 96]. The PDF set CT14 [97] is used. The nonperturbative

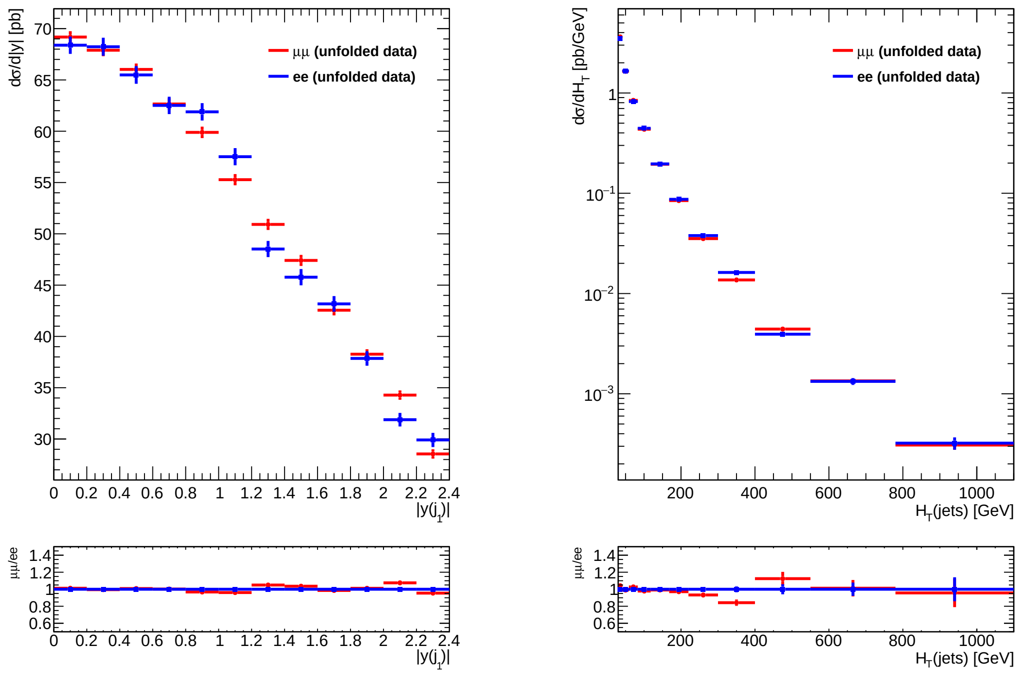

FIGURE 5.29: Comparison of measured cross sections between the $\mu\mu$ and the ee decay channels as a function of the first jet rapidity (left) and the scalar sum of the jets p_{T} (H_{T}) for $N_{jets} \geq 1$ (right). The error bars only stand for the statistical uncertainties of unfolded data.

correction obtained from MG5_AMC and PYTHIA8 is applied. This factor is calculated for each bin of the measured distributions from the ratio of the cross section values obtained with and without multiple parton interactions (MPIs) and hadronisation. This correction is less than 7%.

TABLE 5.10: Predictions at different accuracies. While the matrix elements are calculated at LO, NLO or NNLO, other additional jets described using PYTHIA8 (*PY*).

Prediction	no jet	1 jet	2 jets	3 jets	4 jets
MG5_AMC (LO*)	LO	LO	LO	LO	LO
MG5_AMC (NLO)	NLO	NLO	NLO	LO	*PY*
GENEVA	NNLO	NLO	LO	*PY*	*PY*
Z+1 jet at NNL	-	NNLO	NLO	LO	-

Given the large uncertainty in the LO calculation for the total cross section, MG5_AMC with LO MEs is rescaled to match the pp $\rightarrow$ Z total cross section calculated at NNLO in α_s and includes NLO quantum electrodynamics (QED) corrections with FEWZ [98] (version 3.1b2). The values used to normalise the cross section for MG5_AMC and GENEVA predictions are given in table 5.11. In the table, all the numbers correspond to a 50 GeV mass threshold applied before QED final-state radiation (FSR). In the case of FEWZ, the cross section is computed in the dimuon channel, with a mass threshold applied after QED FSR, but including the photons around the lepton at a distance $R = \sqrt{(\Delta\phi)^2 + (\Delta\eta)^2} < 0.1$. The used number includes a correction computed with the LO sample to compensate the difference in the mass definition. The correction is small, +0.35%. When the mass threshold is applied before FSR, the cross section is assumed to be the same for the muon and electron channels.

The differential cross section has been measured with NLO MG5_AMC prediction, and also compared to LO MG5_AMC, NNLO and GENEVA calculations. The statistical uncertainties of these predictions come from the MC sample statistics. Uncertainties in the ME calculation (denoted $theo.unc.$ in the figure legends) are estimated for MG5_AMC NLO, NNLO, and GENEVA calculations, following the prescriptions recommended by the authors of the generators, respectively. The uncertainty coming from missing terms in the fixed-order calculation is estimated by varying the renormalisation (μ_R) and factorisation (μ_F) scales by factors 0.5 and 2 :

- MG5_AMC NLO sample: an envelope of six combinations of the variations is considered, except two combinations where one scale is varied by a factor 0.5 and the other by a factor 2. The uncertainties in PDF and α_s values are also estimated. The PDF uncertainty is estimated using the set of 100 replicas of the NNPDF 3.0 NLO PDF, and the uncertainty in the α_s value used in the ME is estimated by varying it with ± 0.001. These two uncertainties are added in quadrature to the ME calcuation uncertainties. All these uncertainties are obtained using the reweighting method [99] implemented in the generator.
- GENEVA
  The two scales are varied by the same factor, leading to only two combinations. The uncertainty is symmetrised by using the maximum of the up and down uncertainties for both cases. The uncertainty from the resummation is also estimated using six profile scales [100, 101] and added in quadrature. All these uncertainties are obtained using the reweighting method [31] implemented in the generator.
- NNLO
  The two scales are varied by the same factor, only two combinations.

TABLE 5.11: Values of the pp $\to l^+l^-$ total cross section for the different predictions. The cross section used for the data/MC comparison, the "native" cross section from the MC generator, and the ratio of the two (k) is provided. The phase space of the predictions is also indicated.

Prediction	Phase space	Native cross section [pb]	Calculation	Used cross section [pb]	k
MG5_AMC+PYTHIA8, ≤ 4 j LO+PS	$m_{l^+l^-} > 50$ GeV	1652	FEWZ NNLO	1929	1.17
MG5_AMC+PYTHIA8, ≤ 2 j NLO+PS	$m_{l^+l^-} > 50$ GeV	1977	native	1977	1
GENEVA	$m_{l^+l^-} \in [50, 150]$ GeV	1980	native	1980	1

5.9.3 Single Channel Results

The analysis of Z+jets measurement includes muon and electron channels, only the muon decay channel is presented in details, and the results of electron decay channel relying on the work of colleagues of the CMS Z+jets group are shown in appendix C. The results for the differential cross section are shown from figure 5.30 to figure 5.36

and are compared to the predictions described in section 5.9.2. There are two predictions obtained from MG5_AMC interfaced with PYTHIA8, with one includes ME calculations at LO for up to four partons (labeled "≤4j LO" in the figure) and the other includes ME calculations at NLO for up to two partons (labeled "≤2j NLO"). While the prediction of GENEVA is denoted as "GE", the NNLO Z+1 jet calculation is denoted as $\mathrm{N_{jetti}}$ in the legends.

Figure 5.30 shows the measured cross section as a function of exclusive and the inclusive jet multiplicities. Agreement between the measurement and the NLO MG5_AMC prediction is observed, while the LO MG5_AMC prediction tends to be lower for jet multiplicities of two and three.

The measured cross section as a function of the transverse momentum of the Z boson is presented in figure 5.31. In the low p_{T} region, NLO MG5_AMC shows a better agreement than the NNLL$'_{\tau}$ calculation from GENEVA. In the high p_{T} region, NLO MG5_AMC and GENEVA are equally well describing the data, while the LO MG5_-AMC prediction undershoot the measurement.

The results corresponding to the transverse momentum and the rapidities of the 1^{st}, 2^{nd} and 3^{rd} leading jets are shown in figures 5.32 and 5.33, respectively. The LO MG5_AMC prediction differs from the measurement, while NLO MG5_AMC and $\mathrm{N_{jetti}}$ NNLO calculation have good agreement, showing that adding NLO terms cures this discrepancy. The GENEVA calculation is in good agreement for the measured first leading jet properties.

The total jet activity as measured via the H_{T} variable for inclusive jet multiplicities of 1, 2 and 3, shown in figure 5.34. The LO MG5_AMC calculation predicts fewer events than found in the data for region $H_{\mathrm{T}}<$ 400 GeV. The NLO MG5_AMC prediction gives the best agreement amount the four predictions, and is compatible with the measurement. In the figure of jet H_{T} for at least one jet, NLO MG5_AMC shows better description than the NNLO $\mathrm{N_{jetti}}$ and NNLL$'_{\tau}$ from GENEVA calculations. At lower values of H_{T}, the predictions is slightly overestimated, but the discrepancy is compatible with the theoretical and experimental uncertainties.

The balance in the transverse momentum between the jets and the Z boson (p_{T}^{bal}) is presented in figure 5.35 for inclusive jet multiplicities of 1, 2 and 3. The peak of the p_{T}^{bal} distribution is shifted to larger values with more jets included. The measurement is in good agreement with the NLO MG5_AMC predictions. The LO MG5_AMC calculation does not fully describe the data for the process with at least two jets. As for the GENEVA simulation, it is NLO accuracy for one jet, LO for two jets and for more than three jets comes from PS. The GENEVA simulation does not manage to describe the p_{T}^{bal} variable of Z+jets process. This observation indicates that the NLO correction is important for the description of hadronic activity beyond the jet acceptance used in this analysis.

The JZB distribution for the inclusive one jet events in the full phase space, and separately for p_{T}(Z) below and above 50 GeV is shown in figure 5.36. The NLO MG5_AMC prediction provides a good description of the JZB distribution, while LO MG5_AMC prediction does not. This observation also indicates the importance of the NLO correction.

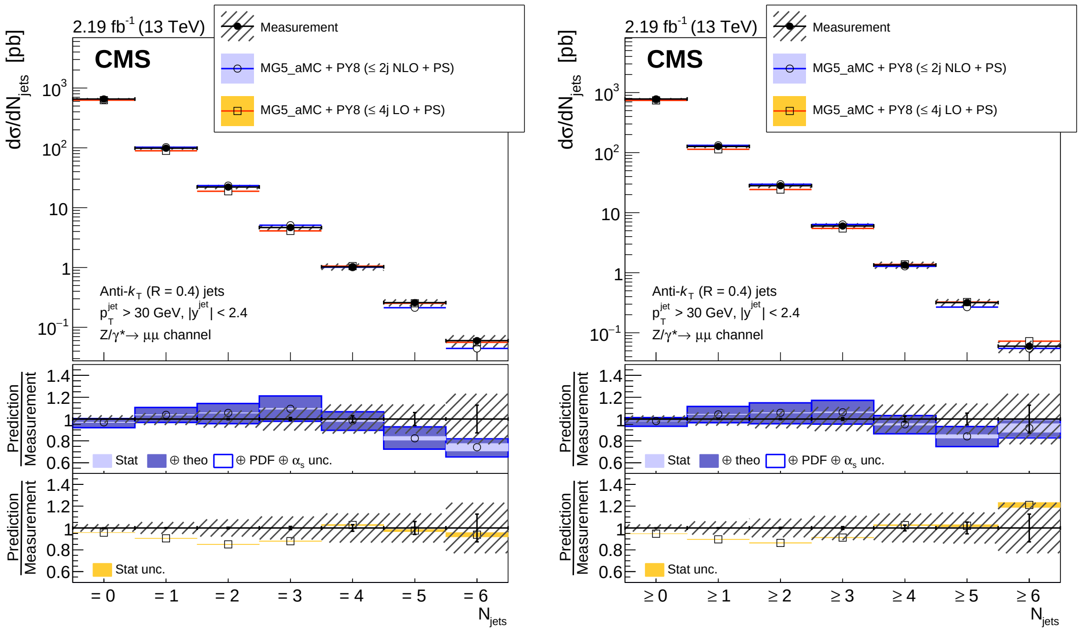

FIGURE 5.30: Measured cross section as a function of the jet exclusive (left) and inclusive (right) multiplicities in the $\mu\mu$ decay channel. The error bar stands for the statistical uncertainty, and the hatched band presents the total uncertainties.

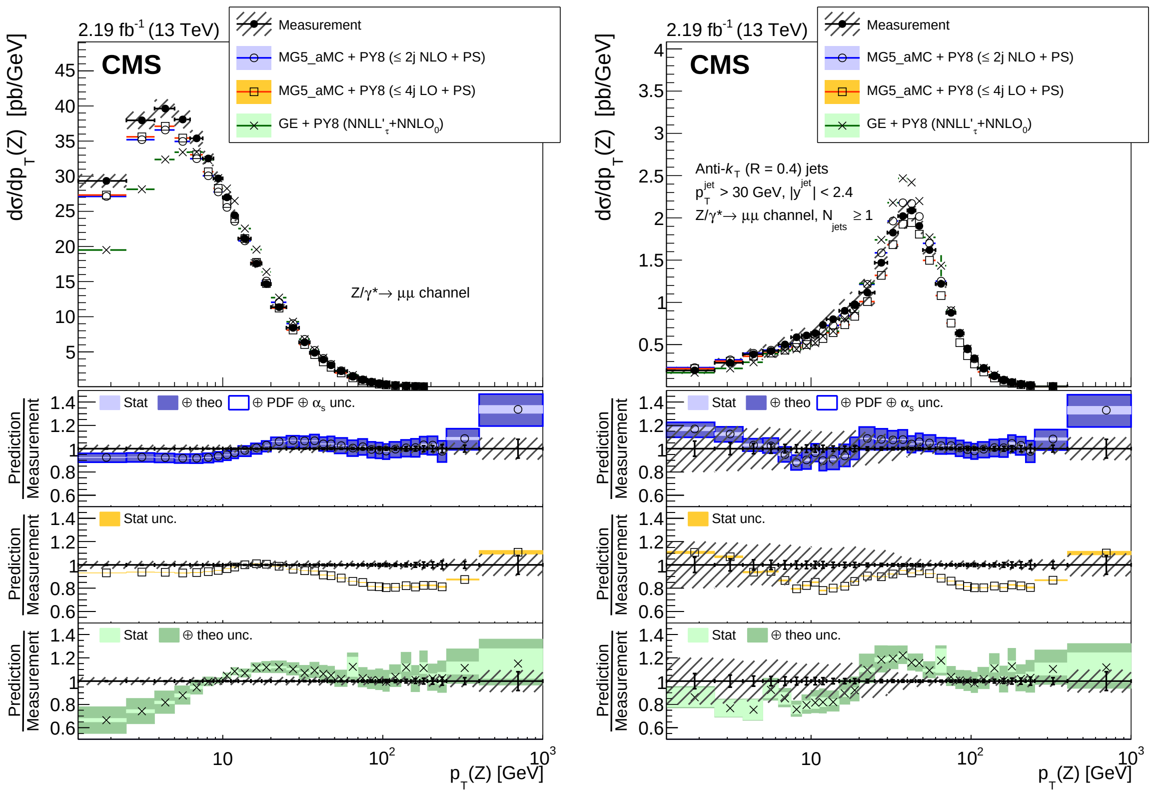

FIGURE 5.31: Measured cross section as a function of the p_T of Z boson for inclusive zero jet (left) and one jet (right) in the $\mu\mu$ decay channel. The error bar stands for the statistical uncertainty, and the hatched band presents the total uncertainties.

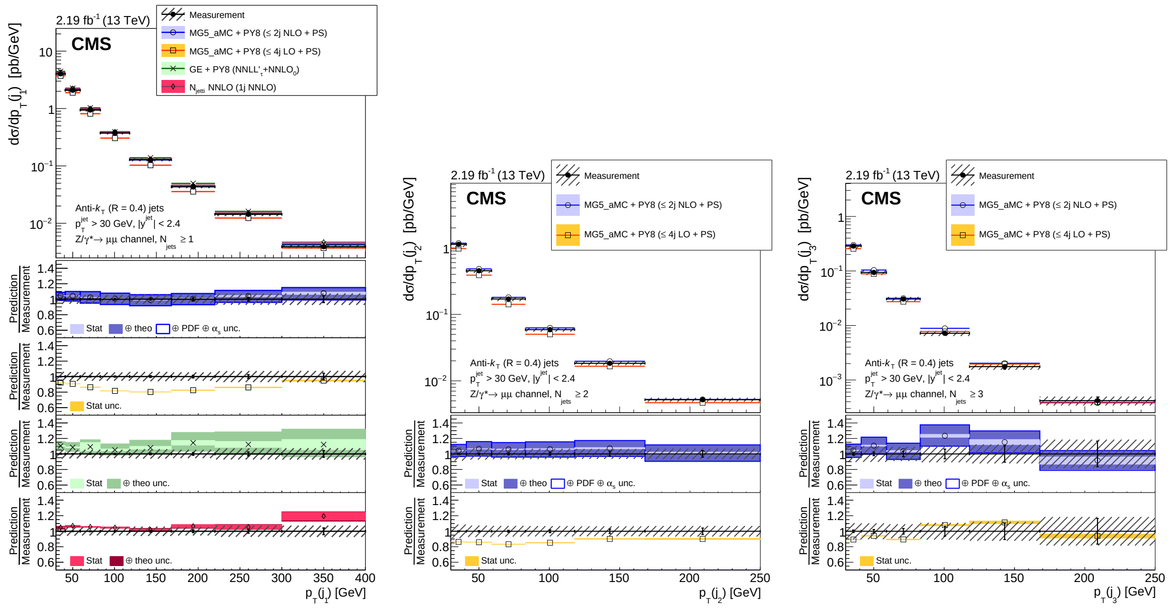

FIGURE 5.32: Measured cross section as a function of p_T of the first leading jet (left), second leading jet (middle) and third jet (right) in the $\mu\mu$ decay channel. The error bar stands for the statistical uncertainty, and the hatched band presents the total uncertainties.

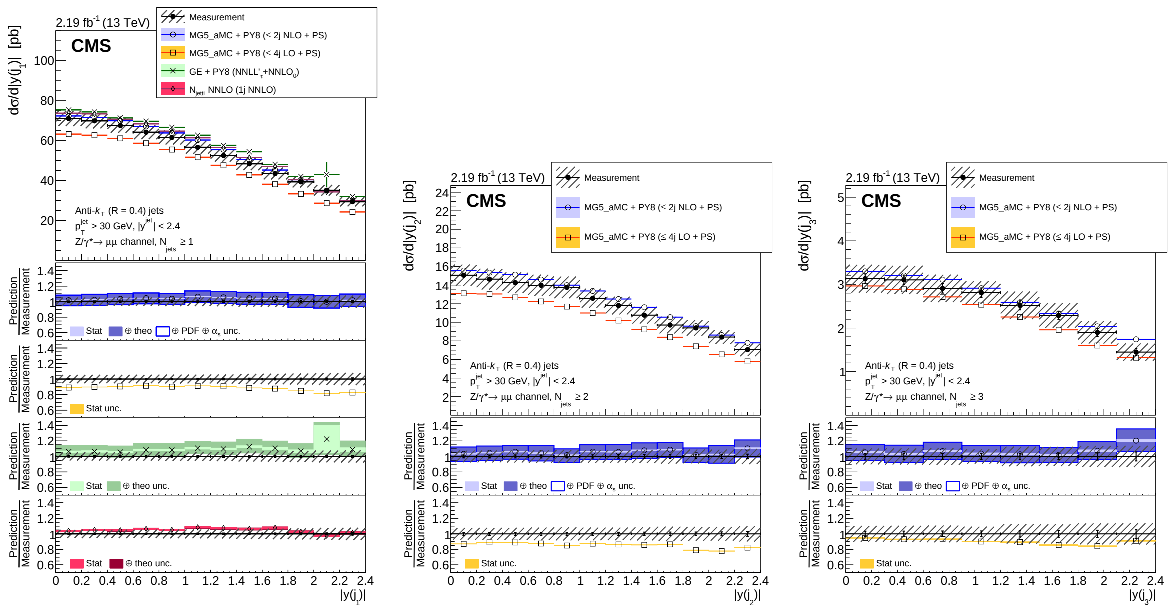

FIGURE 5.33: Measured cross section as a function of absolute rapidity of the first leading jet (left), second leading jet (middle) and third jet (right) in the $\mu\mu$ decay channel. The error bar stands for the statistical uncertainty, and the hatched band presents the total uncertainties.

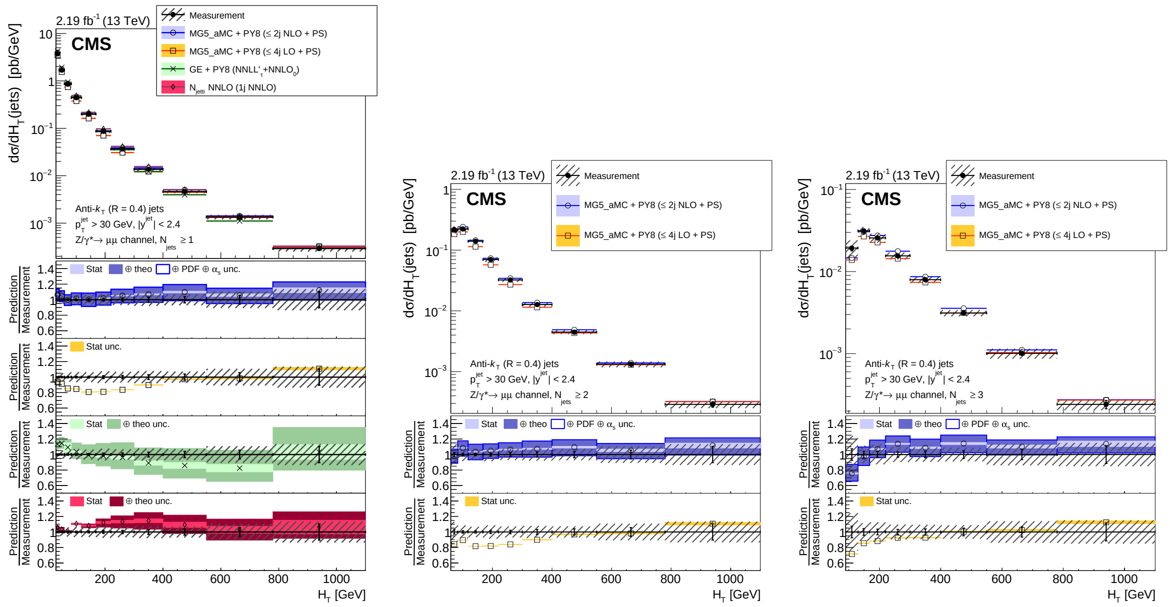

FIGURE 5.34: Measured cross section as a function of the jets H_T for inclusive jet multiplicities of 1 (left), 2 (middle) and 3 (right) in the $\mu\mu$ decay channel. The error bar stands for the statistical uncertainty, and the hatched band presents the total uncertainties.

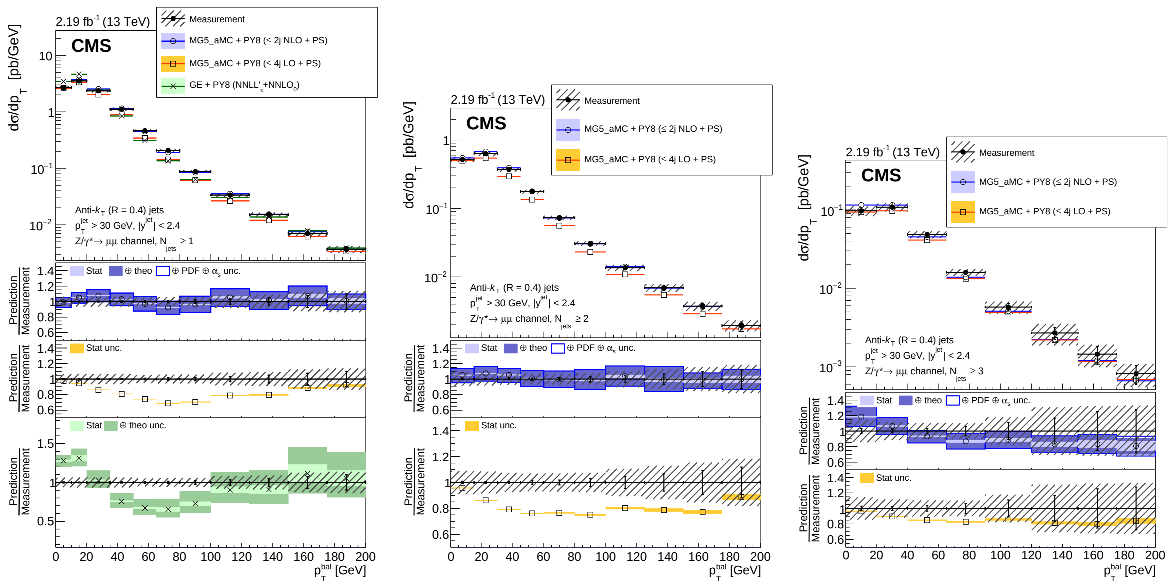

FIGURE 5.35: Measured cross section as a function of the transverse momentum balance between jets and the Z boson (p_T^{bal}) for the jet multiplicity $N_{jets} \geq 1$ (left), $N_{jets} \geq 2$ (middle) and $N_{jets} \geq 3$ (right) in the $\mu\mu$ decay channel. The error bar stands for the statistical uncertainty, and the hatched band presents the total uncertainties.

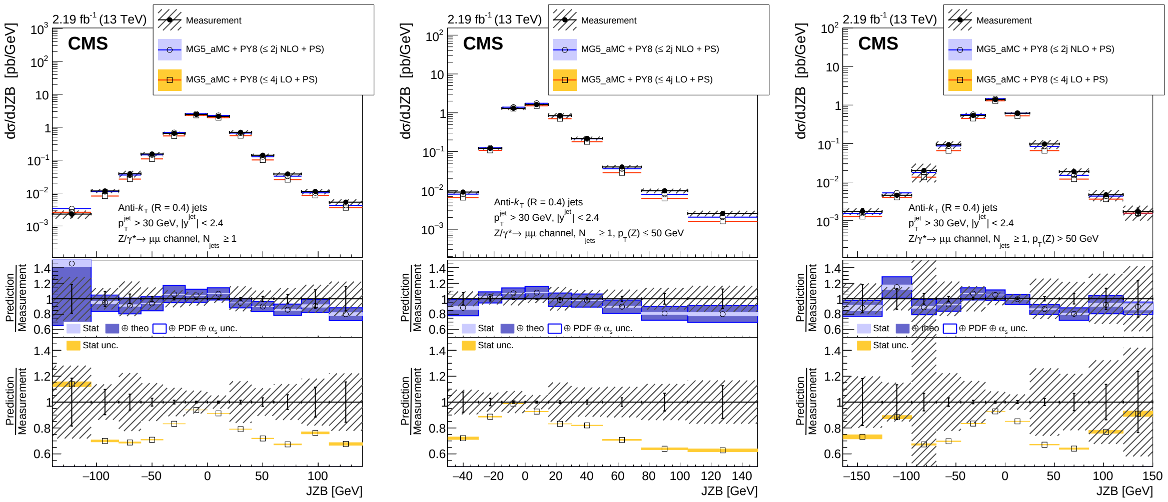

FIGURE 5.36: Measured cross section as a function of JZB variable (left), with extra cut p_{T}(Z)<50 GeV (middle) and p_{T}(Z)>50GeV (right) in the $\mu\mu$ decay channel. The error bar stands for the statistical uncertainty, and the hatched band presents the total uncertainties.

5.10 Combined Differential Cross Sections

The differential cross sections of Z+jets process with the corresponding uncertainties in both muon and electron decay channels have been obtained. In order to gain more precision for the measurement by increasing statistics, we combine the results of the two decay channels. The combined measurement make sense due to the probabilities of a Z boson decaying to $\mu\mu$ and ee are same, and the coupling between a Z boson and the two leptons is leptonic flavor independent, which tells the same observables are measured in both two decay channels. However, the measurements are not totally independent, for example, the same method was used for the unfolding, using the same MC generator to reconstruct the response matrices. The uncertainties coming from the luminosity, the background, the pileup, the jet energy scale and jet energy resolution, are also correlated.

5.10.1 Combination methodology

To combine the two channels, an hybrid method based on weighted mean and the Best Linear Unbiased Estimates (BLUE) method [102] is performed to estimate the cross section values and its covariance matrix. The estimated $x_\alpha^{\text{comb.}}$ of the combined cross section is:

$$x_\alpha^{\text{comb.}} = \sum_{i=1}^{2N} \lambda_{\alpha i} y_i = \sum_{i=1}^{N} \lambda_{\alpha i} x_i^{ee} + \sum_{i=N+1}^{2N} \lambda_{\alpha i} x_{i-N}^{\mu\mu}$$

where α represents the bin number with a range from 1 to N, i is and index taking value between 1 and $2N$, and the superscripts ee and $\mu\mu$ denote the decay channel. The $N \times 2N$ matrix λ contains the coefficients of the electron measurements for $1 \leq i \leq N$

and the coefficients of the muon measurements for $N+1 \le i \le 2N$. In case of the weighted mean method, the equation is simplified to the following:

$$\begin{aligned} x_\alpha^{\text{comb.}} &= \lambda_{\alpha\alpha} y_\alpha + \lambda_{\alpha\alpha+N} y_{\alpha+N} \\ &= \frac{(\sigma_\alpha^{ee})^{-2}}{(\sigma_\alpha^{ee})^{-2} + (\sigma_\alpha^{\mu\mu})^{-2}} x_\alpha^{ee} + \frac{(\sigma_\alpha^{\mu\mu})^{-2}}{(\sigma_\alpha^{ee})^{-2} + (\sigma_\alpha^{\mu\mu})^{-2}} x_\alpha^{\mu\mu} \end{aligned}$$

where the x_α^{ll} are the bin α value of the observable x as measured in the ll decay channel and the σ_α^{ll} are the total uncertainty attached to the related measurement.

In order to estimate the uncertainty on the combination, the BLUE method is applied using the coefficients $\lambda_{\alpha i}$ as determined in the previous equation. That is the covariance matrix of the combined cross section for some observable x, given by:

$$\sigma_{\alpha\beta}^{\text{comb.}} = \sum_{i=1}^{2N} \sum_{j=1}^{2N} \lambda_{\alpha i} \mathcal{M}_{ij} \lambda_{\beta j}$$

where $\mathcal{M}_{ij}$ is a $2N \times 2N$ covariance matrix of the measurement in both decay channels.

The matching $\mathcal{M}$, when taking correlation into account, is defined as:

$$\begin{aligned} \mathcal{M} &= \sum_{s \,\in\, \text{sources}} \mathcal{M}^s \\ &= \sum_{s \,\in\, \{\text{JES, JER, Lumi, Bkg, PU}\}} \left(\begin{array}{c|c} (\sigma^{ee})^s & (\sigma_\alpha^{ee})^s (\sigma_\beta^{\mu\mu})^s \\ \hline (\sigma_\alpha^{ee})^s (\sigma_\beta^{\mu\mu})^s & (\sigma^{\mu\mu})^s \end{array} \right) \\ &\quad + \sum_{s \,\in\, \{\text{MC stat., Eff, LES, LER, Unf}\}} \left(\begin{array}{c|c} (\sigma^{ee})^s & 0 \\ \hline 0 & (\sigma^{\mu\mu})^s \end{array} \right) \end{aligned}$$

where the $(\sigma^{ll})^s$ are the covariance matrices of single channel for the uncertainty source s, obtained as described in section 5.8, and $(\sigma_\alpha^{ll})^s = \sqrt{(\sigma^{ll})_{\alpha\alpha}^s}$. The uncertainties resulting from jet energy scale (JES), jet energy resolution (JER), luminosity (Lumi), background estimation (Bkg) and pileup (PU) of the two decay channels are correlated, and the corresponding covariance matrices are crossed in the off diagonal blocks. While the other uncertainties, such as MC statistics, efficiency correction (Eff), lepton energy scale (LES), lepton energy resolution (LER) and unfolding (Unf), are independent, so their covariance matrices only appear in the diagonal blocks. Therefore, the covariance matrices of the combination for each source of uncertainty as well as the total uncertainties can be obtained.

5.10.2 Combined results

The combined results are presented in this section and compared to four type of theoretical predictions. Figures 5.37 and to 5.41 show the comparisons of the differential cross sections as functions of the jet multiplicities, the transverse momentum of the Z boson, the transverse momentum and the rapidities of the 1^{st}, 2^{nd} and 3^{rd} leading jets, the scalar sum of jets transverse momentum (jet H_{T}) for $N_{jets} \ge$ 1,2 and 3, the transverse momentum balance between the jets and the Z boson (p_{T}^{bal}) and the JZB variables. The details are explained in the following paragraphs. The measured values of the combined results with a detailed break down of errors are listed in tables 5.12 to 5.29.

The measured cross sections as a function of the transverse momentum of the Z boson for inclusive zero jet and one jet are shown in figure 5.37. At the low p_{T} of the inclusive Z, p_{T} less than around 25 GeV, the NLO MG5_AMC and LO MG5_AMC predictions are better to describe the shape of the distribution than the NNLL$'_{\tau}$ calculation from GENEVA. At the high p_{T}, the GENEVA and NLO MG5_AMC predictions are expected to be in agreement with the measurements due to the accuracy (NNLO for GENEVA, NLO MG5_AMC), while the LO MG5_AMC predictions undershoot the measurement despite the normalisation of total cross section to its NNLO value.

On the other case of p_{T}(Z) for at least one jet, the NLO MG5_AMC is the best model for describing the measurement at low p_{T}, better than the GENEVA. The GENEVA prediction is only at LO accuracy for any bin below the jet p_{T} cut (30 GeV), because a second parton is required to conserve the transverse momentum. Given the particular kinematic configurations at low p_{T}(Z), with two back-to-back jets of at least 30 GeV, it is not immediate to ascribe this to the higher-order resummation of beam-thrust in GENEVA. The estimation of the uncertainty in the shape indicates that it is dominanted by the statistical uncertainty, represented by error bars on the plot since the systematic uncertainties are negligible. The shape of the distribution in the region below 10 GeV is better described by GENEVA than the other predictions, as shown by the flat ratio plot. In the intermediate region, GENEVA predicts a steeper rise for the distribution than the other two predictions and than the measurement. In the high p_{T} region, the measurement is described by both the GENEVA and NLO MG5_AMC predictions. While the LO predictions undershoot the measurement again.

The differential cross section as a function of the exclusive and inclusive jet multiplicities up to 6 jets are shown in figure 5.38. The MG5_AMC prediction shows agreement with the measurement. The measured cross section obtain from the LO MG5_AMC prediction tends to be lower than NLO MG5_AMC up to a jet multiplicities of three. The total cross section for Z→ $l^+l^-+\geq 0$jet of the LO MG5_AMC prediction is normalised to FEWZ NNLO, which is similar to the NLO cross section as seen in table 5.11. The smaller cross section seen, when required at least one jet, is explained by a steeply falling spectrum of the leading jet in the LO prediction. The GENEVA prediction describes the measured cross section up to a jet multiplicity of two, but fails for higher jet multiplicities, where one or more jets arise from the parton shower. This effect is not seen in the NLO (LO) MG5_AMC predictions, which give a fair description of the data for multiplicity above three (four).

The jet transverse momenta for the 1^{st}, 2^{nd} and 3^{rd} leading jets are shown in figure 5.39 and table 5.15-5.17. The LO MG5_AMC prediction differs from the measurement, showing a steeper slope in the low p_{T} region. The same feature was observed in the previous measurement [103] [69]. However, this disappears for the NLO MG5_AMC and $\mathrm{N_{jetti}}$ NNLO calculations, showing that adding NLO terms cures this discrepancy. The GENEVA prediction is in good agreement for the measured p_{T} of the first leading jet, while it undershoots the data at low p_{T} for the second jet. The absolute rapidities for

TABLE 5.12: Differential cross section in exclusive jet multiplicity for the combination of both decay channels and break down of the systematic uncertainties.

N_{jets}	$\frac{d\sigma}{dN_{jets}}$ [pb]	Tot. unc [%]	Stat [%]	JES [%]	JER [%]	Eff [%]	Lumi [%]	Bkg [%]	pileup [%]	Unf model [%]	Unf stat [%]
= 0	652	3.0	0.091	1.1	0.046	1.5	2.3	< 0.01	0.22	-	0.026
= 1	97.9	5.1	0.27	4.3	0.18	1.5	2.3	0.012	0.30	-	0.10
= 2	22.2	7.3	0.63	6.7	0.20	1.6	2.3	0.026	0.43	-	0.26
= 3	4.68	10	1.4	9.9	0.39	1.7	2.3	0.13	0.29	-	0.54
= 4	1.01	11	3.5	10	0.24	1.7	2.3	0.43	0.56	-	1.4
= 5	0.275	14	5.0	12	0.081	2.0	2.3	1.2	0.29	-	2.2
= 6	0.045	24	15	17	0.36	1.8	2.4	3.5	1.7	-	6.6

the first three leading jets have been measured and the results are shown in figure 5.40 and table 5.18-5.20. The NLO MG5_AMC, NNLO1j and GENEVA are in very good agreement with data.

The total jet activity as measured via the H_{T} variable for inclusive jet multiplicities of 1, 2 and 3, shown in figure 5.41, and in the table 5.21- 5.23. The LO MG5_AMC calculation predicts fewer events than found in the data for region H_{T}< 400 GeV. The NLO MG5_AMC prediction gives the best agreement amount the four predictions starting from 50 GeV, and is slightly overestimated but compatible with the measurement at lower values of H_{T}. In the figure of jet H_{T} for at least one jet, NLO MG5_AMC shows better description than the $\mathrm{N_{jetti}}$ NNLO and NNLL'_{τ} from GENEVA calculations. The uncertainties for the $\mathrm{N_{jetti}}$ NNLO is larger than in the jet tranverse momentum distribution due to the contribution from the additional jets.

The balance in the transverse momentum between the jets and the Z boson (p_{T}^{bal}) is presented in figure 5.42 and table 5.24- 5.26 for inclusive jet multiplicities of 1, 2 and 3. The peak of the p_{T}^{bal} distribution is shifted to larger values with more jets included. The measurement is in good agreement with the NLO MG5_AMC predictions. The LO MG5_AMC calculation does not fully describe the data for the process with at least two jets. This observation indicates that the NLO correction is important for the description of the hadronic activity beyond the jet acceptance used in the analysis, p_{T} < 30 GeV and $|y|$>2.4. An imbalance in the event, i.e. p_{T}^{bal} not peak at zero, requires two partons in the final state with one of the two out the acceptance. Such events are described with NLO accuracy for NLO MG5_AMC and LO accuracy for the two other samples. As for the GENEVA simulation, it is NLO accuracy for one jet, LO for two jets and for more than three jets comes from PS. The GENEVA simulation does not manage to describe the p_{T}^{bal} variable for muon decay channel of Z+jets process.

The JZB distribution for the inclusive one jet events in the full phase space, and separately for p_{T}(Z) below and above 50 GeV is shown in figure 5.43 and in table 5.27- 5.29. The distribution is not symmetric for the JZB with p_{T}(Z)< 50 GeV due to the upper threshold of the transverse momentum of Z boson. The NLO MG5_AMC prediction provides a good description of the JZB distribution, while both LO MG5_AMC and GENEVA predictions do not. This observation also indicates the importance of the NLO correction.

TABLE 5.13: Differential cross section in inclusive jet multiplicity for the combination of both decay channels and break down of the systematic uncertainties.

N_{jets}	$\frac{d\sigma}{dN_{jets}}$ [pb]	Tot. unc [%]	Stat [%]	JES [%]	JER [%]	Eff [%]	Lumi [%]	Bkg [%]	pileup [%]	Unf model [%]	Unf stat [%]
≥ 0	778	2.8	0.081	0.079	< 0.01	1.5	2.3	< 0.01	0.24	-	0.025
≥ 1	126.2	5.7	0.23	5.0	0.19	1.5	2.3	< 0.01	0.32	-	0.085
≥ 2	28.3	8.0	0.52	7.4	0.22	1.6	2.3	0.073	0.41	-	0.21
≥ 3	6.01	11	1.1	10	0.29	1.7	2.3	0.25	0.35	-	0.46
≥ 4	1.33	12	2.8	11	0.16	1.7	2.3	0.66	0.54	-	1.1
≥ 5	0.320	14	4.8	13	0.10	1.9	2.3	1.5	0.48	-	2.1
≥ 6	0.045	24	15	17	0.36	1.8	2.4	3.5	1.7	-	6.6

TABLE 5.14: Differential cross section in $p_{\mathrm{T}}(\mathrm{Z})$ ($N_{jets} \geq 1$) for the combination of both decay channels and break down of the systematic uncertainties.

$p_{\mathrm{T}}(\mathrm{Z})$ [GeV]	$\frac{d\sigma}{dp_{\mathrm{T}}(\mathrm{Z})}$ $[\frac{\mathrm{pb}}{GeV}]$	Tot. unc [%]	Stat [%]	JES [%]	JER [%]	Eff [%]	Lumi [%]	Bkg [%]	LES [%]	LER [%]	pileup [%]	Unf model [%]	Unf stat [%]
$0 - 1.25$	0.066	27	9.4	24	1.6	1.6	2.3	< 0.1	1.9	1.4	0.62	5.9	2.2
$1.25 - 2.5$	0.205	20	5.4	19	1.5	1.6	2.3	< 0.1	1.1	0.57	0.56	2.0	1.3
$2.5 - 3.75$	0.305	18	4.3	18	1.2	1.5	2.3	< 0.1	0.95	0.46	0.27	1.7	1.1
$3.75 - 5$	0.376	18	3.7	17	1.3	1.6	2.3	< 0.1	1.2	0.27	0.69	1.2	1.0
$5 - 6.25$	0.422	18	3.6	17	1.2	1.5	2.3	< 0.1	0.93	0.14	0.76	1.7	1.1
$6.25 - 7.5$	0.498	17	3.3	16	1.1	1.5	2.3	< 0.1	0.85	0.14	0.55	1.7	1.0
$7.5 - 8.75$	0.556	16	3.0	15	1.0	1.5	2.3	< 0.1	0.88	0.10	0.51	2.0	0.99
$8.75 - 10$	0.601	15	2.8	14	0.95	1.6	2.3	< 0.1	0.94	0.060	0.33	2.7	0.93
$10 - 11.25$	0.65	16	2.7	15	0.86	1.6	2.3	< 0.1	0.99	0.035	0.33	3.1	0.91
$11.25 - 12.5$	0.73	14	2.6	13	0.92	1.5	2.3	< 0.1	0.83	0.15	0.31	3.3	0.91
$12.5 - 15$	0.78	15	2.0	14	1.1	1.6	2.3	< 0.1	0.74	0.13	0.33	2.8	0.71
$15 - 17.5$	0.89	15	2.0	14	1.1	1.5	2.3	< 0.1	1.5	0.14	0.094	2.3	0.69
$17.5 - 20$	1.00	15	1.9	15	1.1	1.5	2.3	< 0.1	1.2	0.016	0.17	1.1	0.65
$20 - 25$	1.15	14	1.3	14	1.1	1.6	2.3	< 0.1	1.1	0.062	0.14	1.3	0.42
$25 - 30$	1.44	13	1.2	13	0.74	1.6	2.3	< 0.1	0.97	0.022	0.31	1.3	0.36
$30 - 35$	1.77	10	1.0	9.8	0.39	1.5	2.3	< 0.1	0.71	0.036	0.47	1.9	0.32
$35 - 40$	2.01	7.6	0.84	6.7	0.13	1.6	2.3	< 0.01	0.34	0.059	0.36	1.6	0.28
$40 - 45$	2.04	6.0	0.82	5.0	0.067	1.6	2.3	< 0.01	0.14	0.049	0.38	1.5	0.28
$45 - 50$	1.905	4.9	0.81	3.7	0.030	1.6	2.3	< 0.01	0.19	0.034	0.40	1.0	0.29
$50 - 60$	1.616	3.8	0.63	2.4	0.038	1.5	2.3	0.012	0.23	0.039	0.42	0.74	0.23
$60 - 70$	1.204	3.3	0.71	1.4	0.031	1.6	2.3	0.018	0.52	0.031	0.22	0.53	0.26
$70 - 80$	0.881	3.2	0.79	0.93	0.022	1.6	2.3	0.024	0.66	0.024	0.38	0.52	0.30
$80 - 90$	0.634	3.3	0.89	0.55	0.015	1.6	2.3	0.028	0.94	0.0024	0.25	0.62	0.35
$90 - 100$	0.444	3.3	1.1	0.30	0.025	1.6	2.3	0.031	0.81	0.0024	0.36	0.74	0.42
$100 - 110$	0.334	3.3	1.2	0.28	0.0080	1.6	2.3	0.026	0.67	0.0022	0.25	0.77	0.48
$110 - 130$	0.2213	3.3	1.0	0.17	0.0070	1.6	2.3	0.021	0.88	0.019	0.20	0.79	0.41
$130 - 150$	0.1308	3.4	1.3	0.11	0.010	1.7	2.3	0.022	0.88	0.023	0.076	0.88	0.54
$150 - 170$	0.0813	3.6	1.6	0.14	0.012	1.7	2.3	0.016	0.76	0.027	0.12	1.0	0.67
$170 - 190$	0.0516	3.9	2.0	0.091	0.017	1.8	2.3	0.022	0.87	0.017	0.17	1.1	0.84
$190 - 220$	0.0317	4.0	2.2	0.088	0.0084	1.8	2.3	0.035	0.69	0.033	0.10	1.1	0.90
$220 - 250$	0.01836	4.5	2.8	0.041	0.0031	1.8	2.3	0.041	0.83	0.020	0.11	1.4	1.2
$250 - 400$	0.00508	4.5	2.6	0.022	0.0037	2.0	2.3	0.065	0.80	0.0046	0.12	1.4	1.1
$400 - 1000$	0.000187	7.9	6.2	0.019	0.00077	1.7	2.4	0.11	1.7	0.065	0.58	2.6	2.4

TABLE 5.15: Differential cross section in 1st jet p_{T} ($N_{jets} \geq 1$) for the combination of both decay channels and break down of the systematic uncertainties.

$p_{\mathrm{T}}(j_1)$ [GeV]	$\frac{d\sigma}{dp_{\mathrm{T}}(j_1)}$ $[\frac{\mathrm{pb}}{GeV}]$	Tot. unc [%]	Stat [%]	JES [%]	JER [%]	Eff [%]	Lumi [%]	Bkg [%]	pileup [%]	Unf model [%]	Unf stat [%]
$30 - 41$	3.99	5.8	0.30	5.0	0.17	1.5	2.3	< 0.01	0.38	0.34	0.11
$41 - 59$	2.07	5.3	0.36	4.4	0.18	1.5	2.3	0.012	0.33	0.35	0.13
$59 - 83$	0.933	5.1	0.45	4.2	0.17	1.6	2.3	0.015	0.25	0.26	0.18
$83 - 118$	0.377	5.1	0.60	4.1	0.20	1.6	2.3	0.051	0.28	0.24	0.24
$118 - 168$	0.1301	5.1	0.93	4.1	0.22	1.6	2.3	0.070	0.057	0.31	0.38
$168 - 220$	0.0448	4.9	1.4	3.7	0.21	1.6	2.3	0.077	0.21	0.30	0.59
$220 - 300$	0.01477	6.4	2.0	5.3	0.32	1.6	2.3	0.066	0.30	0.37	0.85
$300 - 400$	0.00390	7.0	3.4	5.2	0.24	1.7	2.3	0.097	0.28	0.72	1.4

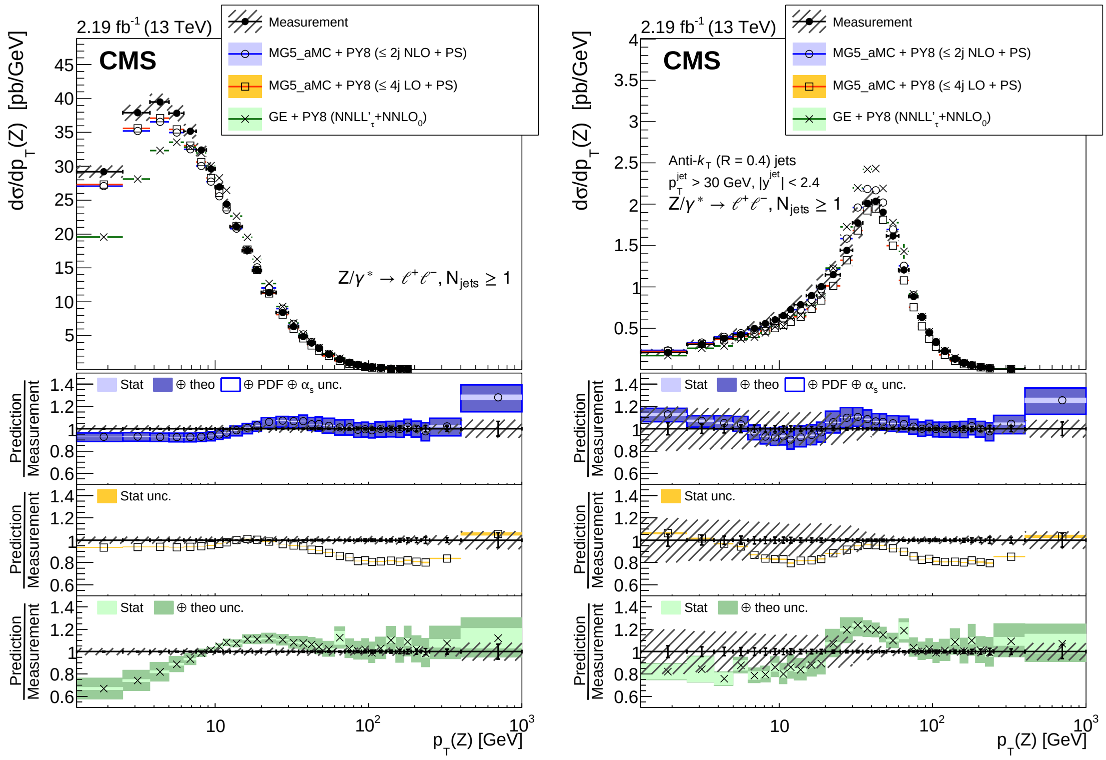

FIGURE 5.37: Measured cross section as a function of the p_T of Z boson for inclusive zero jet (left) and one jet (right). The error bar of the data stands for the statistical uncertainty, and the hatched band presents the total uncertainties.

TABLE 5.16: Differential cross section in 2nd jet p_T ($N_{jets} \geq 2$) and break down of the systematic uncertainties for the combination of both decay channels.

$p_T(j_2)$ [GeV]	$\frac{d\sigma}{dp_T(j_2)}$ $[\frac{pb}{GeV}]$	Tot. Unc [%]	Stat [%]	JES [%]	JER [%]	Eff [%]	Lumi [%]	Bkg [%]	PU [%]	Unf model [%]	Unf stat [%]
30 – 41	1.124	8.3	0.58	7.7	0.22	1.6	2.3	0.032	0.51	0.38	0.24
41 – 59	0.456	7.3	0.74	6.6	0.14	1.6	2.3	0.050	0.32	0.34	0.31
59 – 83	0.173	6.4	1.1	5.6	0.16	1.6	2.3	0.15	0.31	0.39	0.44
83 – 118	0.0589	5.6	1.7	4.4	0.17	1.6	2.3	0.22	0.48	0.21	0.66
118 – 168	0.0187	6.0	2.3	4.6	0.20	1.7	2.3	0.25	0.19	0.13	0.89
168 – 250	0.00518	6.5	3.4	4.6	0.33	1.7	2.3	0.22	0.21	0.19	1.3

TABLE 5.17: Differential cross section in 3rd jet p_T ($N_{jets} \geq 3$) and break down of the systematic uncertainties for the combination of both decay channels.

$p_T(j_3)$ [GeV]	$\frac{d\sigma}{dp_T(j_3)}$ $[\frac{pb}{GeV}]$	Tot. Unc [%]	Stat [%]	JES [%]	JER [%]	Eff [%]	Lumi [%]	Bkg [%]	PU [%]	Unf model [%]	Unf stat [%]
30 – 41	0.287	10.	1.2	9.8	0.27	1.6	2.3	0.055	0.42	0.93	0.49
41 – 59	0.0969	9.1	1.8	8.4	0.16	1.7	2.3	0.29	0.39	1.0	0.72
59 – 83	0.0305	7.8	2.9	6.4	0.32	1.7	2.3	0.49	0.67	1.2	1.1
83 – 118	0.00755	11.	4.8	8.7	0.46	1.9	2.3	0.83	0.74	0.83	1.7
118 – 168	0.00180	10.	8.2	3.6	0.40	1.8	2.4	0.83	0.52	1.3	3.0
168 – 250	0.000342	17.	14.	6.1	0.20	1.8	2.3	0.71	1.5	2.3	5.3

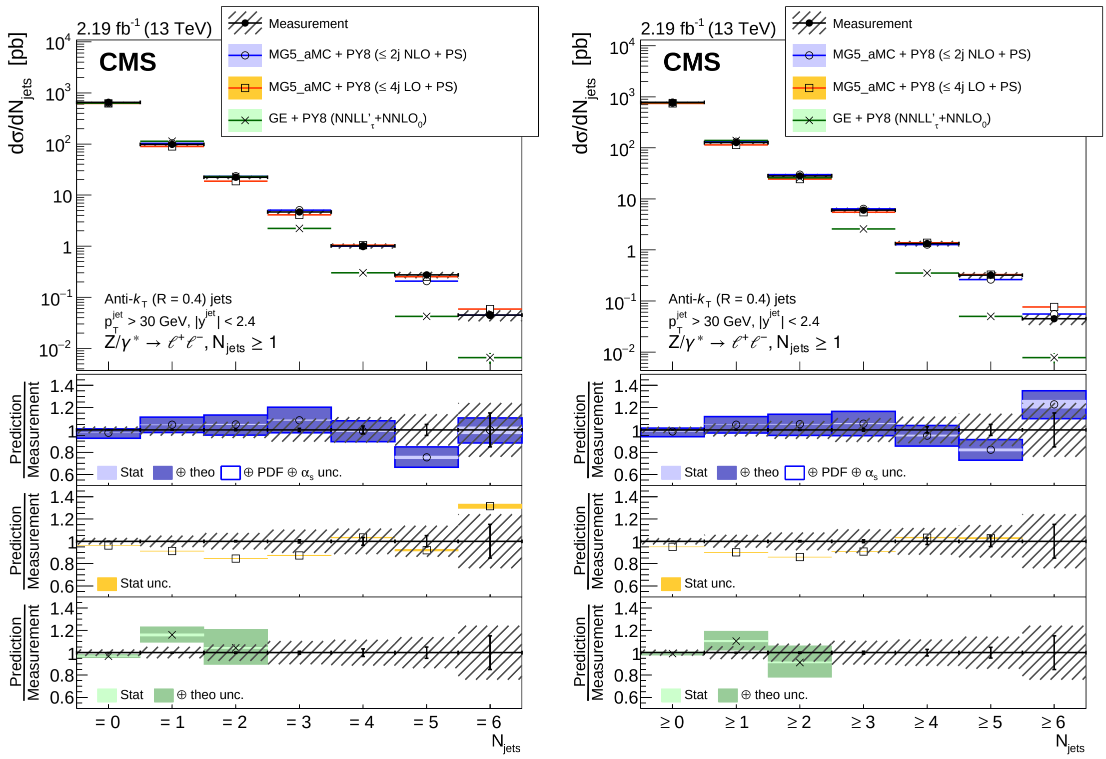

FIGURE 5.38: Measured cross section as a function of the jet exclusive (left) and inclusive (right) multiplicities up to 4 jets. The error bar stands for the statistical uncertainty, and the hatched band presents the total uncertainties. The light shade stands for the statistical uncertainty of predictions, and the darker shade present the total theoretical uncertainty.

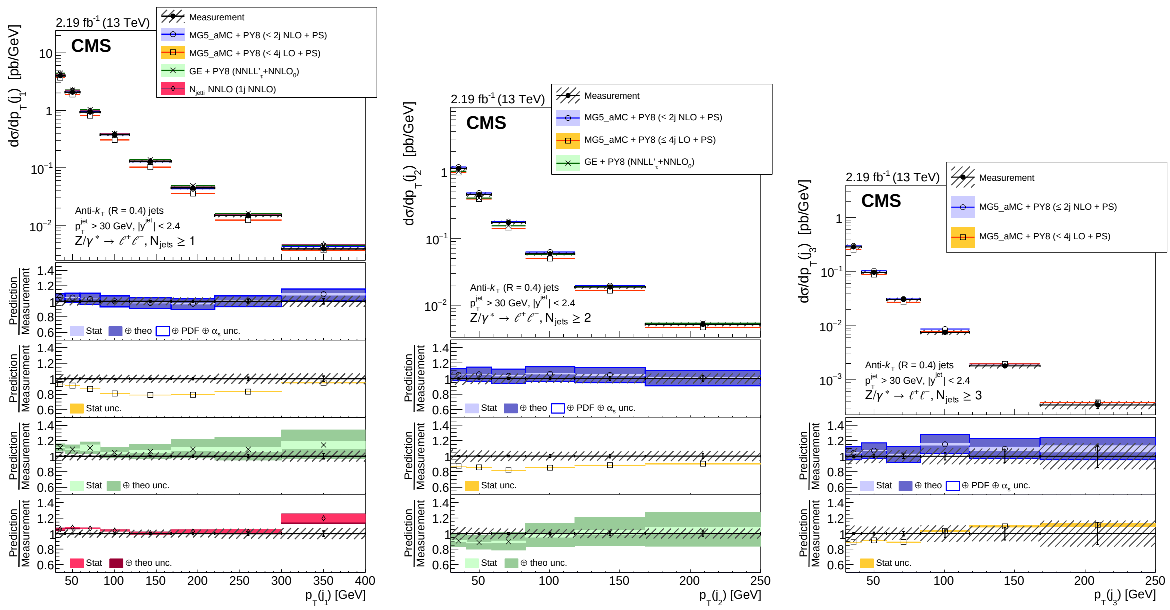

FIGURE 5.39: Measured cross section as a function of p_T of the first leading jet (left), second leading jet (middle) and third jet (right). The error bar stands for the statistical uncertainty, and the hatched band presents the total uncertainties. The light shade stands for the statistical uncertainty of predictions, and the darker shade present the total theoretical uncertainty.

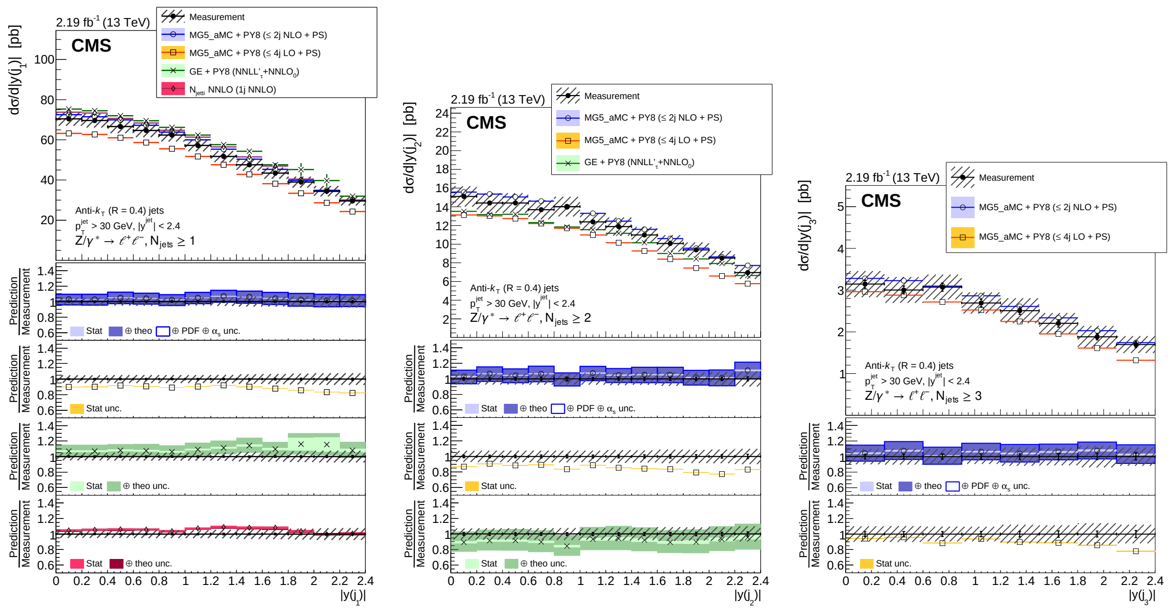

FIGURE 5.40: Measured cross section as a function of absolute rapidity of the first leading jet (left), second leading jet (middle) and third jet (right). The error bar stands for the statistical uncertainty, and the hatched band presents the total uncertainties. The light shade stands for the statistical uncertainty of predictions, and the darker shade present the total theoretical uncertainty.

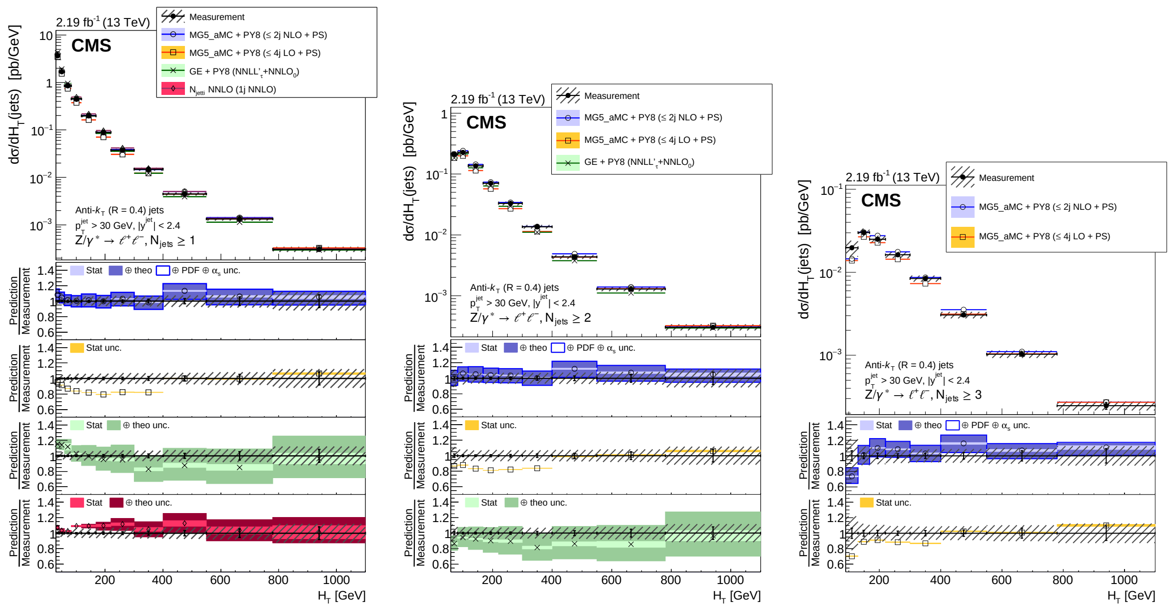

FIGURE 5.41: Measured cross section as a function of H_T of jets for the jet multiplicity $N_{jets} \geq 1$ (left), $N_{jets} \geq 2$ (middle) and $N_{jets} \geq 3$ (right). The error bar stands for the statistical uncertainty, and the hatched band presents the total uncertainties. The light shade stands for the statistical uncertainty of predictions, and the darker shade present the total theoretical uncertainty.

l

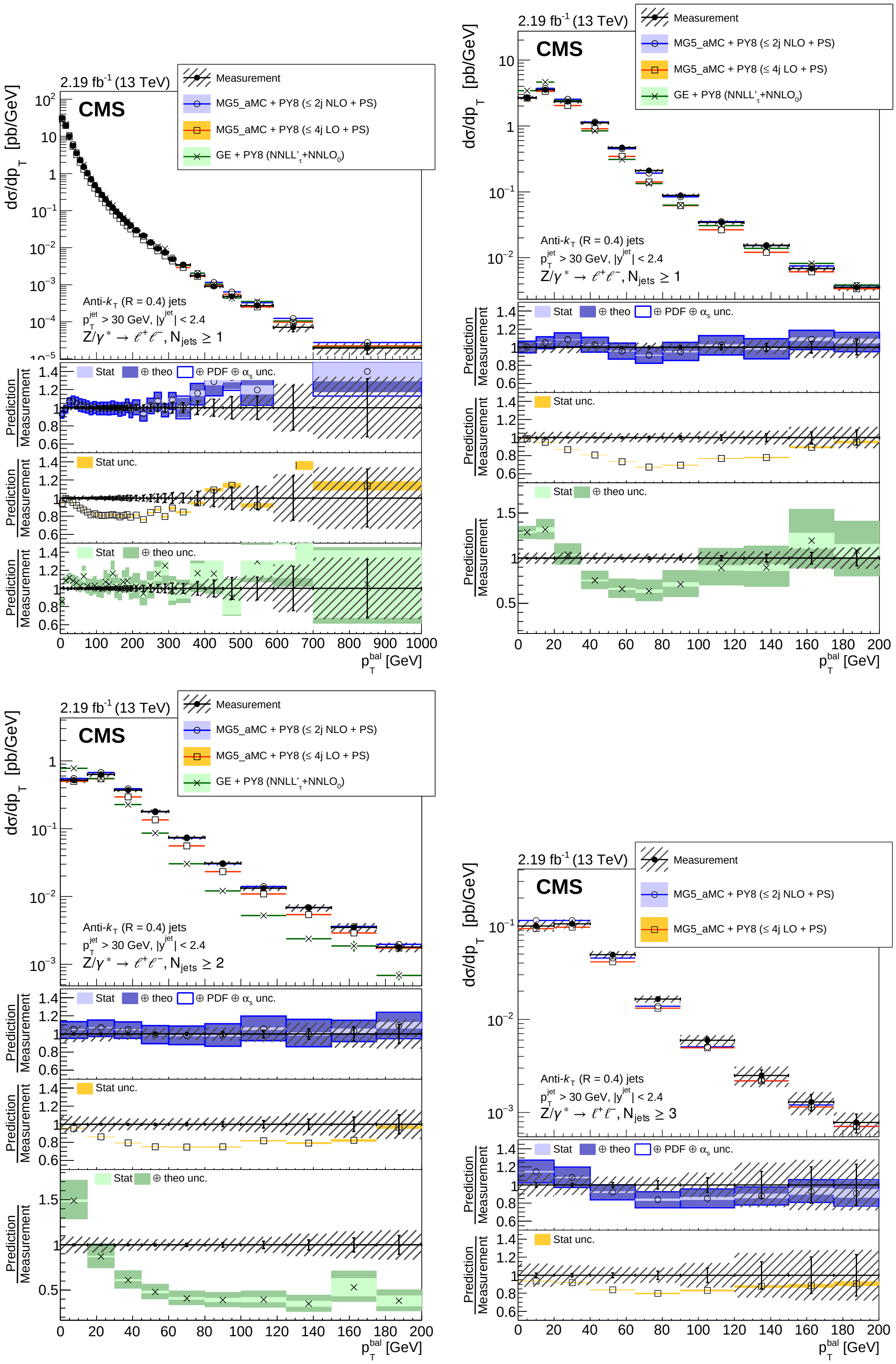

FIGURE 5.42: Measured cross section as a function of the transverse momentum balance between jets and the Z boson (p_{T}^{bal}) for the jet multiplicity $N_{jets} \geq 0$ (top left), $N_{jets} \geq 1$ (top right), $N_{jets} \geq 2$ (bottom left) and $N_{jets} \geq 3$ (bottom right). The error bar stands for the statistical uncertainty, and the hatched band presents the total uncertainties.

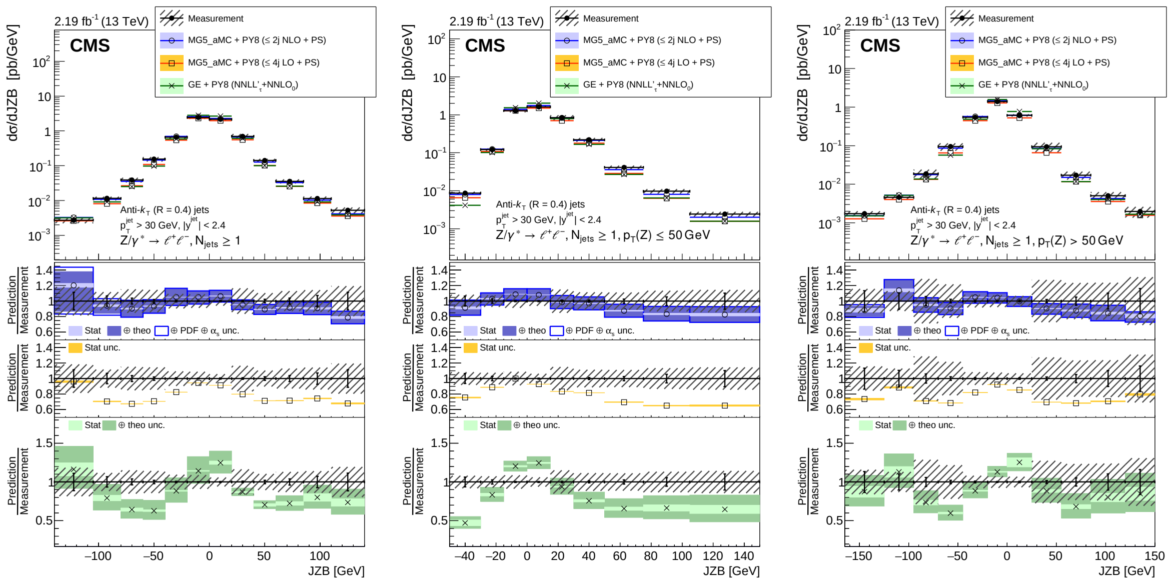

FIGURE 5.43: Measured cross section as a function of JZB variable (left), with extra cut p_T(Z)<50 GeV (middle) and p_T(Z)>50GeV (right). The error bar stands for the statistical uncertainty, and the hatched band presents the total uncertainties.

TABLE 5.18: Differential cross section in 1st jet $|\eta|$ ($N_{\text{jets}} \geq 1$) and break down of the systematic uncertainties for the combination of both decay channels.

$\lvert y(j_1)\rvert$	$\frac{d\sigma}{d\lvert y(j_1)\rvert}$ [pb]	Tot. Unc [%]	Stat [%]	JES [%]	JER [%]	Eff [%]	Lumi [%]	Bkg [%]	PU [%]	Unf model [%]	Unf stat [%]
0 − 0.2	70.4	4.9	0.70	3.9	0.075	1.5	2.3	0.016	0.23	0.11	0.25
0.2 − 0.4	69.6	4.9	0.72	4.0	0.084	1.5	2.3	0.016	0.28	0.14	0.26
0.4 − 0.6	66.7	5.0	0.73	4.1	0.12	1.5	2.3	0.015	0.18	0.14	0.26
0.6 − 0.8	64.6	5.2	0.72	4.3	0.17	1.6	2.3	0.014	0.30	0.15	0.26
0.8 − 1	62.4	5.1	0.77	4.2	0.071	1.5	2.3	0.013	0.19	0.17	0.28
1 − 1.2	57.2	5.1	0.82	4.2	0.19	1.5	2.3	0.012	0.29	0.24	0.29
1.2 − 1.4	51.7	5.4	0.88	4.5	0.17	1.5	2.3	0.0088	0.28	0.25	0.31
1.4 − 1.6	47.6	6.2	0.91	5.5	0.073	1.5	2.3	0.0057	0.31	0.31	0.32
1.6 − 1.8	43.5	6.5	0.94	5.7	0.22	1.5	2.3	0.0037	0.35	0.21	0.34
1.8 − 2	39.0	6.9	0.98	6.2	0.40	1.5	2.3	0.0031	0.41	0.32	0.35
2 − 2.2	34.4	7.5	1.1	6.8	0.47	1.5	2.3	0.0034	0.68	0.40	0.39
2.2 − 2.4	29.6	7.6	1.2	6.8	0.74	1.5	2.3	0.0079	0.75	0.35	0.44

TABLE 5.19: Differential cross section in 2nd jet $|\eta|$ ($N_{\text{jets}} \geq 2$) and break down of the systematic uncertainties for the combination of both decay channels.

$\lvert y(j_2)\rvert$	$\frac{d\sigma}{d\lvert y(j_2)\rvert}$ [pb]	Tot. Unc [%]	Stat [%]	JES [%]	JER [%]	Eff [%]	Lumi [%]	Bkg [%]	PU [%]	Unf model [%]	Unf stat [%]
0 − 0.2	15.1	7.2	1.6	6.4	0.099	1.6	2.3	0.081	0.31	0.26	0.62
0.2 − 0.4	14.4	7.3	1.7	6.5	0.046	1.6	2.3	0.085	0.15	0.33	0.63
0.4 − 0.6	14.4	7.4	1.7	6.5	0.14	1.6	2.3	0.076	0.41	0.35	0.64
0.6 − 0.8	13.7	7.5	1.8	6.6	0.27	1.6	2.3	0.072	0.34	0.27	0.68
0.8 − 1	14.0	7.5	1.8	6.7	0.15	1.6	2.3	0.065	0.12	0.092	0.71
1 − 1.2	12.38	7.4	1.9	6.5	0.11	1.6	2.3	0.066	0.35	0.13	0.71
1.2 − 1.4	11.88	8.2	1.8	7.4	0.093	1.6	2.3	0.062	0.24	0.10	0.68
1.4 − 1.6	10.99	7.7	2.0	6.9	0.16	1.6	2.3	0.050	0.55	0.11	0.76
1.6 − 1.8	10.07	8.8	2.1	8.0	0.26	1.6	2.3	0.046	0.51	0.19	0.78
1.8 − 2	9.39	8.4	2.2	7.5	0.35	1.6	2.3	0.039	0.70	0.44	0.84
2 − 2.2	8.52	8.8	2.2	8.0	0.51	1.6	2.3	0.030	0.57	0.65	0.84
2.2 − 2.4	6.96	9.8	2.6	8.8	0.47	1.6	2.3	0.029	1.1	1.2	0.95

TABLE 5.20: Differential cross section in 3rd jet $|\eta|$ ($N_{\text{jets}} \geq 3$) and break down of the systematic uncertainties for the combination of both decay channels.

$\lvert y(j_3)\rvert$	$\frac{d\sigma}{d\lvert y(j_3)\rvert}$ [pb]	Tot. Unc [%]	Stat [%]	JES [%]	JER [%]	Eff [%]	Lumi [%]	Bkg [%]	PU [%]	Unf model [%]	Unf stat [%]
0 − 0.3	3.14	9.9	3.1	8.9	0.27	1.7	2.3	0.28	0.31	0.15	1.1
0.3 − 0.6	3.00	10.	3.2	9.3	0.12	1.7	2.3	0.28	0.34	0.088	1.1
0.6 − 0.9	3.07	9.6	3.2	8.6	0.19	1.6	2.3	0.25	0.24	0.0072	1.2
0.9 − 1.2	2.69	9.4	3.3	8.2	0.19	1.7	2.3	0.25	0.27	0.33	1.2
1.2 − 1.5	2.51	12.	3.6	11.	0.19	1.6	2.3	0.23	0.21	0.79	1.3
1.5 − 1.8	2.20	11.	4.0	10.	0.16	1.6	2.3	0.22	0.14	0.63	1.4
1.8 − 2.1	1.88	14.	3.9	13.	0.14	1.7	2.3	0.22	1.3	1.8	1.4
2.1 − 2.4	1.70	12.	4.4	10.	0.73	1.7	2.3	0.20	1.1	2.4	1.6

TABLE 5.21: Differential cross section in H_{T} ($N_{\text{jets}} \geq 1$) and break down of the systematic uncertainties for the combination of both decay channels.

H_{T} [GeV]	$\frac{d\sigma}{dH_{\text{T}}}$ [$\frac{\text{pb}}{\text{GeV}}$]	Tot. Unc [%]	Stat [%]	JES [%]	JER [%]	Eff [%]	Lumi [%]	Bkg [%]	PU [%]	Unf model [%]	Unf stat [%]
30 − 41	3.66	6.2	0.68	5.4	0.21	1.5	2.3	0.018	0.40	0.92	0.20
41 − 59	1.684	4.6	0.60	3.5	0.15	1.5	2.3	0.0048	0.26	1.1	0.22
59 − 83	0.852	5.3	0.73	4.4	0.23	1.5	2.3	0.0054	0.29	0.64	0.28
83 − 118	0.449	6.1	0.78	5.3	0.12	1.6	2.3	0.015	0.35	0.55	0.31
118 − 168	0.198	5.9	0.98	5.1	0.20	1.6	2.3	0.040	0.17	0.40	0.40
168 − 220	0.0887	6.3	1.6	5.3	0.37	1.6	2.3	0.078	0.36	0.32	0.64
220 − 300	0.0373	6.9	1.7	6.0	0.095	1.7	2.3	0.14	0.20	0.17	0.68
300 − 400	0.0149	6.8	2.4	5.6	0.21	1.6	2.3	0.20	0.17	0.21	1.0
400 − 550	0.00448	7.4	3.3	5.7	0.21	1.8	2.3	0.36	0.64	0.29	1.3
550 − 780	0.00134	8.2	5.4	4.8	0.15	1.6	2.3	0.40	1.2	0.23	2.1
780 − 1100	0.000306	12.	8.2	7.5	0.22	1.8	2.3	0.59	0.70	0.56	3.2

TABLE 5.22: Differential cross section in H_{T} ($N_{\text{jets}} \geq 2$) and break down of the systematic uncertainties for the combination of both decay channels.

H_{T} [GeV]	$\frac{d\sigma}{dH_{\text{T}}}$ [$\frac{\text{pb}}{\text{GeV}}$]	Tot. Unc [%]	Stat [%]	JES [%]	JER [%]	Eff [%]	Lumi [%]	Bkg [%]	PU [%]	Unf model [%]	Unf stat [%]
60 − 83	0.212	11.	2.2	10.	0.27	1.5	2.3	0.093	0.67	0.96	0.68
83 − 118	0.227	7.9	1.1	7.2	0.12	1.6	2.3	0.063	0.45	0.63	0.42
118 − 168	0.1370	6.7	1.1	5.9	0.18	1.6	2.3	0.038	0.31	0.59	0.42
168 − 220	0.0705	7.3	1.4	6.5	0.29	1.6	2.3	0.11	0.36	0.31	0.57
220 − 300	0.0329	7.1	1.6	6.2	0.11	1.7	2.3	0.16	0.18	0.29	0.64
300 − 400	0.01360	6.8	2.2	5.7	0.20	1.6	2.3	0.22	0.33	0.29	0.90
400 − 550	0.00436	7.3	3.1	5.8	0.18	1.8	2.3	0.37	0.57	0.28	1.2
550 − 780	0.00129	8.1	5.1	5.1	0.17	1.6	2.3	0.41	1.1	0.21	1.9
780 − 1100	0.000304	12.	8.0	7.2	0.25	1.7	2.3	0.58	0.67	0.41	3.1

TABLE 5.23: Differential cross section in H_{T} ($N_{\text{jets}} \geq 3$) and break down of the systematic uncertainties for the combination of both decay channels.

H_{T} [GeV]	$\frac{d\sigma}{dH_{\text{T}}}$ [$\frac{\text{pb}}{\text{GeV}}$]	Tot. Unc [%]	Stat [%]	JES [%]	JER [%]	Eff [%]	Lumi [%]	Bkg [%]	PU [%]	Unf model [%]	Unf stat [%]
90 − 130	0.0198	22.	6.6	20.	1.0	1.5	2.3	0.19	0.99	5.2	2.2
130 − 168	0.0301	12.	3.7	11.	0.35	1.7	2.3	0.15	0.39	2.1	1.2
168 − 220	0.0250	11.	3.6	9.5	0.17	1.7	2.3	0.19	0.42	0.74	1.2
220 − 300	0.0162	9.2	2.7	8.2	0.29	1.7	2.3	0.29	0.20	0.73	1.0
300 − 400	0.00842	8.4	3.3	7.0	0.12	1.7	2.3	0.37	0.24	0.43	1.3
400 − 550	0.00306	8.8	4.1	7.0	0.22	1.8	2.3	0.55	0.73	0.40	1.5
550 − 780	0.00103	10.	6.5	6.7	0.34	1.7	2.3	0.54	1.1	0.22	2.5
780 − 1100	0.000246	13.	9.3	6.4	0.17	1.7	2.3	0.68	0.91	2.7	3.5

TABLE 5.24: Differential cross section in p_T^{bal} ($N_{\text{jets}} \geq 1$) and break down of the systematic uncertainties for the combination of both decay channels.

p_T^{bal} [GeV]	$\frac{d\sigma}{dp_T^{\text{bal}}}$ [$\frac{\text{pb}}{\text{GeV}}$]	Tot. Unc [%]	Stat [%]	JES [%]	JER [%]	Eff [%]	Lumi [%]	Bkg [%]	PU [%]	Unf model [%]	Unf stat [%]
0 – 10	2.67	6.1	0.54	5.3	0.54	1.5	2.3	0.010	0.48	1.1	0.17
10 – 20	3.53	6.2	0.42	5.4	0.34	1.5	2.3	0.013	0.41	1.2	0.14
20 – 35	2.34	6.4	0.43	5.2	0.32	1.6	2.3	0.012	0.32	2.3	0.15
35 – 50	1.116	6.0	0.60	4.0	0.75	1.6	2.3	0.027	0.30	3.2	0.23
50 – 65	0.469	4.8	0.88	2.9	0.82	1.7	2.3	0.058	0.10	2.1	0.36
65 – 80	0.210	5.0	1.3	0.80	0.87	1.9	2.3	0.18	0.35	3.5	0.54
80 – 100	0.0885	5.3	1.8	2.2	0.82	2.1	2.4	0.40	0.66	2.8	0.75
100 – 125	0.0344	6.9	2.8	3.0	0.67	2.2	2.4	0.64	0.44	4.2	1.1
125 – 150	0.0155	7.6	4.2	4.4	0.58	2.1	2.4	0.71	0.55	2.5	1.6
150 – 175	0.00685	12.	6.3	7.8	0.23	2.2	2.4	0.78	0.68	4.5	2.3
175 – 200	0.00356	12.	8.3	5.2	0.84	2.3	2.5	0.73	0.53	4.7	2.9

TABLE 5.25: Differential cross section in p_T^{bal} ($N_{\text{jets}} \geq 2$) and break down of the systematic uncertainties for the combination of both decay channels.

p_T^{bal} [GeV]	$\frac{d\sigma}{dp_T^{\text{bal}}}$ [$\frac{\text{pb}}{\text{GeV}}$]	Tot. Unc [%]	Stat [%]	JES [%]	JER [%]	Eff [%]	Lumi [%]	Bkg [%]	PU [%]	Unf model [%]	Unf stat [%]
0 – 15	0.522	9.0	0.87	8.5	0.51	1.5	2.3	0.048	0.59	0.39	0.32
15 – 30	0.632	8.2	0.68	7.6	0.36	1.5	2.3	0.031	0.49	0.97	0.26
30 – 45	0.371	6.4	0.89	5.5	0.43	1.6	2.3	0.054	0.37	1.4	0.35
45 – 60	0.179	6.2	1.2	5.1	1.0	1.6	2.3	0.14	0.23	0.87	0.47
60 – 80	0.0743	6.6	1.6	4.7	1.3	1.9	2.3	0.38	0.33	2.6	0.60
80 – 100	0.0310	7.3	2.5	5.0	1.4	2.3	2.4	0.82	0.38	2.7	0.91
100 – 125	0.0133	8.8	4.1	5.2	1.4	2.3	2.4	1.2	0.66	4.0	1.4
125 – 150	0.00684	12.	5.6	9.2	1.0	2.6	2.4	1.4	0.63	4.2	1.9
150 – 175	0.00352	15.	7.9	11.	0.16	2.6	2.4	1.5	0.20	5.3	2.6
175 – 200	0.00179	16.	10.	11.	0.43	2.3	2.5	1.3	0.83	4.2	3.1

TABLE 5.26: Differential cross section in p_T^{bal} ($N_{\text{jets}} \geq 3$) and break down of the systematic uncertainties for the combination of both decay channels.

p_T^{bal} [GeV]	$\frac{d\sigma}{dp_T^{\text{bal}}}$ [$\frac{\text{pb}}{\text{GeV}}$]	Tot. Unc [%]	Stat [%]	JES [%]	JER [%]	Eff [%]	Lumi [%]	Bkg [%]	PU [%]	Unf model [%]	Unf stat [%]
0 – 20	0.100	13.	2.3	11.	0.92	1.5	2.3	0.13	0.65	4.4	0.79
20 – 40	0.106	11.	1.8	10.	0.75	1.6	2.3	0.14	0.33	2.8	0.66
40 – 65	0.0492	9.2	2.6	7.5	1.4	1.7	2.3	0.35	0.36	3.0	1.0
65 – 90	0.0165	8.5	4.6	4.1	1.6	2.2	2.4	1.3	0.22	4.1	1.7
90 – 120	0.00595	14.	8.1	8.1	2.1	2.4	2.4	2.3	0.67	4.6	2.9
120 – 150	0.00250	25.	15.	17.	0.91	2.7	2.4	3.2	1.7	6.8	5.0
150 – 175	0.00130	28.	20.	16.	1.5	2.7	2.4	3.2	2.2	4.3	6.9
175 – 200	0.00078	28.	23.	9.7	2.2	2.9	2.5	3.4	0.89	8.6	8.0

TABLE 5.27: Differential cross section in JZB ($N_{\text{jets}} \geq 1$) and break down of the systematic uncertainties for the combination of both decay channels.

JZB [GeV]	$\frac{d\sigma}{d\text{JZB}}$ [$\frac{\text{pb}}{\text{GeV}}$]	Tot. Unc [%]	Stat [%]	JES [%]	JER [%]	Eff [%]	Lumi [%]	Bkg [%]	PU [%]	Unf model [%]	Unf stat [%]
−200 − −165	0.00033	40.	32.	14.	2.4	1.6	2.5	0.28	0.86	13.	15.
−165 − −140	0.00061	32.	24.	13.	1.6	1.6	2.5	0.40	3.9	8.6	10.
−140 − −105	0.00272	18.	11.	11.	1.4	1.6	2.4	0.11	1.6	6.6	4.8
−105 − −80	0.0115	12.	6.7	7.6	0.70	1.7	2.4	0.13	0.70	2.5	2.9
−80 − −60	0.0391	15.	3.8	12.	0.75	1.7	2.4	0.063	0.84	5.9	1.7
−60 − −40	0.154	14.	2.2	12.	0.79	1.7	2.3	0.049	0.59	6.9	0.90
−40 − −20	0.658	9.4	1.0	6.8	1.5	1.7	2.3	0.015	0.53	5.1	0.39
−20 − 0	2.45	8.8	0.48	7.7	0.62	1.6	2.3	0.0050	0.48	2.9	0.17
0 − 20	2.15	5.7	0.70	4.5	0.74	2.1	2.3	0.0065	0.17	1.3	0.24
20 − 40	0.70	16.	1.0	15.	1.7	1.6	2.3	0.033	0.41	5.4	0.38
40 − 60	0.142	10.	2.3	8.5	1.3	1.8	2.3	0.19	0.27	4.1	0.93
60 − 85	0.0356	13.	3.9	11.	1.9	1.9	2.4	0.55	1.0	2.7	1.6
85 − 110	0.0114	14.	7.3	9.1	0.83	2.1	2.4	0.94	2.0	5.8	3.0
110 − 140	0.0053	19.	11.	12.	0.64	2.4	2.5	1.1	1.5	7.9	4.4
140 − 165	0.00138	44.	23.	26.	0.83	2.7	2.7	2.0	4.8	24.	9.0
165 − 200	0.00031	54.	43.	19.	2.0	3.6	3.1	3.8	2.9	21.	15.

TABLE 5.28: Differential cross section in JZB with extra cut p_{T}(Z)<50 GeV and break down of the systematic uncertainties for the combination of both decay channels.

JZB [GeV]	$\frac{d\sigma}{d\text{JZB}}$ [$\frac{\text{pb}}{\text{GeV}}$]	Tot. Unc [%]	Stat [%]	JES [%]	JER [%]	Eff [%]	Lumi [%]	Bkg [%]	PU [%]	Unf model [%]	Unf stat [%]
−50 − −30	0.00871	8.1	6.4	1.1	1.2	1.8	2.3	0.047	0.94	2.4	2.6
−30 − −15	0.1217	7.4	2.8	4.2	4.0	2.3	2.3	0.073	0.25	1.2	0.99
−15 − 0	1.29	8.7	0.71	7.6	0.30	1.6	2.3	0.0086	0.63	3.0	0.23
0 − 15	1.625	6.1	0.66	5.0	0.68	2.0	2.3	0.015	0.25	1.3	0.21
15 − 30	0.84	15.	0.84	14.	1.5	1.6	2.3	0.017	0.35	3.4	0.29
30 − 50	0.220	11.	1.3	11.	1.4	1.6	2.3	0.041	0.093	1.2	0.50
50 − 75	0.0412	11.	2.7	9.0	1.4	1.8	2.3	0.31	0.42	4.5	1.1
75 − 105	0.0097	13.	5.5	9.5	0.61	2.4	2.4	0.92	1.1	6.1	2.2
105 − 150	0.00242	14.	10.	6.2	1.4	2.4	2.4	1.3	0.89	5.1	3.8
150 − 200	0.00024	43.	38.	16.	1.2	3.1	2.7	2.8	0.47	7.1	10.

TABLE 5.29: Differential cross section in JZB with extra cut p_{T}(Z)≥50 GeV and break down of the systematic uncertainties for the combination of both decay channels.

JZB [GeV]	$\frac{d\sigma}{d\text{JZB}}$ [$\frac{\text{pb}}{\text{GeV}}$]	Tot. Unc [%]	Stat [%]	JES [%]	JER [%]	Eff [%]	Lumi [%]	Bkg [%]	PU [%]	Unf model [%]	Unf stat [%]
−165 − −125	0.00173	16.	13.	2.9	0.44	1.7	2.4	0.23	1.6	3.4	4.8
−125 − −95	0.00456	13.	10.	4.1	2.1	1.9	2.4	0.22	0.59	2.0	3.5
−95 − −70	0.0187	29.	5.9	25.	1.0	1.9	2.4	0.17	0.54	5.3	2.1
−70 − −45	0.095	22.	2.3	20.	0.52	1.7	2.4	0.071	0.38	3.4	0.77
−45 − −20	0.546	8.2	1.1	4.7	1.1	1.7	2.3	0.028	0.22	1.1	0.35
−20 − 0	1.39	7.6	0.61	6.9	0.20	1.5	2.3	0.016	0.48	0.33	0.18
0 − 25	0.613	6.8	0.99	5.6	1.4	2.1	2.3	0.045	0.37	1.1	0.30
25 − 55	0.094	27.	2.0	26.	3.5	1.7	2.3	0.20	0.62	3.5	0.68
55 − 85	0.0172	23.	5.3	19.	3.5	2.2	2.4	0.76	1.5	10.	1.8
85 − 120	0.0050	24.	10.	18.	4.0	2.2	2.5	1.2	2.4	8.6	3.6
120 − 150	0.00197	31.	16.	19.	1.2	2.6	2.7	1.8	2.7	16.	5.5

5.11 Conclusions

The results in this chapter are the measured differential cross sections for the production of a Z boson in association jets, where the Z boson decays into two charged leptons with $p_{\mathrm{T}} > 20GeV$ and $|\eta| < 2.4$. The data recorded with the CMS detector at the LHC during 2015 proton-proton collision, at a center-of-mass energy of 13 TeV, corresponds to an integrated luminosity of 2.19 fb^{-1} These cross section measurements provides stringent tests of perturbative QCD. The production of Z + jets is also an important background for a number of SM processes, such as top quark production, Higgs boson production, vector boson fusion and WW scattering, as well as many searches for physics beyond the SM.

The cross section has been measured as functions of the exclusive and inclusive jet multiplicities up to 6, of the transverse momentum p_{T} of the Z boson, jet kinematic variables including jet p_{T} , the jet rapidity (y) and the scalar sum of the jet transverse momenta (H_{T}) for $N_{jets} \geq 1$,2 and 3. The transverse momentum balance between the jets and the Z boson (p_{T}^{bal}) and the JZB variables. Jets with $p_{\mathrm{T}} > 30GeV$ and $|\eta| < 2.4$ are used in the definition of the different jet quantities.

The present results are compared to four different calculations: two predictions obtained from MG5_AMC interfaced with PYTHIA8, with one includes ME calculations at LO for up to four partons and the other includes ME calculations at NLO for up to two partons, a third with a combination of NNLO calculation with NNLL resummation based on GENEVA, and the fourth a fixed order NNLO calculation of Z and one jet. The first three calculations include parton showering based on PYTHIA8.

The measurements are in good agreement with the results of the NLO multiparton calculation. Even the measurements for events with more than 2 jets agree within the $\approx 10\%$ measurement and 10% theoretical uncertainties, although this part of the calculation is only LO. The multiparton LO prediction does not described well the measurement. The transverse momentum balance between the Z boson and the hadronic recoil, which is expected to be sensitive to soft-gluon radiation, has been measured for the first time at the LHC. The multiparton LO prediction fails to described the measurement while the The multiparton NLO prediction provides a very good description for jet multiplicities computed with NLO accuracy.

The NNLO+NNLL predictions provide similar agreement for the measurement of the variable of two leading jets, but fail to describe more jets. At the low p_{T} of the Z boson, the NLO prediction provides a better description than the NNLO+NNLL calculation, however a similar description is observed for both calculations at high transverse momentum.

The results suggest using multiparton NLO predictions for the estimation of the Z+ jets contribution at the LHC in measurements and searches, and its associated uncertainty.

Chapter 6

Conclusion

LHC is the current most powerful particle collider on Earth, which provides excellent environment for the study of the high energy physics. After the first period of data-taking, the Higgs has been discoveried in 2012, confirming the existence of Brout-Englert-Higgs mechanism. As a powerful hadron collider, LHC also provides nice chances to study in details the productions of vector bosons, the Higgs boson and heavy quarks (b, t) produced from interactions between partons contained in the protons of the beams.

In this thesis the first measurement of the differential cross section of Z boson production in association with jets in p-p collisions at 13 TeV has been presented. The data recorded by the CMS detector during 2015, corresponding to the integrated luminosity of 2.19 fb^{-1}, has been analysed. The measurements of Z boson plus jets processes are very important and crucial for deep understanding and modeling of QCD interactions. In particular, the process of Z plus jets offers an ideal condition for the study of hadronic jet production and gluon radiation in general. Moreover, this process is also an important background for a number of SM processes and beyond SM searches. A precise knowledge of the kinematic dependencies of processes with jets up to large jet multiplicity is essential to exploit the potential of the LHC experiments. Comparison of the measurements with different predictions motivates the developments of the MC generator and improves the understanding of the prediction uncertainties.

The differential cross section is measured as a function of Z transverse momentum p_{T}, jet multiplicities, jet transverse momentum, jet rapidity, jet H_T, p_{T} balance and JZB. The measurements of Z boson plus jets processes have been compared with four type of theoretical predictions at LO, NLO, NNLO accurancy with different MC generators:

- MG5_AMC interfaced with PYTHIA8 with LO MEs calculations for up to four partons.
- MG5_AMC@NLO interfaced with PYTHIA8 using NLO ME calculations for up to two partons.
- NNLO calculations for Z+1 jet using the N-jettiness subtraction scheme.
- GENEVA with NNLO calculation for Drell-Yan production combined with higher-order gluon resummation.

We present the first comparison of combined higher order resummation of GENEVA to the measurements. In the measurement of the cross sections as a function of jet multiplicities up to 3, jet p_{T} and rapidity of the 1^{st}, 2^{nd} and 3^{rd} leading jet, and jet H_T, LO MG5_AMC prediction is in agreement with measurements within uncertainties, while MG5_AMC@NLO provides better descriptions of the measurements. However, agreement between GENEVA calculation and measurements is observed in the same variables for jet multiplicities only up to two jets. This is consistent with the fact that GENEVA prediction includes 2 partons at LO ME calculations, and the third parton coming from the parton showering. On the case of p_{T}(Z) for inclusive and at least one jet processes, MG5_AMC@NLO is the best model for describing the measurement at low p_{T}, better than GENEVA. For the distributions of the measurement as a function of p_{T} balance between hadron recoil and Z boson (p_{T} balance and JZB), the LO MG5_AMC and GENEVA predictions do not fully describe the data, while the MG5_-AMC@NLO prediction provides a good descriptions. For the distributions of the jet transverse momenta for the 1^{st}, 2^{nd} and 3^{rd} leading jet, the LO MG5_AMC predicted spectrum differs from the measurement, showing a steeper slope in the low p_{T} region. While the comparison with NLO MG5_AMC and $\mathrm{N_{jetti}}$ NNLO calculations show that adding NLO terms cures this discrepancy.

Even though GENEVA has not provided better descriptions of the measurements compared to NLO MG5_AMC, GENEVA probably shows the way to follow in the future. The worse description of GENEVA could be due to a reduced work on tuning of PYTHIA to data. But GENEVA combines, for the first time in a MC, NNLO ME calculation and higher order gluon resummations. It means that the tuned parameters in PYTHIA should have a reduced importance.

The differential cross section of Z boson production in association with jets has been measured with 7 TeV and 8 TeV data collected in the CMS experiment [69, 70]. The analysis presented in the thesis is the first time where the Z+jets process is measured at 13 TeV in CMS experiment. It is also the first time to use GENEVA prediction for comparison, and look at p_{T} balance, JZB variables in CMS experiment. We expect probably 150 fb^{-1} data at 13 TeV after the whole Run2 period until end of this year, then it is possible to measure the Z+jets process with more jet, and also measure the 2D differential cross section of Z+jets.

In summary, the predictions the NLO multiparton calculation by MG5_AMC@NLO interfaced with PYTHIA8 gives better descriptions. The prediction of GENEVA shows good agreement with measurement with accurancy at NLO ($N_{jets} \geq 1$), while for LO accurancy it still needs to be improved. The measurement results suggest to use multiparton NLO predictions for the estimation of the Z + jets at CMS in the SM measurement and searches, along with its associated uncertainties.

Appendix A

Muon HLT Efficiency Study

A.1 Introduction

To precisely measure different observables in the frame of the Standard Model and in search for new physics, the identification and precise energy measurement of muons, electrons, photons, and jets over a large energy range and at high luminosities are essential. Detecting muons is one of CMS's most important tasks as its name "Compact Muon Solenoid". Therefore, it is crucial to study and understand well the behaviour of the detected muons and in particular its efficiency.

The muon candidates used for the present analysis are selected from the particle flow collection, and have passed particular High Level Trigger (HLT) paths. We need to understand the HLT muon trigger behaviour and compute HLT muon trigger efficiency in order to correct for experimental effects.

In this chapter we introduce the HLT trigger, the muon efficiency computing methods, the double muon leg efficiency study, luminosity re-weight, and the double muon path efficiency study. The considered double muon triggers paths are:

- `HLT_Mu17_TrkIsoVVL_Mu8_TrkIsoVVL` (pre-scaled)
- `HLT_Mu17_TrkIsoVVL_TkMu8_TrkIsoVVL` (pre-scaled)
- `HLT_Mu17_TrkIsoVVL_Mu8_TrkIsoVVL_DZ`
- `HLT_Mu17_TrkIsoVVL_TkMu8_TrkIsoVVL_DZ`

A.1.1 HLT muon trigger

HLT muon trigger path consists of two different chains: one is the HLT muon reconstruction chain and another is the HLT filter logic. HLT muon reconstruction chain is the common segment for all the trigger paths including muons. This guarantees to use only one kind of reconstruction producer, which is independent of the amounts of HLT trigger paths. Even though, only one muon candidate subset might be revelant for a trigger path, all the path of muons (up to 4) must pass through the same initial filter in the reconstruction chain. This filter is applied on the Level-1 gobal muon trigger. It is vitally important to guarantee that all the trigger paths use the same collections. This enormouly simplifies the logic and facilitates the addition of new trigger paths.

HLT muon reconstruction chain consists of the following steps:

- Convert the parameters of Level-1 (L1) muon candidates into the seeds for the standalone muon reconstruction: RecoMuon/L2MuonSeedGenerator.
- The Level-2 (L2) muon reconstruction: RecoMuon/L2MuonProducer.
- Involve the calorimetric isolation in the L2 candidates: RecoMuon/ L2MuonIsolationProducer.
- The global muon reconstruction (Level-3 muon reconstruction), using the L2 muon candidates as seeds, is the regional reconstruction in the CMS tracker: RecoMuon/L3MuonProducer.
- Tracker isolation for L3 candidates: RecoMuon/L3MuonIsolationProducer.

The trigger filters can be interleaved with the previous reconstruction code, and they are specific for each trigger path. The trigger filters aims to stop the trigger sequence for those muon candidates which fail to the conditions provided via the configuration files, and provide a reduced list of candidates as output. Here, we use single muon trigger path with isolation sequence proceeds as example: L1 filter (filter the L1 candidates according to their quality, pT, $\cdots$); L1 seeds for L2, and L2 reonstruction; Filter on L2 output; Calorimetric isolation; L2 isolation filter; L3 reconstruction; Filter on L3 output; Track isolation; L3 isolation filter. Trigger workflow is shown in the figure A.1.

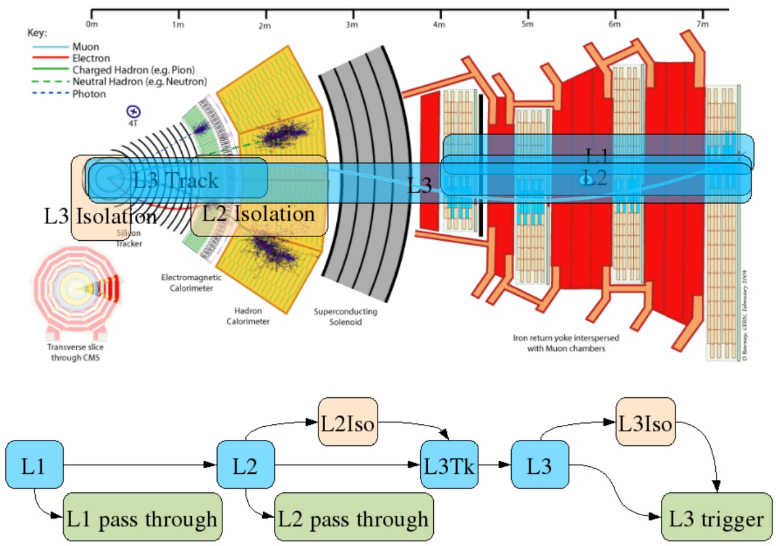

FIGURE A.1: Trigger workflow

A.1.2 Computing methods

There are a few methods to compute the muon trigger efficiency, for example the Tag and Probe (TnP) method, the component method, the reference-trigger method, and ortogonal trigger method. TnP and reference trigger methods are used here to compute the muon efficiency.

Tag and Probe is a generic method to measure any defined object efficiency from data on narrow di-lepton resonances like Z boson or J/ψ. The "tag" is required to pass a series of tight selections designed to obtain the desired particle type. The "tag" is usually referred to as "golden" electrons or muons, and the fake rate of selections should be negligible ($\ll 1\%$). The "probe" often with desired selections is picked by pairing these objects with tags such that the invariant mass of the combination is consistent with the mass of the resonance. The efficiency is measured by counting the number of the "probe" particles that pass the desired selection criteria:

$$\varepsilon = \frac{P_{pass}}{P_{all}} \tag{A.1}$$

The reference-trigger is a powerful method to measure the effiency of complex trigger paths, such as double muon trigger, combination of triggers. This method starts by choosing the reference trigger and computing its efficiency ϵ_{ref}. Then, obtain the complex efficiency after passing the reference trigger $\epsilon_{\text{complex}\,|\,\text{ref}}$. Finally, estimate the complex trigger efficiency regardless of the reference trigger $\epsilon_{\text{complex}} = \epsilon_{\text{complex}\,|\,\text{ref}} \times \epsilon_{\text{ref}}$. The chosen reference trigger should have a high efficiency on the events passing the complex trigger paths in order not to bias the result.

A.2 Feasibility study of a dZ Filter

The HLT doube muon trigger paths with dZ filter are often used for the analysis involved with the leptonic decay of Z vector boson since they are non-prescaled. The dZ refers to $\langle d_z \rangle$, the relative difference Δz of z-coordinate of the vertex position of the muons. The dZ filter consists of applying a cut on $\langle d_z \rangle$: $\langle d_z \rangle < 0.2$ cm. The dZ filter is applied in the HLT trigger path to ensure that the two muons originate from the same vertex. But, the dZ filter could cause the trigger inefficiency due to suboptimal tracking in HLT. To see if such a dZ filter could be applied to double muon HLT, we estimated the dZ filter inefficiency with data collected in 2015 to predict the situation for 2016 before the collision starts in 2016.

The HLT doube muon trigger paths with dZ filter mentioned in this section are:

- `HLT_Mu17_TrkIsoVVL_Mu8_TrkIsoVVL_DZ`
- `HLT_Mu17_TrkIsoVVL_TkMu8_TrkIsoVVL_DZ`

The dZ filter study is based on $\sqrt{s} = 13$ TeV proton-proton collision collected by CMS detector during 2015 with 25ns bunch crossing. The integrated luminosity for data is 2.1 fb^{-1}. The Monte Carlo(MC) sample DYJetsToLL_M-50 is used for the study. Here two isolated muons are selected with $p_T > 20$ GeV, $|\eta| \leq 2.4$, and the invariant mass of two muon are in the 91 ± 20 GeV window.

We look at the dZ filter efficiency as a function of the pile-up and of $p_{\mathrm{T}}(Z)$ for data and MC as shown in the figure A.2. The dZ filter global efficiency in data is 9% lower than in the MC. The dZ inefficiency increases when the pile-up increases, while for MC it's more flat. We also obtain the dZ efficiency as a function of η, the inefficiency is higher in the large η area (figure A.3). The variable $p_{\mathrm{T}}(Z)$ has dependence on jet multiplicity, especially for DY process: at low $p_{\mathrm{T}}(Z)$, the Z+0jet dominates, at high $p_{\mathrm{T}}(Z)$, the Z plus several jets process are dominant. It seems no dependence on $p_{\mathrm{T}}(Z)$.

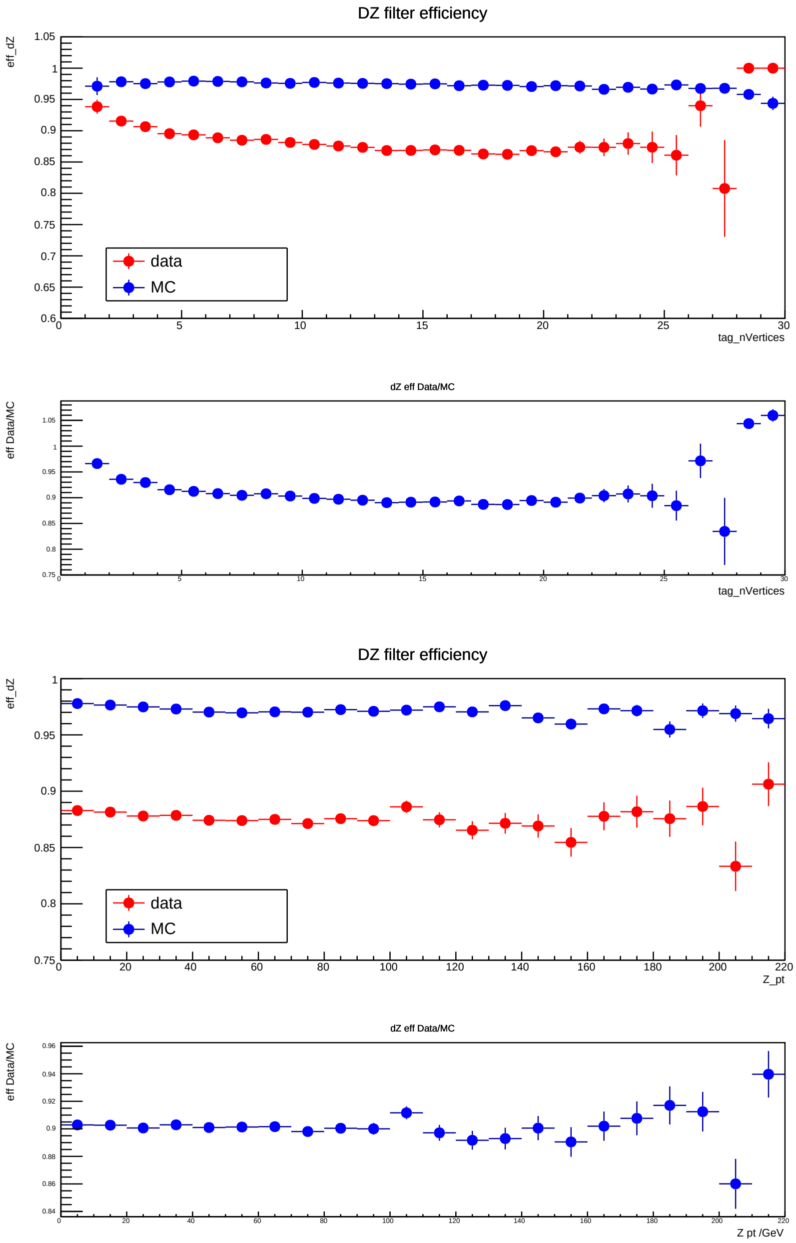

FIGURE A.2: The dZ filter efficiency as a function of the pile-up (left) and $p_{\mathrm{T}}(Z)$ (right) obtained from data and MC

The correlations with instaneous the luminosity and with bunch crossing number (from run 259809 to 259891) are also interesting (figure A.4). The dZ filter efficiency decreases at high luminosity, and also shows dependence on the bunch crossing number. At high luminosity, there is more pile-up and the tracker HIPs (Hit and Impact Point) is sub-optimal, as a consequence, the dZ filter has a lower efficiency. When we look at the

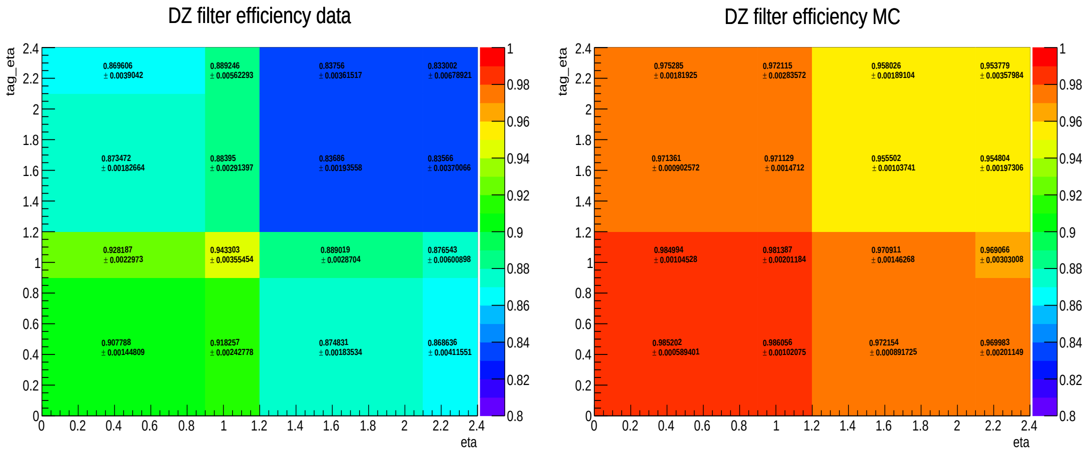

FIGURE A.3: The dZ filter efficiency as a function of η of two muons obtained from data (left) and MC (right)

dZ filter efficiency as a function of bunch crossing (bx) from run 259809 to 259891, the efficiency is higher in the beginning of each train, decreases inside the train, and after the empty bx in the begin of next train the efficiency goes back again. This is because of the charge accumulation.

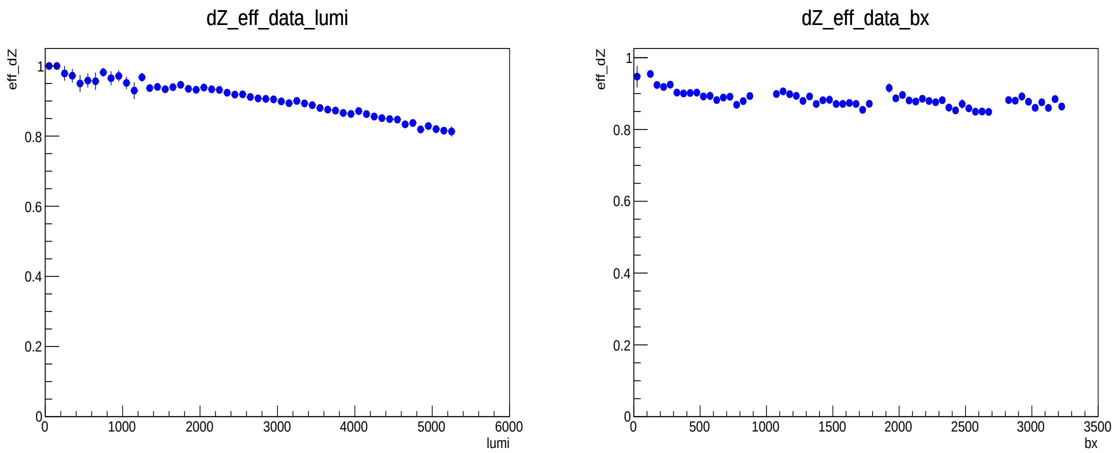

FIGURE A.4: The dZ filter efficiency as a function of luminosity (left) and bunch crossing number (right) in data. Bunch crossing distribution is from run 259809 to 259891.

In order to improve the dZ efficiency, we think to remove the Strip cluster charge cut (CCC). The original CCC cut is a loose one (> 1620). Here, we also compare the loose cut with tiny cut (> 800) or no CCC cut. After the modification, we also check the effect on dZ filter efficiency as function of pile-up, $p_T(Z)$, instaneous luminosity and bunch crossing number. The results are shown in the figures A.5, A.6 and A.7. If we reduce the CCC cut or don't apply the CCC cut, the dZ filter efficiency becomes higher. After this series of dZ filter study, the Muon POG decided to remove the CCC cut for the dZ filter.

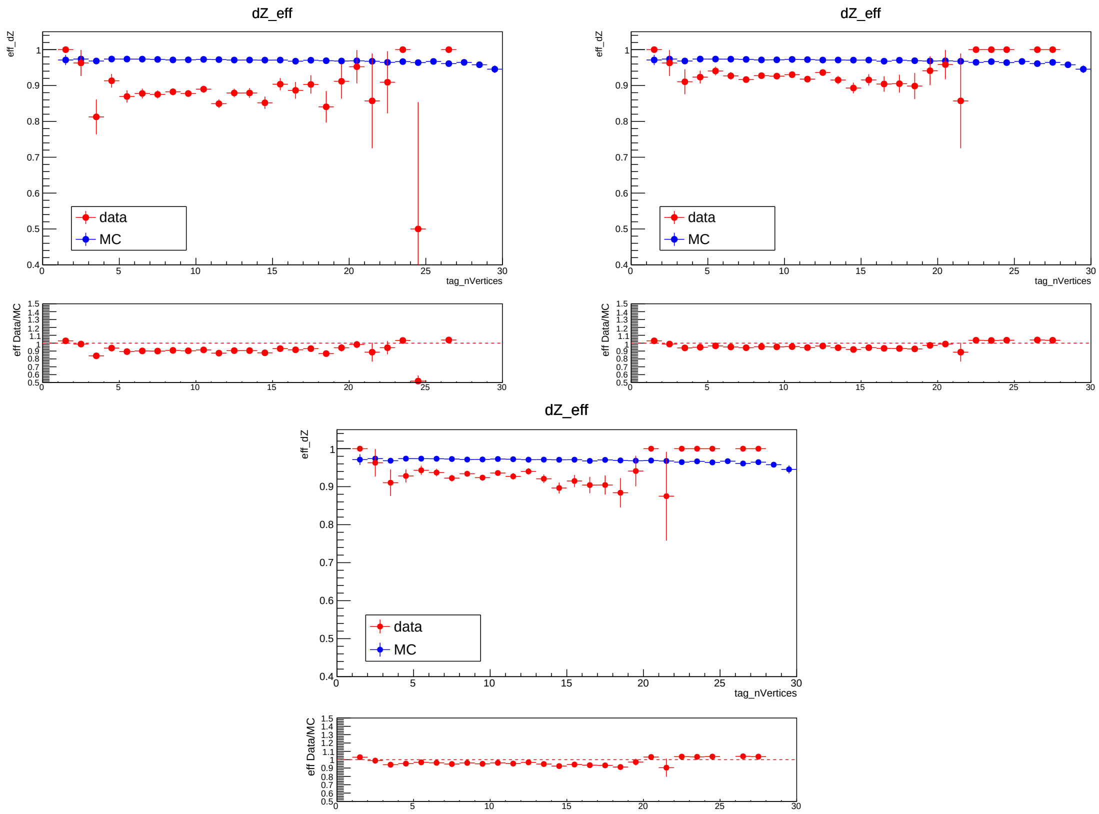

FIGURE A.5: The dZ filter efficiency with original CCC cut (top left), tiny CCC cut (top right) and no CCC cut (bottom) as a function of pile-up

A.3 HLT Double Muon Trigger in 2016 data

HLT double muon trigger is widely used in many physics analyses, and is also used to provide a data sample used to understand detector response and resolution. It is vital to study and fully understand HLT double muon trigger during the data taking, and afterwards obtain the HLT double muon trigger efficiency and scale factor.

We quickly looked into the data immediately after we got the first version of dataset, because there were two issues spotted and quickly fixed in the muon detector in early 2016:

- inefficiency in the central barrel ($|\eta| \leq 0.2$).
- inefficiency in overlap regions($0.9 \leq |\eta| \leq 1.2$).

The first issue was understood as coming from a swap of L1 BMTF (Barrel Muon Tracker Finder) η in central muon wheel, which affect both L3 and tracker muon reconstruction. A fix deployed at L1 from run 273423 on. The first 90 pb^{-1} were affected. The second issue was a bug in matching between L2 seed and the L1 candidate produced by the OMTF(Overlep Muon Tracker Finder). This only affect the L3 muon reconstruction, and has been fixed at HLT from run 274094 on. 500 pb^{-1} of data were affected.

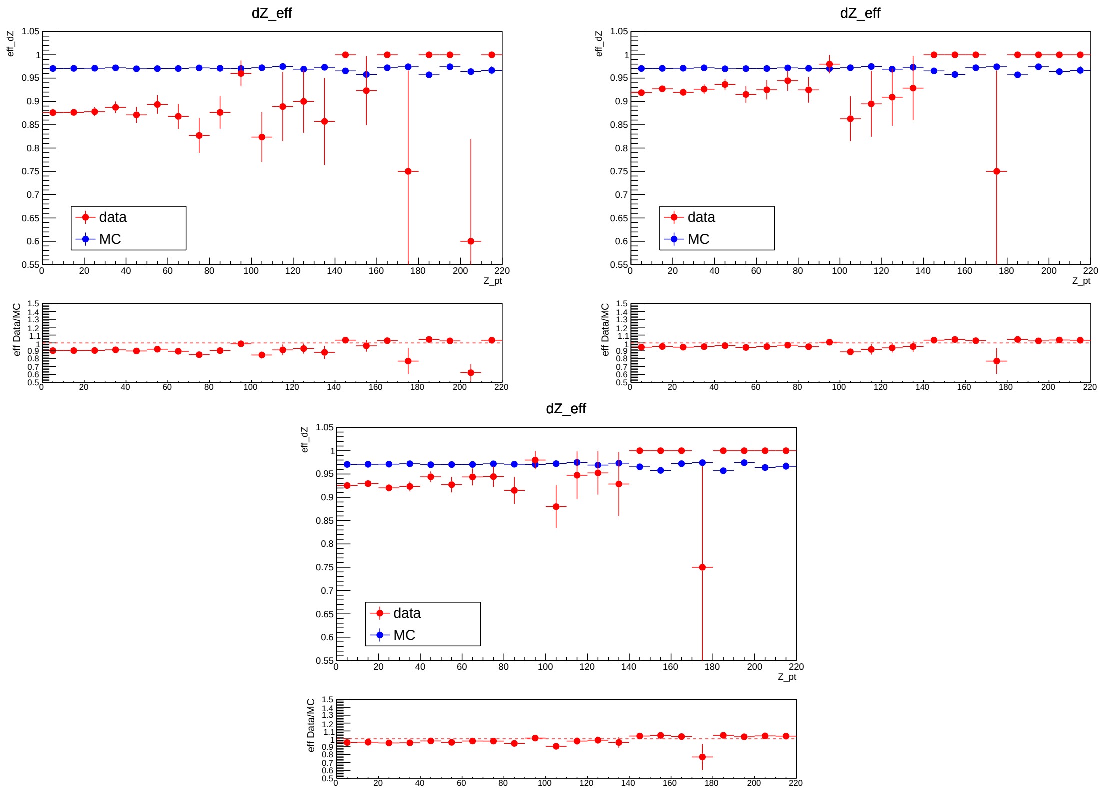

FIGURE A.6: The dZ filter efficiency with original CCC cut (top left), tiny CCC cut (top right) and no CCC cut (bottom) as a function of $p_T(Z)$

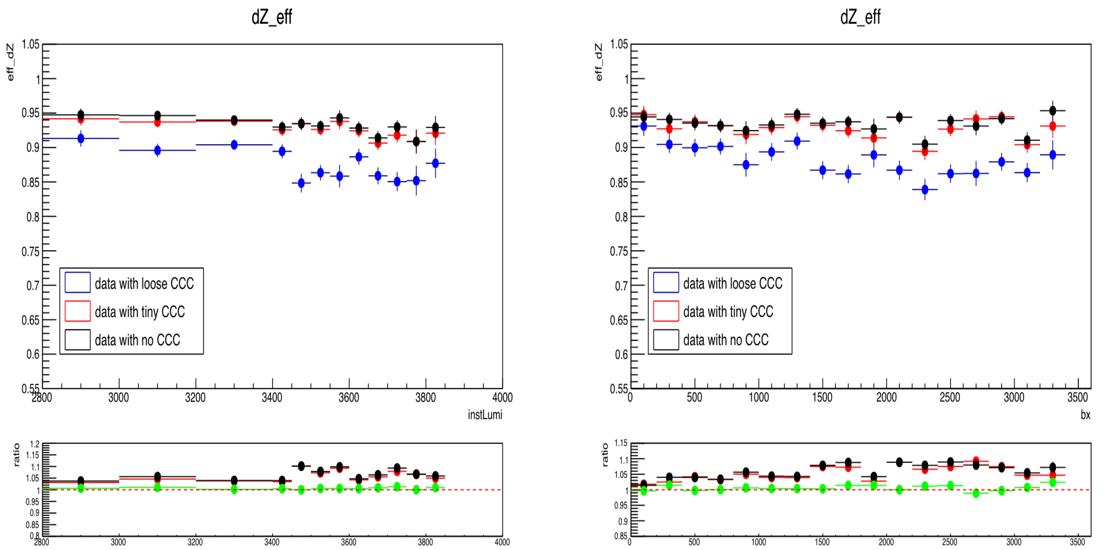

FIGURE A.7: The dZ filter efficiency of data with original, tiny and no CCC cut as a function of instaneous luminosity (left) and bunch crossing number (right)

Those two issues could affect the efficiency of the HLT double muon trigger. In order to understand the effects from the issues, we need to study the HLT double muon trigger. HLT double muon trigger has two double muon trigger legs, for example the trigger

HLT_Mu17_TrkIsoVVL_Mu8_TrkIsoVVL has DoubleIsoMu17Mu8_Mu17leg and DoubleIsoMu17Mu8_Mu8leg. The HLT double muon trigger will be fired on condition that the two legs of the double muon trigger are both fired. So before looking at the HLT double muon trigger, we should check the status of the corresponding double muon legs.

We use the dataset DoubleMuon/Run2016B-PromptReco-v2/AOD. Tag and Probe (TnP) method is used. The condition of the tag is $p_T > 22$GeV, $|\eta| \leq 2.4$, passing IsoMu20 trigger and tight ID. The probe is the trigger to be checked. There are two HLT double muon trigger paths to be checked:

- HLT_Mu17_TrkIsoVVL_Mu8_TrkIsoVVL
- HLT_Mu17_TrkIsoVVL_TkMu8_TrkIsoVVL

The correponding double muon trigger legs are:

- DoubleIsoMu17Mu8_Mu17leg
- DoubleIsoMu17Mu8_Mu8leg
- DoubleIsoMu17TkMu8_Mu17leg
- DoubleIsoMu17TkMu8_TkMu8leg

The results are shown shown in figure A.8. It is obvious that after the issue has been fixed, from run 273423 on, the double muon leg efficiency in the barrel region is improved.

A.3.1 HLT Double Muon Path

After the check on the double muon trigger legs, we moved to the double muon trigger path. This study is also based on 2016 RunB double muon dataset with 800 pb^{-1} integrated luminosity. The reference trigger method is used to obtain the efficiency of the double muon trigger path. The double muon trigger path mentioned above and the double muon trigger path with DZ filter is checked with the reference trigger Mu17_IsoTrkVVL. Each efficiency plot includes 4 figures:

- the efficiency of reference trigger ϵ_{Mu17} (Mu17_IsoTrkVVL).
- the efficiency of the reference trigger triggered by double muon data,

$$\epsilon_{\mathrm{ref}} = 1 - (1 - \epsilon_{\mathrm{Mu17}}) \times (1 - \epsilon_{\mathrm{Mu17}}). \tag{A.2}$$

- the double muon trigger path efficiency passing referring to the reference trigger $\epsilon_{\text{double muon trigger path} \mid \text{ref}}$.
- the final double muon trigger efficiency,

$$\epsilon_{\text{double muon trigger path}} = \epsilon_{\text{double muon trigger path} \mid \text{ref}} \times \epsilon_{\mathrm{ref}}. \tag{A.3}$$

The efficiency of `HLT_Mu17_TrkIsoVVL_Mu8_TrkIsoVVL` is computed in comparison between run $\leq$ 273423 and run > 273423, shown in the figure A.13. Its efficiency is improved after the first issue is fixed (run > 273423). We also observe the same situation for HLT_Mu17_TrkIsoVVL_Mu8_TrkIsoVVL_DZ, figure A.10. If we compare the efficiency of the HLT double muon trigger path with and without DZ filter in the same run range, we could notice that the HLT trigger path with DZ filter is around 5.0% lower.

The two issues were quickly fixed in the beginning of data taking in 2016, and the runB was fixed from run 274094. The integrated luminosity for the runs > 274094 used here is 4 fb^{-1}. HLT double muon trigger efficiencies of `HLT_Mu17_TrkIsoVVL_Mu8_-TrkIsoVVL` and `HLT_Mu17_TrkIsoVVL_Mu8_TrkIsoVVL_DZ` are performed, and the results is shown in the figure A.11. The efficiency `Mu17_IsoTrkVVL` is obviously better than the previous runs. The HLT doulbe muon trigger with DZ filter has lower efficiency than the one without DZ filter.

There was still a problem of HIPs (Hit and Impact Point) before the end of August in 2016. In order to slove it, new setting of the strip APV (Analogue Pipeline Voltage mode) readout chip has been deployed. The HIPs problem is solved for runG and runH dataset. We separate the total dataset into two part, before or after HIPs fixed, and then make comparison between them. The computing method is the same like previous ones. If we compare the HLT double muon trigger with / without DZ filter in the same run range, we could conclude that the trigger with DZ filter has lower efficiency. When we look at the same trigger condition, the efficiency of the double muon trigger with or without DZ filter are both improved after the HIPs problem fixed.

These efficiency value are used by the Z+jets CMS for the 2016 data analysis (unpublished).

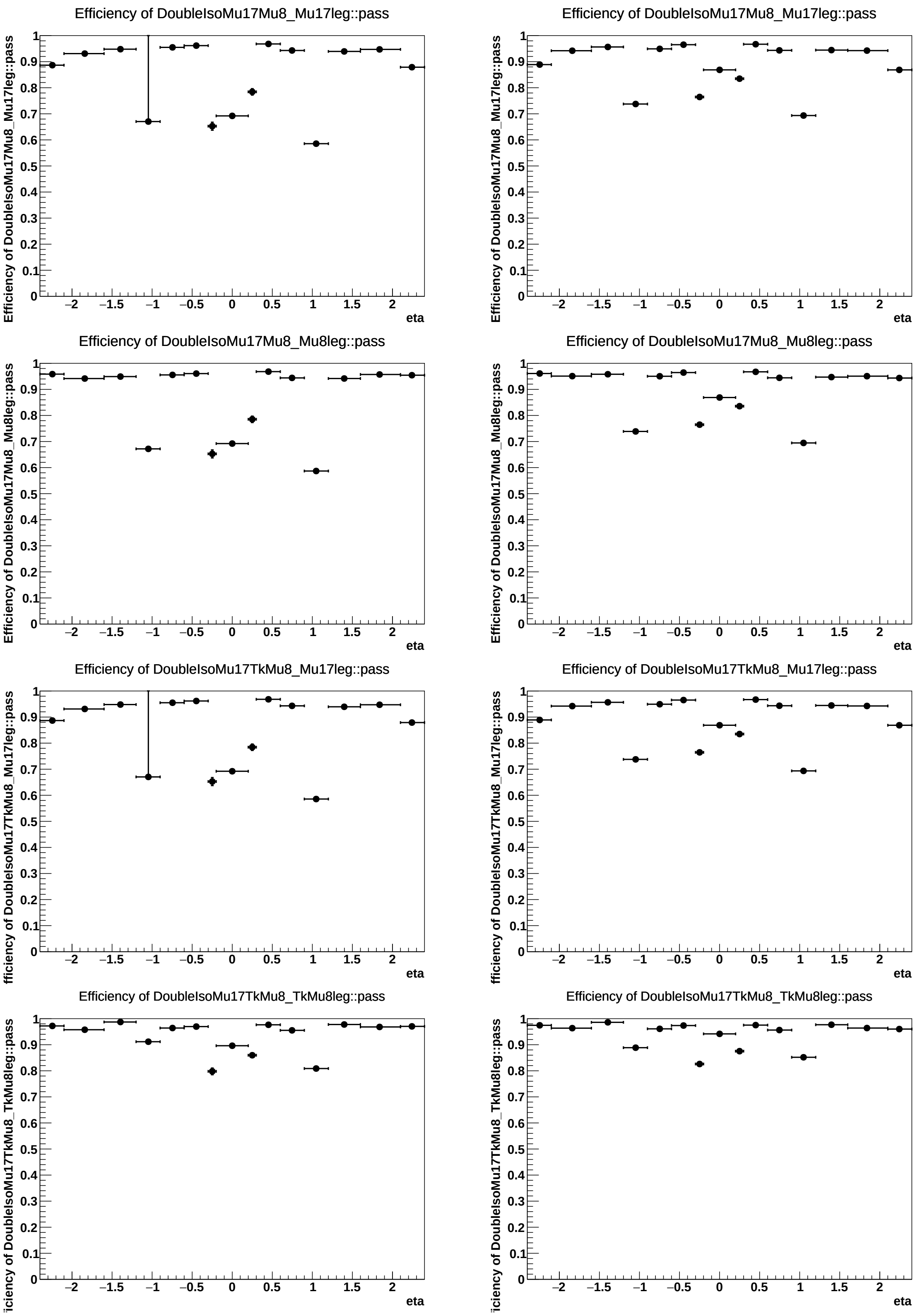

FIGURE A.8: The double muon path leg efficiency before run 273423 (left), and after run 273423 (right). From the top to the bottow are: two DoubleIsoMu17Mu8_IsoMu17leg efficiency, DoubleIsoMu17Mu8_IsoMu8leg efficiency, DoubleIsoMu17TkMu8_IsoMu17leg and DoubleIsoMu17TkMu8_-TkMu8leg efficiency.

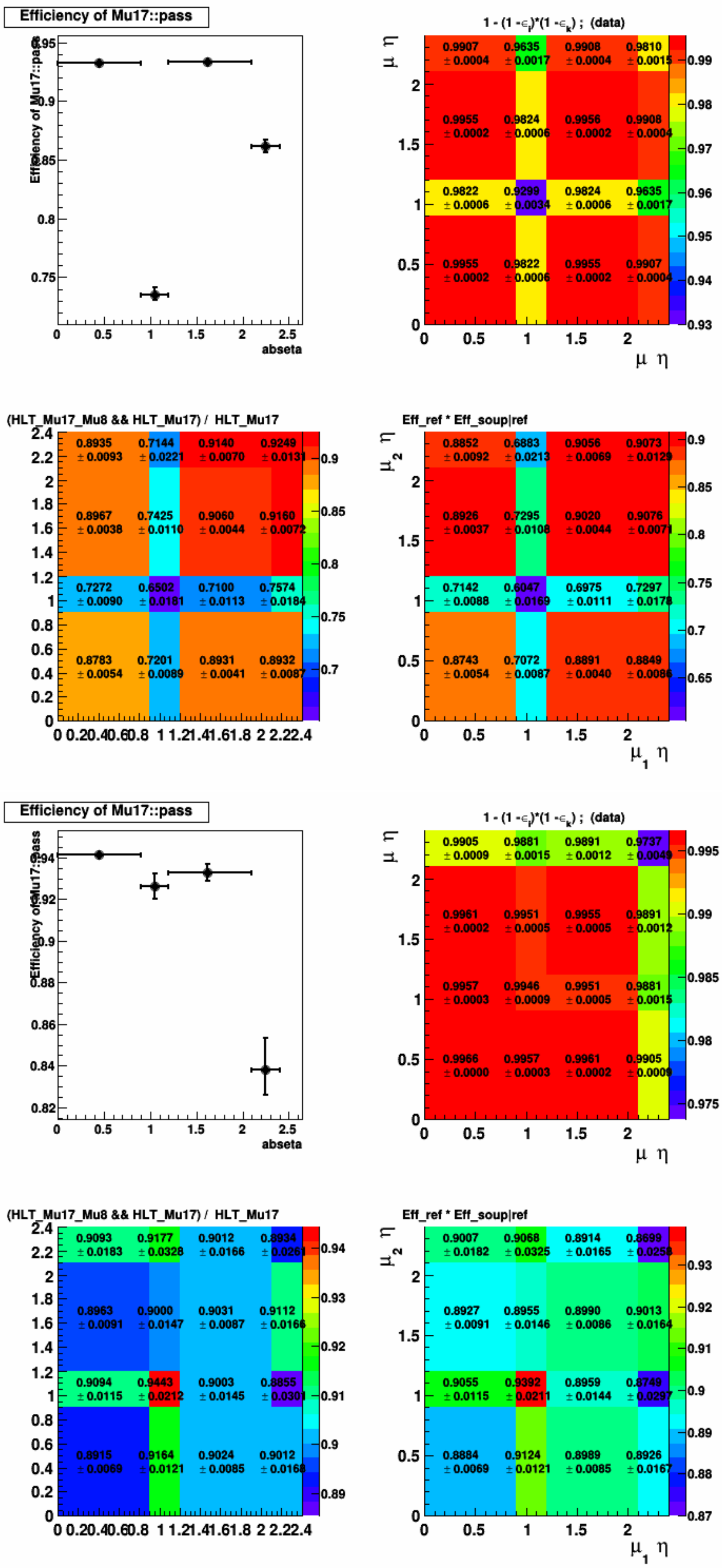

FIGURE A.9: HLT double muon path efficiency `HLT_Mu17_TrkIsoVVL_Mu8_TrkIsoVVL` before run 273423 (top) and after run 273423 (bottom)

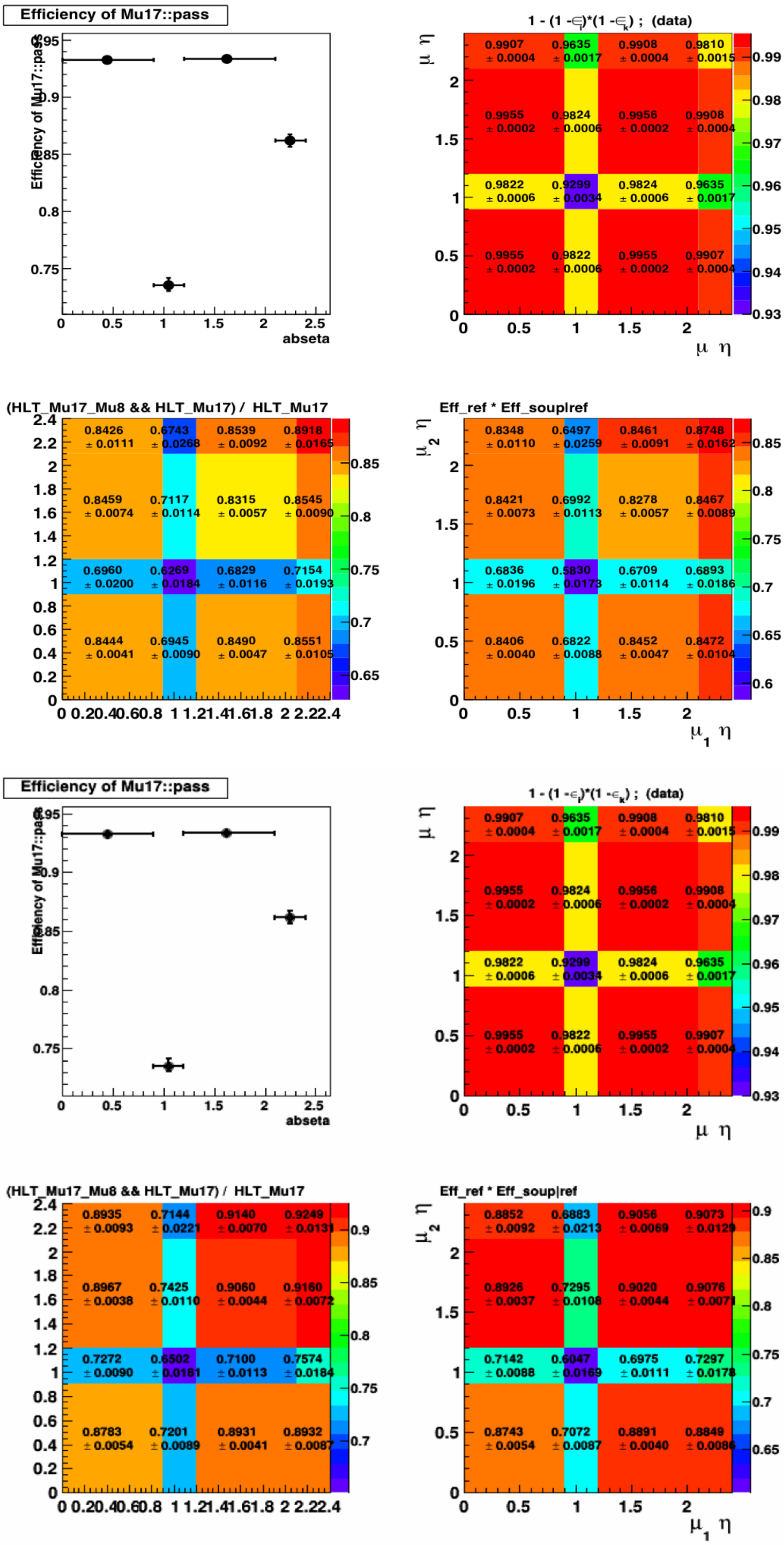

FIGURE A.10: HLT double muon path efficiency `HLT_Mu17_-TrkIsoVVL_Mu8_TrkIsoVVL_DZ` before run 273423 (top) and after run 273423 (bottom)

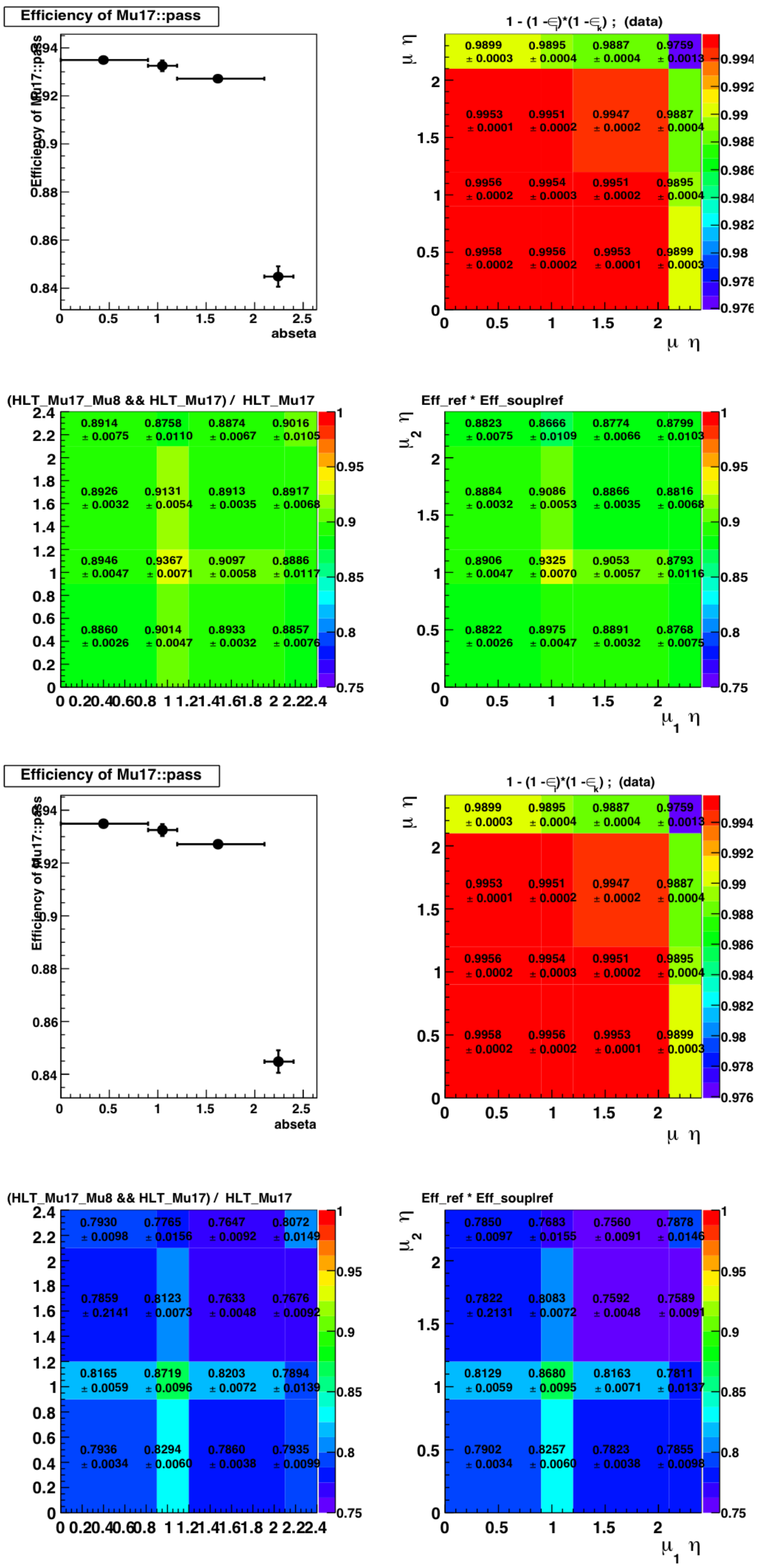

FIGURE A.11: HLT double muon path efficiency `HLT_Mu17_TrkIsoVVL_Mu8_TrkIsoVVL` (top) and `HLT_Mu17_TrkIsoVVL_Mu8_TrkIsoVVL_DZ` (bottom) after run 274094

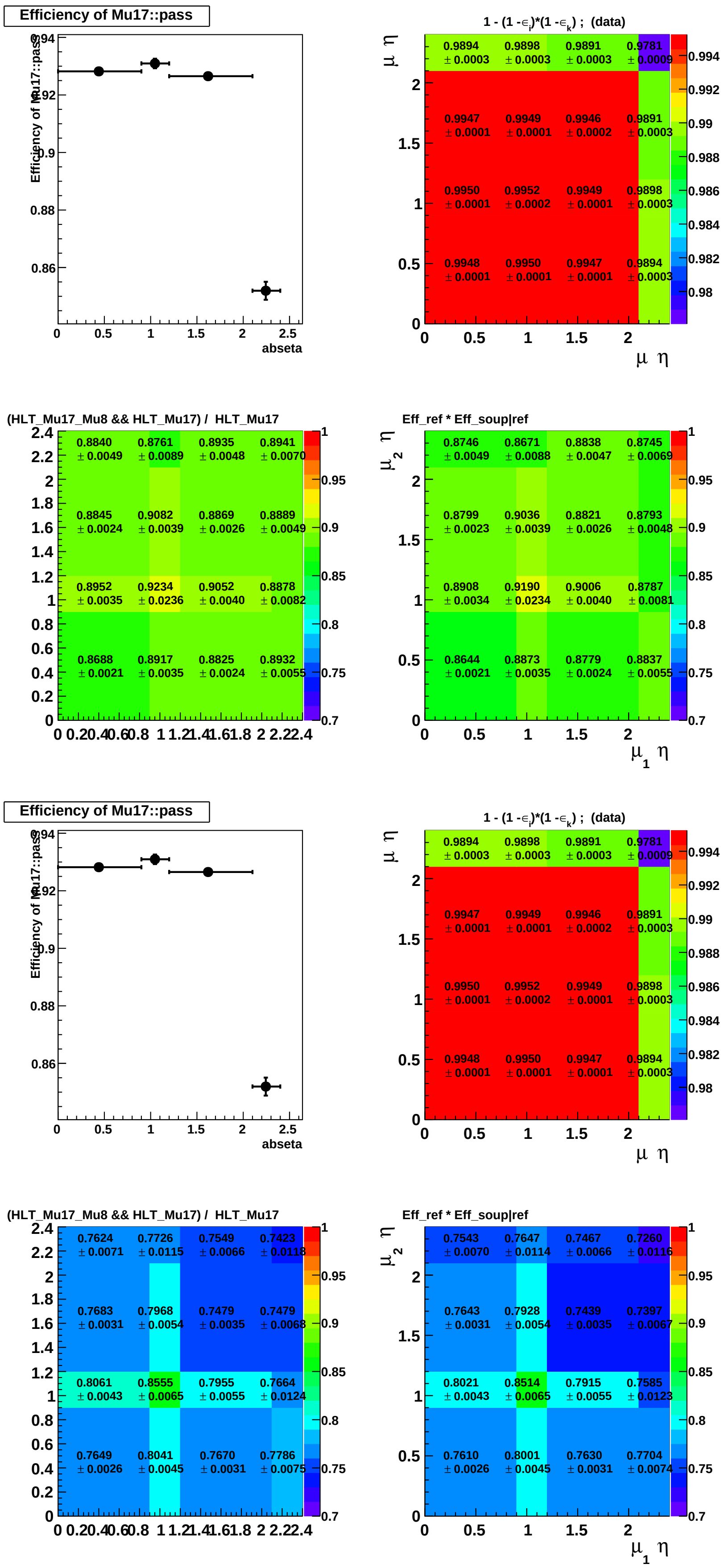

FIGURE A.12: HLT double muon path efficiency `HLT_Mu17_TrkIsoVVL_Mu8_TrkIsoVVL` (top) and `HLT_Mu17_TrkIsoVVL_Mu8_TrkIsoVVL_DZ` (bottom) for runB, runC, runD, runE and runF

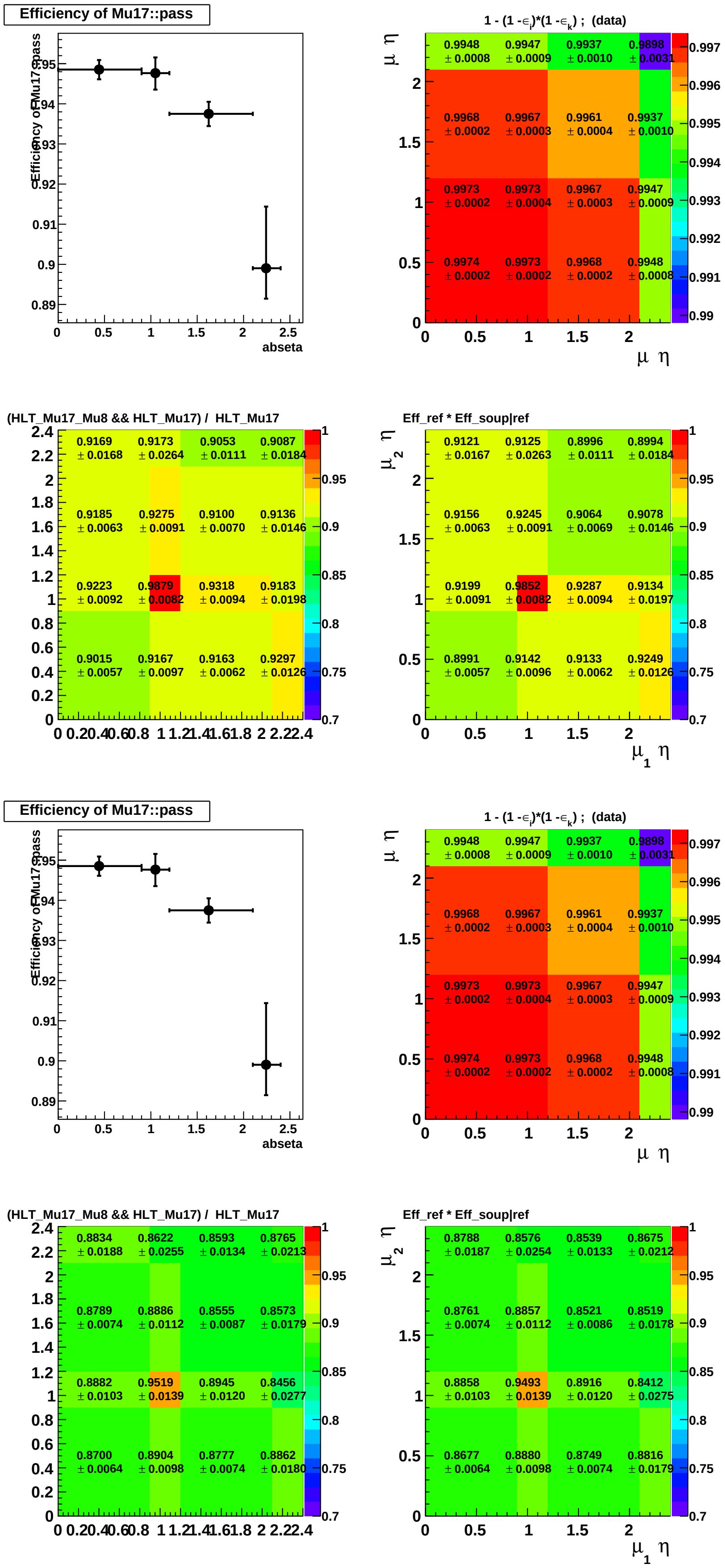

FIGURE A.13: HLT double muon path efficiency `HLT_Mu17_TrkIsoVVL_Mu8_TrkIsoVVL` (top) and `HLT_Mu17_TrkIsoVVL_Mu8_TrkIsoVVL_DZ` (bottom) for runG and runH

Appendix B

Data Simulation Comparison in Electron Channel

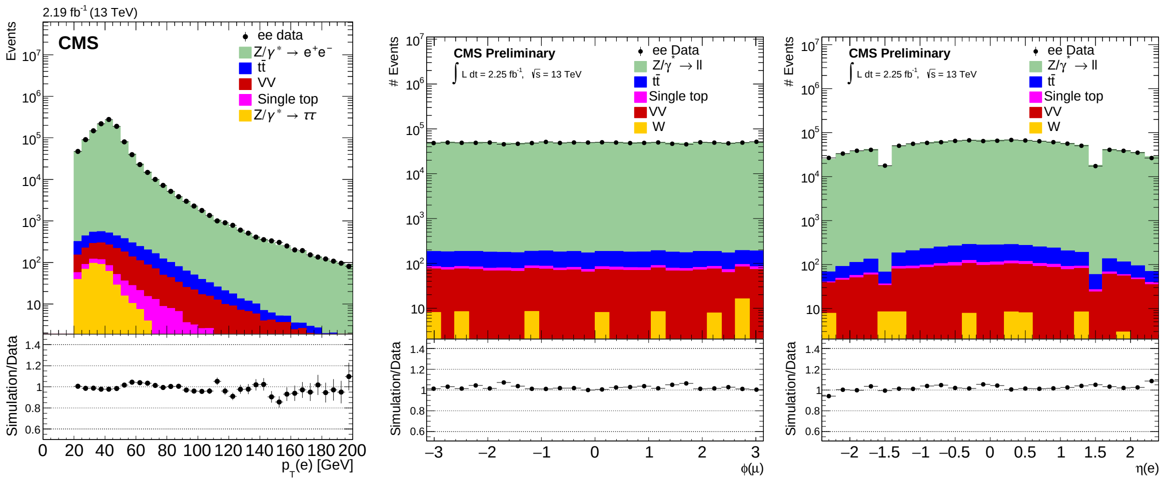

FIGURE B.1: Data to simulation comparison of electron transverse momenta, $p_{\mathrm{T}}(e)$, azimuthal angle, $\phi(e)$ and pseudo-rapidity, $\eta(e)$.

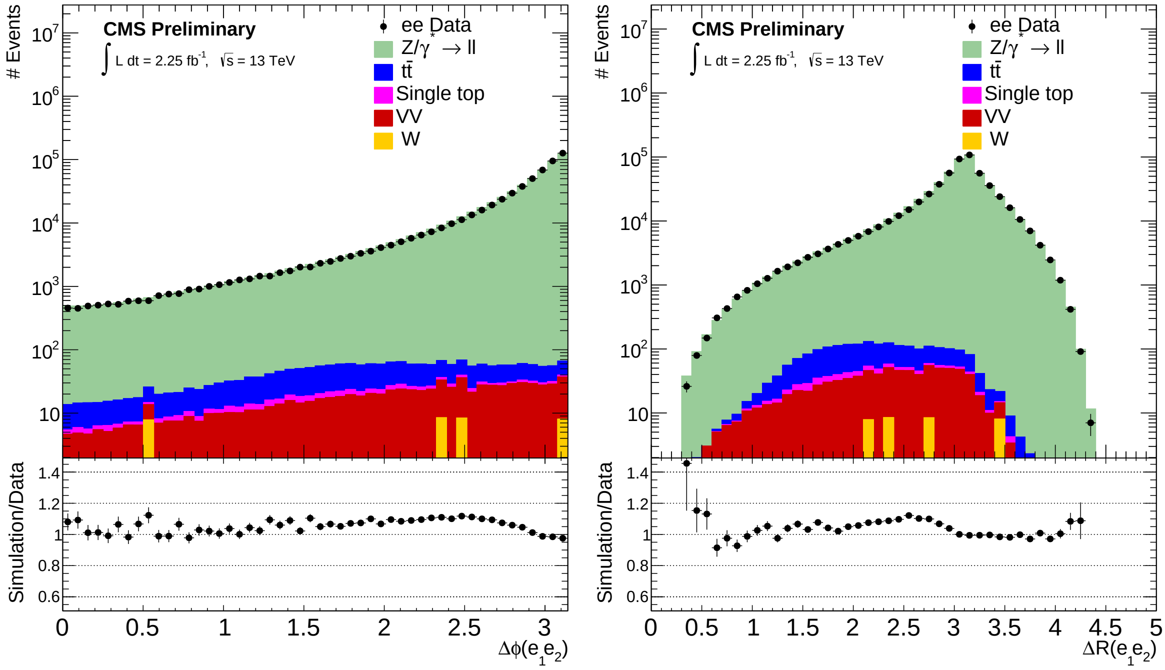

FIGURE B.2: Data to simulation comparison of the two electrons correlations in azimuthal angle, $\Delta\Phi(e_1e_2)$ and separation, $\Delta R(e_1e_2)$.

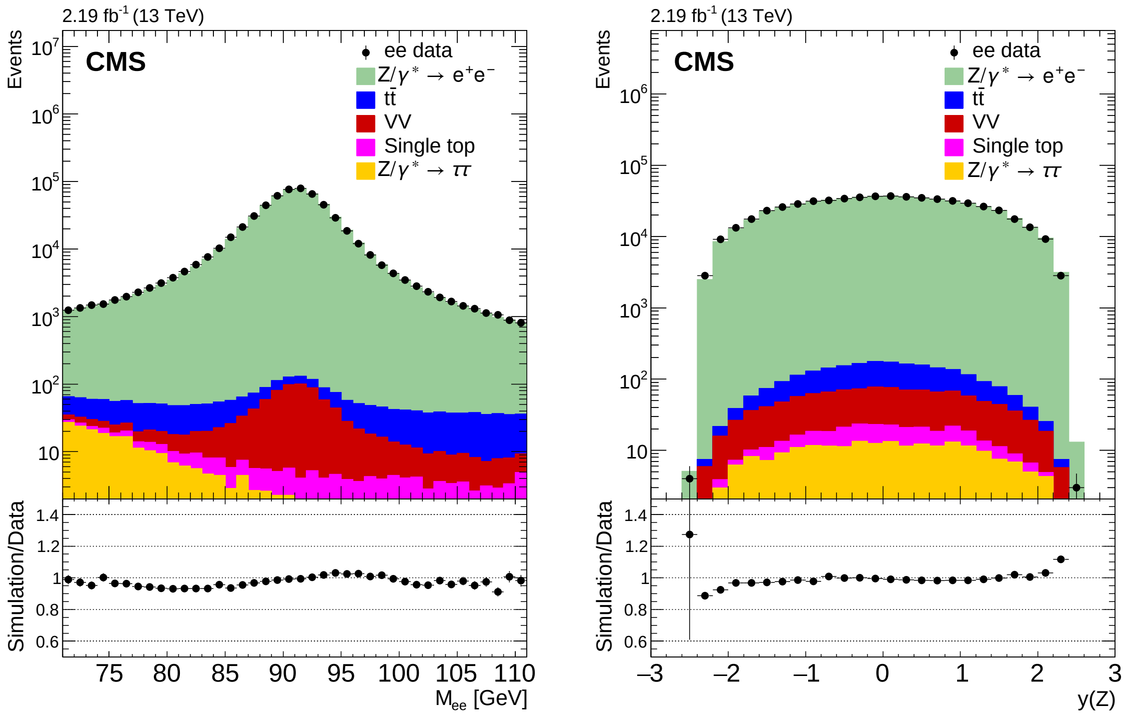

FIGURE B.3: Data to simulation comparison of the Z candidate invariant mass and rapidity for the ee sample.

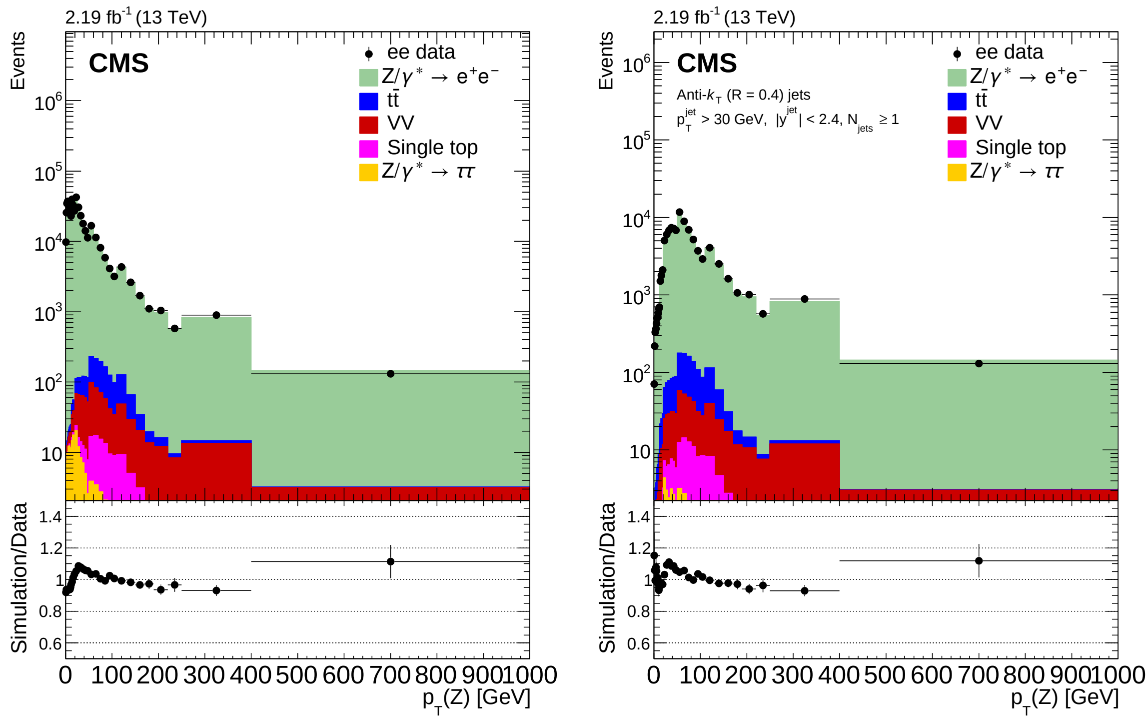

FIGURE B.4: Data to simulation comparison of the Z candidate transverse momentum for the ee sample for inclusively zero jet (left) and one jet (right).

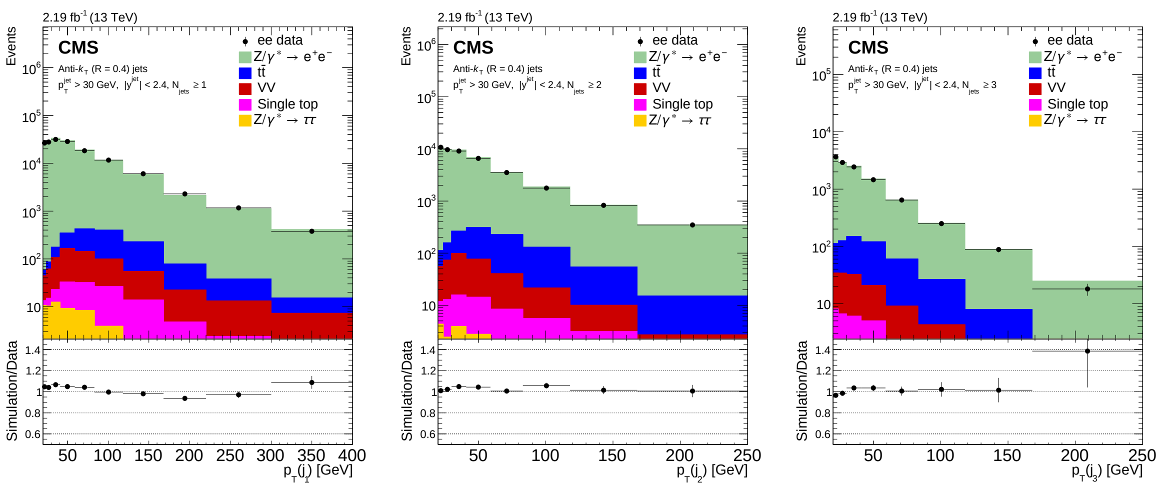

FIGURE B.5: Data to simulation comparison of jet transverse momenta for the 3 first jets obtained from the ee sample.

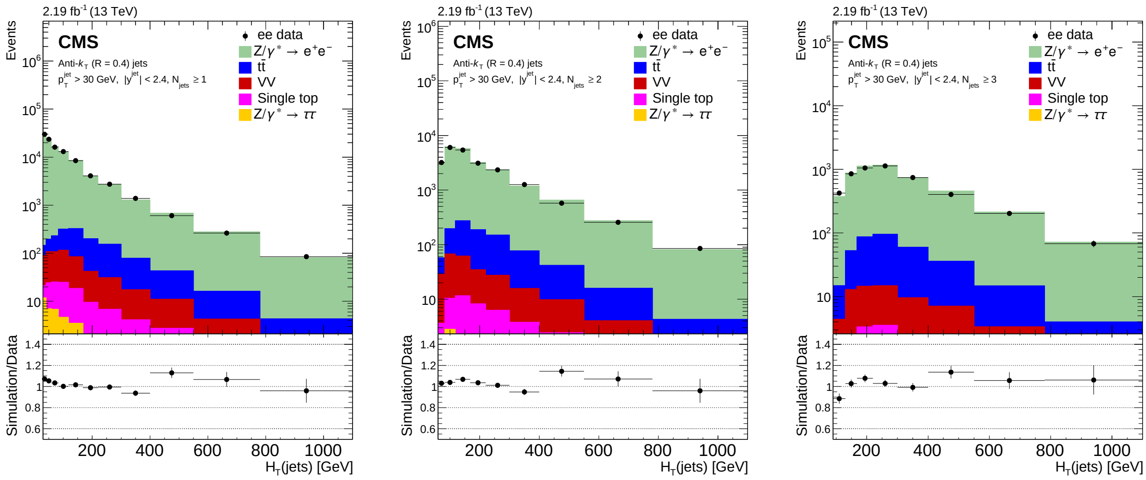

FIGURE B.6: Data to simulation comparison of H_T of the jets for inclusive jet multiplicities of 1 (left), 2 (middle) and 3 (right) obtained from the ee sample.

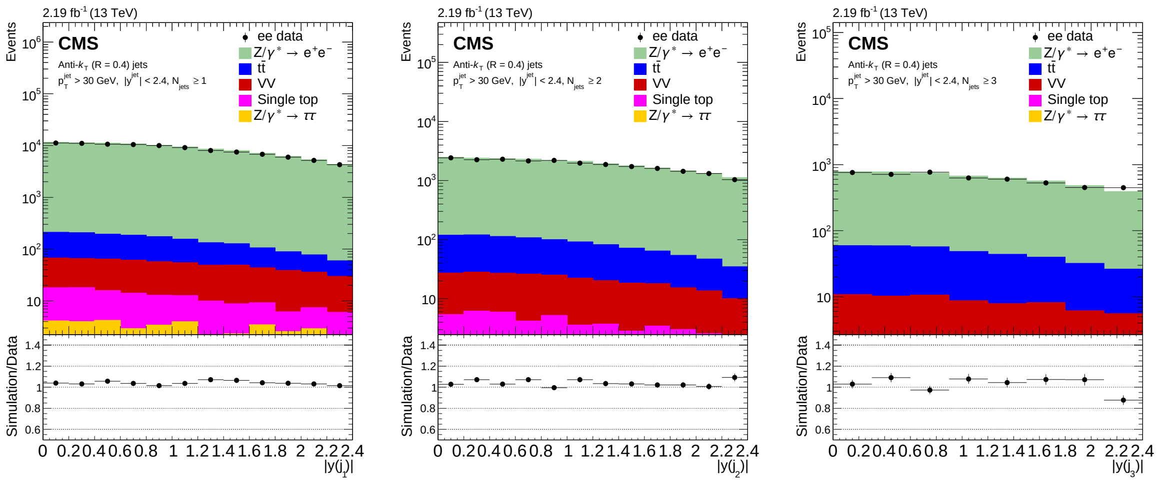

FIGURE B.7: Data to simulation comparison of jet rapidity distributions for the 3 first jets obtained from the ee sample.

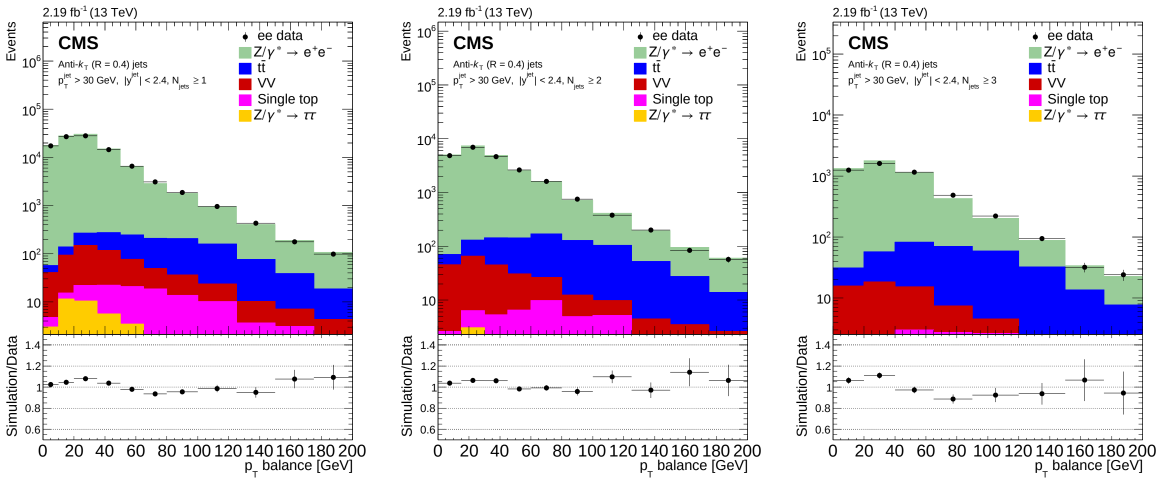

FIGURE B.8: Distribution of events as a function of the transverse momentum balance between the Z boson and the sum of the jets for inclusively one jet (left) two jets (middle) and three jets (right) for the ee sample.

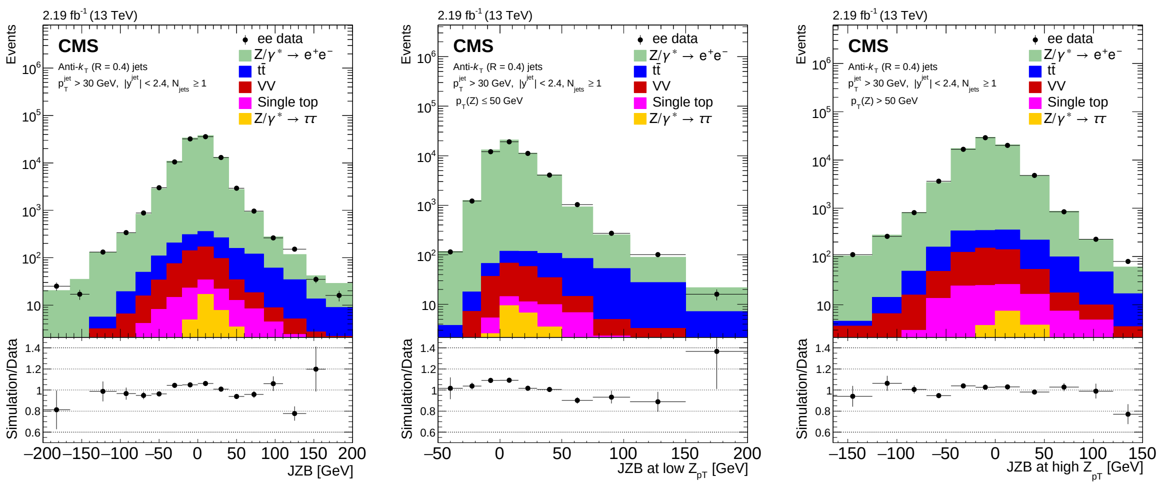

FIGURE B.9: Distribution of events as a function of JZB variable (see text), for the full phase space (left) and limited to $p_{\mathrm{T}}(Z) < 50\mathrm{GeV}$ (middle) and $p_{\mathrm{T}}(Z) > 50\mathrm{GeV}$ (right) for the ee sample.

Appendix C

Electron channel results

The analysis of Z+jets measurement of electron decay channel relying on the work of colleagues of the CMS Z+jets group are shown in this section. Similiar results have been obtained.

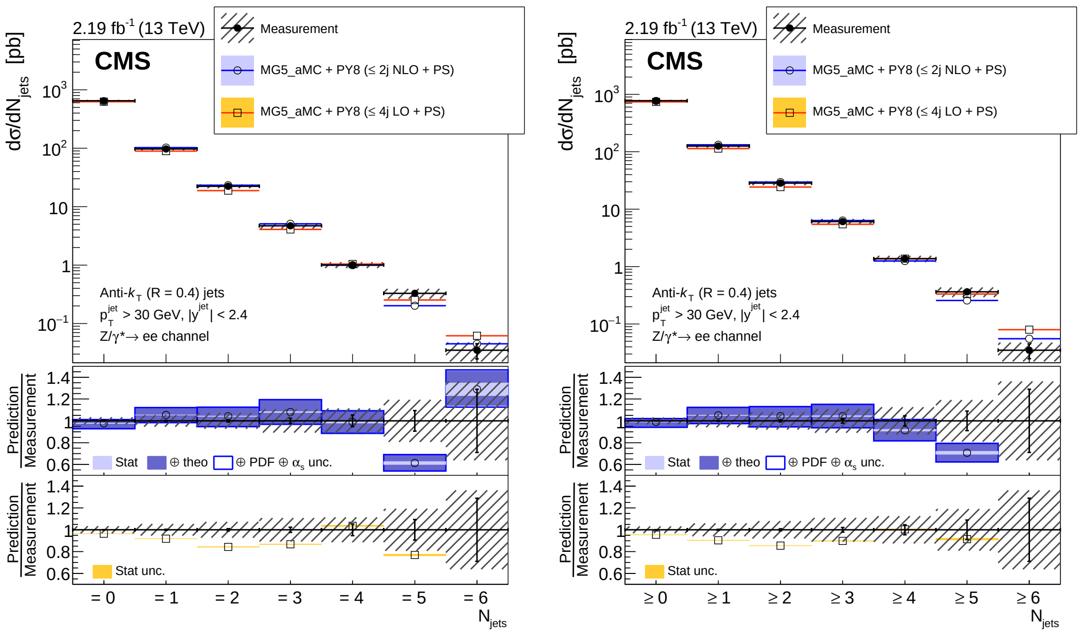

FIGURE C.1: Measured cross section as a function of the jet exclusive (left) and inclusive (right) multiplicities in the ee decay channel. The error bar stands for the statistical uncertainty, and the hatched band presents the total uncertainties.

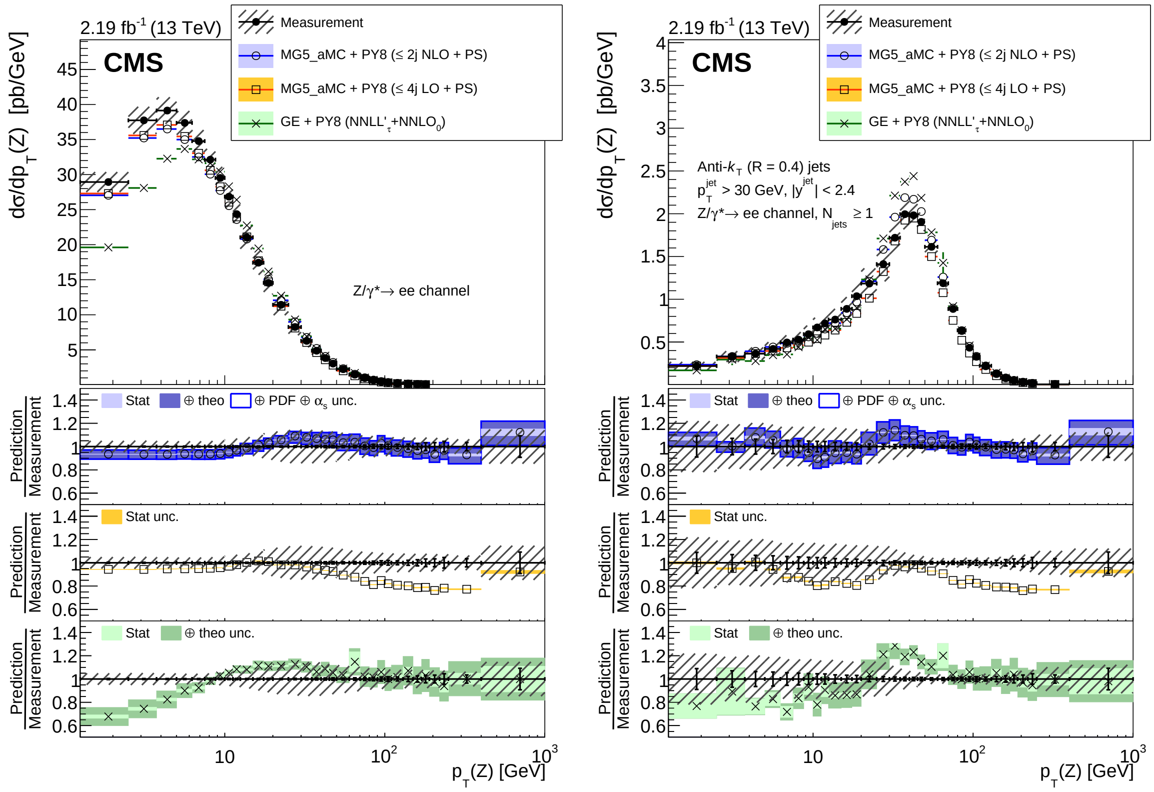

FIGURE C.2: Measured cross section as a function of the p_T of Z boson for inclusive zero jet (left) and one jet (right) in the ee decay channel. The error bar stands for the statistical uncertainty, and the hatched band presents the total uncertainties.

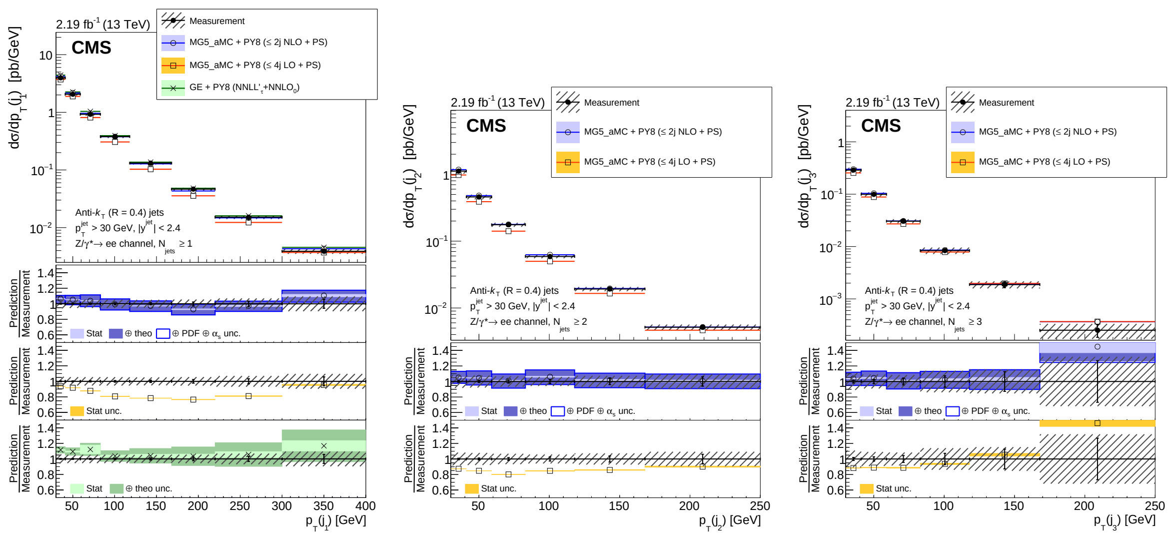

FIGURE C.3: Measured cross section as a function of p_T of the first leading jet (left), second leading jet (middle) and third jet (right) in the ee decay channel. The error bar stands for the statistical uncertainty, and the hatched band presents the total uncertainties.

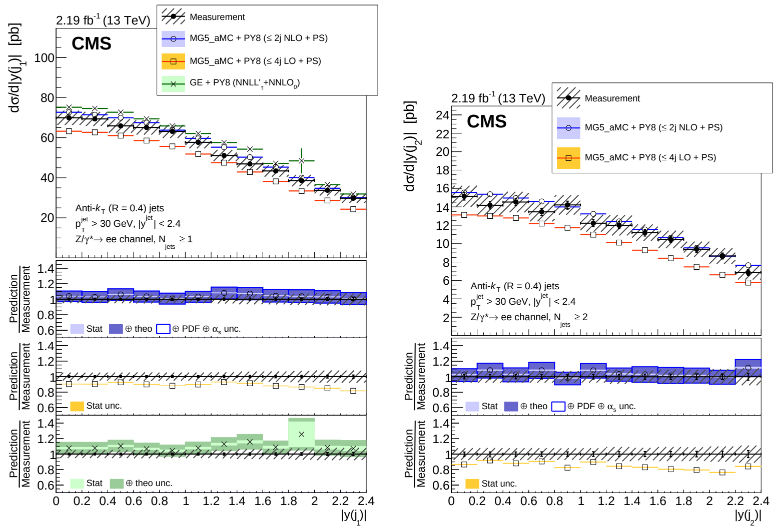

FIGURE C.4: Measured cross section as a function of absolute rapidity of the first leading jet (left), second leading jet (middle) and third jet (right) in the ee decay channel. The error bar stands for the statistical uncertainty, and the hatched band presents the total uncertainties.

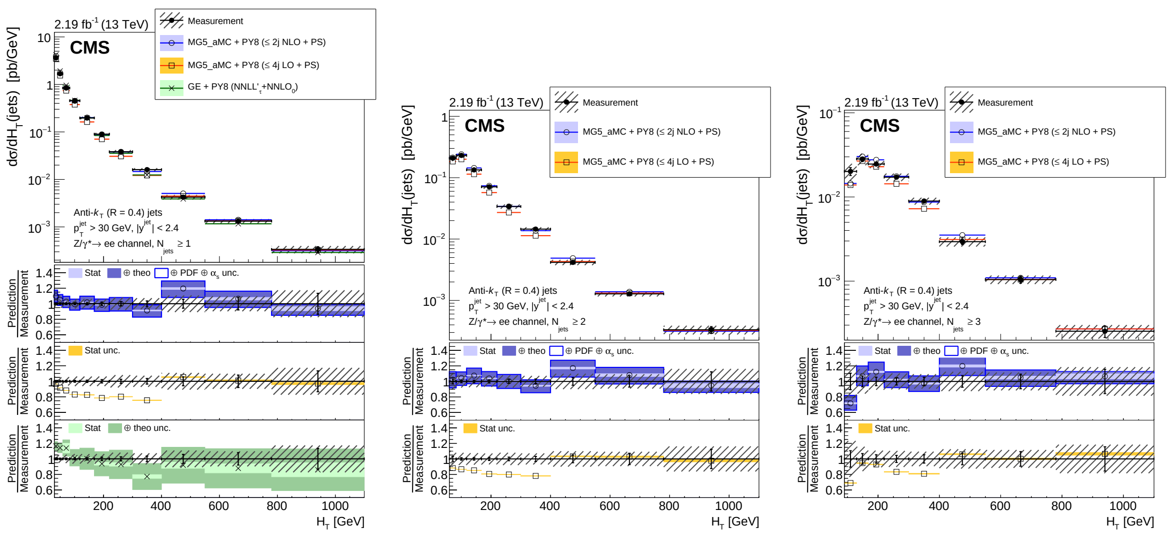

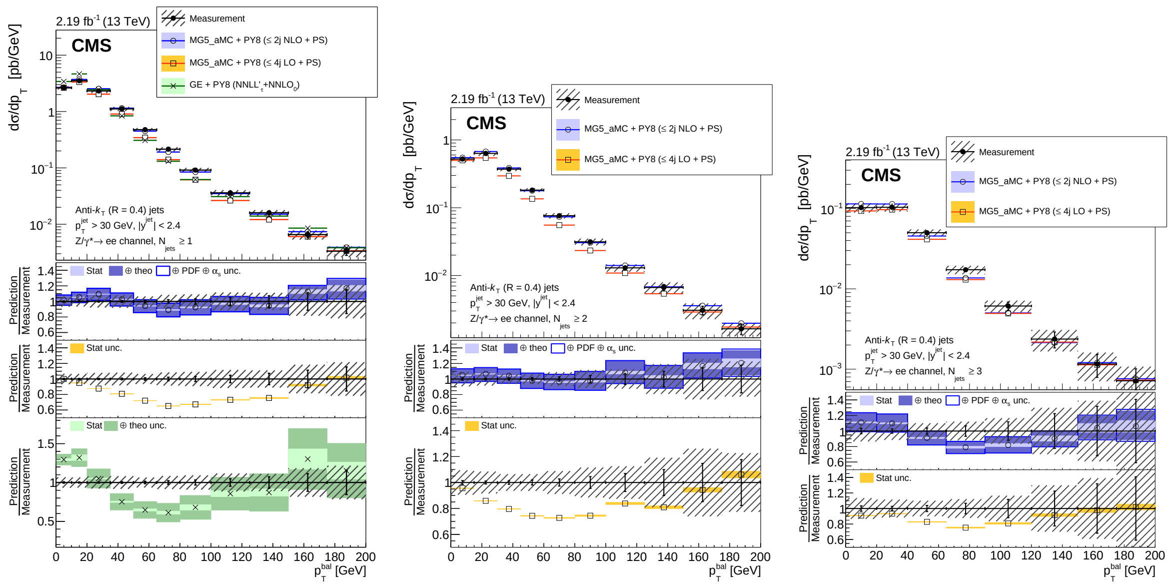

FIGURE C.5: Measured cross section as a function of the transverse momentum balance between jets and the Z boson (p_T^{bal}) for the jet multiplicity $N_{jets} \geq 1$ (left), $N_{jets} \geq 2$ (middle) and $N_{jets} \geq 3$ (right) in the ee decay channel. The error bar stands for the statistical uncertainty, and the hatched band presents the total uncertainties.

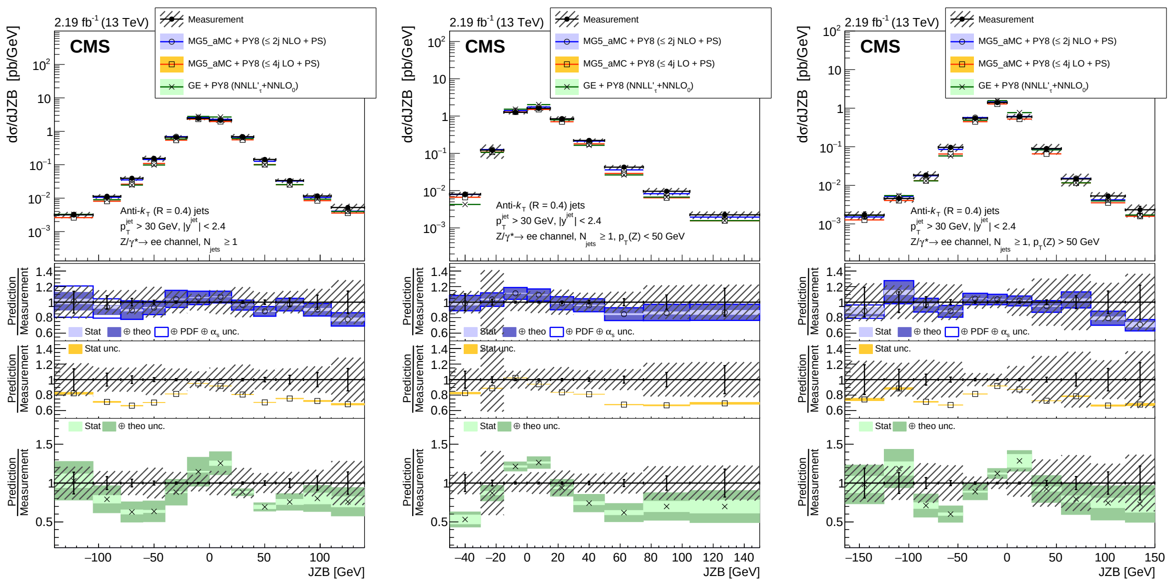

FIGURE C.6: Measured cross section as a function of JZB variable (left), with extra cut p_T(Z)<50 GeV (middle) and p_T(Z)>50GeV (right) in the ee decay channel. The error bar stands for the statistical uncertainty, and the hatched band presents the total uncertainties.

Bibliography

[1] Albert M Sirunyan et al. "Measurement of differential cross sections for Z boson production in association with jets in proton-proton collisions at $\sqrt{s} = 13$ TeV". In: (2018). arXiv: 1804.05252 [hep-ex].

[2] CMS Collaboration. "Measurement of the differential production cross section of Z bosons in association with jets in pp collisions at sqrt(s) = 8 TeV". In: CMS-PAS-SMP-13-007 (2014). URL: http://cds.cern.ch/record/1728322.

[3] CMS Collaboration. "Measurement of the double differential cross section of Z bosons produced in association with jets in pp collisions at $\sqrt{s}$ = 8 TeV". In: CMS-PAS-SMP-14-009 (2014). URL: http://cds.cern.ch/record/1728345.

[4] David J Griffiths. *Introduction to elementary particles; 2nd rev. version*. Physics textbook. New York, NY: Wiley, 2008. URL: https://cds.cern.ch/record/111880.

[5] Donald H. Perkins. *Introduction to High Energy Physics*. 4th ed. Cambridge University Press, 2000. DOI: 10.1017/CBO9780511809040.

[6] Michael E. Peskin and Daniel V. Schroeder. *An Introduction to quantum field theory*. Reading, USA: Addison-Wesley, 1995. URL: http://www.slac.stanford.edu/~mpeskin/QFT.html.

[7] G. Dissertori, I.G. Knowles, and M. Schmelling. *Quantum Chromodynamics: High Energy Experiments and Theory*. International series of monographs on physics. Clarendon Press, 2003. ISBN: 9780198505723. URL: https://books.google.be/books?id=%5C_rqDQgAACAAJ.

[8] David J. Gross and Frank Wilczek. "Ultraviolet Behavior of Nonabelian Gauge Theories". In: *Phys. Rev. Lett.* 30 (1973). [,271(1973)], pp. 1343–1346. DOI: 10.1103/PhysRevLett.30.1343.

[9] William E. Caswell. "Asymptotic Behavior of Nonabelian Gauge Theories to Two Loop Order". In: *Phys. Rev. Lett.* 33 (1974), p. 244. DOI: 10.1103/PhysRevLett.33.244.

[10] S. A. Larin and J. A. M. Vermaseren. "The Three loop QCD Beta function and anomalous dimensions". In: *Phys. Lett.* B303 (1993), pp. 334–336. DOI: 10.1016/0370-2693(93)91441-O. arXiv: hep-ph/9302208 [hep-ph].

[11] Vardan Khachatryan et al. "Measurement and QCD analysis of double-differential inclusive jet cross sections in pp collisions at $\sqrt{s} = 8$ TeV and cross section ratios to 2.76 and 7 TeV". In: *JHEP* 03 (2017), p. 156. DOI: 10.1007/JHEP03(2017)156. arXiv: 1609.05331 [hep-ex].

[12] S. D. Drell and Tung-Mow Yan. "Massive Lepton Pair Production in Hadron-Hadron Collisions at High-Energies". In: *Phys. Rev. Lett.* 25 (1970). [Erratum: Phys. Rev. Lett.25,902(1970)], pp. 316–320. DOI: 10.1103/PhysRevLett.25.316,10.1103/PhysRevLett.25.902.2.

[13] John C. Collins, Davison E. Soper, and George F. Sterman. "Factorization of Hard Processes in QCD". In: *Adv. Ser. Direct. High Energy Phys.* 5 (1989), pp. 1–91. DOI: 10.1142/9789814503266_0001. arXiv: hep-ph/0409313 [hep-ph].

[14] Karl Jakobs. "Physics at the LHC – From Standard Model measurements to Searches for New Physics". In: *Proceedings, 2011 European School of High-Energy Physics (ESHEP 2011): Cheile Gradistei, Romania, September 7-20, 2011*. 2014, pp. 309–358. DOI: 10.5170/CERN-2014-003.309. arXiv: 1206.7024 [hep-ex]. URL: http://inspirehep.net/record/1120513/files/arXiv:1206.7024.pdf.

[15] Charalampos Anastasiou et al. "High precision QCD at hadron colliders: Electroweak gauge boson rapidity distributions at NNLO". In: *Phys. Rev.* D69 (2004), p. 094008. DOI: 10.1103/PhysRevD.69.094008. arXiv: hep-ph/0312266 [hep-ph].

[16] Ringaile Placakyte. "Parton Distribution Functions". In: *Proceedings, 31st International Conference on Physics in collisions (PIC 2011): Vancouver, Canada, August 28-September 1, 2011*. 2011. arXiv: 1111.5452 [hep-ph]. URL: https://inspirehep.net/record/954990/files/arXiv:1111.5452.pdf.

[17] F. D. Aaron et al. "Inclusive Deep Inelastic Scattering at High Q^2 with Longitudinally Polarised Lepton Beams at HERA". In: *JHEP* 09 (2012), p. 061. DOI: 10.1007/JHEP09(2012)061. arXiv: 1206.7007 [hep-ex].

[18] H. Abramowicz et al. "Measurement of high-Q2 neutral current deep inelastic e^+p scattering cross sections with a longitudinally polarized positron beam at HERA". In: *Phys. Rev.* D87.5 (2013), p. 052014. DOI: 10.1103/PhysRevD.87.052014. arXiv: 1208.6138 [hep-ex].

[19] Serguei Chatrchyan et al. "Measurement of the differential and double-differential Drell-Yan cross sections in proton-proton collisions at $\sqrt{s} = 7$ TeV". In: *JHEP* 12 (2013), p. 030. DOI: 10.1007/JHEP12(2013)030. arXiv: 1310.7291 [hep-ex].

[20] Yuri L. Dokshitzer. "Calculation of the Structure Functions for Deep Inelastic Scattering and e+ e- Annihilation by Perturbation Theory in Quantum Chromodynamics." In: *Sov. Phys. JETP* 46 (1977). [Zh. Eksp. Teor. Fiz.73,1216(1977)], pp. 641–653.

[21] V. N. Gribov and L. N. Lipatov. "Deep inelastic e p scattering in perturbation theory". In: *Sov. J. Nucl. Phys.* 15 (1972). [Yad. Fiz.15,781(1972)], pp. 438–450.

[22] L. N. Lipatov. "The parton model and perturbation theory". In: *Sov. J. Nucl. Phys.* 20 (1975). [Yad. Fiz.20,181(1974)], pp. 94–102.

[23] Guido Altarelli and G. Parisi. "Asymptotic Freedom in Parton Language". In: *Nucl. Phys.* B126 (1977), pp. 298–318. DOI: 10.1016/0550-3213(77)90384-4.

[24] Patrick L.S. Connor, Francesco Hautmann, and Hannes Jung. *TMDplotter 2.2.0*. URL: http://tmdplotter.desy.de.

[25] Patrick L. S. Connor et al. "TMDlib 1.0.8 and TMDplotter 2.1.1". In: *PoS* DIS2016 (2016), p. 039. DOI: 10.3204/PUBDB-2016-05953.

[26] Richard D. Ball et al. "Parton distributions with LHC data". In: *Nucl. Phys.* B867 (2013), pp. 244–289. DOI: 10.1016/j.nuclphysb.2012.10.003. arXiv: 1207.1303 [hep-ph].

[27] Stefan Weinzierl. "Introduction to Monte Carlo methods". In: (2000). arXiv: hep-ph/0006269 [hep-ph].

[28] Stefan Höche. "Introduction to parton-shower event generators". In: *Proceedings, Theoretical Advanced Study Institute in Elementary Particle Physics: Journeys Through the Precision Frontier: Amplitudes for Colliders (TASI 2014): Boulder, Colorado, June 2-27, 2014*. 2015, pp. 235–295. DOI: 10.1142/9789814678766_0005. arXiv: 1411.4085 [hep-ph]. URL: http://inspirehep.net/record/1328513/files/arXiv:1411.4085.pdf.

[29] Tanju Gleisberg et al. "SHERPA 1. alpha: A Proof of concept version". In: *JHEP* 02 (2004), p. 056. DOI: 10.1088/1126-6708/2004/02/056. arXiv: hep-ph/0311263 [hep-ph].

[30] J. Alwall et al. "The automated computation of tree-level and next-to-leading order differential cross sections, and their matching to parton shower simulations". In: *JHEP* 07 (2014), p. 079. DOI: 10.1007/JHEP07(2014)079. arXiv: 1405.0301 [hep-ph].

[31] Simone Alioli et al. "Drell-Yan production at NNLL′+NNLO matched to parton showers". In: *Phys. Rev.* D92.9 (2015), p. 094020. DOI: 10.1103/PhysRevD.92.094020. arXiv: 1508.01475 [hep-ph].

[32] Simone Alioli et al. "Combining Higher-Order Resummation with Multiple NLO Calculations and Parton Showers in GENEVA". In: *JHEP* 09 (2013), p. 120. DOI: 10.1007/JHEP09(2013)120. arXiv: 1211.7049 [hep-ph].

[33] Torbjörn Sjöstrand et al. "An Introduction to PYTHIA 8.2". In: *Comput. Phys. Commun.* 191 (2015), pp. 159–177. DOI: 10.1016/j.cpc.2015.01.024. arXiv: 1410.3012 [hep-ph].

[34] Johan Alwall et al. "MadGraph 5 : Going Beyond". In: *JHEP* 1106 (2011), p. 128. DOI: 10.1007/JHEP06(2011)128. arXiv: 1106.0522 [hep-ph].

[35] Stefano Frixione and Bryan R. Webber. "Matching NLO QCD computations and parton shower simulations". In: *JHEP* 06 (2002), p. 029. DOI: 10.1088/1126-6708/2002/06/029. arXiv: hep-ph/0204244 [hep-ph].

[36] Neil D. Christensen and Claude Duhr. "FeynRules - Feynman rules made easy". In: *Comput. Phys. Commun.* 180 (2009), pp. 1614–1641. DOI: 10.1016/j.cpc.2009.02.018. arXiv: 0806.4194 [hep-ph].

[37] Neil D. Christensen et al. "A Comprehensive approach to new physics simulations". In: *Eur. Phys. J.* C71 (2011), p. 1541. DOI: 10.1140/epjc/s10052-011-1541-5. arXiv: 0906.2474 [hep-ph].

[38] Adam Alloul et al. "Automated mass spectrum generation for new physics". In: *Eur. Phys. J.* C73.2 (2013), p. 2325. DOI: 10.1140/epjc/s10052-013-2325-x. arXiv: 1301.5932 [hep-ph].

[39] Rikkert Frederix et al. "Automation of next-to-leading order computations in QCD: The FKS subtraction". In: *JHEP* 10 (2009), p. 003. DOI: 10.1088/1126-6708/2009/10/003. arXiv: 0908.4272 [hep-ph].

[40] S. Frixione, Z. Kunszt, and A. Signer. "Three jet cross-sections to next-to-leading order". In: *Nucl. Phys.* B467 (1996), pp. 399–442. DOI: 10.1016/0550-3213(96)00110-1. arXiv: hep-ph/9512328 [hep-ph].

[41] S. Frixione. "A General approach to jet cross-sections in QCD". In: *Nucl. Phys.* B507 (1997), pp. 295–314. DOI: 10.1016/S0550-3213(97)00574-9. arXiv: hep-ph/9706545 [hep-ph].

[42] Torbjorn Sjostrand, Stephen Mrenna, and Peter Z. Skands. "PYTHIA 6.4 Physics and Manual". In: *JHEP* 05 (2006), p. 026. DOI: 10.1088/1126-6708/2006/05/026. arXiv: hep-ph/0603175 [hep-ph].
[43] Torbjorn Sjostrand, Stephen Mrenna, and Peter Z. Skands. "A Brief Introduction to PYTHIA 8.1". In: *Comput. Phys. Commun.* 178 (2008), pp. 852–867. DOI: 10.1016/j.cpc.2008.01.036. arXiv: 0710.3820 [hep-ph].
[44] Bo Andersson et al. "Parton Fragmentation and String Dynamics". In: *Phys. Rept.* 97 (1983), pp. 31–145. DOI: 10.1016/0370-1573(83)90080-7.
[45] Iain W. Stewart, Frank J. Tackmann, and Wouter J. Waalewijn. "N Jettiness: An Inclusive Event Shape to Veto Jets". In: *Phys. Rev. Lett.* 105 (9 Aug. 2010), p. 092002. DOI: 10.1103/PhysRevLett.105.092002. URL: https://link.aps.org/doi/10.1103/PhysRevLett.105.092002.
[46] Christian W. Bauer, Frank J. Tackmann, and Jesse Thaler. "GenEvA. I. A New framework for event generation". In: *JHEP* 12 (2008), p. 010. DOI: 10.1088/1126-6708/2008/12/010. arXiv: 0801.4026 [hep-ph].
[47] Christian W. Bauer, Frank J. Tackmann, and Jesse Thaler. "GenEvA. II. A Phase space generator from a reweighted parton shower". In: *JHEP* 12 (2008), p. 011. DOI: 10.1088/1126-6708/2008/12/011. arXiv: 0801.4028 [hep-ph].
[48] Lyndon Evans and Philip Bryant. "LHC Machine". In: *JINST* 3 (2008), S08001. DOI: 10.1088/1748-0221/3/08/S08001.
[49] S. Chatrchyan et al. "The CMS experiment at the CERN LHC". In: *JINST* 3 (2008), S08004. DOI: 10.1088/1748-0221/3/08/S08004.
[50] "LEP Design Report: Vol.2. The LEP Main Ring". In: CERN-LEP-84-01 (1984).
[51] P. Adzic et al. "Energy resolution of the barrel of the CMS electromagnetic calorimeter". In: *JINST* 2 (2007), P04004. DOI: 10.1088/1748-0221/2/04/P04004.
[52] CMS Internal. *Energy Response and Longitudinal Shower Profiles Measured in CMS HCAL and Comparison With Geant4*. 2007.
[53] G. Bayatian et al. "Design, performance and calibration of the CMS forward calorimeter wedges". In: *Eur. Phys. J.* C53 (2008), pp. 139–166. DOI: 10.1140/epjc/s10052-007-0459-4.
[54] M. Jeitler. "The upgrade of the CMS trigger system". In: *JINST* 9 (2014), p. C08002. DOI: 10.1088/1748-0221/9/08/C08002.
[55] Wolfgang Adam. "Track and vertex reconstruction in CMS". In: *Nucl. Instrum. Meth.* A582 (2007), pp. 781–784. DOI: 10.1016/j.nima.2007.07.091.
[56] CMS Internal. "Track reconstruction in the CMS tracker". In: CERN-CMS-NOTE-2006-041, CMS-NOTE-2006-041 (2005).
[57] CMS Collaboration. "Particle-Flow Event Reconstruction in CMS and Performance for Jets, Taus and MET". In: (2009).
[58] CMS Collaboration. *Track Reconstruction in the CMS tracker (in preparation)*. CMS Physics Analysis Summary CMS-PAS-SMP-14-009. 2009.
[59] Serguei Chatrchyan et al. "Performance of CMS muon reconstruction in pp collision events at $\sqrt{s} = 7$ TeV". In: *JINST* 7 (2012), P10002. DOI: 10.1088/1748-0221/7/10/P10002. arXiv: 1206.4071 [physics.ins-det].
[60] Vardan Khachatryan et al. "Performance of Electron Reconstruction and Selection with the CMS Detector in Proton-Proton Collisions at $\sqrt{s} = 8$ TeV". In:

JINST 10.06 (2015), P06005. DOI: 10.1088/1748-0221/10/06/P06005. arXiv: 1502.02701 [physics.ins-det].

[61] S. Baffioni et al. "Electron reconstruction in CMS". In: *Eur. Phys. J.* C49 (2007), pp. 1099–1116. DOI: 10.1140/epjc/s10052-006-0175-5.

[62] W. Adam et al. "Reconstruction of electrons with the Gaussian sum filter in the CMS tracker at LHC". In: *eConf* C0303241 (2003). [J. Phys.G31,N9(2005)], TULT009. DOI: 10.1088/0954-3899/31/9/N01. arXiv: physics/0306087 [physics.data-an].

[63] Matteo Cacciari, Gavin P. Salam, and Gregory Soyez. "The Anti-k(t) jet clustering algorithm". In: *JHEP* 04 (2008), p. 063. DOI: 10.1088/1126-6708/2008/04/063. arXiv: 0802.1189 [hep-ph].

[64] Matthias Schröder. "Performance of jets at CMS". In: *J. Phys. Conf. Ser.* 587.1 (2015), p. 012004. DOI: 10.1088/1742-6596/587/1/012004.

[65] CMS Internal. *Jet energy scale and resolution performances with 13TeV data*. Tech. rep. June 2016. URL: https://cds.cern.ch/record/2160347.

[66] "Measurement of inclusive jet cross sections in $Z/\gamma^* \to e^+e^-$ + jets production in $p\bar{p}$ collisions at $\sqrt{s}$ = 1.96 TeV". In: *Phys. Rev. Lett.* 100 (10 2008), p. 102001. DOI: 10.1103/PhysRevLett.100.102001. URL: http://link.aps.org/doi/10.1103/PhysRevLett.100.102001.

[67] Georges Aad et al. "Measurement of the production cross section of jets in association with a Z boson in pp collisions at $\sqrt{s} = 7$ TeV with the ATLAS detector". In: *JHEP* 1307 (2013), p. 032. DOI: 10.1007/JHEP07(2013)032. arXiv: 1304.7098 [hep-ex].

[68] **ATLAS** Collaboration. "Measurement of the production cross section for Z/γ^* in association with jets in pp collisions at $\sqrt{s} = 7$ TeV with the ATLAS detector". In: *Phys. Rev. D* 85 (3 2012), p. 032009. DOI: 10.1103/PhysRevD.85.032009. URL: http://link.aps.org/doi/10.1103/PhysRevD.85.032009.

[69] V. Khachatryan et al. "Measurements of jet multiplicity and differential production cross sections of $Z+$ jets events in proton-proton collisions at $\sqrt{s} = 7$ TeV". In: *Phys.Rev.* D91 (2015), p. 052008. DOI: 10.1103/PhysRevD.91.052008. arXiv: 1408.3104 [hep-ex].

[70] Vardan Khachatryan et al. "Measurements of differential production cross sections for a Z boson in association with jets in pp collisions at $\sqrt{s} = 8$ TeV". In: *JHEP* 04 (2017), p. 022. DOI: 10.1007/JHEP04(2017)022. arXiv: 1611.03844 [hep-ex].

[71] Yuri L. Dokshitzer, Dmitri Diakonov, and S. I. Troian. "On the Transverse Momentum Distribution of Massive Lepton Pairs". In: *Phys. Lett.* 79B (1978), pp. 269–272. DOI: 10.1016/0370-2693(78)90240-X.

[72] John C. Collins, Davison E. Soper, and George F. Sterman. "Transverse Momentum Distribution in Drell-Yan Pair and W and Z Boson Production". In: *Nucl. Phys.* B250 (1985), pp. 199–224. DOI: 10.1016/0550-3213(85)90479-1.

[73] The CMS collaboration. "Determination of jet energy calibration and transverse momentum resolution in CMS". In: *Journal of Instrumentation* 6.11 (2011), P11002. URL: http://stacks.iop.org/1748-0221/6/i=11/a=P11002.

[74] CMS Collaboration. *Jet energy scale uncertainty sources*.

[75] S. Agostinelli et al. "GEANT4—a simulation toolkit". In: *Nucl. Instrum. Meth. A* 506 (2003), p. 250. DOI: 10.1016/S0168-9002(03)01368-8.

[76] Stefano Frixione Rikkert Frederix. "Merging meets matching in MC@NLO". In: (2012), pp. 01–41. DOI: 10.1007/JHEP12(2012)061. arXiv: 1209.6215 [hep-ph].

[77] CMS Collaboration. *Underlying Event tunes and Double Parton Scattering*. CMS Physics Analysis Summary GEN-14-001. DESY, 2014. URL: https://cms-physics.web.cern.ch/cms-physics/public/GEN-14-001-pas.pdf.

[78] Richard D. Ball et al. "Parton distributions for the LHC Run II". In: *JHEP* 04 (2015), p. 040. DOI: 10.1007/JHEP04(2015)040. arXiv: 1410.8849 [hep-ph].

[79] Carlo Oleari. "The POWHEG-BOX". In: (2010), p. 01. DOI: 10.1016/j.nuclphysbps.2010.08.016. arXiv: 1007.3893 [hep-ph].

[80] Michal Czakon and Alexander Mitov. "Top++: A Program for the Calculation of the Top-Pair Cross-Section at Hadron Colliders". In: *Comput. Phys. Commun.* 185 (2014), p. 2930. DOI: 10.1016/j.cpc.2014.06.021. arXiv: 1112.5675 [hep-ph].

[81] T. Gehrmann et al. "W^+W^- Production at Hadron Colliders in Next to Next to Leading Order QCD". In: *Phys. Rev. Lett.* 113.21 (2014), p. 212001. DOI: 10.1103/PhysRevLett.113.212001. arXiv: 1408.5243 [hep-ph].

[82] Michiel Botje et al. "The PDF4LHC Working Group Interim Recommendations". In: (2011). arXiv: 1101.0538 [hep-ph].

[83] Jon Butterworth et al. "PDF4LHC recommendations for LHC Run II". In: *J. Phys.* G43 (2016), p. 023001. DOI: 10.1088/0954-3899/43/2/023001. arXiv: 1510.03865 [hep-ph].

[84] CMS Internal. *Baseline muon selections for Run-II*. 2018. URL: https://twiki.cern.ch/twiki/bin/viewauth/CMS/SWGuideMuonIdRun2#Muon_Identification (visited on 02/23/2018).

[85] CMS Internal. *Cut Based Electron ID for Run 2*. 2017. URL: https://twiki.cern.ch/twiki/bin/view/CMS/CutBasedElectronIdentificationRun2Archive Spring15_selection_25ns (visited on 05/10/2017).

[86] CMS Collaboration. "Pileup Jet Identification". In: (2013).

[87] J. Han and A. Bodek. *Rochester Muon Momentum Correction*.

[88] Andreas Hocker and Vakhtang Kartvelishvili. "SVD approach to data unfolding". In: *Nucl. Instrum. Meth.* A372 (1996), pp. 469–481. DOI: 10.1016/0168-9002(95)01478-0. arXiv: hep-ph/9509307 [hep-ph].

[89] G. D'Agostini. "A Multidimensional unfolding method based on Bayes' theorem". In: *Nucl. Instrum. Meth.* A362 (1995), pp. 487–498. DOI: 10.1016/0168-9002(95)00274-X.

[90] CMS Internal. *Recommended Jet Energy Corrections and Uncertainties For Data and MC*. URL: https://twiki.cern.ch/twiki/bin/view/CMS/JECDataMC.

[91] CMS Public. *Jet Energy Corrections: Official Software Tools for applying JEC Corrections and Uncertainties*. URL: https://twiki.cern.ch/twiki/bin/view/CMSPublic/%20WorkBookJetEnergyCorrections.

[92] Johan Alwall et al. "Comparative study of various algorithms for the merging of parton showers and matrix elements in hadronic collisions". In: *Eur.Phys.J.* C53 (2008), p. 473. DOI: 10.1140/epjc/s10052-007-0490-5. arXiv: 0706.2569 [hep-ph].

[93] Johan Alwall, Simon de Visscher, and Fabio Maltoni. "QCD radiation in the production of heavy colored particles at the LHC". In: *JHEP* 02 (2009), p. 017. DOI: 10.1088/1126-6708/2009/02/017. arXiv: 0810.5350 [hep-ph].

[94] Iain W. Stewart, Frank J. Tackmann, and Wouter J. Waalewijn. "N-Jettiness: An Inclusive Event Shape to Veto Jets". In: *Phys. Rev. Lett.* 105 (2010), p. 092002. DOI: 10.1103/PhysRevLett.105.092002. arXiv: 1004.2489 [hep-ph].

[95] Radja Boughezal, Xiaohui Liu, and Frank Petriello. "Phenomenology of the Z-boson plus jet process at NNLO". In: *Phys. Rev.* D94.7 (2016), p. 074015. DOI: 10.1103/PhysRevD.94.074015. arXiv: 1602.08140 [hep-ph].

[96] Radja Boughezal et al. "Z-boson production in association with a jet at next-to-next-to-leading order in perturbative QCD". In: *Phys. Rev. Lett.* 116 (2016), p. 152001. DOI: 10.1103/PhysRevLett.116.152001. arXiv: 1512.01291 [hep-ph].

[97] Sayipjamal Dulat et al. "New parton distribution functions from a global analysis of quantum chromodynamics". In: *Phys. Rev. D* 93 (2016), p. 033006. DOI: 10.1103/PhysRevD.93.033006. arXiv: 1506.07443 [hep-ph].

[98] Kirill Melnikov and Frank Petriello. "Electroweak gauge boson production at hadron colliders through $O(\alpha_s^2)$". In: *Phys. Rev. D* 74 (2006), p. 114017. DOI: 10.1103/PhysRevD.74.114017. arXiv: hep-ph/0609070 [hep-ph].

[99] Rikkert Frederix et al. "Four-lepton production at hadron colliders: aMC@NLO predictions with theoretical uncertainties". In: *JHEP* 02 (2012), p. 099. DOI: 10.1007/JHEP02(2012)099. arXiv: 1110.4738 [hep-ph].

[100] Riccardo Abbate et al. "Thrust at N^{3}LL with Power Corrections and a Precision Global Fit for $\alpha_s(m_Z)$". In: *Phys. Rev. D* 83 (2011), p. 074021. DOI: 10.1103/PhysRevD.83.074021. arXiv: 1006.3080 [hep-ph].

[101] Zoltan Ligeti, Iain W. Stewart, and Frank J. Tackmann. "Treating the b quark distribution function with reliable uncertainties". In: *Phys. Rev. D* 78 (2008), p. 114014. DOI: 10.1103/PhysRevD.78.114014. arXiv: 0807.1926 [hep-ph].

[102] A. Valassi. "Combining correlated measurements of several different physical quantities". In: *Nucl. Instrum. Meth.* A500 (2003), pp. 391–405. DOI: 10.1016/S0168-9002(03)00329-2.

[103] Serguei Chatrchyan et al. "Jet Production Rates in Association with W and Z Bosons in pp Collisions at $\sqrt{s} = 7$ TeV". In: *JHEP* 1201 (2012), p. 010. DOI: 10.1007/JHEP01(2012)010. arXiv: 1110.3226 [hep-ex].